Acoustic mapping and monitoring of the seabed
From single-frequency to multispectral multibeam backscatter

Gaida, T.C.

DOI
10.4233/uuid:52b8e925-b619-45f8-9056-39454e82fe02

Publication date
2020

Document Version
Final published version

Citation (APA)
Gaida, T. C. (2020). *Acoustic mapping and monitoring of the seabed: From single-frequency to multispectral multibeam backscatter*. [Dissertation (TU Delft), Delft University of Technology]. https://doi.org/10.4233/uuid:52b8e925-b619-45f8-9056-39454e82fe02

Acoustic mapping and monitoring of the seabed

From single-frequency to multispectral multibeam backscatter

Acoustic mapping and monitoring of the seabed

From single-frequency to multispectral multibeam backscatter

Dissertation

for the purpose of obtaining the degree of doctor
at Delft University of Technology,
by the authority of the Rector Magnificus Prof. dr. ir. T.H.J.J. van der Hagen,
chair of the Board for Doctorates,
to be defended publicly on
Thursday 10 September 2020 at 12:30 o'clock

by

Timo Constantin GAIDA

Master of Science in Geophysics,
Christian-Albrechts-Universität zu Kiel, Germany,
born in Northeim, Germany.

The dissertation has been approved by the promoters.

Composition of the doctoral committee:

Rector Magnificus	chairman
Prof. dr. D.G. Simons	Delft University of Technology, promoter
Prof. dr. ir. M. Snellen	Delft University of Technology, promoter
Independent members:	
Prof. dr. V. Van Lancker	Ghent University and Royal Belgian Institute of Natural Sciences
Prof. dr. ir. E.C. Slob	Delft University of Technology
Prof. dr. ir. C.P.A. Wapenaar	Delft University of Technology
Dr. ir. G. Blacquiere	Delft University of Technology
Other member:	
Dr. T.A.G.P. van Dijk	Deltares and University of Illinois, external Ph.D. advisor

Keywords: Multibeam echosounder, acoustic backscatter, sediment classification, habitat mapping, multispectral, coastal monitoring

Printed by: IPSKAMP printing

ISBN 978-94-028-2129-1

Contents

Summary

With the increasing human activities in the marine environment, such as fisheries, dredging, coastal protection or construction of marine infrastructure, seabed sediment and habitat mapping have become highly relevant for the development of sustainable marine management strategies. Compared to traditional mapping methods, primarily based on bed sampling, multibeam echosounding belongs to the cutting-edge technology to time-efficiently acquire high-resolution bathymetric and backscatter (BS) data over large areas. Using classification methods to combine the acoustic data with ground-truthing, large-scale maps can be automatically and objectively produced, that enables to describe the distribution of benthic habitats or quantify marine resources. However, acoustic sediment classification still does not allow to discriminate between the entire heterogeneity of the seabed and is generally applied to a single multibeam echosounder (MBES) dataset by means of revealing the seabed state only at a given time instant.

Two challenging issues addressed within the scope of this thesis are summarized as: (1) Investigation on the applicability of repetitive multibeam (single-frequency) BS measurements for monitoring the seabed; and (2) Evaluation of the potential of multispectral BS to increase the acoustic discrimination between different seabed environments. Six study sites that comprise two single-frequency (300 kHz) MBES time series datasets and four multispectral (90 to 450 kHz) MBES datasets were considered. A processing algorithm, that accounts for sonar settings and environmental conditions, was developed for single-frequency and further extended to multispectral MBES data.

In a study carried out in the Cleaver Bank (The Netherlands), the applicability of two unsupervised sediment classification methods, namely the Bayesian and principal component analysis, to a multitemporal MBES dataset (time period of 15 months) was investigated. Both methods achieved a good repeatability of the classification results, indicating its suitability for monitoring strategies. Within a second study, that was carried out in a more dynamic environment of the Ameland inlet (The Netherlands) over a time period of two years, the influence of the environment and the MBES system on the actual BS strength was assessed. It was shown that repetitive BS measurements can provide a reliable strategy to monitor coastal nourishments. Sedimentary processes, such as erosion and deposition of certain sediments as well as grain size sorting, could be visualized via the BS-based sediment maps. Hence, acoustic sediment classification contributes to current nourishment monitoring strategies, that merely determine volume changes based on bathymetric measurements.

Furthermore, an extension of the Bayesian classification method to multispectral BS data was developed and applied to MBES datasets (100 to 400 kHz) acquired in the Bedford Basin and in the Patricia Bay (both Canada). Integrating the information retrieved at a single frequency into a multispectral classification map allowed for an improved acoustic discrimination between different seabed environments. The combination of the lowest and highest frequency revealed the most additional information about the seabed. Nevertheless, the benefit of multiple frequencies highly depends on the local seabed.

As also shown in two additional studies (90 to 450 kHz) carried out in the Vlietland Lake and Port of Rotterdam (both The Netherlands), an increased acoustic discrimination was mainly observed for fine sediments (mud to sandy mud). For the coarser sediments (e.g., sand with shells, gravel), currently no clear increase in acoustic discrimination could be identified based on the performed analysis of multi-frequency multibeam data. Emphasizing here that the range and the spatial coverage of the coarser sediments were limited in the considered studies and more investigations are required. Observations on the fine sediments revealed enormous variations in the BS level at the lowest frequencies (90 and 100 kHz). This was co-located with a significant variation in the measured depth between the lowest and highest frequencies, due to a larger penetration into the subsurface of the lower frequencies. Therefore, a model to simulate bathymetric measurements in a layered medium was developed. The comparison of the modeling results with the MBES measurements and the geological settings indicated that the BS and bathymetry measured at the different frequencies correspond to different parts of the surficial seabed and shallow subsurface. These observations indicate the potential for 3D sediment classification in areas with depositions of fine sediments on the seabed. All these findings can result in the establishment of multispectral multibeam echosounding as a novel strategy for revolutionizing acoustic seabed mapping.

Finally, different Kriging methods combined with a new approach to classify the interpolated MBES BS into distinct classes were tested in order to produce a full-coverage sediment map from sparsely distributed MBES data. The application to the Cleaver Bank datasets and a comparison with ground-truthing and traditional sediment maps (i.e., based only on bed samples) demonstrated that this approach resolves lateral heterogeneities on a kilometer scale and outperforms traditional mapping. The developed method allows to retrieve a full-coverage sediment map when weather conditions, time limitations or inaccessibility of an area hampers the acquisition of a full-coverage MBES dataset.

Samenvatting

Met de toenemende menselijke activiteiten in het mariene milieu, zoals visserij, baggeren, kustbescherming of de bouw van mariene infrastructuur, is in het kaart brengen van zeebodemsedimenten en habitats zeer relevant geworden voor de ontwikkeling van strategieën voor duurzaam marien beheer. In vergelijking met traditionele karteringmethodes, voornamelijk gebaseerd op bemonstering, is multibeam echosounding een geavanceerde technologie om efficiënt hoge-resolutie bathymetrische en backscatter (BS) gegevens over grote gebieden te verkrijgen. Met behulp van methodes om de akoestische gegevens te combineren met informatie uit de monsters, kunnen grootschalige kaarten automatisch en objectief worden geproduceerd, waarmee de verdeling van sediment of benthische habitats kan worden beschreven. Bij aanvang van het promotieonderzoek was de verwachting dat met verdere aanpassingen aan de methodes voor akoestische classificatie van sedimenten, de mogelijkheden van de methodes om de verschillende sedimenten van elkaar te onderscheiden, dat wil zeggen een onderscheid te maken tussen de gehele heterogeniteit van de zeebodem, nog verder vergroot kan worden. Verder worden nu in het algemeen de methodes toegepast op een enkele set van multibeammetingen (MBES), waarbij dus specifiek de zeebodemtoestand op een enkel tijdstip in kaart wordt gebracht.

De twee uitdagende kwesties die in het kader van dit proefschrift dus worden behandeld, kunnen worden samengevat als: (1) Onderzoek naar de toepassing van herhaalde multibeam ('single'-frequentie) BS-metingen om de ruimtelijke sedimentverdelingen in tijd te volgen; en (2) Onderzoek naar het potentieel van multispectrale BS om de akoestische discriminatie tussen verschillende zeebodemomgevingen te vergroten. Zes onderzoekslocaties met twee 'single'-frequentie (300 kHz) MBES-datasets in een tijdreeks en vier multispectrale (90 tot 450 kHz) MBES datasets zijn geanalyseerd. Een verwerkingsalgoritme, dat rekening houdt met sonarinstellingen en omgevingscondities, werd ontwikkeld voor 'single'-frequentie en verder uitgebreid tot multi-spectrale MBES-gegevens.

In een onderzoek op de Klaverbank (Nederland) is de toepasbaarheid van twee 'unsupervised' sedimentclassificatiemethoden, namelijk de Bayesian en een aanpak gebaseerd op de 'Principal Component Analysis', getest op data verkregen gedurende herhaalde MBES-metingen (tijdsperiode van 15 maanden). Beide methodes bereikten een goede herhaalbaarheid van de classificatieresultaten, hetgeen de geschiktheid ervan voor monitoringstrategieën aangeeft. In een tweede onderzoek, dat werd uitgevoerd in de meer dynamische omgeving van het Amelander zeegat (Nederland) gedurende een periode van twee jaar, werden de invloeden van de omgeving en het MBES-systeem op de werkelijke BS-sterkte beoordeeld. Er is aangetoond dat het gebruik van herhaalde BS-metingen een betrouwbare strategie is om kust suppleties te volgen. Sedimentaire processen, zoals erosie en afzetting van sedimenten en sediment korrelgroottesortering, kunnen worden gemonitord via de op BS gebaseerde sedimentkaarten. Vandaar dat de akoestische classificatie van sedimenten bijdraagt aan de huidige monitoringsstrategieën voor suppleties, die alleen volumeveranderingen bepalen op basis van bathymetrische metingen.

Bovendien werd, uitgaande van de Bayesian classificatiemethode, een multispectrale classificatiemethode ontwikkeld en toegepast op MBES-datasets (100 tot 400 kHz) van het Bedford Basin en Patricia Bay (beide Canada). Het integreren van de informatie van de verschillende frequenties in een multispectrale classificatiekaart zorgde voor een verbeterde akoestische discriminatie tussen verschillende zeebodemomgevingen. De combinatie van de laagste en hoogste frequentie gaf de meeste aanvullende informatie over de zeebodem. Desalniettemin hangt de toegevoegde waarde van het gebruik van meerdere frequenties sterk af van de lokale zeebodem.

Zoals ook blijkt uit aanvullende studies (90 tot 450 kHz), uitgevoerd in het Vlietlandmeer en de haven van Rotterdam (beide Nederland), wordt een verhoogde akoestische discriminatie gerealiseerd voor fijne sedimenten (slib tot zandige slib) als gebruik wordt gemaakt van meerdere frequenties. Voor de grove sedimenten (bijvoorbeeld zand met schelpen of grind) kon geen duidelijke toename van akoestische discriminatie worden geïdentificeerd op basis van de gebruikte analyse technieken. Hierbij moet wel benadrukt worden dat de verscheidenheid en bedekkingsgraad van de grove sedimenten beperkt waren in de bestudeerde gebieden en dat meer onderzoek op dit gebied nodig is. Waarnemingen van de fijne sedimenten onthulden enorme variaties in het BS-niveau bij de laagste frequenties (90 en 100 kHz). Dit ging samen met een significante variatie in de gemeten bathymetrie tussen de laagste en hoogste frequenties, door grotere penetratie van lagere frequenties in de ondergrond. Voor verdere studie werd een model ontwikkeld om bathymetrische metingen in een gelaagd medium te simuleren. De vergelijking van de modelresultaten met de MBES-metingen en de geologie gaf aan dat de BS en bathymetrie, zoals gemeten bij de verschillende frequenties, overeenkomen met verschillende delen van de oppervlaktebodem en ondiepe ondergrond. Deze waarnemingen geven het potentieel aan voor 3D-sedimentclassificatie in gebieden met afzettingen van fijne sedimenten op de zeebodem. Al deze bevindingen kunnen resulteren in het gebruik van multispectrale multibeam echosounding, een revolutie voor het in kaart brengen van zeebodems.

Ten slotte zijn verschillende Kriging methodes gecombineerd met een nieuwe aanpak om de geïnterpoleerde MBES BS in verschillende klassen te classificeren, om een sedimentkaart met volledige dekking te maken op basis van MBES gegevens zonder volledige dekking. De toepassing op de Klaverbankdata en een vergelijking met sediment monsters en traditionele sedimentkaarten (gebaseerd op monsters) toonden aan dat deze benadering laterale heterogeniteit op een schaal van kilometers oplost en beter presteert dan traditionele kartering. De ontwikkelde methode maakt het mogelijk om een sedimentkaart met volledige dekking te verkrijgen, ook wanneer weersomstandigheden, tijdslimieten of ontoegankelijkheid van een gebied de verwerving van MBES-gegevens met volledige dekking belemmeren.

Nomenclature

Latin symbols

a	Particle size
$\boldsymbol{a}$	Eigenvector (PCA)
A	Ensonified footprint, area
A_0	Unit area (defined as $1\,\mathrm{m}^2$)
A_b	Ensonified footprint in beam limited regime
A_p	Ensonified footprint in pulse limited regime
$\mathbf{A}$	Eigenvector matrix (PCA)
b	Number of correlated variables (PCA)
b_p	Beam pattern, directivity pattern
B	Bulk modulus
B_w	Receiver bandwidth
$BP\,(BP_T, BP_R)$	Beam pattern, directivity pattern in dB (Transmission and Reception)
BS	Backscatter strength in dB
BS_c	Backscatter correction term in dB
c, c_p	Sound speed, compressional wave velocity
c_s	Shear wave velocity
$\tilde{c}$	Complex sound velocity
$\hat{c}$	Sound speed ratio between two layers
$\dot{c}$	Cluster centroid (k-means clustering)
C	Curvature
C_1, C_2	Coefficients in Kirchhoff approximation (APL)
C_h	Structure function in Kirchhoff approximation (APL)
C_p	Transfer coefficient (Layered backscatter model)
d	Distance between sediment layers
d_0	Reference length of $1\,\mathrm{mm}$
d_{50}	Median grain size
d_e	Spatial delay on array elements at beamforming
dx_{slope}	Spatial resolution of slope correction
D	Number of samples used for interpolation (Kriging)
e	Euler's number
E	Coefficient in forward loss equation (APL)
EL	Echo level
f	Frequency
F	Slope averaging integral (APL)
$\mathbf{F}$	Data matrix (PCA)
g	Standard deviation of the interface relief amplitude
g_0	Reference length of $1\,\mathrm{cm}$

G	Acoustic array response
h	Water depth, Water column
$\tilde{h}$	Distance between sample points (Kriging)
H	Hypothesis in Bayesian decision rule
i	Imaginary unit
I	Acoustic intensity
I_b	Backscattered acoustic intensity
I_{dB}	Acoustic Intensity in decibel relative to 1 µPa
I_i	Incident acoustic intensity
I_{ref}	Reference intensity equal to 0.67×10^{-18} W/m^2
I_s	Scattered acoustic intensity
J	Number of scatterers
k	Wavenumber
$\dot{k}$	Number of clusters (k-means clustering)
K	Modified wavenumber in composite roughness approximation (APL)
L_n	Number of layers
$L(L_T, L_R)$	Array length (Transmitter and Receiver)
m	Number of Gaussian distributions (Bayesian)
	Array element (i.e., hydrophone or projector)
M	Total number of bins per histogram (Bayesian)
	Number of receiving elements
Mz	Median grain size in logarithmic scale
n	Number of measurements per BS histogram bin (Bayesian)
	Number of samples within interpolation neighbourhood (Kriging)
	Number of measurements per correlated variable (PCA)
N	Number of classified data points (multispectral Bayesian)
	Number of pairs of sample points (Kriging)
N_s	Number of scatterpixels per beam
p	Acoustic pressure
p_0	Acoustic pressure amplitude 1 m away from source
p_{dB}	Acoustic pressure in decibel relative to 1 µPa
p_i	Incident acoustic pressure
p_r	Reflected acoustic pressure
p_{ref}	Reference pressure equal to 1 µPa
p_{rms}	Root-mean-square acoustic pressure
p_{rms_b}	Backscattered root-mean-square acoustic pressure
p_{rms_i}	Incident root-mean-square acoustic pressure
p_t	Transmitted (refracted) acoustic pressure
P	Acoustic power
PSE	Prediction Standard Error (Kriging)
q	Strength (coefficient) of Gaussian distribution (Bayesian)
q_c	Coefficients in Kirchhoff approximation (APL)
Q_1, Q_2	Coefficient in composite roughness approximation (APL)
r	Distance to the source, Slant range
R	Reflection coefficient

$\hat{R}$	Pearson correlation coefficient
R_a	Rayleigh parameter
R_r	Lossy Rayleigh coefficent (APL)
RL	Forward reflection loss
$RMSE$	Root-Mean-Square estimation Error (Kriging)
$RMSSE$	Root-Mean-Square Standardized estimation Error (Kriging)
$\mathbf{R}$	Covariance matrix (PCA)
s	Transmitted sound pressure signal
s_0	Unsampled location (Kriging)
s_A, s_B	Signal measured at sub-array A and B
S	Sediment suspension concentration
$\dot{S}$	Cluster (k-means clustering)
S_a	Salinity
SH	Transducer sensitivity in dB
SL	Source level in dB
t	Time instant
t_D	Two-way travel time of signal for all angles
t_{nadir}	Two-way travel time of signal at nadir
δt	Travel time in sediment layer
T	Transmission coefficient
T_e	Integration time
TL	Transmission loss in dB
TS	Target strength in dB
T_w	Water temperature
u	Proportionality constant for scattering
U	Acoustic shadowing (APL)
v_1, v_2	Coefficients in large-roughness scattering approximation (APL)
V	Large-scale rms slope (APL)
w	Coefficient in composite roughness approximation (APL)
W	Hanning tapering function
x	Space coordinate, Horizontal distance between receiver and scatterer Sampled location (Kriging)
δx	Distance between array elements or scatterers
Δx	Grid cell size
x_s	Data point within the cluster (k-means)
x_{lb}	Lower bound of ensonified footprint
x_{ub}	Upper bound of ensonified footprint
$\boldsymbol{x}$	Vector containing Gaussian parameters (Bayesian)
X_1, X_2, X_3	Coefficients in roughness interpolation function (APL)
y	Space coordinate, BS value of bin in the BS histogram (Bayesian)
$\bar{y}$	Mean of Gaussian distribution (Bayesian)
Y	Complex function in composite roughness approximation (APL)
$\mathbf{Y}$	Matrix containing principal components (PCA)

z	Space coordinate
Z	measured value (Kriging)
$\hat{Z}$	predicted value (Kriging)

Greek symbols

α	Attenuation coefficient in dB/m
α_s	Attenuation coefficient due to suspended material in water in dB/m
α_w	Attenuation coefficient due to dissolved substances in water in dB/m
$\hat{\alpha}$	Attenuation coefficient in Neper/m
β	Decision matrix of Bayesian decision rule
γ	Spectral exponent (APL)
$\tilde{\gamma}$	Semivariogram (Kriging)
Γ	Gamma function (APL)
δ	Loss parameter
Δ	Laplace operator
ϵ_x	Along-track slope
ϵ_y	Across-track slope
ε	random and auto-corrlated error (Kriging)
ζ	Structure function in Kirchhoff approximation (APL)
η	Spectral strength (APL)
H	Power bottom relief spectrum (APL)
$\theta(\theta_R, \theta_T)$	Steering angle (at reception and transmission)
Θ	Beam angle
κ	Kappa coefficient
κ_c	Coefficient in forward loss equation (APL)
λ	Acoustic wavelength
$\lambda_{\mathrm{bedform}}$	Bedform wavelength
$\tilde{\lambda}$	Weighting factor (Kriging)
$\dot{\lambda}$	Eigenvalue (PCA)
$\boldsymbol{\Lambda}$	Eigenvalue matrix (PCA)
μ	Shear modulus
$\tilde{\mu}$	Deterministic trend or function (Kriging)
ν	Kinematic viscosity
$\hat{\nu}$	Degree of freedom (Bayesian)
ρ	Density
$\hat{\rho}$	Density ratio between two layers
ρ_w	Water density
ρ_s	Sediment density
σ	Standard dev. of measurements per BS histogram bin (Bayesian) Prediction standard error (Kriging)
σ_b	Backscattering cross section
$\tilde{\sigma}_b$	modified backscattering cross section in layered medium
σ_{cr}	Composite roughness backscattering cross section

σ_{kr}	Kirchhoff roughness backscattering cross section
σ_{lr}	Large-roughness backscattering cross section
σ_{mr}	Medium-roughness backscattering cross section
σ_{pr}	Perturbation roughness backscattering cross section
σ_r	Roughness backscattering cross section
σ_s	Scattering cross section
σ_t	Target's backscattering cross section
σ_v	Volume backscattering cross section
$\hat{\sigma}_v$	Volume scattering parameter
σ_y	Standard deviation of Gaussian distribution (Bayesian)
τ	Pulse length
τ_{eff}	Effective pulse length
τ_n	Nominal pulse length
$\Upsilon_1, \Upsilon_2, \Upsilon_3$	Coefficients in equation for attenuation of suspended material
$\Delta\varphi$	Phase delay or theoretical phase difference
$\widehat{\Delta\varphi}$	Estimated phase difference
ϕ, ϕ_i	Incident angle (between incident wave and surface normal)
ϕ_{fl}	Incident angle assuming a flat seabed
ϕ_{crit}	Critical incident angle
ϕ_{int}	Intromission incident angle
ϕ_s	Scattering angle (between scattered wave and surface normal)
χ^2	Chi-square goodness of fit value
$\chi^2_{\hat{v}}$	Reduced Chi-square goodness of fit value
ψ	Grazing angle (APL)
ω	Circular frequency
$\Omega(\Omega_R, \Omega_T)$	Beam opening angle (at reception and transmission)

Acronyms

General acronyms

AC	Acoustic Class
ADC	Analog to Digital Converter
ADCP	Acoustic Doppler Current Profiler
APL	Applied Physics Laboratory
ARC	Angular Response Curve
ASC	Acoustic Sediment Classification
BS	Backscatter
CO	Composite roughness approximation
CTD	Conductivity, Temperature, Depth
DGPS	Differential Global Positioning System
EMODnet	European Marine Observation and Data network
GPS	Global Positioning System
GSF	Generic Sensor Format
GUI	Graphical User Interface
KED	Kriging with External Drift
KI	Kirchhoff approximation
LA	Large-roughness scattering approximation
LAT	Lowest Astronomical Tide
MAC	Multispectral Acoustic Class
MBES	Multibeam Echosounder
NAP	Normaal Amsterdams Peil
NCS	Netherlands Continental Shelf
OCK	Ordinary Cokriging
OK	Ordinary Kriging
RTK	Real Time Kinematic
SBES	Singlebeam Echosounder
SBP	Sub-Bottom Profiler
SCK	Simple Cokriging
SIM	Sonar Interface Module
SK	Simple Kriging
SSC	Sediment Suspension Concentration
SSS	Side-Scan Sonar
SVP	Sound Velocity Profiler/Probe
TVG	Time Varying Gain
UCK	Universal Cokriging
UN	Unassigned
UK	Universal Kriging
VO	Volume scattering approximation

Sediment acronyms

C	Clay
sC	sandy Clay
FS	Fine Sand
gS	gravelly Sand
gM	gravelly Mud
gmS	gravelly muddy Sand
(g)S	slightly gravelly Sand
G	Gravel
mS	muddy Sand
mS SH	muddy Sand with Shells
msG	muddy sandy Gravel
sC	sandy Cobble
sG	sandy Gravel
sM	sandy Mud
sM SH	sandy Mud with Shells
S	Sand
S SH	Sand with Shells
S tSH	Sand with traces of Shells
S mSH	Sand with medium amount of Shells
S hSH	Sand with high amount of Shells

1

Introduction

1.1. Background

1.1.1. Mapping the marine environment

The world ocean's exhibit the largest biodiversity on the planet, control the climate, supply enormous amount of natural resources and provide great potential for renewable energies. The marine seabed serves thereby as habitats for benthic organisms, contains resources such as sediments, minerals and metals, supports the foundation of offshore wind farms or acts as a natural barrier for coastal erosion. In order to optimally use the marine resources and, at the same time, protect marine species and coastal areas, mapping and monitoring of the marine seabed are required.

While radar (radio detection and ranging) or optical sensors are used to map the terrestrial surface, mapping the bottom of the ocean's in a similar spatial resolution requires to a large extent the use of acoustic sensors [1]. The application of electromagnetic waves is limited to very shallow environments and clear waters, as water is a highly dissipative medium resulting in a rapid attenuation of light and radio waves [2]. In contrast, the attenuation of acoustic waves is significantly lower, and thus the travel distance is much higher. Therefore, acoustic waves are highly suitable for the application in the underwater environment [3].

Since the first sonar (sound navigation and ranging) was introduced in the beginning of the 20th century, various acoustic systems have been developed to explore and visualize the underwater environment [4]. Due to the diversity of the applications, the acoustic system varies in frequency, aperture and mounting configuration (Fig. 1.1).

In the 1920s singlebeam echosounders (SBESs) were invented to determine the seabed bathymetry [4]. These systems are mounted on the vessel and transmit an acoustic pulse in a narrow beam towards the seabed. Measuring the sound speed and the travel time of the signal in the water column allows to calculate the water depth. In the 1960s Side-scan sonars (SSSs) were developed and solely designed for high-resolution acoustic imaging of the seabed [4]. The main types of SSSs operate in a frequency range between 65 to 500 kHz and are generally towed behind the vessel at a short distance to the seabed [5]. The SSS emits an acoustic pulse across a wide angular range forming a wide swath (stripe) perpendicular to the survey direction and measures the backscattered signal intensity at the seabed as a function of time.

Since the multibeam echosounder (MBES) emerged in the late 1970s on the market, it became the most efficient sensor to determine the seabed bathymetry [4]. Depending on the water depth, the frequency of the acoustic signal ranges between 12 to 700 kHz to map areas ranging from the deep sea to shallow lagoons [5]. The system transmits an acoustic pulse that is narrow in the survey direction and forms a wide swath perpendicular to it. During the reception, beam steering allows to estimate the travel time of the signal for a large number of pre-defined beam angles along the swath (typically 200 to 800 beams). Therefore, the MBES enables to map large areas in a relatively short time period by covering an area of up to seven times the water depth [5]. In addition to the acquisition of the bathymetry, both the MBES and SBES can be used, in a similar way as a SSS, to image the seabed properties by using the reflected and scattered signal intensity at the seabed.

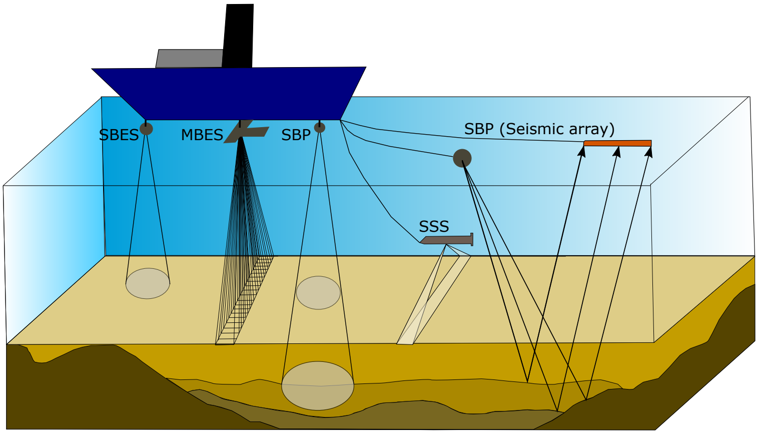

Figure 1.1: Various acoustic systems to investigate the seabed and subsurface.

In the 1930s, seismic systems, which also employ acoustic waves although with a lower frequency (< 10 kHz), were developed to explore the subsurface of the seabed [5]. Two different configurations of a sub-bottom profiling system (SBP) are established. Either the sound source and the receiver are combined in a transducer (similar to the SBES and MBES) and mounted on a vessel or separated, as a sound source (e.g., boomer, sparker, air guns) and receiver (e.g., hydrophone array) towed behind the vessel (Fig. 1.1). Due to the lower frequencies, the acoustic signal penetrates into the subsurface where reflection occurs at contrasting impedance in the sediments. The actual penetration depth depends on the employed signal frequency and the geoacoustic properties of the sediment.

While seismic systems are applied for the investigation of the subsurface, SBES, SSS and MBES are mainly invented to map the seabed. In this context mapping the seabed is twofold: revealing the seabed morphology (i.e., water depth) and visualizing the seabed properties (e.g., sediments).

1.1.2. Acoustic imaging of the seabed

Acoustic imaging of the seabed utilizes the backscattered signal that contains information about the composition of the seabed and about natural or man-made obstacles such as stones or pipelines. This technique involves two different mechanisms. The first one requires that the acoustic sensor is closely above the seabed where the obstacle hinders the propagation of the acoustic wave (i.e., acoustic shadowing) [3]. The second process is directly related to the sound scattering at the seabed, where the frequency, the incident angle and the composition of the seabed determines the amount of the scattered energy [6]. This process is physically quantified by the backscatter (BS) strength, which is defined as the ratio between the intensities of the backscattered and incident wave per unit area (expressed in decibels) [4].

Whereas the acoustic shadowing is mostly beneficial for SSS, the actual measurement of the BS strength is of use for both the SSS and MBES. To derive the actual BS strength from the received echo at the sonar, the influence of the environment (e.g., water column properties, seabed morphology) on the sound propagation as well as system effects (e.g., sonar settings, transducer sensitivity) during the transmitting and receiving process requires consideration [7]. Sound propagation effects can be corrected for by measuring the water column properties and using sound propagation models. On the other hand, imperfect corrections of the system effects often complicate the measurement of the actual BS strength, and therefore the measured and processed data are often considered as a relative measure of the BS strength.

Even though the SSS mostly achieves higher spatial resolution because it is towed closer to the seabed and thus shorter sound pulses and higher frequencies can be applied, the MBES outperforms the SSS in terms of BS processing capabilities. Beam steering during sound reception at the MBES not only enables the determination of the water depth across the sonar swath with an accurate geographical positioning but also provides the angles of the incoming signals in the various beams. The measured seabed morphology in combination with the angular information allows to measure the backscattered signal as a function of the incident angle on the seabed. This provides the following advantages: firstly, it allows to produce a precise georeferenced acoustic image, called BS mosaic, in which the angular dependency of BS is removed; secondly the BS angular response curve, which is characteristic for each sediment, can be employed as an additional sediment characterization tool. Measuring remotely the relative BS strength enables to characterize and distinguish sediments over larger areas with a remarkable quality. This capability has originated a rapid developing research field of acoustic sediment and habitat classification in the last two decades with the aim to automatically and objectively produce sediment or habitat maps [8].

1.1.3. Acoustic sediment and habitat classification

Traditional sediment or habitat mapping was purely based on in situ measurements (e.g., bed samples or sediment cores), which were extended to large-scale maps by interpolation techniques or expert interpretation. In fact, in situ measurements provide locally a detailed and accurate description of the seabed properties but it is difficult to obtain an accurate representation of the spatial seabed heterogeneity.

The development of acoustic techniques allowed to couple the conventional in situ sampling with the extensive acoustic data to extend the detailed information to a large area and to reveal small-scale heterogeneities. Conventionally, the acoustic image (i.e., BS mosaic) was divided into regions of similar acoustic characteristics (known as acoustic facies [9] or acoustic themes [10]) based on expert interpretation. In a next stage, the ground truth information was used to label the regions with a corresponding sediment or habitat type [3, 11].

With increasing computing performance, acoustic sediment classification methods were invented to automatically and objectively classify the acoustic data in order to produce large-scale thematic maps (e.g., sediment or habitat maps) [10, 12, 13]. In general, the approaches are divided into two different categories, that means, model (physical) and image-based (empirical) methods [8]. The former compares different characteristics of the acoustic data, such as the signal echo envelope or the angular response pattern of the BS strength, with physical models to reveal the seabed properties via an inversion process [14–16]. Image-based techniques explore acoustic patterns and statistical relationships of similar BS features (e.g., relative BS strength, angular response pattern or textural features) [17, 18]. While model-based techniques require no ground truth information in theory, this approach highly depends on a calibrated system and works poorly in complex environments where it is difficult to model the interaction of the acoustic pulse with the seabed. Contrary, image-based techniques need ground truth information, but can be applied to uncalibrated data and are applicable in complex environments as long as they are sufficiently sampled. In addition, image-based techniques can also incorporate other environmental predictors, for instance, bathymetry and their second derivatives or even hydrodynamic information [19–21].

Image-based techniques can be further grouped into unsupervised and supervised classification [8]. Supervised methods (e.g., random forest, decision tree) require predefined classes of the ground truth data in order to train an algorithm to map, for example, sediment types (output value) based on the acoustic data (input value). In an optimal case the trained algorithm allows to determine the sediment types for all locations covered with acoustic data (e.g., [20]). Unsupervised approaches (e.g., k-means clustering) classify the acoustic data in a first step by identifying similarities or patterns in the acoustic information. The actual class labeling using the ground truth information is carried out in a subsequent and independent step. The class labeling is conducted by identifying the highest correlation between the acoustic class and certain sediment properties (e.g., sediment type, median grain size or shell content) revealed from the ground truth data (e.g., [22]).

1.2. Scope of the thesis

Acoustic sediment classification based on MBES BS has significantly improved the way to map marine sediments [8]. While the majority of the scientific studies have employed a single MBES dataset to map the spatial distribution of sediments or habitats, only a few studies have used repetitive MBES BS measurements to monitor the seabed over a given time period [23–25]. This becomes, in particular, relevant when assessments of the impact of anthropocentric activities on the natural marine system are required. In general, the use of BS data for seabed monitoring is a highly discussed research issue [7]. As previously outlined, an accurate measurement of the BS strength suffers from system and environmental effects. The magnitude of their influence varies among study sites and the operating systems. However, the actual repeatability of the measured BS level in time and the assessment of the effect of the environment on the BS level has only been studied to a limited extent [26–28]. Recently, several studies were conducted for the calibration of the MBES to tackle the systems effects (e.g., [26, 29]), but the proposed approaches are often not feasible for every study site. Thus, alternative approaches that allow the use of MBES BS for monitoring purposes are needed without requiring the system to be fully calibrated. In addition, feasibility studies in different environments need to be accomplished. Within the scope of this thesis, two MBES time series[1] datasets are employed that were acquired in a relatively stable environment (Cleaver Bank, The Netherlands) and a dynamic environment (Ameland inlet system, The Netherlands) (Fig. 1.2). In the first study, the dataset is investigated by two different unsupervised classification methods with a specific focus on the repeatability of the acoustic results. In the second study, the value of MBES BS time series measurements, in addition to MBES bathymetry, to monitor the evolution of a nourished seabed over time is investigated. At the same time, the influence of the environment and the sonar system on the actual BS strength is analyzed in order to evaluate the applicability of repetitive MBES BS measurements for seabed monitoring.

Next to the drive to establish MBES BS as a tool for seabed monitoring, the development of technologies and methodologies to further improve the acoustic discrimination between different seabed environments is of particular interest. In general, MBES BS allows to discriminate between various types of sediments. Nevertheless, seabed heterogeneities and limitations in the geoacoustic resolution of MBES BS can lead to ambiguous mapping results. This occurs when different sediment types or properties have a similar acoustic response resulting in similar BS levels. As previously described, the BS strength is also dependent on the frequency. Experimental and theoretical research demonstrated that specific sediment types have a different acoustic response at various frequencies [30–32]. In that regard, BS data acquired at multiple frequencies is promising to reduce ambiguous acoustic classification results. A recent innovation in the MBES technology, which enables to collect spatially and temporally BS at multiple frequencies, opens a new research

---

[1] The terminology time series is used in two different ways. For the majority of the thesis, time series defines repetitive measurements of MBES backscatter and bathymetry data over time. In the second case, used mainly in Chapter 6, time series also refers to the acoustic signal measured as a function of time.

field with the aim to further increase the acoustic discrimination between different seabed environments. This research field is still in the initial stage and currently there is only a limited number of studies that utilizes multispectral BS (e.g., [33–36]). In order to assess the benefit of multi-frequency MBES data for various environments, four multispectral datasets (Patricia Bay and Bedford Basin, Canada; Vlietland Lake and Port of Rotterdam, The Netherlands) are examined in this thesis (Fig. 1.2) by developing methods to process, interpret and classify the datasets.

In this thesis, a specific focus is given to the Netherlands, since the majority of the employed MBES datasets were acquired in the Netherlands (Fig. 1.2). To date, only a few countries implemented and standardized acoustic classification methods in their national mapping program (e.g., Ireland, Norway). There is still a large part of the sediments in coastal waters that are either not mapped at all or based on traditional sediment mapping, i.e., interpolation of sediment samples and cores. In the case of the Netherlands, acoustic sediment and habitat mapping still play a subordinate role and current sediment maps in the Dutch North Sea are mainly based on traditional mapping techniques [37, 38], except for a few studies (e.g., [13, 19, 39]). Considering the numerous MBESs installed on different vessels and the comparatively extensive acquisition efforts in the Netherlands, an establishment of acoustic sediment classification would support an optimal use of MBES data in order to map unexplored areas and to improve current sediment and habitat maps.

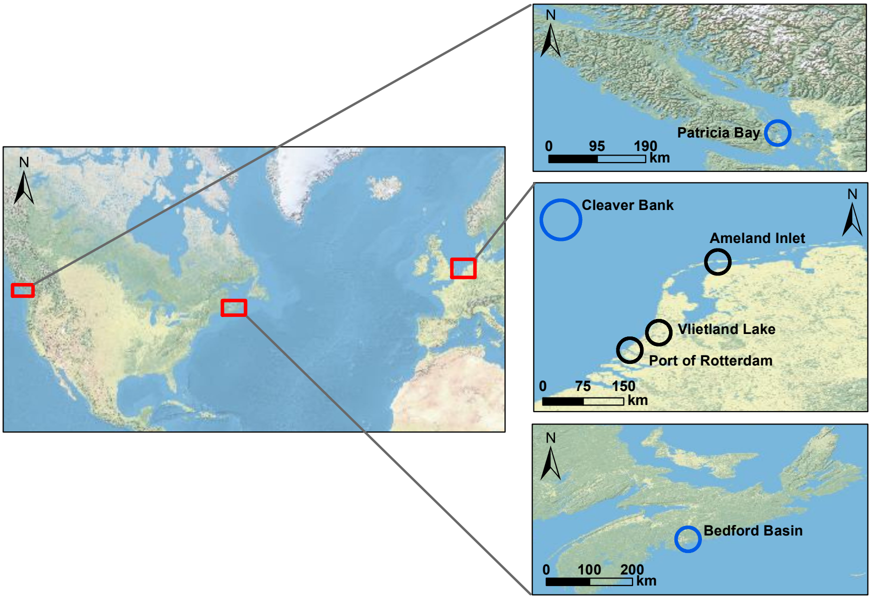

Figure 1.2: Geographical overview of the study sites. Black color indicates participation and blue color indicates no participation in the data acquisition.

1.3. Research objectives

This chapter visualizes the enormous potential of acoustic classification based on MBES BS for mapping seabed sediments and habitats. In terms of the state-of-the-art in MBES technology and acoustic sediment classification, three main research objectives are defined.

1. Investigation on the applicability of repetitive MBES BS measurements for environmental monitoring of the seabed.
2. Evaluation of the potential of multi-frequency MBES BS to increase the acoustic discrimination between different seabed environments.
3. Development, improvement and comparison of classification methods to generate large-scale sediment maps from acoustic data with a specific focus on the Netherlands.

1.4. Thesis outline

Chapter 2 provides information about the acoustic theory with a focus on acoustic wave propagation, the reflection and scattering process, the sonar equation and the concept of beamforming and bathymetric measurements. The sonar equation is used to explain the workflow of processing MBES data. The majority of the data processing tools are developed within this thesis in order to process the collected MBES data. In addition, an acoustic BS model, known as the Applied Physics Laboratory (APL) - model [40], is described to simulate the BS strength. This model is utilized for the interpretation of the experimental data and further used as an input for the developed MBES bottom detection model described in Chapter 6.

Chapter 3 compares current BS-based sediment classification techniques, such as the Bayesian classification method and the principal component analysis, and evaluates the repeatability of the classification results using multitemporal MBES BS datasets[2].

Chapter 4 assesses the applicability of repetitive MBES measurements (time series)[2] to monitor sediment distributions with a main focus on the application to underwater nourishments. Therefore, an evaluation is carried out to investigate to what extent external sources, other than the seabed properties, affect the measured BS strength and the acoustic sediment classification.

Chapter 5 presents a novel development of an objective and semi-automatic method to classify multi-frequency MBES BS data. Furthermore, the use of multi-frequency BS to increase the acoustic discrimination is analyzed.

---

[2] The terminologies multitemporal and time series both indicate MBES measurements over time. In Chapter 3 the term multitemporal is preferably used because the MBES surveys aimed to cover a large area without a specific focus on retrieving a series of measurements from the same location. The term time series, used in Chapter 4, indicates repetitive MBES surveys, which aimed to cover the same area multiple times.

Chapter 6 is a follow-up on the previous chapter, where the effect of frequency dependent signal penetration on multi-frequency BS and bathymetry data is investigated. A model to simulate the MBES bathymetric measurements in a layered medium is developed and used as an interpretation tool for the measured multi-frequency MBES data.

Chapter 7 introduces geostatistical modeling and presents a new approach to classify interpolated MBES BS to produce full-coverage sediment maps from sparsely distributed MBES data. The results are compared with traditional sediment maps, primarily based on bed sampling, and BS-based sediment classification results (i.e., Bayesian classification method).

Chapter 8 provides the main conclusions and an outlook for future research.

Published articles

This thesis consists to a large extent of articles that are published in dedicated journals. These articles present the general theory about underwater acoustics only to a limited extent, while some information about the data processing are partly repeated. Therefore, a theoretical background about underwater acoustics and a description of the acoustic data processing are provided in the second chapter. The following chapters contain the main parts of the articles and treat the three main research objectives. Some repetitions in particular in the different chapter introductions may occur. To allow the readership to read the chapters individually, the introduction from the published articles were kept unchanged. Nevertheless, repeated methodologies and study area descriptions are moved to the chapters where they are introduced for the first time. Some mathematical symbols, abbreviations and terms are modified with respect to the published articles to allow a consistent notation in this thesis. References to sections and figures among the chapters are added to indicate the relation between the research published in the different articles.

2

Acoustic theory

Everything should be made as simple as possible, but not simpler.

Albert Einstein

This chapter summarizes some background information about underwater acoustics to provide sufficient knowledge for a better understanding of subsequent chapters. Starting with the wave equation, various measures of sound are presented. The interaction of sound with the seabed, that means reflection and scattering, is explained. A specific focus lies on scattering and the introduction to the modeling of backscattering. A widely used scattering model, known as the Jackson model or APL-model, is outlined. The APL-model is used throughout the thesis to support the interpretation of the multibeam backscatter measurements. It is further used as an input for a model to simulate the backscatter strength in a layered medium and for a model to simulate the bathymetric measurement of a multibeam echosounder (MBES). An overview of the working principle of a MBES is provided and the concept of beamforming is described. Furthermore, the bathymetric measurement techniques of a MBES, known as amplitude and phase detection, are explained. The sonar equation, providing the necessary elements to process MBES data in order to retrieve a measure of the backscatter strength, is stated. Lastly, the algorithm to account for the seabed morphology, when retrieving the backscatter from MBES data, is explained.

2.1. Acoustic waves

The wave equation is the basis for describing wave motion in any medium. The solution of the wave equation, using specific boundary conditions, provides an exact equation for the propagation of the wave. To derive the wave equation the principle of the conservation of mass and Newton's second law are used. Combining both principles yields to the linear wave equation [41]

$$\Delta p = \frac{\partial^2 p}{\partial x^2} + \frac{\partial^2 p}{\partial y^2} + \frac{\partial^2 p}{\partial z^2} = \frac{1}{c^2}\frac{\partial^2 p}{\partial t^2} \tag{2.1}$$

where p is the acoustic pressure of the propagating wave in space x, y and z as a function of time t, Δ is the Laplace operator and c is the propagation speed of the wave. Here, the medium is assumed to be homogeneous in space. As can be seen from Eq. (2.1), the wave equation relates the space and time derivatives of the acoustic pressure describing the propagation of the wave [42]. Considering the propagation in three dimensions in an isotropic and dissipative medium, it can be shown that a solution of Eq. (2.1) for a spherical coordinate system is a spherical pressure wave with the acoustic pressure expressed in the complex notation form as

$$p(r,t) = p_0 \frac{1}{r} e^{i(kr-\omega t)} e^{-\hat{\alpha} r} \tag{2.2}$$

where p_0 is the pressure amplitude 1 m from the source, k is the wavenumber ($k = \frac{\omega}{c}$) and ω is the circular frequency defined as $\omega = 2\pi f$ with f the frequency of the acoustic wave. Here, r is a space variable which defines the distance from the observer location to the source. The term $1/r$ describes the decrease of the pressure amplitude p with r caused by the spherical energy spread of the expanding wavefront, known as spherical spreading. The term $e^{-\hat{\alpha} r}$ considers the decay of the pressure amplitude due to scattering and absorption, known as sound attenuation. This scattering implies a redistribution of energy in angles away from the original propagation direction without an overall energy loss and absorption involves a conversion to a different energy form (mostly heat) [2]. Here, attenuation is defined by the parameter $\hat{\alpha}$ (expressed in Neper/m). For convenience the attenuation is generally expressed by the attenuation coefficient α in decibel per meter [dB/m], with respect to $\hat{\alpha}$ via $\alpha = 20\hat{\alpha}\log e$.

Restricting the wave propagation into a single direction x, i.e., the pressure does not depend on y and z, the 3D wave equation (Eq. (2.1)) is simplified to 1D and its solution is

$$p(x,t) = p_0 e^{i(kx-\omega t)} \tag{2.3}$$

with a constant amplitude p_0 and a phase depending on a single Cartesian space coordinate x. The phase of this wave (i.e., $kx - \omega t$) is constant at all points in a plane perpendicular to the x-axis. Hence this wave is called plane wave with plane wavefronts of constant peak-to-peak amplitudes normal to the propagation direction. Taking the real part of Eq. (2.3) gives the acoustic pressure p in the trigonometric notation form [2]

$$p(x,t) = p_0 \cos(kx - \omega t). \tag{2.4}$$

Plane waves and spherical waves are the main tools to model the propagation of acoustic waves. Although sources of underwater sound are in practice point sources generating spherical waves, at a certain distance from the source the curvature of the spherical wavefront is negligible. When these conditions are satisfied, plane waves can be assumed for modeling local processes such as scattering. Spherical waves are descriptive when the decrease of the amplitude with the propagation from a point-like source must be considered (e.g., accounting for transmission loss in sonar processing) [4].

Compressional and shear waves

In fluids, such as water, solely acoustic waves also known as longitudinal waves, compressional waves or P-waves exist. When traveling through the medium, these waves generate compression and extension in successive regions parallel to the propagation direction. In these regions the particles are displaced and the local density is changed with respect to the equilibrium density. These density changes are subject to a restoring force, which is determined by a parameter of the medium, known as bulk modulus. It can be shown that the speed of a compressional wave c_p in a fluid, also known as sound speed, can be related to the density ρ and the bulk modulus B as follows [2]

$$c_p = \sqrt{\frac{B}{\rho}}. \tag{2.5}$$

When sound interacts with an object or the seabed, i.e., solid medium, a second wave type exists. This wave generates a displacement perpendicular to the propagation direction and is called shear wave, transversal wave or S-wave. The transverse motion is subject to a restoring force proportional to the displacement. The proportionality constant relating the restoring force to the displacement is the shear modulus (i.e., ratio of shear stress to shear strain). The shear wave velocity c_s can be related to the density ρ and the shear modulus μ as follows [2]

$$c_s = \sqrt{\frac{\mu}{\rho}}. \tag{2.6}$$

Given a fluid medium, the shear modulus becomes zero and consequently, as seen in Eq. (2.6), fluids do not allow propagation of shear waves.

The sound speed in the water column varies with temperature, salinity and pressure due to the depth. In practice, the sound speed in the water column can be either directly measured using a small acoustic transducer and a reflecting surface or indirectly retrieved from the measurements of other variables via an empirical equation such as [43]

$$c_p = 1449 + 4.6T_w - 0.055T_w^2 + 0.00029T_w^3 + (1.34 - 0.01T_w)(S_a - 35) + 0.016h \tag{2.7}$$

with c_p the sound speed (in m/s), T_w the water temperature (in °C), S_a the salinity (in PSU) and h the water depth (in m). This equation is limited to a depth of

1000 m. Typical sound speeds in the oceans vary between 1450 and 1520 m/s. In shallow water environments, such as the study areas presented in this work, the water masses can be well mixed and thus the sound speed variations within the water column are small (Fig. 2.1). The difference among the sound velocity profiles are caused by seasonal temperature variations and location dependent salinity variations. The study areas differ between pure freshwater (Vlietland Lake), mixed zones with a fluvial and marine influence (Port of Rotterdam), coastal zones with a tidal influence (Ameland inlet), coastal basins connected to the open sea (Bedford Basin and Patricia Bay) and the open sea (Cleaver Bank).

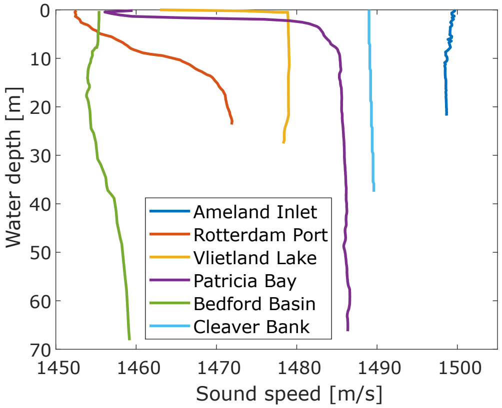

Figure 2.1: Examples of measured sound speeds in the study areas for a given time instant and location. The geographical location of the study areas are shown in Fig. 1.2.

2.1.1. Measure of sound

The propagation of sound exhibits acoustic energy consisting of a kinetic (particle motion) and a potential part (work by elastic forces) [4]. Here, the acoustic intensity I is defined as the mean energy carried by an acoustic wave per unit area. For a plane wave, the acoustic intensity I is related to the acoustic pressure amplitude p_0 or the root-mean-square (rms) pressure p_{rms} as follows

$$I = \frac{p_0^2}{2\rho c} = \frac{p_{\mathrm{rms}}^2}{\rho c}. \tag{2.8}$$

The p_{rms} represents an effective value and is obtained for a plane harmonic wave with amplitude p_0 via

$$p_{\mathrm{rms}}^2 =< p^2 >= \frac{1}{T_e}\int_0^{T_e} p_0^2 \sin^2(kx - \omega t)\mathrm{d}t = \frac{p_0^2}{2} \tag{2.9}$$

with <> describing the mean and T_e the integration time. Another measure is the acoustic power P received by an area A, which is linked to the intensity I via

$$P = IA = \frac{p_{\mathrm{rms}}^2}{\rho c}A. \tag{2.10}$$

Due to the large range of the measured magnitudes, acoustic levels are commonly presented in decibels (logarithmic scale). Note that the use of decibel values requires a reference level. The pressure reference p_{ref} in underwater acoustics is 1 μPa, which corresponds to a reference value in intensity of $I_{\mathrm{ref}}= 6.7 \times 10^{-19}$ W/m^2 with $\rho= 1000$ kg/m^3 and $c= 1500$ m/s. It follows that the absolute pressure and intensity level in decibel relative to 1 μPa are expressed as

$$\begin{aligned} p_{\mathrm{dB}} &= 20 \log \left(\frac{p}{p_{\mathrm{ref}}}\right) \\ I_{\mathrm{dB}} &= 10 \log \left(\frac{I}{I_{\mathrm{ref}}}\right) \end{aligned} \tag{2.11}$$

where the notation is dB re 1 μPa.

2.2. Interaction of sound with the seabed

The interaction of sound with the seabed comprises reflection, transmission and scattering. The contribution of each physical process varies with the frequency and incident angle of the acoustic wave, the geoacoustic parameters of the sediment and the roughness of the surface. In the ideal case of a perfectly flat surface the sound is reflected and transmitted while scattering is absent. The surface then acts as an acoustic mirror reflecting most of the sound at an angle equal to the incident angle (the other part is transmitted into the second medium). However, surfaces, such as the seabed, always exhibit a certain degree of roughness and heterogeneity inducing scattering of the acoustic energy to all angles. Scattering is most significant when the acoustic wavelength is comparable or smaller than the roughness and heterogeneity scale [4].

The interaction of sound with the seabed and subsurface can be described with an increasing complexity by assuming the sediment to be a fluid, elastic or poroelastic medium. In general, scattering and reflection in marine sediments are adequately modeled by assuming them to be a fluid [6]. This simplifies the acoustic modeling as, for example, shear waves can be neglected (Section 2.1, Eq. (2.6)). The remaining part of this chapter considers the marine sediments as a fluid when describing the interaction of sound with sediments. Therefore, the subsequent chapters only deal with compressional waves and for simplification the compressional wave speed (also called sound speed) is defined as c instead of c_p.

2.2.1. Reflection and transmission

Consider a plane acoustic wave arriving at a flat interface between two media with different geoacoustic properties. This interaction can be described by a balance between the incident, the transmitted and the reflected wave (Fig. 2.2). The continuity condition of the acoustic field at the interface and the change of the medium properties (e.g., from water to sediment) describe the alteration of the propagation characteristics of the acoustic wave.

Firstly, the incident wave, arriving with an angle ϕ_1 at the interface, is symmetrically reflected relative to the normal to the interface. This is called specular reflection and generates a reflected wave propagating with an angle ϕ_1.

Secondly, the incident wave is transmitted into the second medium and the propagation direction ϕ_2 of the so-called refracted wave can be expressed via Snells law

$$\frac{\sin(\phi_2)}{\sin(\phi_1)} = \frac{c_2}{c_1} \tag{2.12}$$

with c_1 and c_2 as the compressional wave speed in the first and second medium, respectively.

Finally, the relation between the incident pressure p_i, reflected pressure p_r and transmitted pressure p_t is defined via the reflection coefficient $R = p_r/p_i$ and transmission coefficient $T = p_t/p_i$. The reflection and transmission coefficient are expressed as

$$R(\phi_1) = \frac{\rho_2 c_2 \cos\phi_1 - \rho_1 c_1 \cos\phi_2}{\rho_2 c_2 \cos\phi_1 + \rho_1 c_1 \cos\phi_2}, \tag{2.13a}$$

$$T(\phi_1) = \frac{2\rho_2 c_2 \cos\phi_1}{\rho_2 c_2 \cos\phi_1 + \rho_1 c_1 \cos\phi_2} = 1 + R(\phi_1). \tag{2.13b}$$

with the subscripts 1 and 2 denoting the water and sediment layer, respectively.

As visualized in Fig. 2.2, coarse sediments (e.g., sandy gravel) exhibit higher reflection and transmission coefficients than fine sediments (e.g., sandy mud) due to the higher density and sound speed. A seabed with a sound speed larger than that in water exhibits a critical angle ϕ_{crit}, for which ϕ_2= 90° implying that all refracted energy travels horizontally. This prevents sound transmission into the second medium for all angles larger than the ϕ_{crit}, resulting in total reflection indicated by $|R|$= 1. (Fig. 2.2). In a seabed with a sound speed smaller than that in water, a critical angle does not exist, but instead there is an angle of intromission ϕ_{int}. At this angle the acoustic energy is fully transmitted into the seabed without any reflection (Fig. 2.2) [6].

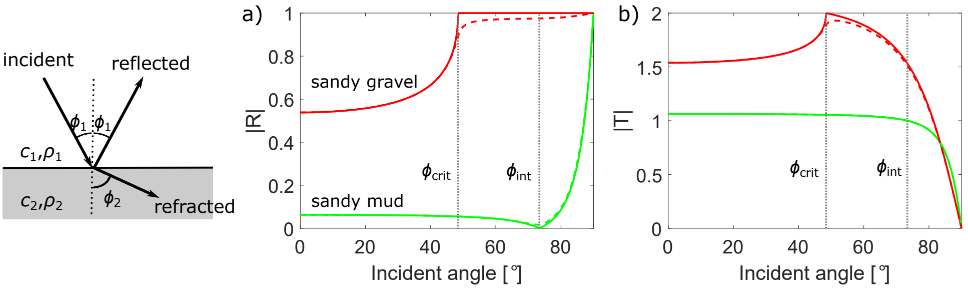

Figure 2.2: Flat-interface a) reflection and b) transmission coefficient for representative sandy mud and sandy gravel seabed. Geoacoustic parameters are retrieved from Hamilton [44] (see Appendix B.1). Water: c_1= 1479 m/s, ρ_1= 1000 kg/m^3; sandy mud: c_2= 1460 m/s, ρ_2= 1149 kg/m^3, α_2= 12.6 dB/m; sandy gravel: c_2= 1977 m/s, ρ_2= 2492 kg/m^3, α_2= 41.0 dB/m. Solid lines visualize lossless case (α_2= 0) and dashed lines indicate lossy case (α_2= see above).

Sediments represent in general a dissipative medium (or lossy medium). This loss is typically accounted for by introducing a complex sound speed $\tilde{c}$, and is expressed as a function of the sediment attenuation coefficient $\hat{\alpha}_2$ and the circular frequency ω as follows

$$\tilde{c}_2 = c_2 - \frac{i|c_2|^2\hat{\alpha}_2}{\omega}. \tag{2.14}$$

Using the complex sound speed $\tilde{c}_2$ in Eq. (2.13), the description of sound reflection and transmission requires small modifications. It thus follows that there is no perfect reflection in contrast with the ideal fluid case (non dissipative). This implies that the acoustic wave can be transmitted and propagated through the subsurface even beyond the critical angle (see Fig. 2.2). Furthermore, Eq. (2.14) implies that attenuation effects in sediments are conventionally expressed with the complex sound speed [4].

The presented reflection model, based on the fluid theory, is an idealization of a perfect flat interface and is not expected to simulate all acoustic interaction with the seabed [6].

2.2.2. Scattering

For high-frequency acoustics, the actual roughness and heterogeneity of the seabed become important and the sound interaction with the seabed is more complex. Irregularities at the interface scatter the incident wave in angles away from the angle of reflection [2]. The scattering is described by the fundamental ratio called scattering cross section. It is a ratio of the intensity of the sound scattered by a unit area I_s to the incident plane wave intensity I_i measured at a distance of 1 m to the scattering source (Fig. 2.3). Accordingly, the scattering cross section σ_s is defined with respect to the incident angle ϕ_i and the scattered angle ϕ_s as follows

$$\sigma_s(\phi_i, \phi_s) = \frac{I_s(\phi_s)}{I_i(\phi_i)} \tag{2.15}$$

with σ_s as a dimensionless ratio defined per unit area and per unit solid angle[1]. Considering only the scattering back towards the direction of the incoming wave, i.e., $\phi_i = \phi_s$, the backscattering cross-section σ_b is obtained

$$\sigma_b(\phi_i) = \frac{I_s(\phi_i)}{I_i(\phi_i)}. \tag{2.16}$$

For the specific condition of $\phi_i = \phi_s$, I_s is noted as I_b, which is called the backscattered intensity per unit area. The more widely used term is the backscatter strength BS which is the decibel equivalent to the backscattering cross section [46]

$$BS(\phi_i) = 10\log(\sigma_b(\phi_i)) = 10\log\left(\frac{I_b(\phi_i)}{I_i(\phi_i)}\right) \tag{2.17}$$

---

[1] In this thesis the scattering cross section is defined as a dimensionless ratio of two intensities in agreement with the Applied Physics Laboratory model (APL-model) [40, 45]. For example, Urick [46] mentioned that the scattering cross section can also be defined as the ratio of the scattered power to the incident intensity.

with BS defined in decibel per 1 m^2 at 1 m distance from the source[2]. The target strength TS defines the scattering from an arbitrary area or object and is related to the backscatter strength as follows

$$TS(\phi_i) = BS(\phi_i) + 10\log\left(\frac{A}{A_0}\right) \tag{2.18}$$

with A_0= 1 m^2 as the reference unit.

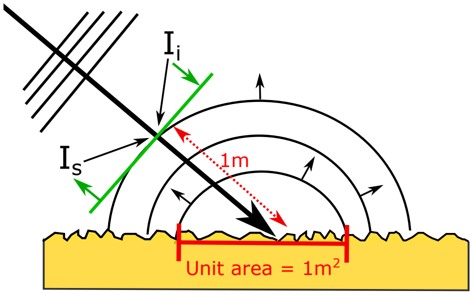

Figure 2.3: Conceptual definitions of backscatter strength BS and backscattering cross section σ_b.

Lambert's law

The angular backscatter response from a rough surface at high frequencies of both sound and light can be approximated by Lambert's law [47]. Let sound of intensity I_i be intercepted at an angle ϕ_i on an area A on the seabed. The acoustic power arriving at that area is $P_i = I_i A\cos\phi_i$. This power is assumed by Lambert's law to be radiated proportional to the cosine of the scattering angle ϕ_s, so that the scattered intensity I_s at a unit distance in direction ϕ_s can be written as [46]

$$I_s = uI_i\cos\phi_i\cos\phi_s A \tag{2.19}$$

with u a proportionality constant. For a unit area the decibel equivalent of Lambert's law is

$$10\log\frac{I_s}{I_i} = 10\log u + 10\log(\cos\phi_i\cos\phi_s) \tag{2.20}$$

and for the backscattered direction, with $\phi_i = \phi_s$, [46]

$$BS(\phi_i) = 10\log u + 10\log(\cos^2\phi_i) = 10\log u + 20\log(\cos\phi_i). \tag{2.21}$$

Assuming no transmission into the lower medium and an equal distribution over the upper half-space, it can be shown by integration that $u = 1/\pi$. The backscatter

---

[2] As mentioned previously in this thesis, $BS(\phi_i)$ is not only angular dependent but also frequency dependent. In general, a MBES generates signals with a very narrow frequency bandwidth (i.e., can be considered as single-frequency or monochromatic) and therefore the common notation of the backscatter strength does not explicitly include the frequency dependency. Still, the backscatter strength can be written as $BS_f(\phi_i)$ or $BS(\phi_i, f)$. The same holds for the backscattering cross-section $\sigma_b(\phi_i)$ and the target strength $TS(\phi_i)$.

strength at normal incidence is therefore $10\log(1/\pi) = -5\,\mathrm{dB}$ and defines the upper limit of BS. Field observations of scattering from rough interfaces (e.g., rocky seabed) indicate that Lambert's law might be applicable for the entire angular range for these sediments while for fine sediments the validity is limited to oblique and grazing angles [4].

Interface roughness and volume scattering

More sophisticated scattering models distinguish between interface roughness scattering (also known as interface scattering or roughness scattering) and volume scattering

$$\sigma_b(\phi) = \sigma_r(\phi) + \sigma_v(\phi) \tag{2.22}$$

with σ_b, σ_r and σ_v as dimensionless cross sections per unit area and solid angle. Interface roughness scattering σ_r is caused by the relief of the interface. Volume scattering σ_v results from the transmission of the incident wave into the sediment and scattering at heterogeneities within the sediment volume (Fig. 2.4). The contribution of both scattering mechanisms depends on the sediment type and the incident angle. While in general for coarse sediments the interface scattering dominates over the entire angular domain, volume scattering becomes generally dominant at oblique angles for fine sediments (an example is given in Fig. 2.5).

For interface scattering the relation between the acoustic wavelength and the interface relief is crucial. This can be quantified by the Rayleigh parameter [48]

$$R_a = 2gk\cos\phi \tag{2.23}$$

with g the standard deviation of the interface relief amplitude and $k = 2\pi/\lambda$ the wavenumber. Here, λ is the acoustic wavelength, being related to the acoustic frequency via $c = f\lambda$. A high Rayleigh parameter ($R_a >> 1$) indicates an acoustically rough interface with a dominance of scattering and negligible contribution of the coherent reflection whereas a low value ($R_a << 1$) represents an acoustically smooth interface with higher importance of reflection. As it can be expected from Eq. (2.23), modeling the interface scattering requires statistical information on the seabed roughness.

The interface scattering can be described by the facet reflection domain around normal incidence and using the Bragg scattering domain at oblique and grazing incidence (Fig. 2.4) [4]. The facet reflection assumes the seabed to consist of numerous facets with a random orientation distributed over the average surface plan. Each of the facets reflects the incident wave around its specular reflection. The majority of the facets is oriented parallel to the interface. It follows, that with increasing incidence angle less facets with a specular reflection equal to the incoming wave direction exist and therefore the BS strength is maximum around normal incidence [4]. Bragg scattering occurs when the incident acoustic wave, with a wavelength small compared to the micro-scale roughness (i.e., high Rayleigh parameter), is scattered at points (i.e., scatterers) along the interface and undergoes constructive interference. Constructive interference exists when the scattered waves are in phase due to the fact that the difference between the path length of the scattered

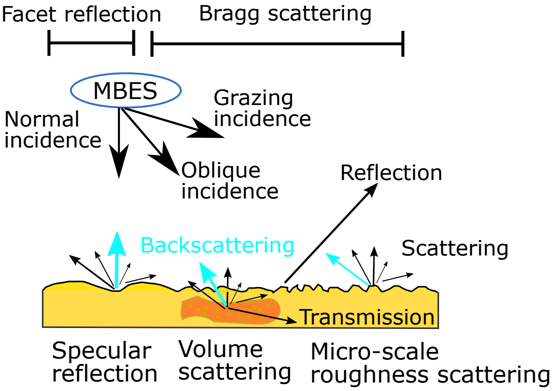

Figure 2.4: Sound interaction with a rough interface. Physical processes of volume scattering and interface roughness scattering (i.e., specular reflection and micro-scale roughness scattering) are presented.

waves are equal to an integer multiple of the wavelength: $2\delta x \sin\phi = n\lambda$, with δx the distance between the scatterers and $n = 1, 2, ...$ as a positive integer.

The volume scattering results from sediment heterogeneities consisting of continuous fluctuations of geoacoustic parameters and discrete heterogeneities (e.g., gas bubbles, shells or stones) in the sediment volume. The volume backscatter strength associated to the sediment heterogeneities are either treated empirically [45, 49] or the discrete scatterers are modeled individually and the contributions are incoherently summed [50]. Furthermore, volume scattering needs to account for the sound transmission through the water-sediment interface (Eq. (2.13)b) and for the ensonified sediment volume which is bounded by the sound absorption in a semi-infinite sediment layer.

2.2.3. Applied Physics Laboratory model (APL-model)

Scattering models are based on the synthesis between models for roughness scattering and volume scattering. Interface roughness scattering models are grouped into the scattering approximation being used [6]. The most commonly used roughness scattering models are the Kirchhoff approximation (also known as tangent-plane approximation) and small-roughness perturbation method (sometimes referred as Rayleigh-Rice perturbation theory). The Kirchhoff approximation is most applicable in the facet reflection domain around normal incidence and the perturbation method in the Bragg domain at oblique and grazing incidence [6]. Furthermore, the sediment can be treated with an increasing complexity as fluid, elastic or poroelastic medium.

In this thesis the APL-model [40], which is a modified version of the model developed by Jackson *et al.* [49], is employed (Fig. 2.5). This model assumes the sediment to be a semi-infinite, dissipative and homogeneous fluid without layering or gradients. The APL-model has implemented the Kirchhoff approximation around normal incidence and the composite roughness approximation for oblique and grazing incidence angles [4]. The latter is based on the small-roughness perturbation approximation including corrections for acoustic shadowing and large-scale bottom slopes. Beside the signal parameters (f, ϕ) and the geoacoustic parameters of the sediment (ρ, c, α, $\hat{\sigma}_v$) and water (ρ, c), the spectral exponent γ and the spectral strength η describing the roughness of the sediment are required for both the Kirchhoff and composite roughness approximation (Table 2.1).

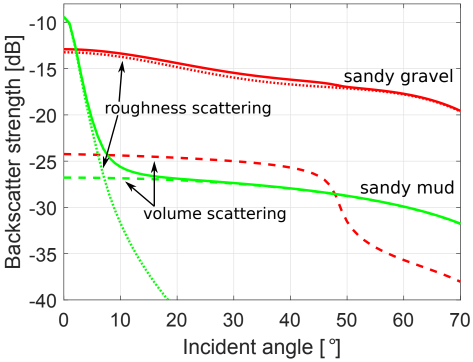

Figure 2.5: APL-model: Backscatter strength at 90 kHz for representative sandy mud and sandy gravel seabed. Individual contribution of roughness and volume scattering are shown as well. Same geoacoustic parameters as used in Fig. 2.2 are employed. In addition, sandy mud: $\gamma = 3.25$, $\eta = 5.17 \times 10^{-4}\,\mathrm{cm}^4$, $\hat{\sigma}_v = 0.001$; sandy gravel: $\gamma = 3.5$, $\eta = 2.19 \times 10^{-2}\,\mathrm{cm}^4$, $\hat{\sigma}_v = 0.002$ are used (see also Appendix B.1).

For very rough seabeds (e.g., gravel and rock), the corresponding roughness parameters fall outside the validity range of the Kirchhoff and composite roughness approximation. Therefore, the APL-model employs an empirical equation referred to as large-roughness scattering approximation, which is still based on the main input parameters of the Kirchhoff and composite roughness method.

All above means that interface roughness scattering is modeled by a synthesis between the following models:

- The Kirchhoff approximation is valid for smooth to moderately rough bottoms (e.g., clay to sand) and incident angles near normal incidence.
- The composite roughness approximation is valid for smooth to moderately rough bottoms (e.g., clay to sand) and incident angles away from normal incidence.
- The large-roughness scattering approximation is used for very rough bottoms (e.g., gravel and rock) for the entire angular range.

To achieve a smooth transition between the validity domain of each model an interpolation is used.

The expression for volume scattering in the APL-model accounts for the effect of refraction at a perfectly flat water-sediment interface and attenuation in a statistically homogeneous sediment. It is further generalized to allow for the effect of attenuation on the transmission coefficient and to correct for acoustic shadowing

Table 2.1: Signal and geoacoustic input parameters for the APL-model. The APL-model consists of the Kirchhoff approximation (KI), composite roughness approximation (CO), large-roughness scattering approximation (LA) and volume scattering approximation (VO). Column ”Model” indicates in which model the parameter is required. Column ”Medium” indicates for which medium the parameter needs to be determined (i.e., sediment (S) or water (W)).

Symbol	Definition	Unit	Medium	Model
ϕ	Incident angle	[°]	-	KI/CO/LA/VO
f	Frequency	[Hz]	-	KI/CO/LA/VO
ρ	Density	[kg/m^3]	W/S	KI/CO/LA/VO
c	Sound speed	[m/s]	W/S	KI/CO/LA/VO
α	Attenuation coefficient	[dB/m]	S	KI/CO/LA/VO
γ	Spectral exponent	[-]	S (bottom relief)	KI/CO/LA
η	Spectral strength	[cm^4]	S (bottom relief)	KI/CO/LA
$\hat{\sigma}_v$	Volume parameter	[-]	S	VO

and large-scale bottom slopes [40]. The actual scattering by the sediment heterogeneities is treated empirically using the volume scattering parameter $\hat{\sigma}_v$. No attempt was made to relate $\hat{\sigma}_v$ to a specific scattering mechanism [49]. Instead reasonable values were obtained by comparing the model predictions with experimental data [40]. This is in contrast to the roughness scattering where γ and η are measurable variables (e.g., via stereophotography). A detailed description of the APL-model is provided in Appendix B.

2.3. Multibeam echosounder theory

2.3.1. Multibeam echosounder and ancillary sensors

A MBES has a transmission and a reception module, which can be either separated into two units (e.g., R2Sonic 2026) or both located in one unit (e.g., Kongsberg EM2040C and EM3002) (Fig. 2.6). The transmission and reception module form the sonar head. Some MBESs, such as a specific version of the Kongsberg EM 2040C (Fig. 2.6), have two sonar heads mounted with a certain angle to each other to obtain a increased seabed coverage. Transducer arrays, for transmission (array of projectors) and reception (array of hydrophones) of the acoustic signal, are located within each module.

Most transducers utilize the piezoelectric effect inherent to certain ceramics to generate and receive an acoustic signal [4]. Applying an electrical field to a piezoelectric material induces a mechanical deformation. A mechanical deformation on the other hand generates an acoustic wave. At reception, the behavior of the piezoelectric material is inverse. An acoustic wave applies a certain stress to these materials which generates an electrical voltage.

In addition to the projector array, the transmission module contains a power supply, signal generator, power amplifier and impedance matching unit [4]. The power supply is responsible for a constant and sufficient electrical energy at the transmitting line. The signal generator generates a low-voltage electrical signal with a given frequency, duration and phase content. The power amplifier transforms the low- to a high-voltage signal in order to allow the transducer (i.e, array of projectors) to generate the expected sound level. At the same time, the amplifier needs to guarantee a low distortion rate of the already shaped signal. The impedance matching unit improves the power transfer of the electrical load from the amplifier to the transducer. In the most advanced MBES, the transmission module also adjusts the angular distribution of the transmitter energy with respect to the platform motion (i.e., pitch stabilization).

The receiving module consists of the hydrophone array as well as a preamplifier, analog to digital converter (ADC) and filters. It carries out the echo level correction as a function of time (TVG) to keep the signal in the dynamic range of the receiver and performs the conversion from the electrical voltage to digitized values via the ADC. Furthermore, the receiving module performs frequency filtering, corrections for the platform motion (i.e., roll stabilization), beamforming and the bathymetric measurements (via amplitude detection or phase detection [51]).

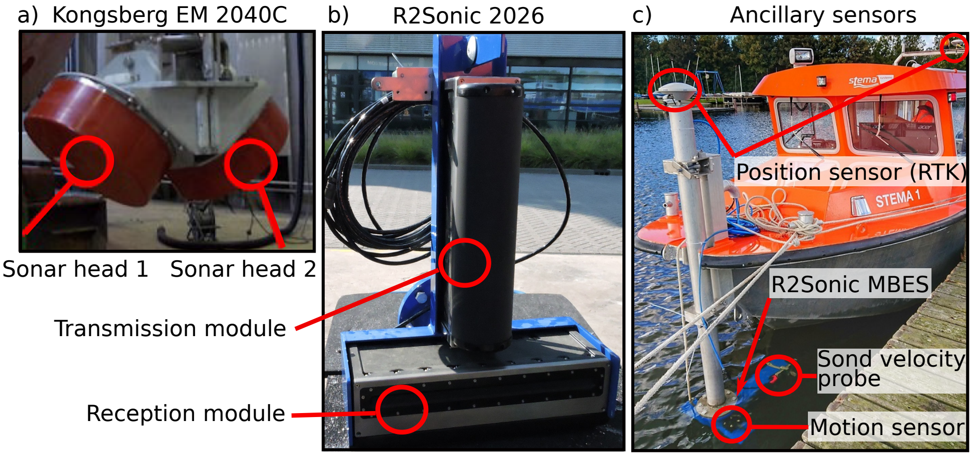

Figure 2.6: a) High-frequency dual-head Kongsberg EM2040C MBES used in the Ameland inlet (Chapter 4) (200 to 400 kHz). b) High-frequency single-head R2Sonic 2026 MBES (90 to 450 kHz). This system was used in the Bedford Basin and Patricia Bay in Canada (Chapter 5) and in the Port of Rotterdam and Vlietland Lake in the Netherlands (Chapter 6). The location of the study sites are shown in Fig. 1.2 c) Ancillary sensor installation during the survey in the Vlietland Lake.

In order to obtain accurate bathymetric and backscatter measurements, the MBES needs to receive and process data from ancillary sensors: a positioning system for the geographical location of the vessel, a motion sensor for corrections of the vessel movement, a sound velocity probe at the receiving module for accurate beamforming and a sound velocity profiler (SVP) for the water column to provide input for the ray tracing (Fig. 2.6). Different positioning systems are in use with an increase in accuracy from GPS (Global positioning system, ~meter-level) over DGPS (Differential GPS, ~decimeter-level) to RTK (Real-time kinematic, ~centimeter-level) [52]. Via a graphical user interface (GUI) installed on an external computer, the operating parameters for the MBES and the ancillary sensors are controlled, the real-time processing results are visualized and the MBES data is stored. A sonar interface module (SIM) communicates with the GUI, receives the data from the MBES and the ancillary sensors, time tags the sensor data and relays the data streams to the sonar head.

2.3.2. Concept of beamforming

The MBES is an active sonar, that means it serves as a sound source and also as a receiver. During reception, beamforming (also know as beam steering) allows to realize the maximum acoustic response in a given angular direction. Hence, beamforming in reception works as a spatial filter by filtering out sound from unwanted directions (e.g., noise) and echoes from other locations at the seabed [2]. During transmission, the transducer array can be electronically steered to account for the platform motion in order to provide a narrow angular distribution of the acoustic energy vertically into the water column.

The intrinsic requirement for beamforming is the availability of at least two receiver or projector elements. The signals, arriving at each element, are combined in order to achieve constructive interference for sources located (i.e, scatterers) at particular angles whereas others experience destructive interference. Let's assume a plane acoustic wave propagating in the x-y plane towards an array consisting of M elements aligned along the x-axis (Fig. 2.7). The summed output is maximum if the wavefront arrives from a direction perpendicular to the array. In that case all receiver elements of the array receive the signal at the same time and summing their measured signal yields to constructive interference. In case that the wavefront impinges with an angle ϕ between the propagation direction and the plane normal to the array axis, as shown in Fig. 2.7, the receiver elements m receive the signal delayed by the additional time necessary for sound to travel to the different receivers. For example, at receiver element m_1 the signal arrives t_1 later compared to the reference element m_0, and so on. The delay can be expressed in space with ϕ or in time with t_m as follows

$$\sin\phi = \frac{d_{e_1}}{\delta x}, \frac{d_{e_2}}{2\delta x} \quad \text{and} \quad t_1 = \frac{d_{e_1}}{c}, t_2 = \frac{d_{e_2}}{c} \tag{2.24}$$

where d_e is the propagation-path delay and δx is the distance between each element. The corresponding phase delay $\Delta\varphi$ for element m_1 is

$$\Delta\varphi = \omega t_1 = 2\pi f \frac{d_{e_1}}{c} = \frac{2\pi}{\lambda} d_{e_1} = \left(\frac{2\pi}{\lambda}\sin\phi\right)\delta x. \tag{2.25}$$

By writing the phase delay of the signal in the complex notation form $e^{i\frac{2\pi}{\lambda}\sin\phi\delta x}$, the summation over all receiver elements leads to the acoustic array response with respect to the incoming wave direction ϕ as follows (modified from [46])

$$G(\phi) = \sum_{m=0}^{M-1} e^{i\frac{2\pi}{\lambda}\sin\phi\delta x m}. \tag{2.26}$$

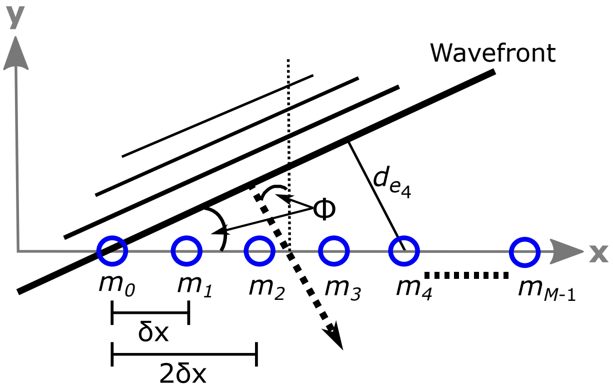

Figure 2.7: Acoustic wave impinging on an array consisting of M receiver elements.

The concept of phase delays can also be used to amplify acoustic waves from selective directions (i.e., angles) by applying electronic delays to the receiver elements. In case the electronic delay, related to angle θ which is known as the steering angle, is such that the delays correct the differences in travel time for the incoming wave (angle ϕ), constructive interference results in a maximization of the output pressure. Localizing the maximum pressure yields to an estimate of the direction of the incoming wave. The acoustic array response for a steered direction θ can be written as

$$G(\phi,\theta) = \sum_{m=0}^{M-1} e^{i\frac{2\pi}{\lambda}(\sin\phi - \sin\theta)\delta x m}. \tag{2.27}$$

Here, $G(\phi,\theta)$ is the acoustic array response for the given steering direction θ with respect to the incoming wave direction ϕ. The squared magnitude of the normalized array response for an incident plane wave, known as the beam pattern of the array, is [2]

$$b_p(\phi,\theta) = \left|\frac{G(\phi,\theta)}{G_{max}}\right|^2 = \left|\frac{\sum_{m=0}^{M-1} e^{ik(\sin\phi - \sin\theta)\delta x m}}{M}\right|^2 \tag{2.28}$$

with $k = \frac{2\pi}{\lambda}$ the wavenumber .

Fig. 2.8 visualizes the beam pattern for two steering angles obtained from Eq. (2.28). The main lobe, quantified as the half power width (or −3 dB width) and known as the beam width Ω, defines the spatial resolution of the beamforming. The main lobe increases by $1/\cos(\theta)$ with increasing steering angle, as seen in Fig. 2.8. Next to the main lobe, the undesirable side lobes are located, which add noise from other directions than the steering direction. They can be reduced by accounting for the contribution of the individual elements to a lower and higher extent. This is accomplished by using weighting functions, e.g., Hanning or Hamming weighting. The disadvantage is a broadening of the main lobe.

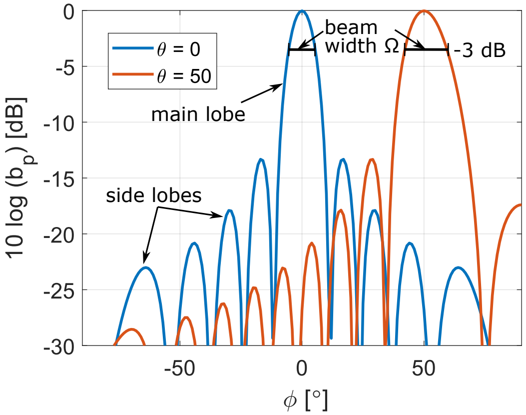

Figure 2.8: Beam pattern for two steering angles. The y-axis presents the beam pattern BP in decibels retrieved via $BP = 10\log(b_p)$ and the x-axis shows the arriving angle ϕ of the wavefront.

2.3.3. Bathymetric measurements

Bathymetric measurements require the estimation of the travel time of the signal to the seabed. In MBESs, the time of arrival is estimated from the amplitude of the signal or the interferometric phase (known as phase detection) [53]. In general, amplitude detection is applicable around nadir (i.e., vertically below the vessel) and phase detection is used away from nadir.

Amplitude detection

Amplitude detection uses either the maximum amplitude of the receiving signal or is based on the computation of the center of gravity (COG) of the signal envelope. The time of arrival t_D (two-way travel time) in the COG method is estimated from the acoustic pressure p as [53]

$$t_D = \frac{\sum t_j p(t_j)}{\sum p(t_j)} \tag{2.29}$$

where t_j is the time sample. As shown in the equation, the COG requires a summation over the samples with the indices j.

Interferometry

The interferometry principle is based on constructive and destructive interference between acoustic waves (or electromagnetic waves). Considering two waves from coherent sources, the resulting intensity depends on the phase difference between both waves [4]. As already shown in Fig. 2.7 for the beamforming, the phase delay $\Delta\varphi$ from a coherent source (e.g., scatterer at the seabed) between two receivers is geometrically related to the path-length difference d_e via Eq. (2.25). While in beamforming the sensitivity of the array is increased in a given angular direction by applying a time delay to the receiver elements, in interferometry the accurate time of arrival is estimated using the measured phase difference between two closely located receivers.

In order to perform phase detection with a MBES, the full array is divided into two sub-arrays. In a first step the received signals on both sub-arrays are beamformed focussing the two sub-arrays in the desired direction (e.g., 64° in Fig. 2.9). As a next step, the phase difference $\widehat{\Delta\varphi}$ between these two signals is calculated, providing an estimate of the arrival time of the signal. In general, a sub-array represents half of the receiving elements of the full-array of a MBES. The phase difference $\widehat{\Delta\varphi}$ between the complex signal envelopes s_A and s_B measured at sub-array A and B is calculated as [54]

$$\widehat{\Delta\varphi} = \arg\{s_A s_B^*\} \tag{2.30}$$

where s_B^* denotes the complex conjugate of the signal measured at sub-array B. In general, both variables $\Delta\varphi$ and $\widehat{\Delta\varphi}$ represent a phase difference. Nevertheless, $\Delta\varphi$ is called phase delay to indicate that this is a theoretical expression whereas $\widehat{\Delta\varphi}$ represents a measured value.

A phase difference of zero (zero-phase crossing) represents the estimated time of arrival and thus the bottom detection of the MBES for the beamformed direction. As seen in Fig. 2.9, the calculated phase difference is ambiguous and discontinuities, known as phase jumps, occur.

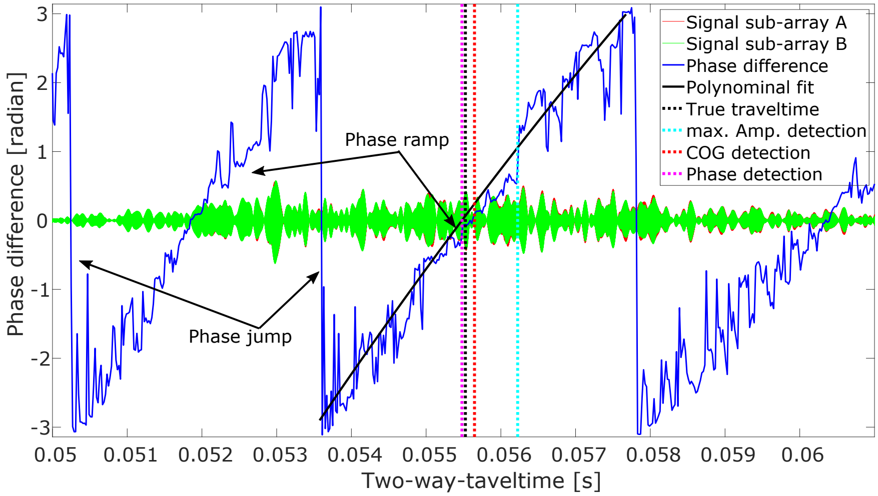

Figure 2.9: Phase difference $\widehat{\Delta\varphi}$ between a simulated pressure signal measured at sub-array A and B. Both sub-arrays consist of 128 receiver elements in which the sub-array centers are 20.5 cm apart. The phase difference is calculated from the beamformed signals at 64°. A second-order polynomial is fitted to the phase difference to identify the zero-crossing. The dashed lines indicate the estimated time of arrival by the amplitude detection methods and phase detection method. In addition, the true travel time is indicated by the black dashed line.

Between the phase jumps the so-called phase ramps are located containing the actual the zero-crossing. Different approaches exist to overcome the ambiguity and to select the zero-crossing in the correct interval [4]. In this thesis, the estimated time of arrival using the COG detection is used to locate the phase ramp. Furthermore, the phase difference is intrinsically noisy and the zero-crossing instant needs to be determined with a low-order polynomial fit. In Fig. 2.9, a second-order polynomial equation is fitted to the phase ramp using a least-square method.

2.4. Sonar equation

In Section 2.2.2 the dependency of the backscatter strength BS on the composition of the seabed, the angle of incidence ϕ on the seabed, and the acoustic frequency f is shown [6][3]. It follows that the backscatter strength contains information about the seabed properties [56]. However, before any useful information can be extracted from the received acoustic echo level EL at the MBES, an appropriate processing is necessary to account for the measurement configuration, water column properties and the hardware and software settings of the sonar. The terms affecting $BS_f(\phi)$(in dB per 1 m^2 at 1 m) are expressed by the sonar equation (modified from [57, 58])

$$BS_f(\phi) = EL - SL - BP_T(f, \theta_T) + TL - PG - SH(f) - BP_R(f, \theta_R) - 10\log(A) \quad (2.31)$$

where SL is the source level (in dB re 1 µPa at 1 m), modulated by the transmission beam pattern BP_T as a function of f and the transmission angle (i.e., steering angle) θ_T with respect to the sonar axis (see Section 2.3.2). PG (in dB) is the receiver gain applied by the receiver electronics, SH (in dB re 1 V/µPa) is the transducer sensitivity with respect to f, and BP_R is the beam pattern at reception expressed as a function of f and the receiving angle θ_R with respect to the sonar axis. The received echo level EL is formed by the signal scattered and reflected within the instantaneously ensonified area A (in m^2). As it is shown in Section 2.2.2, BS_f is defined per unit area and therefore one needs to account for the ensonified area A. The transmission loss TL accounts for the energy loss of an acoustic wave propagating through the water column (see Section 2.1). It depends on the water column properties and the travel distance r of the signal to the seabed and can be written as

$$TL = 2\alpha r + 40\log(r) \quad (2.32)$$

where α is the absorption coefficient depending on the temperature, salinity, acidity, pressure, and f [59, 60]. The second term in Eq. (2.32) accounts for the energy loss of the signal due to geometrical spreading (see Section 2.1). Fig. 2.10 presents a visual overview of the various angles defined in this thesis.

The sonar equation (Eq. (2.31)) allows for the theoretical extraction of the absolute backscatter strength from the received signal at the MBES. However, the necessary variables and parameters might not be available from the sonar producer or might not be measured with a sufficient accuracy. Even when all variables are properly documented, the conversion from analog to digital values and vice versa at reception and transmission often exhibits a discrepancy between the design and actual hardware implementation. In addition, aging of the MBES components might change the sensitivity of the system hardware over time [58]. In

---

[3] The majority of Section 2.4 has been published in Geosciences **8** (12), 455 (2018) [55].

such a case frequently performed relative or absolute calibrations of the MBES systems using natural reference areas or a calibrated singlebeam echosounder can be conducted [26, 29]. If no calibration is performed, the backscatter data has to be considered as uncalibrated data.

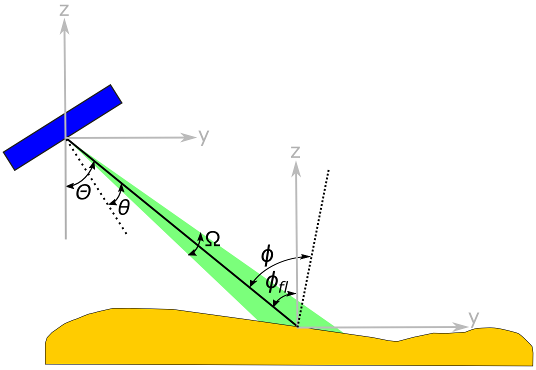

Figure 2.10: Definition of various angles: Steering angle θ, beam angle Θ, beam opening angle Ω, incident angle on the seabed ϕ and incident angle assuming a flat seabed ϕ_{fl}.

Ensonified footprint and true incident angle

As shown in Eq. (2.31), the area A ensonfied by the transmitted pulse is required for the calculation of the backscatter strength. A depends on the sonar characteristics and the seabed morphology, i.e., the across-track slope ϵ_y and along-track slope ϵ_x (radians). The ensonified footprint area in the pulse limited regime A_p and in the beam limited regime A_b, respectively, are expressed by [17]

$$A_p = \Omega_T r \frac{c\tau_{\mathrm{eff}}}{2\sin(\phi_{\mathrm{fl}} - \epsilon_y)\cos(\epsilon_x)} \tag{2.33}$$

and

$$A_b = r^2 \Omega_T \Omega_R \tag{2.34}$$

where c is the sound speed in water, τ_{eff} is the effective pulse length, and ϕ_{fl} is the incident angle with respect to nadir and a flat seabed. The footprint used in Eq. (2.31) is selected based on $A = \min(A_p, A_b)$. In this thesis, the beam angle Θ is defined with respect to the vertical (nadir), and thus equal to ϕ_{fl}. The beam angle Θ differs from the steering angle at reception θ_R by the mounting angle of the MBES and in case the MBES applies real-time roll correction also by the platform motion. The beam width Ω_T and Ω_R (also know as the beam opening angle and representing the −3 dB width of the main lobe, Fig. 2.8) for transmission and reception can be approximated for a continuous line array with length L and equally spaced transducer elements by [4]

$$\Omega(\theta) = \frac{\lambda}{L}\frac{1}{\cos(\theta)}. \tag{2.35}$$

From Eq. (2.35) follows, that when keeping the array length constant, the beam width changes with varying frequency.

The effect of a seabed slope on the backscatter level (i.e., compared to flat seabed assumption) can be expressed via the backscatter correction term BS_c [17]

$$BS_c = 10 \log \left(\frac{c\tau_{\text{eff}} r \Omega_T}{2 \sin(\phi_{\text{fl}} - \epsilon_y) \cos \epsilon_x} \right) \tag{2.36}$$

with BS_c in decibels.

Furthermore, the incident angle with respect to the actual seabed ϕ can be calculated from ϕ_{fl} (degrees) according to [17]

$$\cos(\phi) = \frac{\sin(90 - \phi_{\text{fl}}) + \cos(90 - \phi_{\text{fl}})\epsilon_y}{\sqrt{1 + \epsilon_x^2 + \epsilon_y^2}}. \tag{2.37}$$

The required across-track ϵ_y and along-track slopes ϵ_x are calculated from the bathymetric data with respect to the heading of the vessel and the orientation of the sonar axis (Fig. 2.11). The heading is averaged over a reasonable (i.e., spatial resolution vs. heading variability) number of pings ($\sim$ 50 to 200). The area covered by the selected pings in along-track and by the MBES swath in across-track is divided into surface patches. Each patch consists of a few consecutive pings and a few beams around the central beam.

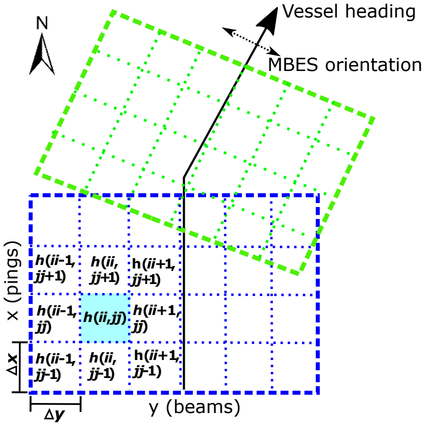

Figure 2.11: Moving grid for MBES seabed slope correction.

Using the surface patches, ϵ_y and ϵ_x are calculated via a 2D finite difference method as follows

$$\begin{aligned} \epsilon_x &= \frac{h(ii-1,jj-1)+2h(ii,jj-1)+h(ii+1,jj-1)-h(ii-1,jj+1)-2h(ii,jj+1)-h(ii+1,jj+1)}{8\Delta x}, \\ \epsilon_y &= \frac{h(ii+1,jj-1)+2h(ii+1,jj)+h(ii+1,jj+1)-h(ii-1,jj-1)-2h(ii-1,jj)-h(ii-1,jj+1)}{8\Delta x} \end{aligned} \tag{2.38}$$

with h the water depth and a grid cell size of Δx (i.e., $\Delta x = \Delta y$). The grid cell size defines the spatial resolution of the slope correction dx_{slope} as follows $dx_{\text{slope}} = 3\Delta x$ (in unit length). As an example, Fig. 2.12 shows the effect of the seabed slope on backscatter for a survey track line covering a rough seabed morphology (for some areas ϵ_x and $\epsilon_y > 20°$). The backscatter correction term BS_c reaches values above 2 dB and the true incident angle ϕ differs by more than 20° compared to the beam angle Θ (i.e., also ϕ_{fl}) for the steepest slopes. Both result in a difference of partly more than 5 dB between the backscatter mosaics presenting the uncorrected and corrected backscatter data. The magnitude varies with the actual beam angle and the orientation of the beam angle to the seabed morphology (represented by ϵ_x and ϵ_y) as well as with the sediment type. It shows that in environments with a rough seabed morphology, this correction is essential to retrieve reasonable backscatter levels.

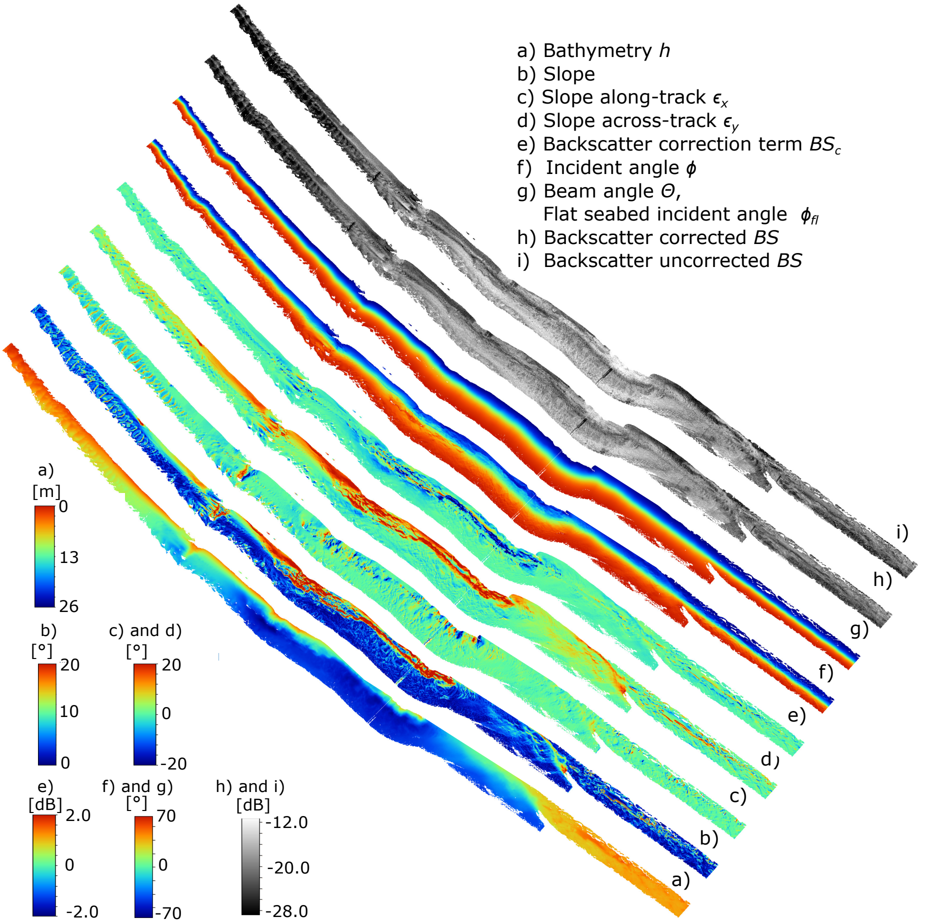

Figure 2.12: MBES seabed slope correction. Effect of seabed slope on backscatter visualized for a track line acquired in an area with rough morphology in the Ameland inlet.

3

Sediment classification with multitemporal multibeam backscatter

Individually we are one drop.
Together, we are an ocean.

Ryunosuke Satoro

In the previous chapter the sonar equation was introduced explaining the necessary steps taken to process the multibeam echosounder (MBES) data. The resulting backscatter (BS) data provides the input for the classification methods introduced in this chapter. Here, a detailed explanation of the two different classification methods, i.e., a method based on the principal component analyses in conjunction with k-means clustering and the Bayesian classification method, is given. Both classification methods are applied to a multitemporal MBES dataset, which was acquired in the Cleaver Bank (The Netherlands) using a Kongsberg EM3002 MBES (300 kHz) during five different surveys with two different vessels between 2013 and 2015. A particular focus lies on the method comparison and the repeatability of the acoustic classification derived from MBES BS measurements over time. Based on the ground truth information, the acoustic discrimination performance of this monochromatic BS data is discussed.

The majority of this chapter has been published in IEEE Journal of Oceanic Engineering **44** (1), 142-155 (2019) [61] and is a part of two PhD projects together with Leo Koop. Some parts are also included in [55] and [62].

3.1. Introduction

Acoustic remote sensing with multibeam echosounders (MBESs) is extensively used for mapping the seabed morphology because of the systems' capability to map large areas in relatively short time periods. However, capabilities of these acoustic underwater techniques extend beyond the determination of only the seabed bathymetry. They also exhibit strong potential for classifying the seabed sediments by investigating the sediment backscatter (BS) strength that can be derived from the intensities of the received echo. The BS strength is physically attributed to seabed properties such as sediment bulk density, seabed roughness, volume heterogeneity, discrete scatterers and sediment layering [6, 32, 63]. The contribution of each factor to the BS strength is dependent on the complexity of the seabed, acoustic frequency and angle of incidence (Section 2.2). Several regional studies have revealed a relationship of BS to sediment properties such as median grain size [19, 64], grain-size distribution [65–67], shell or gravel content [68] for a specific study area and frequency. However, other studies have shown that in diverse environments additional factors such as benthic fauna [69, 70], activity of benthic organisms [71], sediment compaction [72] or natural hydrocarbons [73, 74] may influence the BS strength of the seabed as well.

In general, classification methods employing measured BS data can be divided into model-based and image-based (i.e., empirical) methods [8]. Model-based methods are attributed to techniques that perform inversion based on physical BS models either to exploit the measured BS strength directly [75] or the angular BS response [10] to invert for sediment properties (e.g., mean grain size, roughness spectrum, volume scattering coefficient). Image-based methods are based on statistical relationships and patterns within the BS data [8, 22]. Whereas model-based methods require accurate models for predicting the BS strength and well-calibrated systems for measuring the BS strength [32, 76], image-based techniques are also applicable to relative BS values from poorly calibrated or uncalibrated systems.

Brown *et al.* [8] gives a review of various strategies and methods employing acoustic remote sensing techniques including singlebeam echosounder, side-scan sonar and MBES to produce sediment or habitat maps. Around 150 studies utilizing acoustic survey techniques published during the last two decades were presented. This is a good indicator for the intensive research already carried out and the still ongoing development in the scientific field of acoustic seabed classification. Among others, they classify image-based methods in objective/subjective and supervised/unsupervised strategies. The classification methods applied in this study, i.e., the Principal Component Analysis (PCA) and Bayesian mehtod, can be referred to as image-based, objective and unsupervised strategies. The PCA and Bayesian classification method have been successfully applied to MBES BS in several studies [13, 19, 22, 77] .

Using the full MBES acoustic data content gives the opportunity for the development of marine-landscape maps displaying topography and the seabed sediment distribution simultaneously. Because of physical and biological, as well as anthropogenic processes, the seabed is a time-varying environment. Monitoring this dynamic environment requires good repeatability of the methods for acoustic sediment classification (ASC). That means the data gathering, processing, and interpretation must lead to equal results for different measurement campaigns if the environment does not change. However, regarding the use of MBES measurements for sediment classification, repeatability of the results is a topic of concern. Anderson *et al.* [76] pointed out the acoustic-instrument stability, settings, processing algorithms, range, environmental conditions, and survey methods as critical factors influencing the classification results, and consequently, affect repeatability. Therefore, there is a strong demand from the MBES BS community for data quality control, standardised acquisition and processing steps as well as detailed documentation of the processing chain within MBES systems [7]. In the research field of seabed classification with MBES systems the ultimate goal is to generate consistent and repeatable results within the same area under the same settings from BS data acquired by differing MBES systems or analysed by different processing procedures [7].

The goal of this study is to apply two different classification methods to MBES BS data acquired on different vessels during different surveys carried out in various time periods and to investigate the repeatability and agreement of the resulting sediment maps. To accomplish this goal, the Bayesian approach and PCA in conjunction with k-means clustering approach are applied to BS data acquired with the Dutch vessels Zirfaea and Arca in the Cleaver Bank area in the time period from 2013 to 2015. This study site consists of a significant number of sediment types, and intersecting survey tracks within the source data and allows for the investigation of the repeatability of the results. The classification results are compared to ground truth data to investigate the relationship between acoustic class (AC) and sediment properties. The spatial resolution capabilities of the classification methods are additionally addressed to illustrate the state-of-the-art methods for ASC based on MBESs.

3.2. Study area and data

3.2.1. Geological setting

The study area, the Cleaver Bank, is located about halfway between the United Kingdom and the Netherlands. This area covers about 1.5 % of the entire Netherlands Continental Shelf (NCS). Water depths at the Cleaver Bank range from 25 to 50 m Lowest Astronomical Tide (LAT) except for the deep channel (Botney Cut) that crosses the Cleaver Bank from north-west to south-east, where water depths reach 70 m LAT (Fig. 3.1). This subaqueous palaeochannel is a glacial valley from the Weichselian glaciation incised into Pleistocene deposits and was partially filled in with sandy muds prior to the early-Holocene marine transgression (Botney Cut Formation), probably deposited in a glacio-lacustrine environment [78]. The infill is overlain by more recent Holocene marine sediments, varying from mud to sandy gravel with a layer thickness of 1 to 12 m. In the area surrounding the Botney Cut, Late-Weichselian glacial deposits are mapped as the Boulder Bank Formation, consisting of a blanket till of gravelly sandy clay. Where the Holocene marine deposits overlie the Boulder Bank Formation, these deposits are less than 2 m thick and comprise clean sand and sandy gravel [78]. The Cleaver Bank is the largest area with coarse sediments on the NCS, with up to 30 % being covered with gravel [79]. The abundance of different sediment types from muddy to rocky bottoms causes a high benthic biodiversity [80, 81].

3.2.2. Multibeam data acquisition

The MBES data considered in this work were acquired in the Cleaver Bank area during five surveys carried out within the period from November 2013 to February 2015. The entire survey area is 57 km in the north-south direction and 30 km in the west-east direction. In general, the survey lines are separated by approximately 1500 m except a few lines spaced closer together, overlapping lines, and several cross lines (Fig. 3.1). The swath width ranges from 90 to 180 m depending on the water depth. Two different vessels, the Zirfaea and Arca, were both equipped with a Kongsberg EM3002 single head MBES using a central frequency of 300 kHz. The transmit and receive beam width are both 1.5° for nadir angles. The transmitted pulse length was set to 150 μs and the number of beams were 258 along the entire swath. These parameters were kept constant during each survey. Furthermore, the same transmitted source level, receiver gain and time-varying gain were applied during the different surveys. The acquired MBES data were corrected for roll, pitch and heave. Depending on the different environmental conditions, the water absorption coefficient was calculated for each survey individually. The MBES data were also corrected for tidal effects using the open-source software MB-System.

3.2.3. Ground truth data

The ground truth dataset consists of 104 Hamon and Van Veen grab samples. The samples were taken during the MBES surveys from 2013 to 2015 and a previous survey in 2000. The grab samples were sieved to separate the gravel and shell fragments from the sand and mud fraction. The latter part was analysed by laser-diffraction granulometry. The modified Folk scheme [83], where the threshold for slightly gravelly classes is 1 %, was used to classify the samples. Eight sediment types were identified: sandy Mud (sM), muddy Sand (mS), Sand (S), gravelly muddy Sand (gmS), slightly gravelly Sand ((g)S), gravelly Sand (gS), muddy sandy Gravel (msG), sandy Gravel (sG). The locations of the 104 grab samples are shown in Fig. 3.1. Almost no shell fragments or other biological particles were found to be present in the grab samples. Because the seabed dynamics of the Cleaver Bank are low, the grab samples from 2000 were considered to be valid. The samples from 2013 to 2015 are located on the MBES track while some grab samples taken in 2000 are located at a distance of 25 to 750 m to a track line (Fig. 3.1). During the analysis in this study only the grab samples were considered that are located at a distance less than 25 m from a survey track, i.e., slightly more than the 20 m recommended in [84], and that are in areas with little spatial variation in sediment types. As such, the initial 104 grab samples were reduced to 77 grab samples.

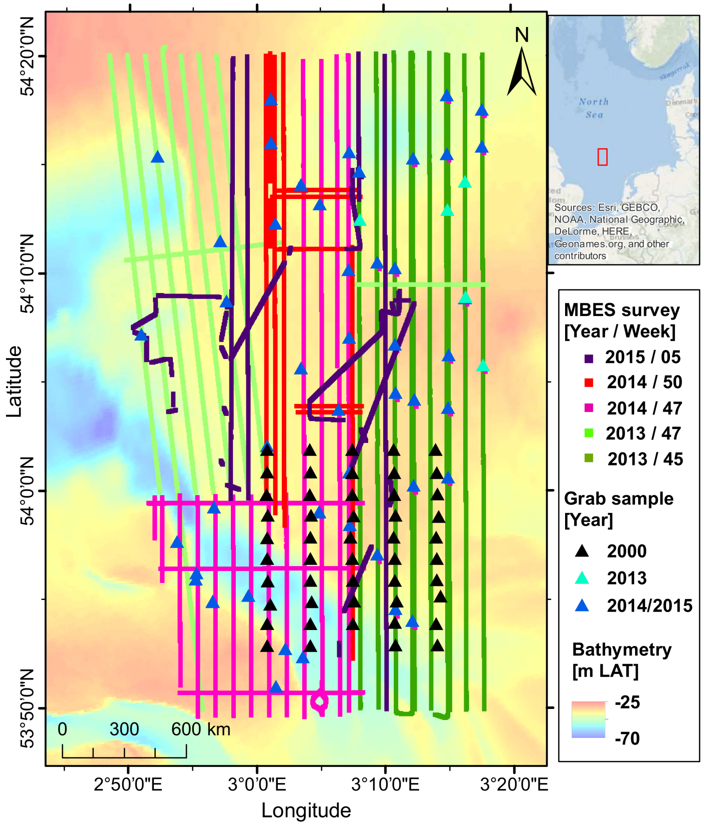

Figure 3.1: MBES tracks of five different surveys carried out from 2013 to 2015 are plotted over the bathymetry of the Cleaver Bank. Bathymetry is received from EMODnet [82]. Grab samples taken in the years 2000 and 2013 to 2015 are denoted by triangles.

3.3. Methods

3.3.1. Multibeam data processing

To obtain a relatively good approximation of the BS strength from the received acoustic echo several steps are carried out within the Kongsberg MBES. The system corrects in real time for transmission loss (attenuation and geometrical spreading), ensonified area as well as for transmission and reception beam pattern [85]. However, the real-time correction for the ensonified area assumes a flat seabed. Therefore, the BS data are corrected for the seabed bathymetry slope in post processing to obtain the true ensonified area (see Section 2.4). However, some of the real-time correction performed by a Kongsberg-system still includes simplification of the marine environment (e.g., constant absorption coefficient, flat seabed assumption for reception process) which might affect the BS strength [7]. In addition, a MBES calibration that would account for the alteration of sonar transducers' sensitivities or deviation of the system configuration from the manufacturer specification was not performed. Taking these factors into account, strictly speaking, the employed acoustic data represent a relative rather than absolute BS strength because the data might still not be entirely independent of the MBES configuration or environmental impacts. Therefore, the terms relative BS strength, BS value or BS level are preferred instead of BS strength.

3.3.2. Bayesian classification method

The Bayesian method for sediment classification employed in this thesis was developed by Simons and Snellen [13], where a detailed description of the theory is given, and developed further by Amiri-Simkooei *et al.* [17]. This section provides an overview of the main concepts and the processing steps taken to generate the acoustic classification maps from monochromatic BS datasets.

Measured BS strength is affected by random fluctuations of the acoustic interaction with the seabed [86] and thus can be considered as a random variable with a certain mean $\bar{y}$ and standard variation σ_y. According to the central limit theorem, measured BS strength per beam, which are determined as the average over BS from independent scatter pixels within a beam, can be assumed to follow a Gaussian distribution [13]. A scatter pixel represents the instantaneously ensonified area of the seabed by the transmitted pulse of the MBES, i.e., the signal footprint. If the frequency and angle of incidence are constant, the BS strength is dependent on the seabed properties. Thus, if the survey area contains m different sediment types, the BS histogram for a selected beam can be represented by a combination of m Gaussian distributions. The modeled BS histogram per beam can be expressed as the summation of the m Gaussian distributions according to

$$f(y_j|\boldsymbol{x}) = \sum_{k=1}^{m} q_k \exp\left(\frac{(y_j - \bar{y}_k)^2}{2\sigma_{\bar{y}_k}^2}\right) \tag{3.1}$$

with y_j the jth BS value in the histogram ($j = 1, \ldots, M$ with M the total number of bins in the histogram). $\boldsymbol{x}$ is the vector containing the unknown parameters: $\boldsymbol{x} = (\bar{y}_1, \ldots, \bar{y}_m; \sigma_{y_1}, \ldots, \sigma_{y_m}; q_1, \ldots, q_m)$ with $\bar{y}_k$ the means, σ_{y_k} the standard deviations, and q_k the strengths of the Gaussian distributions. The unknown parameters are determined by maximizing the match between the modeled and the measured histogram in a least squared sense [13]. To solve the non-linear least squares problem, the trust-region-reflective algorithm is used. This algorithm is a trust-region method and is based on the interior-reflective Newton method [87, 88]. A description of the initialisation of the search bounds for the unknown parameters (i.e., $\bar{y}$, σ_y and q) is given in Appendix A.1.

To determine the optimal number of Gaussians, the Chi-square χ^2 goodness of fit test can be used, where χ^2 is defined as

$$\chi^2 = \sum_{j=1}^{M} \frac{(n_j - f(y_j|\boldsymbol{x})^2}{\sigma_j^2} \tag{3.2}$$

and where n_j denotes the number of measurements per bin of the aforementioned histogram. For the random variable n_j, a Poisson distribution is postulated[1]. The variances σ_j^2 of the measurements per bin j are thus equal to n_j. The goodness of fit statistic is χ^2 distributed with $\hat{\nu} = M - 3m$ degrees of freedom. The goodness of fit criterion is then further defined as the reduced-χ^2 statistic ($\chi^2_{\hat{\nu}} = \chi^2/\hat{\nu}$), having a value close to 1 for a good fit. For large $\hat{\nu}$, the reduced-χ^2 statistic can be approximated by a normal distribution with a mean of 1 and standard deviation of $\sqrt{2/\hat{\nu}}$. That means that, if the value of m reaches $1 \pm \sqrt{2/\hat{\nu}}$, it follows that this m is considered as the number of seabed types that can be discriminated in the survey area based on the BS data. To increase the robustness of the estimation of the optimal number of Gaussians, the χ^2-test is applied to a range of beam angles (in case of seabed slopes incident angles are required, see Section 2.4). The outer beams are preferably utilized for fitting the Gaussians. First of all, larger incident angles include more scatter pixels per area, lowering the Gaussian's standard deviation, and consequently provide increased geoacoustic resolution. Second, the incident angles between 30 and 70° provide the most discrimination potential [40].

The actual classification is based on the Bayes decision rule. In this case, m states or hypotheses, indicated as H_k with $k = 1, \ldots, m$, exist. These hypotheses correspond to the m seabed types present in the surveyed area. In the following, the Bayesian decision rule for multiple hypotheses is used to define which hypothesis is accepted, i.e.,

$$\text{accept} \quad H_k \quad \text{if} \quad \max\{f(y_j|H_i)P(H_i)\} = f(y_j|H_k)P(H_k) \tag{3.3}$$

where $P(H_i)$ is the a priori probability of hypothesis H_i with $i = 1, \ldots, m$. Considering that the measurements are taken for the first time, all hypotheses are equally likely, which results in $P(H_i) = 1/m$. The decision rule is then simplified to

$$\text{accept} \quad H_k \quad \text{if} \quad \max\{f(y_j|H_i)\} = f(y_j|H_k). \tag{3.4}$$

Therefore, the hypothesis that maximizes the likelihood $f(y_j|H)$ is selected for observation y_j. The intersections of the m Gaussians have thus to be determined, which results in m non-overlapping acceptance regions A_k, defining the so-called acoustic classes (ACs). The boundaries of the ACs are determined for a certain number of reference angles (mostly outer beams). The reference angles are selected based on three requirements:

1. providing most consistent results in terms of the location of the Gaussian distributions per dataset,
2. offering high discrimination power (30 to 70°),
3. containing little noise.

---

[1] The requirements for an event being Poisson distributed are that (1) E is the number of times the event occurs in an interval of time or space. (2) $E \in 0 \cup \mathbb{N}$. (3) The events are independent. (4) The probability of the event occurring does not vary with time. (5) Two events cannot occur at the same time. (6) The probability of an event in a small interval is proportional to the length of the interval.

Based on the percentage distribution of the ACs at the reference angles, the ACs are assigned to the BS data at all considered angles (mostly 10 to 65°).

The Bayes decision rule enables one to calculate the probabilities of correct and incorrect decisions $\beta_{k,i}$. The overlap between the Gaussian distributions represents the probability of incorrect decisions (i.e., misclassification). Statistically, $\beta_{k,i}$ denotes the probability that H_k is true but H_i is chosen and can be expressed as

$$\beta_{k,i} = \int_{A_i} f(y|H_k)\,\mathrm{d}y. \tag{3.5}$$

The values of $\beta_{k,i}$ are contained in the so-called decision matrix and can be used to evaluate the probability of (mis)classification. If $k = i$, $\beta_{k,i}$ describes the probability of correct classification and if $k \neq i$, it describes the probability of incorrect classification.

3.3.3. Principal component analysis and k-means clustering

The theory of PCA was first introduced by Pearson [89] and Hotelling [90]. Today, many different variations of PCA exist which are adapted depending on the application purposes. A very detailed explanation of the application to MBES data is given by Eleftherakis *et al.* [22].

PCA is a statistical method to reduce the complexity of a dataset while preserving most of the information content. This is achieved by transforming the original dataset consisting of b (potentially) correlated variables to a new dataset of $l = 1, 2, ..., b$ uncorrelated variables Y_l, the so-called principal components (PCs). Each PC can be seen to account for a part of the variation in the feature values of the original dataset. Therefore, the size of the original dataset can be reduced by considering only the PCs representing a significant portion of the data variability.

The n measurements of the b variables, often called features, are summarized in an $(n \times b)$ data matrix. To account for different magnitudes of the features, the data are standardized. For each feature the mean and standard deviation are determined and the mean is subtracted from the measurements. The result is divided by the standard deviation. The matrix $\mathbf{F}$ contains these standardized measurements. The first step of PCA is the calculation of the covariance matrix $\mathbf{R}$ as

$$\mathbf{R} = \frac{1}{n} \sum_{j=1}^{n} {\mathbf{F}_j}^T \mathbf{F}_j \tag{3.6}$$

with $\mathbf{F}_j$ the j^{th} row of the matrix $\mathbf{F}$. Superscript T denotes the transpose. The second step is to determine the eigenvectors and the corresponding eigenvalues of $\mathbf{R}$ by solving

$$\mathbf{RA} = \mathbf{A}\boldsymbol{\Lambda} \tag{3.7}$$

with $\mathbf{A}$ the $(b \times b)$ eigenvector matrix whose columns are the eigenvectors $\boldsymbol{a}_l$ and $\boldsymbol{\Lambda}$ the $(b \times b)$ eigenvalue matrix where the diagonal elements are the corresponding eigenvalues λ_l of the covariance matrix $\mathbf{R}$.

The obtained eigenvector matrix $\mathbf{A}$ is used to transform the original dataset $\mathbf{F}$ into the new dataset consisting of the PCs. Thus, the original measurements $\mathbf{F}_j$ can be written as a sum over the eigenvectors, i.e.,

$$\mathbf{F}_j = \mathbf{Y}_j \mathbf{A}^T \tag{3.8}$$

with the coefficients for the eigenvectors contained in the row vector $\mathbf{Y}_j$ of matrix $\mathbf{Y}$. Thus, one finds

$$\mathbf{Y}_j = \mathbf{F}_j \left(\mathbf{A}^T\right)^{-1} \tag{3.9}$$

where the full matrix $\mathbf{Y}$ is of size $(n \times b)$, as is the original matrix $\mathbf{F}$, and contains for the n measurements the b coefficients for the eigenvectors. In general, although different definitions exist, the lth column $\mathbf{Y}_l$ of $\mathbf{Y}$ is considered as the lth PC, given by

$$\mathbf{Y}_l = \mathbf{F}\boldsymbol{a}_l. \tag{3.10}$$

The amount of variability in the original dataset which is accounted for by the PC $\mathbf{Y}_l$ is quantified by the eigenvalue λ_l. Based on these eigenvalues a subset of PCs can be selected that represent the majority of the variations in the measurements. For this work, the subset was selected such that 70 to 90 % of the data variability is accounted for [91]. These PCs are then supplied to the k-means algorithm to group the PCs into different clusters.

The k-means clustering algorithm aims to assign the n data points for each of the PCs into $\dot{k}$ predefined clusters $\dot{S}_i$ $(i = 1, ..., \dot{k})$. Thereby the sum of the squared Euclidean distance between the data points and the average of all data points within the cluster, i.e., the so-called cluster centroid, is minimised. The minimisation problem is thus

$$\min \sum_{i=1}^{\dot{k}} \sum_{x_s \in \dot{S}_i} |x_s - \dot{c}_i|^2 \tag{3.11}$$

where x_s is a data point within the cluster $\dot{S}_i$ and $\dot{c}_i$ is the cluster centroid of the cluster $\dot{S}_i$. The application of the k-means algorithm to a dataset requires a predefined number of clusters $\dot{k}$. However, the estimation of how many clusters to use is a well-known issue in unsupervised classification methods [92] and is in general the most subjective part of a cluster analysis. In this study three different statistical methods are applied to the MBES BS dataset to determine the number of clusters.

The statistical methods are applied to the output of the clustering techniques using varying numbers of clusters. The first method, the gap statistic, was proposed by Tibshirani *et al.* [93]. This method calculates the overall within-cluster variance of the dataset and compares this value to an expected value calculated for an appropriate reference distribution. The estimated number of clusters is defined where the logarithmic overall within-cluster variance value is minimized. A detailed mathematical description is found in [93]. The second method, the Silhouette statistic, is developed by Kaufman and Rousseeuw [94]. The average distance of the observations within the clusters and the average distance of the observations to the data points in the nearest clusters is calculated for each number of clusters. The values are called the Silhouette coefficients. The optimal number of clusters is selected where the Silhouette coefficient is maximized. Finally, the David-Bouldin criterion is also used in this study [95]. This method examines the ratio of the within-cluster distance and between-cluster distance. The optimal clustering solution is represented via the smallest David-Bouldin index. In [93], the performance of several cluster number estimation methods including the gap statistic and the Silhouette coefficient was investigated. That study demonstrated that the gap-statistic performs most efficiently.

3.4. Results

In this section, the results of the two classification methods are presented. Both methods employ the MBES BS data for the classification of the seabed sediments.

3.4.1. Application of Bayesian classification method

In this study the receiving beams between 20 and 60° are used for the application of the Bayesian method. The beams between nadir and 20° are not used because firstly, there are too few scatter pixels to meet the central limit theorem requirement and secondly, these beams are less sensitive to sediment properties (e.g., roughness) variation than the outer beams [4]. Often receive beams beyond 60° can also be used for classification but for the data considered here, those beams tended to be too noisy to yield reasonable results.

The estimation of the optimal number of classes is a well-known issue in unsupervised classification methods [92]. For the Bayes method, however, a statistically sound approach is available. Here, the curve fitting procedure as described in Section 3.3.2 is executed for increasing numbers of sediment types m. The number of sediment types present in the area is taken as that value of m for which a further increase in m does not result in a further improvement of the fit. The goodness of fit is quantified through the $\chi^2_{\hat{\nu}}$ statistic. For the Cleaver Bank data, it is found that a maximum of seven sediment types can be discriminated based on the available BS data. Fig. 3.2 shows an example of the $\chi^2_{\hat{\nu}}$ statistic for an increasing number of Gaussians and for the 48° beam from nadir, for both the 2013 and 2014/2015 data, as well as the two sides (starboard and port). It is seen that for the 2013 data as well as for side 2 of the 2014 and 2015 data the use of 7 Gaussians provides a very good fit between modeled and measured histogram, with the $\chi^2_{\hat{\nu}}$ statistic being close to 1. An example, indicating that sometimes the $\chi^2_{\hat{\nu}}$ statistic is inconclusive about the number of Gaussians, is shown for side 1 in Fig. 3.2b. In general, such behavior is found for a limited number of cases and therefore, these results are discarded when determining the number of sediment types. These analyses have been carried out for beam angles between 46° and 60° and for all surveys, not all of which are plotted here. The use of 7 Gaussians is found to reproduce the measurements best.

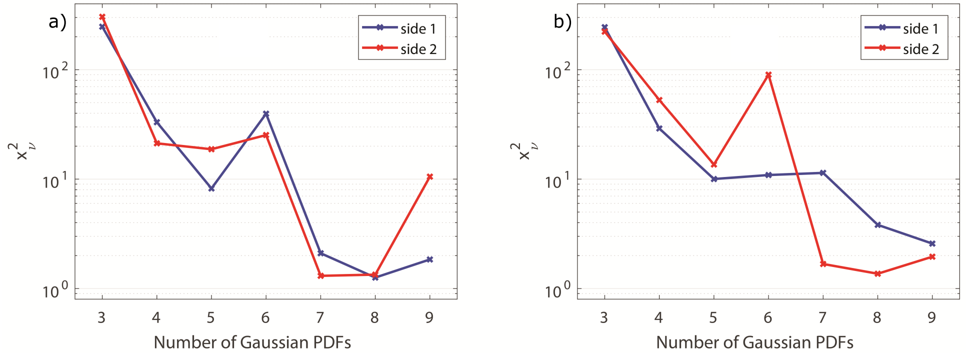

Figure 3.2: The $\chi^2_{\hat{\nu}}$ statistic for the 48° beam angle. The two curves are for the two sides of the MBES, respectively. a) 2013 data and b) 2014 and 2015 data.

As an example, Fig. 3.3 presents the result of the fitting procedure for 7 Gaussians. Here, the histogram of the measured BS data n_j (black line with error bars) per 0.5 dB bin is almost hidden by the modeled BS in red. The variance of the measured data is indicated by the error bars. Also seen are the 7 Gaussians used for the curve fitting in black.

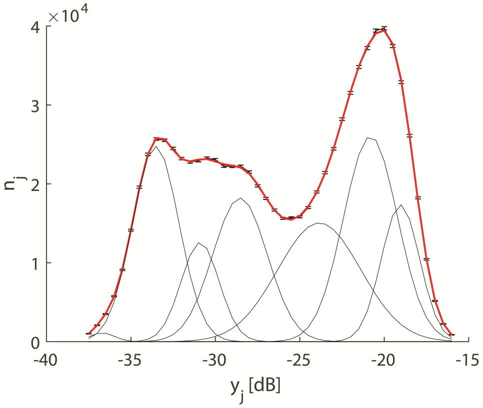

Figure 3.3: Shown here is the histogram of the measured BS data n_j per 0.5 dB bin y_j from the data collected in 2014 and 2015 (black line with error bars) which is almost hidden by the modeled $f(y_j \mid x)$ in red. Also displayed are the 7 Gaussians in black.

After a good fit is found per beam angle and per experiment, the intersections of the Gaussians are used to derive the ranges of BS, corresponding to the different ACs, from which the acoustic classification map is derived as explained in Section 3.3.2. AC_1 to AC_7 correspond to the Gaussians from left to right, and from lowest to highest BS values. The resulting classification map is shown in Fig. 3.4a where each AC is presented with a separate color. Colors have been selected such that from green to purple the BS value increases.

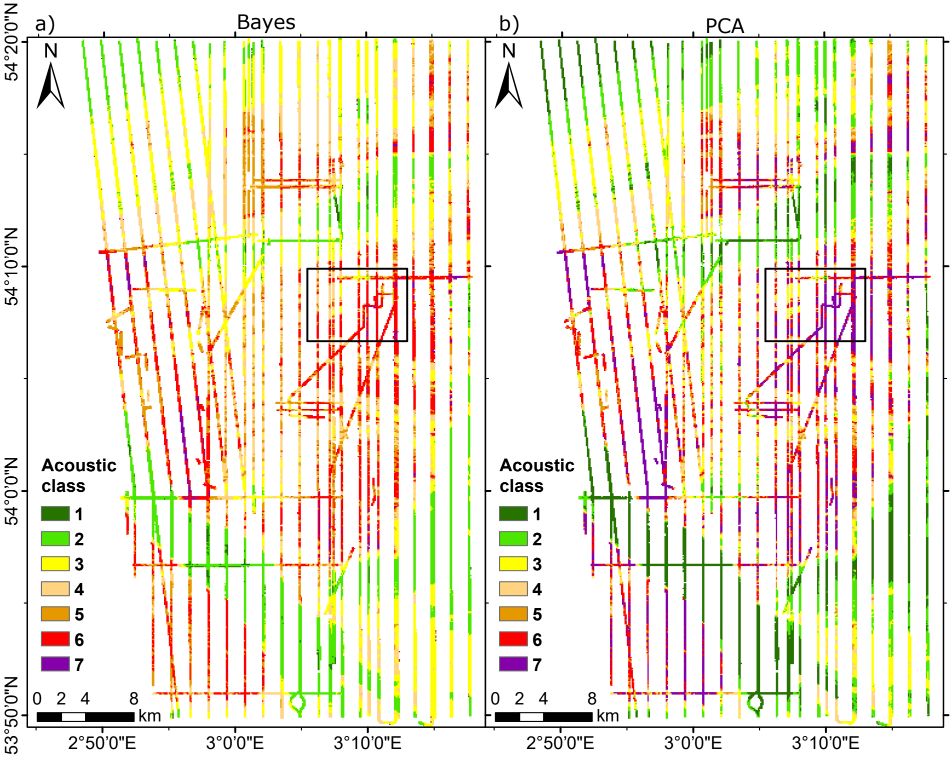

Figure 3.4: Acoustic classification result of a) the Bayesian method and b) the PCA in conjunction with k-means clustering. The grid is resampled to a size of 100 m by 100 m using the mode value of the finer grid. The black square indicates the extent of the area zoomed in Fig. 3.8.

3.4.2. Application of principal component analysis and k-means clustering

PCA in conjunction with a clustering algorithm is a common unsupervised classification technique for seabed classification based on BS [8, 19]. This technique is applicable to relative BS values and therefore, does not necessarily require calibrated MBES. In recent studies, this method was also applied to BS and bathymetry simultaneously [19]. However, in this study PCA and k-means clustering are only applied to BS so that a direct comparison with the classification from the Bayes method can be made.

As with the Bayesian method, for PCA and k-means clustering, beam angles from 20 to 60° are considered. The BS data are averaged over seven pings in the along-track direction and over an angle range of 2 to 4° in across-track direction. To eliminate the angular dependency of BS the global Z-score approach is applied, which is the subtraction of the mean BS level from the BS values and then divided by the standard deviation at each angle [22, 96]. To obtain the same resolution among the entire survey area, surface patches of 10 m by 10 m are constructed.

For each surface patch eight statistical features of the BS distribution are calculated (Table 3.1). The arithmetic mean gives the averaged BS value within the patch. If the distribution is not symmetric, the median value differs from the mean and provides the middle of the distribution. Therefore, the median can be considered as an additional valuable feature. The mode represents the value with the highest occurrence within a patch and defines the main tendency of the feature [22]. The standard deviation shows the variability of the BS and might be valuable to characterize the heterogeneity of the sediment. Due to the fact that outliers are removed during processing, the minimum and maximum value can be used to define data extremes and might also indicate specific characteristics of the seabed. The higher statistical moments, skewness and kurtosis, are measures of the shape of a probability distribution. In previous studies it was shown that the BS distribution can be skewed and described by a K-distribution under certain conditions. For example, it was stated that the shape parameter of the K-distribution can be used as a tool for seabed classification [17, 97–99]. Therefore, the skewness and kurtosis of the BS distribution might provide valuable information about the sediment distribution.

Table 3.1: BS features considered in the first application of PCA.

BS feature	Mean	Std. deviation	Skewness	Kurtosis	Median	Mode	Min	Max
Number	1	2	3	4	5	6	7	8

To identify the most valuable of these features, PCA is applied. PCA analysis indicates that the first 3 PCs contain most of the data variability of around 85 %. Fig. 3.5 displays the ratio of the sum of the correlation between the first three PCs and the eight BS features to the sum of correlation between the remaining PCs and the eight BS features. Eleftherakis *et al.* [22] have chosen the threshold value considering three conditions: (1) it is similar to the mean value (red line), (2) it includes an adequate number of features for PCA and (3) it generates consistent results for each survey. Considering these three conditions the mean, median, mode and the minimum of the BS data are revealed as the most informative features.

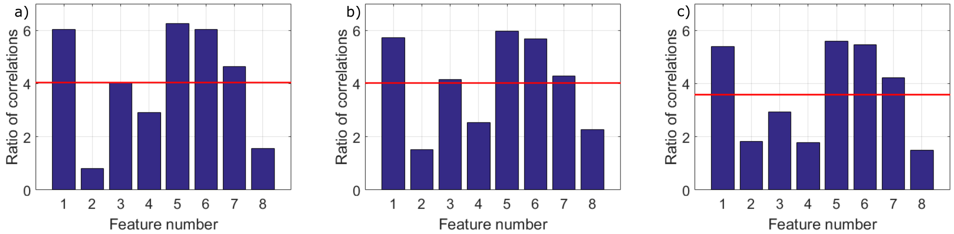

Figure 3.5: Ratio of the sum of the correlation between the first 3 PCs and BS features to the sum of the correlation between the remaining PCs and BS features. The different surveys are considered separately: a) 2013, b) 2014 and c) 2015. The red line indicates the mean value of the ratio of correlation.

These features were used as an input for a second application of PCA to further reduce the complexity of the dataset and simplify the application of the k-means clustering. The analysis shows that the first PC accounts for 98 % of the data variability which indicates high correlation between the selected four BS features. Therefore, only this component is used in the k-means clustering.

To estimate the optimal number of ACs that can be distinguished within the data, the gap statistic, silhouette coefficient and Davies-Bouldin method are applied. The methods use the output of the k-means algorithm which is applied to varying numbers of clusters in the range from 2 to 10. The results of each method are plotted in Fig. 3.6. Each method has different magnitudes of criterion values and therefore the values are normalised. The optimal number of classes estimated and suggested by each method is two, which is indicated by the red dots. This can be understood from Fig. 3.3, showing a histogram of the BS data. Clearly two main peaks are present. These two main peaks are estimated as individual clusters by the statistical methods. However, this is in disagreement with both the ground truth data which reveals eight sediment types, and the Bayesian method which estimates seven clusters, similar to the ground truth data.

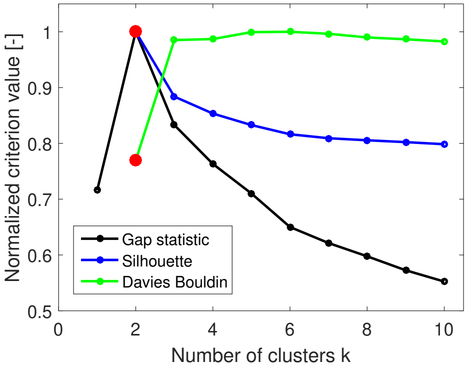

Figure 3.6: Estimating the number of clusters via the Gap statistics, Silhouette coefficient and Davies-Bouldin method. Red circle indicates optimal number of clusters estimated by each method.

To further investigate why the statistical methods only identify two clusters within the BS data the Gap statistics, Silhouette coefficient and Davies-Bouldin methods are applied to synthetic BS histograms. Four different synthetic BS histograms with varying degree of overlap and number of main peaks are shown in Fig. 3.7. Fig. 3.7c represents a similar BS histogram as the measured histogram in Fig. 3.3. Again, the methods only identify the two main peaks as individual clusters. Modeling BS histograms with four and seven main peaks, respectively (Fig. 3.7b and Fig. 3.7d) and applying the statistical methods show that even when the individual peaks are clearly visible, the overlap hampers the clustering methods' ability to identify the peaks as individual clusters. Only the synthetic BS histogram in Fig. 3.7a having peaks with very distinct separations were correctly found to have four clusters by the three methods. This demonstrates that the statistical methods trying to estimate the number of clusters require a clear segmentation of the individual clusters which is not always the case for BS data. Seabed backscattering is a random process having statistical fluctuation leading to a natural overlap of the BS data [6]. In addition, the mostly heterogeneous seabed does not show clear boundaries between sediment types, increasing the overlap within the measured BS data.

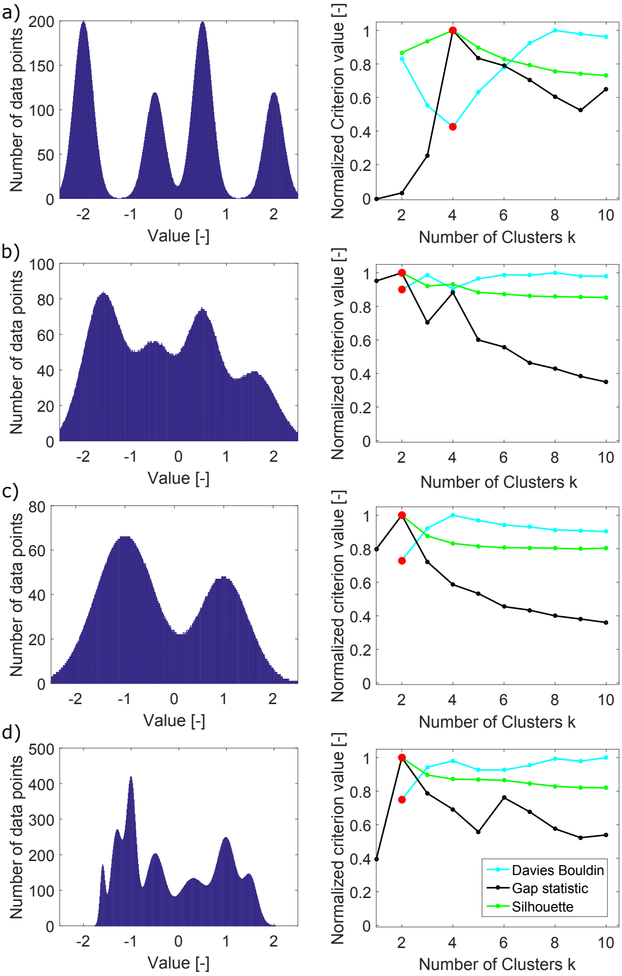

Figure 3.7: (Left) Synthetic histograms generated by modeling a different number of Gaussians. (Right) Application of Davies Bouldin, Gap statistic and Silhouette coefficient to synthetic data. (a) 4 clearly segmented Gaussians. Each statistical method gives 4 clusters as a result. (b) 4 Gaussians with overlapping segmentation. Statistical methods are not able to identify 4 individual clusters. (c) 2 Gaussians representing a hypothetical histogram of BS data of the Cleaver Bank. Statistical methods identify 2 clusters. (d) 7 Gaussians that approximately reproduce the histogram of the BS data of the Cleaver Bank but with added separation. Even in this modeled and simplified case, statistical methods suggest 2 clusters as the optimal number.

In this study, the BS features are highly correlated. It is hypothesized that for situations where this correlation is less, or when additional information such as those derived from bathymetry are added, the overlap in clusters diminishes and separation between clusters would be higher. The Bayesian method accounts for the statistical fluctuation of the BS data [13], and therefore, is able to distinguish between individual overlapping clusters in this study as well. This method estimates seven clusters to be present in the dataset. Based on the result of the Bayesian method and taking into account the fact that the ground truth data reveal eight sediment types (defined by the Folk scheme) as well as to have consistency between the Bayes and PCA/k-means methods, k-means clustering is applied with a choice of seven clusters.

Acoustic classes are obtained from the output of the k-means clustering by sorting the seven clusters according to the averaged BS value of each cluster. Fig. 3.4b displays the resulting acoustic classification map. Compared to the acoustic map of the Bayesian approach (Fig. 3.4a) AC_1 and AC_7 have a very large contribution to the entire map. The resulting map can be divided in six distinct areas based on the criterion of high and low ACs as well as homogeneity and heterogeneity. The most obvious areas are

1) the heterogeneous centrum consisting of mainly ACs with higher BS values
2) the homogenous north-western and south-eastern parts with lower BS values
3) the very homogeneous Botney cut characterised by only AC_1 in the south of the central part
4) the south-western area which is characterised by homogeneously distributed sediments with high BS values
5) just north of the centre a stripe of low BS, homogeneously distributed sediment is located
6) further north in the north-eastern part of the map a very small stripe of heterogeneous, high ACs, sediment is present

These distinct areas are also visible in the acoustic map of the Bayesian method (Fig. 3.4b). The main differences to consider belong to a shift between the ACs, in particular at the low and high classes.

3.4.3. Repeatability of acoustic classification results

In order to examine the repeatability of the classification results over the different surveys, the intersections of the survey lines are quantitatively and qualitative compared. A visual and more qualitatively comparison is shown in Fig. 3.8 where a small area of the Cleaver Bank with a total of eight intersections of survey lines is displayed. All five surveys are represented in this small area of the map. Visually a high agreement in the classification results obtained from the data from different surveys is present. Examples are the intersections displayed in the areas A and B where the acoustic classification indicates for both areas a heterogeneous seabed. At the intersection of the most western 2013 week 45 line and the 2013 week 47 line (area A) both surveys show an area of AC_3, surrounded by AC_6. Area B indicates for both surveys the presence of AC_2 to AC_6 in good agreement. Also the intersection in the areas D, E, F, G and H, which consist of higher classes, AC_5 to AC_7, show a high agreement between the different surveys. However, discrepancies also occur, for example at the intersection of the 2015 survey and the 2013 week 47 survey in area C. The 2013 data show AC_2 whereas the 2015 data show AC_1 for PCA. The Bayesian results in this intersection show AC_3 for the 2013 data and AC_2 for the 2015 data. This is the most apparent disagreement seen on this part of the map.

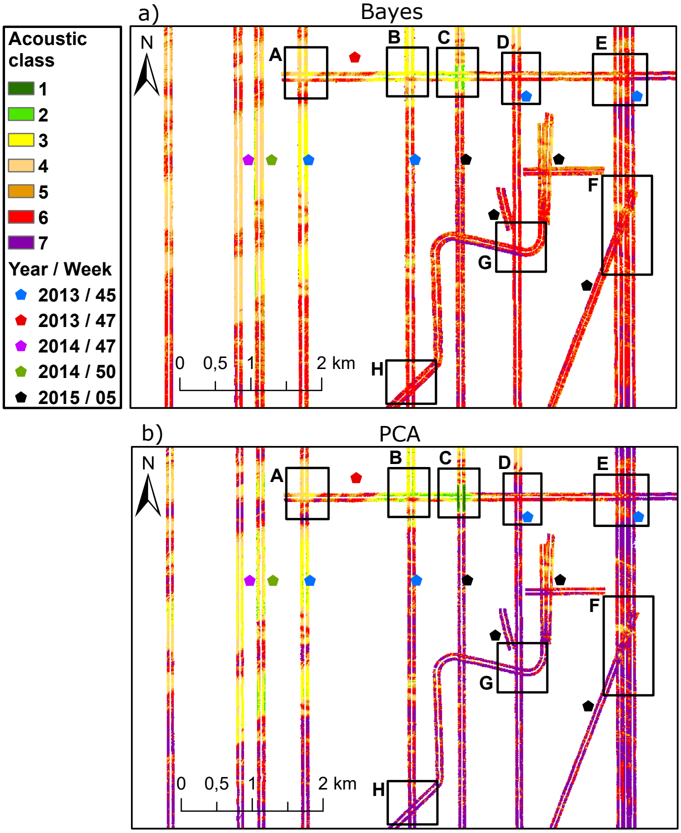

Figure 3.8: Zoomed in area of acoustic classification map generated by a) Bayesian classification and c) PCA in conjunction with k-means clustering. The location of the area is indicated in Fig. 3.4. Different survey lines denoted by the colored pentagons are visible. The grid is resampled to a size of 10 m by 10 m using the mode value of the finer grid.

A high repeatability is also apparent in Fig. 3.9. Here, the ACs of Bayes and PCA determined for the intersecting areas of the 2013 and 2014/2015 surveys are presented in a scatter plot. It is shown that for the majority of the cases the results are in good agreement lining up around the diagonal. The Bayesian method shows a high agreement for AC_2 to AC_6 and a higher deviation for AC_1 and AC_7. While the PCA shows a better agreement of the lowest and highest class, the AC_2 to AC_6 indicate a higher spread between the different surveys.

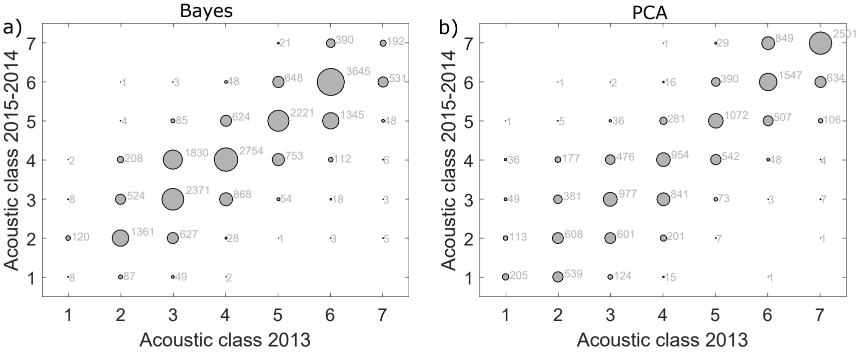

Figure 3.9: Correlation plot of the ACs determined with the a) Bayesian method and b) PCA. The size of the dots and the number indicate the number of matches for the ACs determined for the intersecting areas using the BS data from the different surveys in 2013, 2014 and 2015.

A quantitative evaluation, based on the percental match between the classes of the different surveys (i.e., overall accuracy), is given in Table 3.2. The overall accuracy between the different surveys varies between 53 and 58 % for the Bayesian method and between 51 and 56 % for the PCA method. Accepting a deviation of one AC the overall accuracy increases to 97 and 94 % for the Bayesian and PCA method, respectively.

Table 3.2: Overall accuracy between ACs determined for intersecting areas using BS from datasets acquired in 2013, 2014 and 2015. The number in the brackets indicate that a deviation of 1 AC is accepted.

Datasets	PCA	Bayes	PCA (1)	Bayes (1)
2015/2013	51 %	58 %	94 %	97 %
2014/2013	56 %	58 %	94 %	97 %
2015/2014	55 %	53 %	93 %	94 %

A few plausible explanations for the disagreement of one AC exist. Firstly, even though it would not be expected, it is possible that there was a sediment change from 2013 to 2015, that would explain why the discrepancy is present for both classification methods in, for example, area C. To prove a sediment change at any point a grab sample from both periods at the location would be required, but this is unfortunately not available. For the case where no actual sediment change did occur, it is possible that the BS from locations with different classifications are close to a class boundary and happen to just fall within a neighbouring class e.g., due to a different area coverage of the survey. A further reason for a mismatch could be a directional small-scale morphological influence because of different sailing directions [99]. It also needs to be considered that the discrepancies are mostly not greater than 1 AC (94 and 97 %) which is a reasonable discrepancy by seven distinct classes. Given that this is data from five different surveys carried out over the time period from 2013 to 2015 and that the data were acquired by different vessels, crews, MBES systems and environmental conditions, the results still demonstrate a high degree of repeatability and consistency of the acoustic classifications for both methods.

Although the classification results are in good agreement when comparing the classification from different surveys for one method, the comparison between classification results from applying different methods reveals differences. Whereas the Bayes classification indicates the presence of mainly five types of sediments, since AC_1 and AC_7 are hardly present, the PCA classification shows all sediment types to be almost equally present. The deviations from PCA and Bayesian within the low and high ACs ranges are related to the different mathematical approaches of the methods. Considering Fig. 3.3, it is seen that the Gaussians of AC_1 and AC_7 have only a very small contribution to the histogram of BS measurements. For k-means clustering seven sediment types are assumed. K-means clustering defines the clusters on a simple similarity measurement of the first PC and assigns these clusters based on an increasing BS value. This leads to a more balanced number of data points within the individual clusters, i.e., ACs. Therefore, the PCA results show, in contrast to Bayes, a significant presence of AC_1 and AC_7. Still, the maps obtained with the two different methods indicate a similar spatial distribution of the different sediment types over the area.

3.4.4. Conversion from acoustic class to sediment map

Often, for mapping the spatial distribution of sediments, use is made of maps presenting the Folk class [83]. Here, it is investigated to what extent these types of maps can be derived from the acoustic classification results by assigning sediment types to the ACs. For the assignment the original resolution of both methods is used, which is for the Bayesian method defined by the average over the beams and pings (few meters dependent on water depth and angular range, ungridded) and for the PCA defined by the patch size (10 m by 10 m, gridded). Due to the higher resolution of the Bayesian method, only 72 samples fall into the 25 m radius while 77 samples are considered in the PCA.

As a first step, it is assumed that the lowest AC represents finer sediments whereas the highest AC represents coarser sediments. Here, the order of Folk classes is selected such that it is assumed to represent increasing median grain size. The resulting number of matches between AC number and sediment type at the grab sample location are plotted in Fig. 3.10 for the Bayes and PCA results, respectively. In general, indeed increasing AC is seen to correspond to an increasing median grain size, as represented by the sediment type. The PCA results show a good match of AC_1 with the sediment type sandy mud (Fig. 3.10b). For example, this indicates that the Botney cut is covered by sandy mud. However, the assignment of the sand sediment types from muddy sand to sandy gravel are less clear. For instance, the sediment type sand shows a uniform distribution from AC_1 to AC_5. This indicates additional factors influencing the BS data and causes difficulties in the assignment

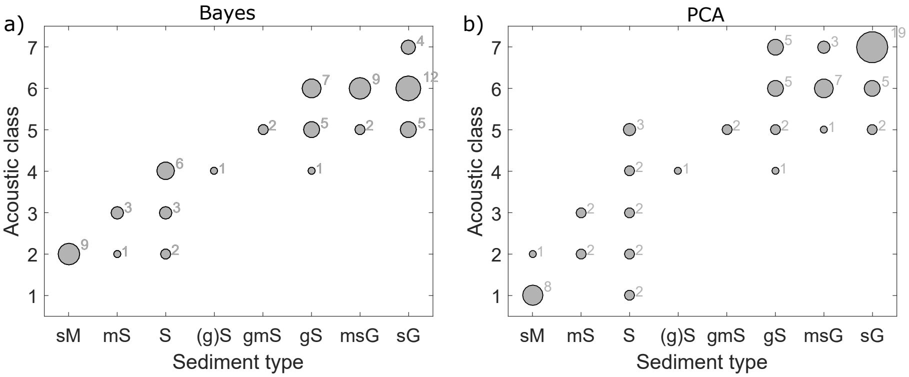

Figure 3.10: Correlation between AC and sediment type at grab sample locations. a) Bayesian method, b) PCA. Dots indicate the number of matches between AC and sediment type. The sediment type is determined after Folk [83].

of sediment type sand to a distinct AC. For the Bayes results (Fig. 3.10a) it is found that AC_1 does not correlate to any grab sample (in the following noted as unassigned (UN)). For all other ACs there is some ambiguity in the relation between sediment type and AC.

Table 3.3: Assignment of sediment type (Folk scheme) to AC. ACs are obtained from applying the Bayes classification method.

Sediment type	UN	sM	mS	S	gmS	gS	msG	sG
Acoustic class	1	2	3	4	5	5-6	5-6	6-7

Fig. 3.11 shows the Folk class map based on the Bayes classification accounting for the mentioned non-uniqueness. The proposed assignment of Folk class to sediment type is presented in Table 3.3. Using this assignment an overall accuracy of 83 % is obtained. It should be noted, however, that especially for AC_5 a unique relation with Folk class is not found and for Fig. 3.11 it is taken to correspond mainly to gravelly sand and muddy sandy gravel. A similar map can be made for the results of PCA, but here only the Bayes results in Fig. 3.11 are presented.

3.5. Discussion

3.5.1. Spatial resolution of classification results

To investigate the scale of information obtained from the acoustic classification, Fig. 3.11 shows more detailed pictures of selected areas in the Cleaver Bank. These areas are selected because grab samples are available and abrupt changes in the ACs occur within a mainly homogeneous area. Whereas, on the main sediment map the high resolution and the agreement between grabs sample and classification result are not obvious, the zoomed in plots do demonstrate these items. Each

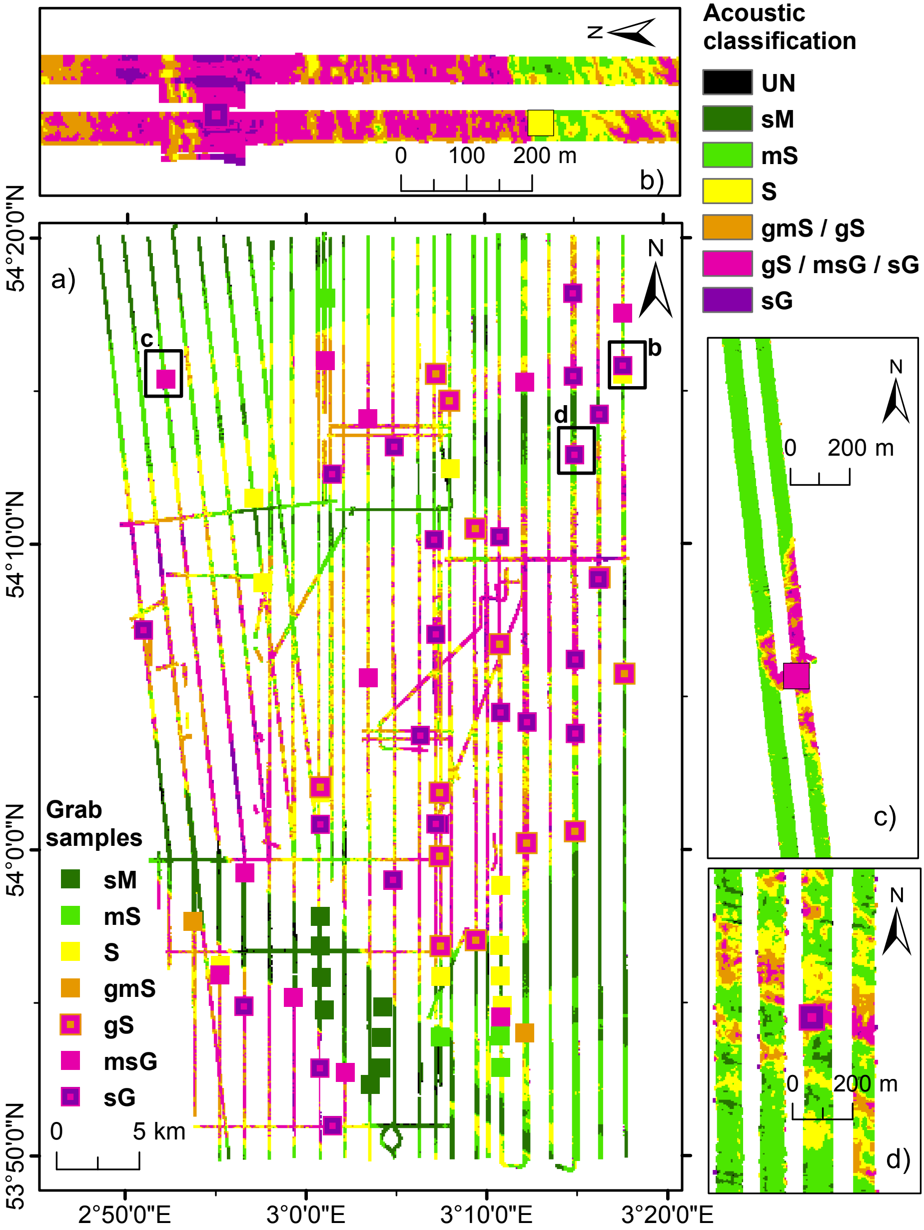

Figure 3.11: Sediment map of the Cleaver Bank obtained from the Bayesian method and ground truth data. Sediment classes range from sandy mud (sM) to sandy gravel (sG). a) Sediment map of the entire survey area of the Cleaver Bank with a resolution of 100 m by 100 m. b), c) and d) represent small areas of the sediment map with a resolution of 3 m by 3 m. The grab samples can be seen in the main map as a color coded squares.

picture depicts strong changes in sediment classes over tens of meters resolved by the acoustic classification method. The sediment type of the grab samples denoted by the colored squares matches well with the classification result. In particular, Fig. 3.11b shows an abrupt change in the sediment map which matches perfectly with the ground truth given sandy gravel and sand as a sediment type. It is notable that the sand grab sample is only approximately 10 m away from the estimated sand to gravel boundary but is perfectly resolved on the sediment map. Fig. 3.11c displays an area which seems to be a homogeneous sandy mud to muddy sand region on the main map but the detailed view reveals a gravelly sediment patch within this area. This patch matches very well with the grab sample of muddy sandy gravel. The detailed pictures display only a few examples of the match between classification result and grab sample. The main map of the Cleaver Bank, in general, also shows good agreement between classification results and ground truth. For instance, the Botney cut is classified with sandy mud which fits to each grab sample taken in that area.

3.5.2. Relation between acoustics and sediment median grain size

In Section 3.4.4 the relation between AC and Folk class is investigated. It is found that no unique relation holds for the frequency and sediments considered in this study. Therefore, in this section it is investigated whether a more unique relationship between AC and median grain size exists. To this end, the median (d_{50} value) of the grab samples are now considered. Except for AC$_7$, the median values increase with class number as seen in Fig. 3.12a which presents the d_{50} value as a function of AC. This reflects an increasing BS value with increasing class number. AC$_7$ does not have a median value higher than that of AC$_6$. This indicates a situation where the highest BS values (AC$_7$) apparently correspond to median grain sizes that are not necessarily higher than those belonging to AC$_6$. Based on this result it can be concluded that, especially for the higher ACs, as for the Folk class also no unique relationship between AC and median grain size exists in the data.

To further investigate this we consider standardized BS values instead of AC. In Fig. 3.12b the BS values (averaged over measurements within 25 m around a grab sample location) are shown as a function of d_{50} values. The BS values are additionally normalized by dividing each BS value by the maximum BS value thus yielding values strictly between -1 and 1. Fig. 3.12b shows a significant positive correlation between BS and median grain size for the fine fraction ($< 1\Phi$ (0.5 mm))[2]. From the data, however, it is found that the magnitude of increase in BS with increasing median grain size is less significant between 1 and -1Φ (0.5 - 2 mm), followed by a plateau and a decrease for even coarser sediments. This indicates that an ambiguity for the relationship between BS values and median grain size exists and hinders the discrimination of sediment types with median grain sizes larger than 1Φ (0.5 mm) using acoustic classification methods based only on BS data (acquired with a frequency of 300 kHz). This is in agreement with the findings of Section 3.4.4

---

[2] In Appendix B the conversion of the median grain size from the unit millimeter to Φ is given.

and indicates that there is no one-to-one relationship between median grain size and BS for the entire grain-size spectrum. Such a positive correlation between BS and median grain size followed by a negative correlation was also observed in [19]. They referred to this change in relationship as a transition point. The transition point in the study of Eleftherakis *et al.* [19] occurred at -3.5Φ (11 mm) using a frequency of 300 kHz. We estimate the transition point at approximately -2Φ (4 mm). That means both transition points occur roughly around the acoustic wavelength (5 mm) of the MBES.

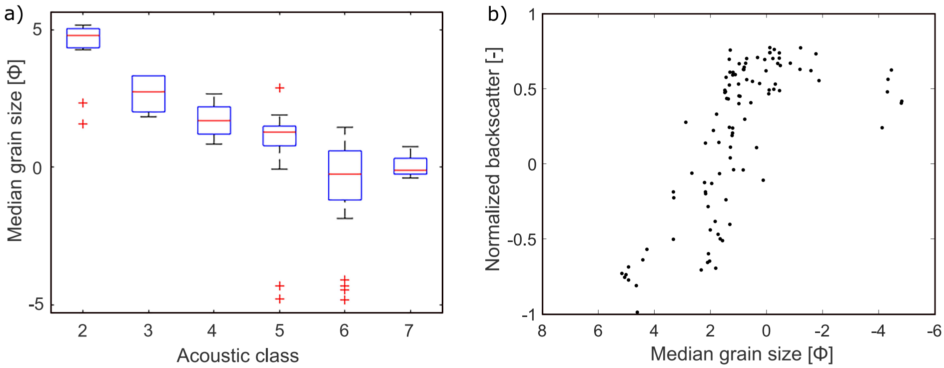

Figure 3.12: a) Box plots of sediment samples that fall within the same AC obtained from the Bayesian method. The bottom and top of the blue rectangle represent the 25th and 75th percentiles, respectively, whereas the red line indicates the median value. The whiskers extend to the minimum and maximum value of the d_{50} values that are not considered outliers. Outliers are marked with red crosses. b) BS values as a function of the median grain size (d_{50}) of grab samples. Dots indicate the averaged and standardized BS values within a maximum radius of 25 m around the grab sample.

3.6. Conclusion

In this study two different acoustic classification methods, namely the Bayesian method and the PCA in conjunction with k-means clustering, were applied to multibeam BS data from the Cleaver Bank in the Dutch North Sea. For both methods, the classification is based on changes in BS values for different sediment types. The data were acquired on two different Dutch vessels during five different surveys carried out in various time periods from 2013 to 2015.

The resulting maps showed a high consistency between the classification results obtained from the different surveys and using a single classification method, despite the use of different vessels and varying time periods. Some discrepancies, however, were observed (a difference of 1 AC); to gain a better understanding of these would require repeated surveys following the same survey patterns and supported by repeated grab samples for each of those surveys. Despite the discrepancies, this study demonstrates the potential of using BS data for achieving repeatable seabed sediment classification results even if the BS data are acquired during different time periods and from MBES systems which are mounted on different ships and thus subjected to different installations, survey settings, and ship crews. It can be concluded that the current state of BS-based sediment classification methods is such that it can be used for marine sediment monitoring where the aim is to identify changes in the sediment over time.

However, the current study clearly shows that monitoring requires the use of a single classification technique. Although, the same large-scale features were resolved, the two different techniques resulted in different maps. For the two methods considered and using BS data only, the difference fully stems from the different approaches used for assigning BS measurements to a certain AC. The Bayesian method accounts for the statistical characteristics of the BS by assuming Gaussian distributed BS values. Whereas the PCA in conjunction with k-means clustering classifies a dataset with respect to similarities of predefined properties and, thereby, neglects the natural fluctuation of BS, which can superimpose the BS variation due to different seabed properties. The PCA method was found to underestimate the number of sediment types within the study area. Still, if additional information, such as bathymetry derived features, are considered the PCA method becomes an essential tool due to the ability of selecting the most valuable features [19, 22].

Finally, it was investigated to what extent Folk classes and median grain sizes can be assigned to ACs. In general, this step is hindered by the fact that sediment bulk density, seabed roughness, volume heterogeneity, discrete scatterers and sediment layering all contribute to the BS strength depending on the seabed complexity, acoustic frequency and incident angle [6, 31, 32]. For the Cleaver Bank area and the MBES (300 kHz) considered here, no unique relation between Folk class and AC could be established. To still be able to map Folk class, a conversion scheme accounting for this non-uniqueness was introduced where a range of Folk classes is assigned to a single AC. With regards to the relationship between median grain size and BS (AC), a strong positive correlation for the fine fraction (< 0.5 mm) followed by a decrease in positive correlation and a change into negative correlation for coarser sediments (> 4 mm) were observed. This constitutes an ambiguity in the relationship between BS and median grain size. Therefore, care must be taken when assigning sediment properties or types (e.g., median grain size or Folk class) to an AC based on MBES BS.

In conclusion, although limitations exist, current seabed classification capabilities are such that they are a valuable asset in long-term monitoring efforts of the marine environment.

4

Monitoring underwater nourishments using multibeam bathymetric and backscatter time series

The previous chapter has shown that despite the use of different ships and multibeam echosounder (MBES) models, repeatable sediment classification results can be obtained. The study area (Cleaver Bank) represented a temporal stable seabed and the focus was on the repeatability of backscatter (BS)-based sediment classification rather than an actual change detection of sediment distributions. In this chapter, the applicability of repetitive MBES measurements to monitor sediment distributions in a very dynamic environment is assessed. A focus lies on underwater nourishments and the role of the MBES, providing both bathymetry and BS, as a monitoring tool. A time series of seven MBES measurements using a Kongsberg EM 2040C MBES (300 kHz), as well as two sets of box cores, several vibrocores and seismic data were acquired of a channel-side nourishment near the Wadden Sea island Ameland (The Netherlands), between April 2017 and May 2019. It is investigated to what extent external sources, others than the seabed properties, affect the measured BS strength and the acoustic sediment classification. The Bayesian sediment classification method, supported by ground-truthing data, is used to produce sediment maps from a time series of MBES BS measurements. Based on the MBES bathymetry and the sediment classification, the evolution of the morphodynamics and sedimentary patterns are analyzed. Lastly, a link between the MBES and seismic data is drawn to connect high-resolution seabed mapping with low-resolution subsurface mapping.

This chapter has been published in Coastal Engineering **158**, 103666 [100].

4.1. Introduction

Coastal erosion is a hazard to humans and infrastructure in coastal zones worldwide. Erosion is mainly driven by storm waves, cross- and long-shore currents but also sea level rise leads to loss of coastal land [101]. For barrier coasts like the Wadden Sea islands, beach and underwater nourishments are an efficient coastal protection strategy to further mitigate erosion and to counteract sea-level rise. In the Netherlands, yearly nourishments exceed 12 million m^3 [102]. Without such human intervention it is unlikely that the natural processes can supply sufficient sediment to hold the Wadden Sea islands in a dynamic equilibrium to relative sea-level rise and further erosions [103]. However, consequences of coastal engineering on the long-term response of the Wadden Sea environment is in general relatively unexplored [103]. Coastal engineering, like nourishments or seawalls, can induce changes of the sediment transport pathways resulting in erosion and deposition in unpredicted areas [104]. A sustainable management of the nourishments requires monitoring strategies of the sediment and morphodynamics in order to understand the impact of the nourishments on the natural dynamics or the ecology.

Acoustic remote sensing with multibeam echosounders (MBESs) is extensively used for mapping the seabed bathymetry because of the capability to map large areas in relatively short time periods; this means covering an area of up to seven times the water depth perpendicular to the sailing direction [4]. State-of-the-art monitoring strategies for dredging or nourishment activities already utilize MBES bathymetry measurements to determine sediment volume changes over time [105, 106]. Applying radiometrical and geometrical corrections to the received signal at the MBES, a measure of the backscatter (BS) strength can be retrieved [4]. This is an intrinsic property of the seabed and therefore applicable to characterize seabed substrate types. As shown by several scientific studies, collecting BS data over large areas allows to extend in situ measurements from a single location (e.g., box core samples or video footage) to a large-scale and high-resolution sediment map [19, 62, 107, 108].

In order to compare repetitive BS measurements over time for monitoring the seabed environment, external sources of variation in the BS measurement need to be investigated. External sources are either related to the acoustic system or the environment. The former includes varying sonar settings, aging antennas, varying transducer sensitivity or biofouling at the transducer. Environmental sources are in particular related to the water column properties due to the occurrence of sediment suspension, gas bubbles or varying salinity and temperature [7]. In addition, the orientation of small-scale bedforms (i.e., organized seabed roughness) relative to the navigation direction causes an azimuthal dependency of the BS strength [109]. An ideal design and implementation of a BS monitoring program requires full control of the acoustic system and the environment [76]. The calibration of a MBES for BS measurements, aiming for a full control of the sources related to the acoustic system, has just recently attracted more attention [7]. Currently, two approaches exist to calibrate the MBES for BS measurements: 1) an absolute calibration via a cross-correlation with a fully calibrated reference system (e.g., singlebeam echosounder) [29, 110–112] or 2) a relative calibration using natural reference areas with a known and temporally stable BS response [26]. As long as the MBES is not calibrated, the measured and processed BS data represent a relative measurement and the correct terminology is either relative BS strength, BS value or BS level (see also Section 3.3.1). To control environmental sources, Montereale-Gavazzi *et al.* [28] used acoustic and optical BS sensors to measure the sediment suspension concentration (SSC) between 0.2 and 2.4 m above the seabed. However, the control of all parameters is often unfeasible due to time or budget limitations, environmental settings or weather conditions and alternative approaches are required as well.

To date, only a limited number of studies employed repetitive MBES BS measurements, either focusing on the temporal reliability of the BS levels [26–28] and the acoustic classification results (Chapter 3, [61]) or using the BS measurements for seabed change detection of natural seabeds via manual interpretation [23] and automatic classification methods [24, 25]. Roche *et al.* [26] showed that the use of natural reference areas allows for comparing BS measurements over time, based on an investigation of uncalibrated BS surveys in a time span of 12 years at three shallow-water areas. Montereale-Gavazzi *et al.* [28] conducted a field experiment of 15 to 47 repetitive tracks in three areas to investigate the effect of short-term hydrodynamic variations and SSC on the BS level over a tidal cycle (∼13 hours). In Chapter 3, the repeatability of five MBES surveys acquired over 15 months in a very stable environment was studied, and it was demonstrated that sediment classification based on MBES BS achieves repeatable results in this stable environment. Montereale-Gavazzi *et al.* [25] used a natural reference area and a consistent data acquisition to assure the temporal stability of the measured BS data, which allowed for the quantification of temporal changes of sediment distributions, and identified the expansion of sandy areas over gravel beds. Despite the few studies, there is still a need to develop strategies to quantify the acoustic reliability of BS measurements, in particular related to the environmental sources but also addressing the system sources when natural reference areas are not at hand. In addition, previous studies have not used repetitive BS measurements to monitor the evolution or impact of human interventions, such as nourishments, on a natural system.

This study aims to exploit the potential of MBES data, providing both bathymetry and BS, to monitor underwater nourishments. To this end, we acquired a time series of seven MBES BS datasets in the tidal inlet of the Wadden Sea island Ameland (The Netherlands) within the period from April 2017 to May 2019. We address the acoustic reliability of the MBES measurements and investigate to what extent we are able to acquire and process a MBES BS time series in such a way that the resulting maps represent the actual seabed properties. At the same time we explore the value of MBES BS time series, in addition to MBES bathymetry, for studying the morphodynamics and distribution of the nourished and native sediments.

4.2. Study area and data

4.2.1. Geological setting

Ameland is one of the back-barrier islands in the north of the Netherlands (Fig. 4.1a). The islands are separated by tidal inlets, connecting the North Sea and the Wadden Sea (back-barrier tidal basin), with flood and ebb tidal deltas on the land and seaward side, respectively. Tidal channels incise the flood tidal delta and are connected to the tidal inlet and the ebb tidal delta. The Ameland inlet extends 6 km into the North Sea with a maximum water depth of 28.5 m and a local tidal range around 2 m. The long-term development of the Ameland inlet results in a period of sediment loss and coastal retreat [113]. The study area is located around the tidal channel, called Borndiep, in the eastern part of the tidal inlet and is about ~80 m south-west from the coastline of Ameland (Fig. 4.1c) with a size of 3.8 km × 0.5 km (Fig. 4.1d). The investigated area comprises a part of the tidal channel and a very steep retrograding channel wall. The main sediment types in the area range from sandy mud to medium sand, with a varying amount of shells and gravel. Since 1947 revetments are being placed close to the shore to prevent the tidal channel from migrating landward [114]. The nourishments were conducted in the central and south-eastern part of the study area, close to the channel wall (Fig. 4.1d).

4.2.2. Acoustic data acquisition

The MBES data acquisition was carried out with a Kongsberg maritime EM 2040C dual-head, operated with the data acquisition software SIS and installed on the survey vessels Siege and Amasus. A Trimble SPS851 GNSS receiver provided real-time kinematic positioning with a horizontal and vertical accuracy of 1 and 2 cm, respectively. The motion sensor was a IXSea Octans gyro. Up to five CTD (conductivity, temperature and depth) measurements per survey were taken with a Valeport sound velocity probe. Table 4.1 reports the sonar settings used to operate the MBES. The MBES datasets are temporally separated by a minimum of 10 weeks and a maximum of 26 weeks (Table 4.2).

Table 4.1: Sonar settings of the EM 2040C, with in brackets the deviating settings of the April 2017 survey.

Center frequency	300 kHz
Frequency spectrum	270 to 330 kHz
Nominal pulse length	145 µs (341 µs)
Number of beams	512
Beam width	1.3° x 1.3°
Swath coverage	70°/−70° (75°/−75°)
Beam spacing	equiangular (equidistant)
Ping modus	dual swath (single swath)
Pulse type	shaped continous wave

A total of 17 track lines were acquired in NW-SE direction with an overlap of about 120 % for adjacent track lines. The navigation equipment, sonar settings as well as the location, number and direction of survey lines were consistent among the different surveys, except for the first survey (April 2017) (Table 4.1). The survey vessel (Siege and Amasus) and the MBES were changed after the first 5 surveys (April 2017 to September 2018: Siege; February to May 2019: Amasus). For data control additional survey lines with different azimuthal directions (~45° interval) covering the same reference area (called ”compass rose” pattern in [109]) as well as calibration lines were acquired. During three surveys in April 2017, September 2018 and May 2019 a rough sea state (wave heights up to 1 m) yielded to a vessel roll of up to 5°, 12° and 5° and a vessel pitch of 8°, 3° and 6° in the north-western part of the survey area, respectively.

Table 4.2: Dataset overview. Pre, intra and post indicate the time of the acoustic measurement or ground-truthing relative to the nourishment period.

Data	Date	
MBES bathymetry and BS	25/04/2017	Pre
	24/05/2017 (bathy only)	Pre
	26/10/2017	Intra
	13/03/2018	Post
	23/05/2018	Post
	17/09/2018	Post
	28/02/2019	Post
	21/05/2019	Post
Sub-bottom profiling	15/11/2017 to 17/11/2017	Intra
Box core sampling	09/05/2017	Pre
	22/05/2018 to 24/05/2018	Post
Vibrocore sampling	22/05/2018 to 23/05/2018	Post
Nourishments	01/06/2017 to 22/02/2018	

The seismic data were acquired in November 2017 with an Edgetech X-star 3200XS sub-bottom system consisting of the SB512i tow fish. A chirp signal with frequencies from 0.5 to 7.2 kHz and a pulse length of 30 ms were used. After filtering, the emitted signal was reduced to a near-Klauder wavelet with a center frequency of 3.5 kHz and an effective bandwidth (between the -6 dB points) of 2.5 to 5.5 kHz. The resulting vertical resolution is about 25 cm. We ran seismic lines mainly in NW-SE direction with a distance of 20 m between adjacent lines. In Fig. 4.1 only the seismic line presented in this study is shown. The data were post-processed with the Delph software suite and the seismic reflectors were manually interpreted with the support of the vibrocores [114]. The time-depth conversion was performed assuming a sound velocity of 1500 m/s for the water column and 1600 m/s for the subsurface.

4.2.3. Ground truth data

Bed sample locations were selected after collecting the MBES data to sample the variations in the BS level observed in the preliminary BS mosaics. A cylindrical box-core sampler was used, with a diameter of 30 cm, which retrieves to a certain extent the undisturbed seabed. We conducted two sampling campaigns in May 2017 (24 samples) and May 2018 (22 samples) (Table 4.2). Each box core was photographed and surface samples (0 to 2 cm) were taken on board for grain-size analysis in the lab. Since the majority of the particles larger than 2 mm were composed of shells and shell fragments, particles larger than 2 mm were sieved out and dry weighted. Grain-size distributions of the mud and sand fractions were determined by laser diffraction (Malvern 2000), a technique that measures the scattering of light. Samples were neither prepared nor peptised and measured without ultrasone conditions.

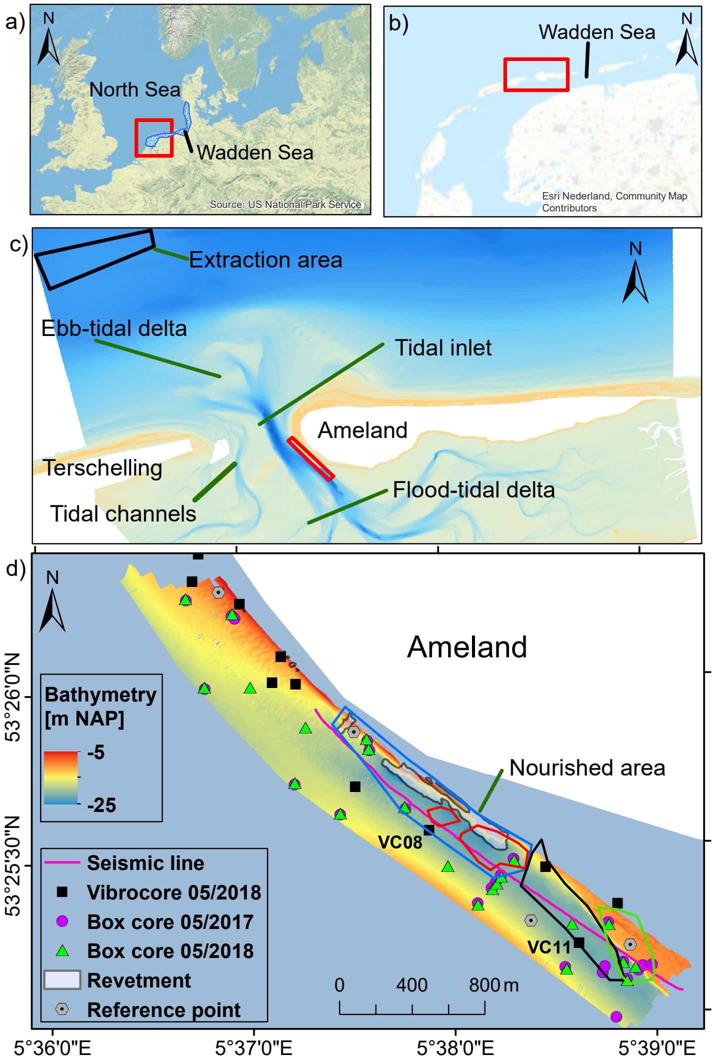

Figure 4.1: Study area: a) North Sea, b) Dutch Wadden Sea, c) Ameland inlet, d) south-west side of Ameland. The red rectangles indicate the smaller subsets from a), b) and c). In d) the actual study area is indicated by the displayed bathymetry (measured in April 2017). Nourishment took place between June 2017 and February 2018 in the indicated dumping areas (colored polygons): June to July 2017 (green), September to October 2017 (black), June to October 2017 (red) and October 2017 to February 2018 (blue). The reference points are used as geographical orientation for subsequent figures.

For the interpretation of BS data in this study, the median grain size, d_{50}, of the mud and sand fractions (volume percentage) is used and we consider the fraction larger than 2 mm (weight percentage) separately. The d_{50} value ranges between 220 to 280 µm, with one sample having a value of 20 µm. The amount of particles larger than 2 mm (shell and gravel) varies between 0 and 18 %.

Sediment cores were taken with a vibrocorer in May 2018 and described, photographed and analyzed in the lab. Sediment layers and grain-size distribution were determined similar to the box core samples.

4.2.4. Nourishments

Underwater nourishments were performed between June 2017 and February 2018. The sediments for the nourishments were extracted from an area to the north-west of Ameland (Fig. 4.1c). Box core and vibrocore samples were taken at several locations in the extraction area before the nourishments started. In general, the surficial and subsurface sediment consists of fine to medium sand with a moderate amount of silt and shell fragments in the extraction area. In the subsurface (50 to 100 cm) also traces of clay were found. At the different sample locations the d_{50} value ranges from 205 to 217 µm except for one location where a d_{50} value of 143 µm was measured. The nourished area is located in the south-east of the study area (Fig. 4.1d).

4.3. Methods

4.3.1. Multibeam data processing

A combination of the software Qimera and developed Matlab scripts are used for bathymetric data processing. Soundings are cleaned with a spline-filter, vertically referenced to Normaal Amsterdams Peil (NAP) and gridded into a 0.5 m by 0.5 m grid using the GIS software packages ARCmap 10.5 and SAGA.

The BS processing algorithm, written in Matlab, is implemented as follows. In the first step the BS ”beam amplitude” data and all necessary sonar and environmental parameters are extracted from the Kongsberg sonar datagrams. The second step is to retrieve the BS strength BS (in dB per 1 m^2 at 1 m) from the received echo level EL (in dB re 1 V) as accurately as possible via the sonar equation (Eq. (2.31), Section 2.4). The external sources related to environmental properties, hardware and sonar settings, contributing to EL, are described by the sonar equation. Within the Kongsberg MBES the hardware- and software-related terms are considered and to a certain extent accounted for during the real-time processing [85]. How well the sonar manufacturer accounts for transducer sensitivity SH and the receiver gain PG and to what extent the conversion of the EL from acoustic pressure (in Pa) to analog values (in dB re 1 V) and finally to digital values (in dB re 1 µPa) is calibrated is not fully known. The following environmental terms require additional post-processing steps for a Kongsberg system. The ensonified area A is not only affected by sonar characteristics (i.e., beam aperture, pulse length) and properties of the study area (i.e., water depth and signal travel distance r) but also by the seabed morphology (see Section 2.4). However, the real-time processing of a Kongsberg MBES assumes a flat seabed and calculates r based on measurements from previous pings [85]. As visualized in Fig. 2.12, in environments with a rough seabed morphology, this simplification has a significant effect on the ensonified footprint and the true incident angle, and consequently on the BS level. To account for both issues, the seabed morphology correction procedure described via Eq. (2.33) to Eq. (2.38) is applied.

The transmission loss TL (in dB) depends on the sound attenuation in the water column and the the energy loss of the signal due to geometrical spreading, as described in Section 2.4 and noted in Eq. (2.32). Sound attenuation in seawater, $\alpha = \alpha_w + \alpha_s$, not only comes from relaxation of dissolved substances and pure water viscosity [4], α_w (in dB/km), but can also be a result of attenuation caused by suspended material, α_s (in dB/km). The coefficient α_w is dependent on temperature, salinity, acidity, pressure and f [59, 60]. The coefficient α_s is dependent on the volume and the geoacoustic properties of the suspended material and f [115]. The Kongsberg real-time processing considers a constant α_w for the entire water column. To calculate a variable α_w with depth the CTD measurements and the expression for α_w, given in [59, 60], are used. The approach to assess the effect of α_s on the BS level due to additional suspended sediment will be described in Section 4.3.2.

BS mosaics are produced by calculating an averaged angular response curve (ARC) over a moving window of 100 pings and then normalizing the BS level at every incident angle with the averaged BS level between 30° and 60° for starboard and port side separately. To improve the quality of the BS mosaics, the average BS level is interpolated between -30° (starboard) and +30° (port). For three surveys (04/17, 09/18 and 05/19) air bubbles near the transducer head generated along-track artifacts in the north-western part of the survey area, which are removed by using an along-track stripe filter. Strong BS artifacts are observed in the northern-middle part of the survey area for the September 2018 measurements. The causes could not be found out and therefore this part is removed from the analysis.

4.3.2. Sediment suspension modeling

Sound attenuation due to suspended material results from the combined effect of viscous absorption and scattering [115]. Viscous absorption defines a frictional energy loss caused by the interaction of the propagating sound field with the viscous fluid and suspended solid particles [116]. Sound scattering represents an energy redistribution by the small rigid particles. Urick [115] demonstrated that sound attenuation caused by suspended material can be estimated by

$$\alpha_s = \left[\frac{k^4 a^3}{96\rho_s} + \frac{k(\frac{\rho_s}{\rho_w} - 1)^2 \Upsilon_1}{2\rho_s(\Upsilon_1^2 + (\frac{\rho_s}{\rho_w} + \Upsilon_2)^2)}\right]\frac{20}{\ln(10)}S \tag{4.1}$$

where $\Upsilon_1 = \frac{9}{2\Upsilon_3 a}(1 + \frac{2}{\Upsilon_3 a})$, $\Upsilon_2 = \frac{1}{2}(1 + \frac{9}{\Upsilon_3 a})$ and $\Upsilon_3 = \sqrt{\frac{\pi f}{\nu}}$. Herein, k is the wavenumber (in m^{-1}), S is the sediment suspension concentration (SSC) (in kg m^{-3}), a is the particle radius (in m), ρ_s and ρ_w are the sediment and water densities (in kg m^{-3}) and ν is the kinematic viscosity (in m^2 s^{-1}). The first term in the squared brackets corresponds to the particle scattering and the second term to the viscous absorption. This equation is valid as long as ka is small compared to unity and $\Upsilon_3 a$ [117]. To assess the sound attenuation due to suspended sediments in our study area, we use measurements from a tidal inlet in the German Wadden Sea as an analogue [118].

4.3.3. Acoustic sediment classification

In this study, the unsupervised Bayesian method for acoustic sediment classification (ASC) is applied to the processed BS data. The method was first developed by Simons and Snellen [13], where a detailed description is given, and further developed by Amiri-Simkooei *et al.* [17] and Gaida *et al.* [55]. In this thesis, Section 3.3.2 and Appendix A.1 provide a detailed description of the method. The main concept of the method is based on the central limit theorem stating that the BS strength from a specific sediment type follows a Gaussian distribution for a sufficient number of measurements. The method employs an optimization technique to fit an increasing number of Gaussian distributions to the measured BS data per beam angle. A Chi-square test is used to define the number of Gaussian distributions yielding to the optimal data fit. Here we apply, following the approach described in Section 3.3.2 [55], the fitting procedure to incident angles between 40 and 65° for starboard and port side to retrieve a statistical robust estimate of the optimal number of Gaussian distributions. When the number of Gaussian distributions is estimated, the boundaries between the Gaussian distributions are determined for three reference angles (in this study between 56 and 63°). The boundaries define the acoustic classes (ACs) and the number of ACs define the number of sediment types which can be distinguished based on the measured BS data in the survey area. Based on the percentage distribution of the ACs at the reference angles, the ACs are assigned to the BS data at all considered angles (in this study 15 to 70°). The application to each survey and each beam angle separately provides a classification approach independent of system dependent sources affecting the absolute BS level, like different transducer sensitivity per sonar head, remaining beam pattern artifacts or changing transducer sensitivity between different surveys. As long as the relative BS level per beam angle (e.g., due to sediment suspension or insufficient CTD measurements) is not affected, the BS can be used for classification. By using the resulting classes from each survey, the classification results can be compared between the different surveys.

The box core samples are used to assign sediment types to the ACs. Therefore, the AC with the highest occurrence (mode) within a radius of 5 m around the sample is calculated and the correlation between sediment types and ACs is evaluated. Based on the correlation, a sediment map is produced from the classified BS data. The calculation of the BS per sample location uses the median of the BS values measured within a radius of 5 m.

4.4. Results

4.4.1. External sources affecting the backscatter level

In order to establish the acoustic reliability of the data, we relate modeled and measured uncertainties of the Ameland BS time series to the external sources affecting the BS level. In this contribution, uncertainty is not strictly considered as a statistical quantity (i.e., standard deviation), it describes rather the variation in BS level caused by the influence of the external source. Table 4.3 summarizes the potential external sources and shows the action which is executed to evaluate or control the particular external source. In addition, the estimated uncertainty in decibels, and whether or not these uncertainties influence the BS mosaics or the ASC, is listed. In the following subsections, we elaborate on the effect of the water column properties, transducer sensitivity and survey azimuth on the BS level in more detail.

Table 4.3: Potential external sources affecting the BS level. Uncertainty represents the averaged value over the angular range from 15 to 70° and the value in the brackets represents the maximum uncertainty within the same angular range. The last two columns indicate whether or not the results are expected to be affected by the specific external source.

External source	Action	Uncertainty	Mosaic	ASC
System settings	Constant (except 04/17 (Table 4.1))	0 dB; (1.4 dB (4.1 dB))	No (yes)	No (no)
Biofouling on sonar heads	Regular checks	Not expected	No	No
Transducer sensitivity (surveys)	Same equipment (except 02/19, 05/19)	Unknown	Possible	No
Transducer sensitivity (sonar heads)	Measured and relat. corrected	0.5 dB to 3.5 dB (4.6 dB)	Yes	No
Survey azimuth	Constant survey lines	1.1 dB (2.2 dB)	Moderate	Moderate
Temperature and salinity	Regular CTD measurements	0.4 dB (0.9 dB)	No	No
Sediment suspension	Modeling based on reference area	0.03 dB (0.06 dB)	No	No
Air bubbles	Avoid rough weather conditions	Unknown	Possible	Possible

Water column: Variation in salinity and temperature

The variation of the water absorption coefficient, α_w, with depths is relatively small, but shows a strong difference among the surveys (e.g., between March and September 2018 of up to 27 dB/km, Fig. 4.2a). This is mainly caused by large seasonal temperature differences. The variation within an individual survey (between 5 to 6 hours) varies for the different surveys. This is indicated by the error bars displaying the lowest and highest absorption coefficient per survey. The causes are probably seasonal and tidal differences in the water mass dynamics, which indicates the importance of regular CTD measurements. Fig. 4.2b displays the difference in sound attenuation per beam angle considering the lowest and highest absorption for a water depth of 25 m. It illustrates the maximum uncertainty of the BS level related to an insufficient sampling of the water column properties (i.e., CTD measurements) in the study area. Solely the October 2017 and May 2018 surveys indicate a noticeable variation in sound attenuation during the survey. The average values are 0.4 and 0.2 dB and the maximum values are 0.9 and 0.4 dB for the outermost beams, respectively. The processing algorithm accounts for the absorption variation in time and depth. However, it needs to be considered that these results are based on 2 to 5 CTD measurements within a time of 5 to 6 h per survey and the maximal variations of the water column properties might not be captured. Therefore, Fig. 4.2b indicates a rough estimate of a potential uncertainty of the BS level due to variation in water column properties.

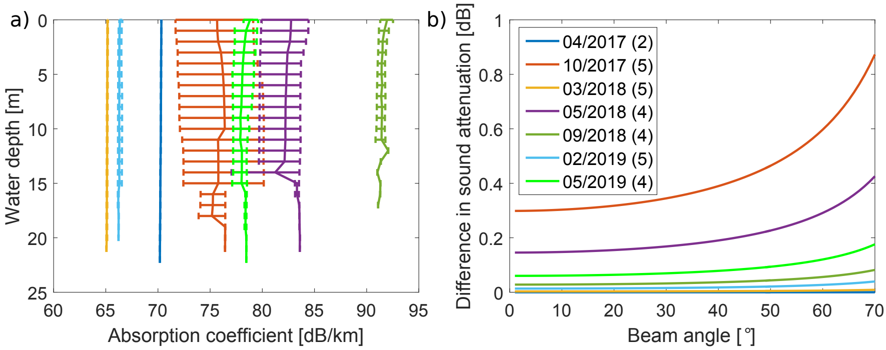

Figure 4.2: a) Averaged absorption coefficient profiles (300 kHz) obtained from CTD profiles measured during the seven MBES surveys. Error bars indicate lowest and highest value of the measured absorption during the entire survey. b) Difference in sound attenuation considering lowest and highest absorption for a water depth of 25 m. Number in brackets represents number of CTD measurements per survey.

Water column: Sediment suspension

In order to estimate the maximum expected sound attenuation α_s caused by suspended sediment, we use the maximum SSCs (S in Eq. (4.1)) measured during a tidal cycle (Scenario 1, 35 mg/l) and a yearly cycle (Scenario 2, 120 mg/l) in a tidal inlet between the German Wadden Sea islands Langeoog and Spiekeroog [118]; an area with similar sedimentary and morphodynamic processes to the Ameland inlet. Bartholomä *et al.* [118] measured SSC values from October 2006 to June 2007 using an in situ laser particle sizer and acoustic doppler current profiler (ADCP) as well as taking water samples from the water column (near water surface to 0.75 m above seabed). We extrapolate the peak values from 0.75 m above the seabed to the entire water column with a slight decrease with increasing distance from the seabed (Fig. 4.3a). This provides a worst-case estimate of the effect of sediment suspension on the BS measurements. Furthermore, we use a maximum water depth of 25 m, an angular range from nadir to 70° and a grain size (a in Eq. (4.1)) of 20 µm (Scenario 1a and 2a) and 250 µm (Scenario 1b and 2b). The grain size of 20 µm displays the lowest d_{50} value obtained from the box core samples in our study area (i.e., lab measurements). The second value results from the reference area where a high rate of flocculation of the fine-grained sediments was observed with an averaged floc size of 250 µm.

Fig. 4.3b represents the sound attenuation over the beam angles for Scenario 1a,b and 2a,b. A maximum sound attenuation of about 2.3 dB is calculated for the highest SSC and the smallest grain size for the outermost beam angle. The decrease in grain size from 250 to 20 µm results in a significant increase in sound attenuation which even exceeds the increase in SSC from 35 to 120 mg/l. The smaller grain size yields to a decrease in sound scattering but it results in an even larger increase in viscous absorption. The sound attenuation of the most extreme case (Scenario 2a) would induce a significant uncertainty for the BS data. However, assuming that in our study area flocculation of the fine grained suspended sediments exists and that the MBES measurements were not conducted shortly after a storm, it is more likely that peak values for sound attenuation in our study area are similar as in Scenario 1b where the sound attenuation does not exceed 0.1 dB. These values would be significantly lower than the uncertainty of 1 dB related to the intrinsic uncertainty of the MBES [85] and therefore the effect is assumed negligible for the datasets considered in this contribution. However, the modeling results also indicate that SSC can lead to a significant effect on the BS level, and therefore surveying during or shortly after storms but also shortly after the nourishments should be avoided.

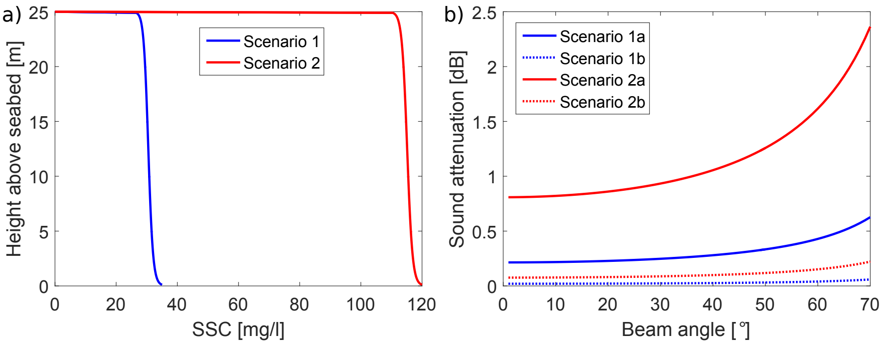

Figure 4.3: a) Peak SSC in the water column in a tidal inlet of the German Wadden Sea as retrieved from [118], as an analogue to the Ameland inlet . Scenario 1 represents the general peak SSC during a tidal cycle and Scenario 2 represents the maximum SSC measured during a yearly cycle. b) Calculated sound attenuation due to sediment suspension with a d_{50} value of (a) 20 µm and (b) 250 µm for a water depth of 25 m and a frequency of 300 kHz based on [115] and [117].

Dual-head transducers

In order to identify a discrepancy in BS levels between the two transducer heads of the Kongsberg EM 2040C MBES, we calculate the averaged ARC for both heads using the MBES BS data from the entire survey area. Due to the large overlap (120 %) and high number of track lines (17), we assume that both transducers ensonify, on average, approximately the same seabed.

The averaged BS values over the angular range from 15 to 70° (Fig. 4.4), show that (1) the transducer heads on the Siege (five surveys with a deviation between sonar heads from 0.5 to 1.4 dB) are better calibrated to each other than on the Amasus (two surveys with a deviation from 3.0 and 3.5 dB) and (2) a high influence of a new installation and a different MBES on the BS level. The estimated difference in the BS levels per incident angle (residual BS curve) between both sonar heads are used to adjust the BS levels relatively to each other (transducer head cross-calibration). This adjustment mitigates the influence on the BS mosaic whereas for the ASC an adjustment is not necessary because the method is applied to each transducer and beam angle separately.

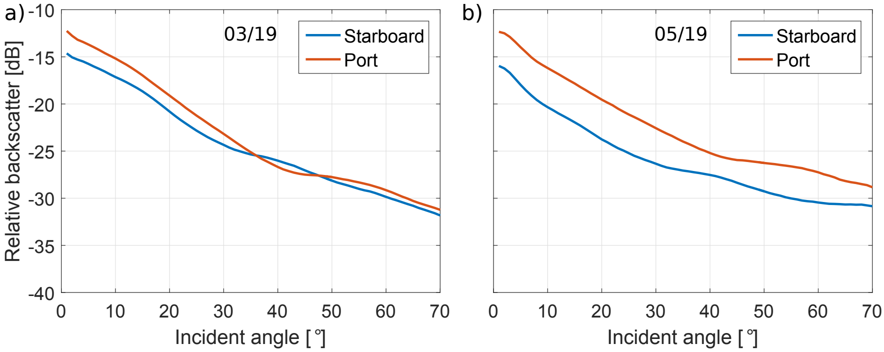

Figure 4.4: Averaged ARCs obtained from the two transducer heads using the entire BS dataset from a) May 2018 (Siege) and b) May 2019 (Amasus).

Survey azimuth

To investigate the influence of the survey line direction (survey azimuth) on the BS level due to organized seabed roughness (e.g., small-scale ripples), we follow the approach developed by Lurton *et al.* [109]. The approach involves a systematic coverage of a reference area with different survey azimuths and comparing the resulting ARC per azimuthal direction. The BS data from both sonar heads are cross-calibrated using the BS residual curves. Comparing the ARCs of six sailing directions from the October 2017 and May 2018 surveys (Fig. 4.5), we observe the largest deviation for the angular range between 20 to 40° with maximum values of 3.4 dB and 4.2 dB in the October 2017 and May 2018 survey, respectively. The maximum deviation averaged over the angular range from 15 to 70° is 2.1 dB and 1.4 dB, respectively. It shows a dependency of the BS level on the azimuth angle and might indicate the existence of organized seabed roughness. Here, one need to consider that these values are rather an overprediction because the incident angles from the different survey line directions do not ensonify exactly the same area on the seabed and slight changes of the seabed properties over time can also have an effect on the measured BS level.

The main survey directions were approximately 120 and 310° for all surveys (i.e., parallel to the shoreline). For these azimuthal directions, we observe an averaged deviation of 0.7 dB and 1.1 dB with maximum values reaching 1.9 dB and 2.2 dB for the October 2017 and May 2019 survey, respectively. That means the effect is lower compared to other azimuthal angles but still for some incident angles the effect of small-scale ripples might mask the actual seabed properties. Using these values as an estimate, one should consider that the orientation of the small-scale ripples might change during the acquisition, which would have the same effect as varying survey azimuths. In general, the averaged values are similar to the intrinsic uncertainty of the MBES (1 dB) [85] and therefore have a minor effect on the BS data and the monitoring purpose in this study. Nevertheless, the results indicate that the survey line direction should be constant during the survey otherwise the effect of small-scale ripples on the BS data becomes more dominant.

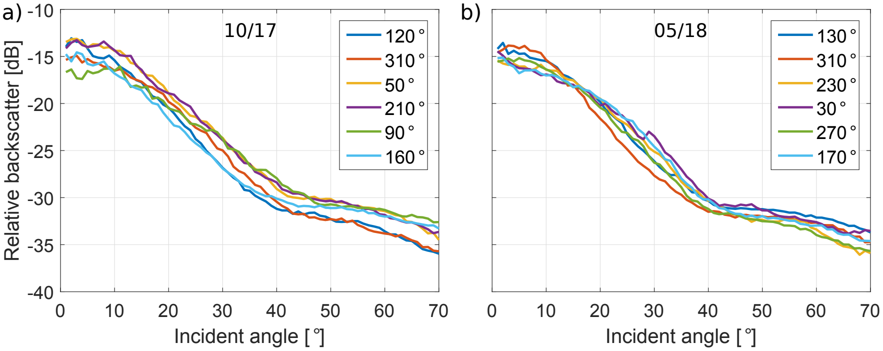

Figure 4.5: Survey azimuth dependency of BS. a) October 2017 and b) May 2018 measurement. Legend indicates the survey direction.

4.4.2. Backscatter and bathymetric time series

The MBES bathymetric time series is used to calculate the differences in bed elevation. The intra-nourishment (10/17) and post-nourishment (03/18 to 05/19) bathymetries are referenced to the pre-nourishment (04/17) bathymetry to indicate bed aggradation and degradation. The April 2017 bathymetry is referenced to a pre-nourishment measurement conducted in May 2017 to indicate the natural seabed dynamics. The bathymetric difference maps represent an aggradation from April 2017 to March 2018 of up to ~10 m vertically (Fig. 4.6). The post-nourishment maps show a degradation in the nourished area and a further aggradation north-west from the nourished area, indicating erosion, sediment transport and deposition towards the tidal inlet. In addition, large bedforms are extensively formed in the northern part of the nourished area and to the north-west of this.

The BS mosaics show, in general, varying patterns over the entire time series, indicating changing seabed properties (Fig. 4.6). High BS levels are observed on the landward side (shoreface) whereas lower BS levels are observed on the tidal-inlet side before the nourishments were conducted (04/17). The intra-nourishment measurement (10/17) shows a lower BS for the areas that were nourished just before the acoustic measurements (blue polygon, Fig. 4.6). This indicates that the rough and hard natural seabed is replaced with smoother and softer nourished material. However, the areas which were nourished three months before the acoustic measurement show high BS values again (green polygon, Fig. 4.6). Similar observations can be made for the post-nourishment measurements, which show higher BS levels for the entire nourished area over time. This indicates that the natural dynamics of the area result in an increase in seabed roughness and hardness of the nourished area. In addition, strong BS variations are observed along the bedforms for all surveys.

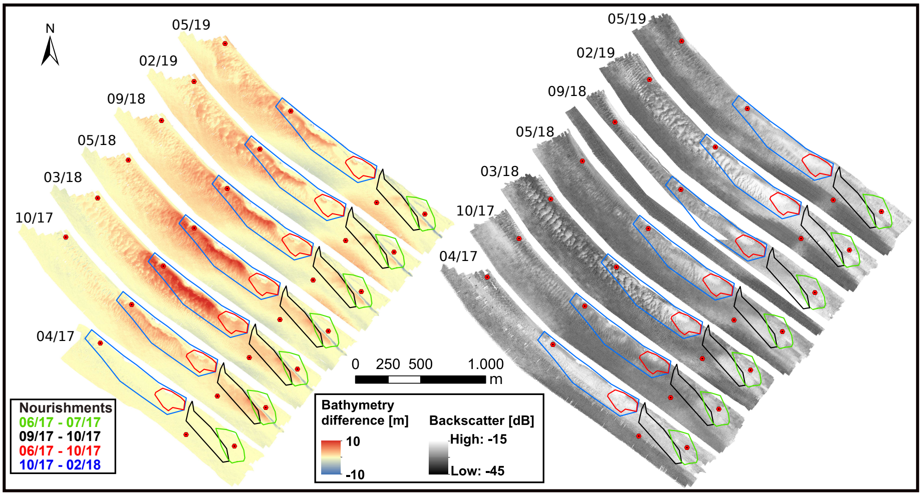

Figure 4.6: MBES time series data acquired between April 2017 and May 2019. (Left) Bathymetry difference with respect to the pre-nourishment survey in April 2017, indicating evolution of sediment volume. April 2017 map is calculated with respect to a MBES bathymetry measurement taken in May 2017. (Right) BS mosaics. For both, the grid cell size is 0.5 m by 0.5 m. The red points are reference points used for geographical orientation (see Fig. 4.1).

4.4.3. Acoustic sediment classification

Estimation of the number of acoustic classes

The results of the Chi-square test for the seven processed MBES BS datasets show that the averaged Chi-square values, including the standard deviation, reach the criterion for an optimal data fit (black dashed line) using five Gaussian distributions nearly for all datasets (Fig. 5.6). The February 2019 dataset shows high standard deviations, indicating varying fitting results for the different angles and sides resulting in an ambiguous estimate between four and seven classes. To comply with the other datasets, five classes are chosen for the classification of the February 2019 BS data as well.

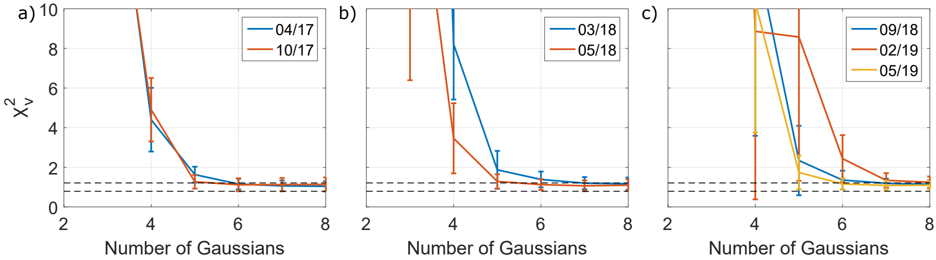

Figure 4.7: Chi-square test applied to the seven MBES BS datasets. The solid lines and their error bars represent the mean and standard deviation of the $\chi^2_{\hat{\nu}}$ values considering the incident angles from 40 to 65° of both the starboard and port sides. The black dashed lines show the $\chi^2_{\hat{\nu}}$ value of $1 \pm \sqrt{2/\hat{\nu}}$, which indicates a good model fit.

Correspondence between acoustics and ground truth

To label each AC and eventually retrieve a sediment map, the acoustics (05/18) are compared with the ground truth data (05/18). Fig. 4.8a indicates a positive correlation of the BS with the weight percentage of grains larger than 2 mm. AC_5 corresponds exclusively to a bottom type containing more than 1 % shell fragments and gravel. AC_4 shows a spread between very little (0.1 %) and a large amount (18 %) of shell fragments and gravel. The sample with the very large amount (18 %) amount of shell fragments contains also 13 % of mud, which is a likely cause for the lower BS value and the classification as AC_4 instead of AC_5. AC_3 is evenly distributed between no shells and traces of shells and AC_2 and AC_1 correspond mainly to samples with no shell content. Here, traces define scattered shell-fragments with a quantity of less than $< 0.1\,\%$. Considering the d_{50} value of the mud and sand fraction, Fig. 4.8b shows that, in general, the sediment is very homogeneous with d_{50} values ranging from 220 to 280 µm in the study area. The BS does not show a correlation to such a small range of d_{50} values. Although AC_1 only contains 1 sample, the d_{50} value of 20 µm (classified as sandy mud (sM) after Folk [83]) discriminates it from the samples in AC_2 with a 3 dB lower BS value. Here, one has to consider that this sample corresponds to a thin sandy mud layer (i.e., a veneer with a thickness of ~1 cm) deposited on a sand layer (d_{50}= 240 µm). Following theoretical BS calculations, one would expect around 8 dB difference between sandy mud and medium sand (see Fig. B.1 in Appendix B), which might indicate that the acoustic signal is also affected by the sand layer underneath.

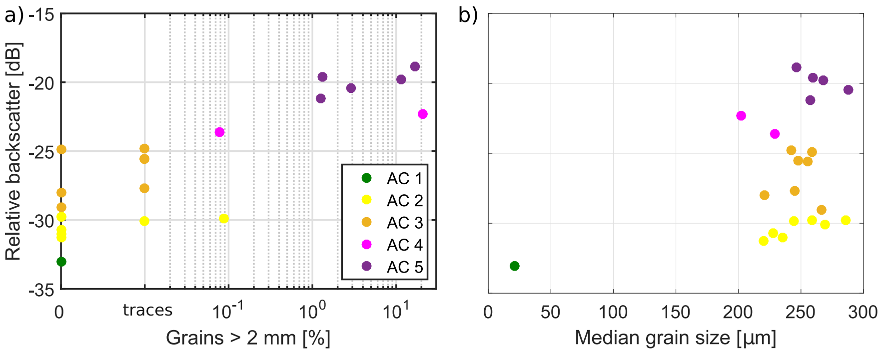

Figure 4.8: Comparison of acoustic data (05/18) with box core samples (05/18). a) BS vs. percentage of grains larger than 2 mm. b) BS vs. median grain size, d_{50} value, of the sand and mud fraction.

A qualitative comparison between the acoustics and box core samples is given in Fig. 4.9. The box core samples (BC007 and BC018), extensively covered with shell fragments, are located in areas with high BS values and high ACs (AC_4 and AC_5). Box core samples (BC005 and BC006), indicating well-sorted fine to medium sand with no shell fragments, are located in areas of low BS and low ACs (AC_2 to AC_3). Box core sample BC015, indicating well-sorted fine to medium sand with traces of shell fragments and gravel, are located in areas of intermediate ACs (AC_3 to AC_4). The quantitative and qualitative comparisons show that the acoustics are mainly driven by the amount of shell fragments in the very homogeneous environment of sand. The final assignment of bottom type to AC, including the accuracy measurement, is listed in Table 4.4. This assignment leads to an overall accuracy of 64 %.

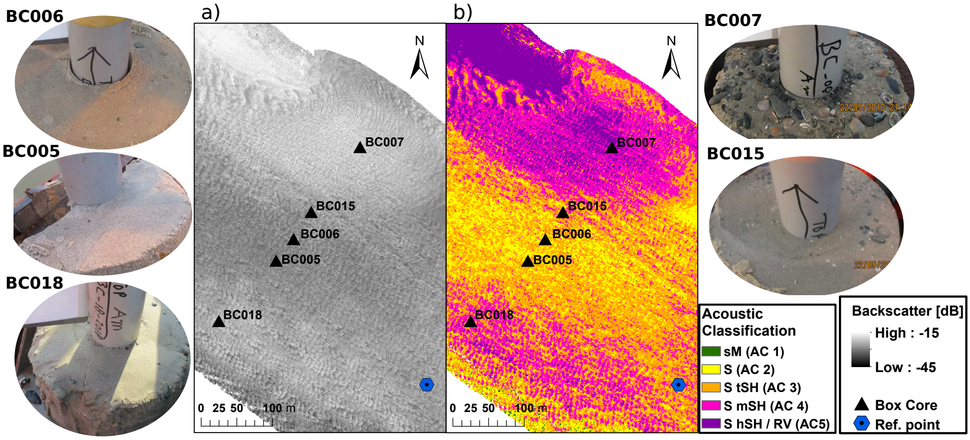

Figure 4.9: Qualitative comparison between acoustics and ground truth. a) BS mosaic (05/18) and b) ASC results (05/18), including box core locations and photos.

Table 4.4: Assignment of sediment type to acoustic class.

AC	Sediment type	Shell content	Accuracy
1	sandy Mud (sM)	0	100 %(1/1)
2	Sand (S)	0	66 %(4/6)
3	Sand with traces of shells (S tSH)	traces	50 % (3/6)
4	Sand with medium amount of shells (S mSH)	0.1 to 1 %	50 % (1/2)
5	Sand with high amount of shells (S hSH)	> 1 %	100 % (5/5)

The first box core sampling (09/05/2017) was conducted 14 days after the pre-nourishment survey (25/04/2017) due to logistical problems and weather conditions. Since we noticed an agreement between d_{50} and AC for dynamically more stable areas (coarse sediments and not in the tidal channel) and a disagreement for areas with higher morphodynamics (finer sediments and tidal channel), we decided not to include the box core samples in the present study because of the time difference. Therefore, solely the box core samples from 22/05/2018 to 24/05/2018 in combination with MBES BS data from 23/05/2018 are used for the assignment of sediment type to AC. The resulting assignment (Table 4.4) is propagated to the entire time series. Although the absolute range in decibels varies between 25 and 30 dB among the MBES BS datasets, a consistent number of ACs is estimated by the Bayesian method for the entire time series. This indicates that the width of the Gaussian distributions and consequently the AC boundaries account for the wider decibel range (Appendix A.2).

4.4.4. Temporal evolution of surficial sediments

The ASC maps, displayed in Fig. 4.10, reveal the temporal evolution of the surficial sediments. The pre-nourishment map (04/17) shows extensively distributed coarse sediments (shell fragments and gravel) towards the coastline of Ameland. The highest amount of shells and gravel is found from the middle to the south-east part of the study area (complies with the to-be nourished area) indicating an extensive shell layer. The intra-nourishment map (10/17) shows that the nourished sand (d_{50}= ∼220 µm) covers the shell layer almost completely (see area in blue and black polygon in Fig. 4.10). Within the blue polygon (Fig. 4.10), the only small purple areas (AC_5) that remain, coincide to some extent with the location of part of the revetments, indicating that the highest AC also corresponds to the revetments. Therefore, it is more difficult to identify the revetments in the pre-nourishment sediment map where an extensive shell layer is located towards the coastline. Further to the south-east, the intra-nourishment map (10/17) indicates a high amount of surficial shell fragments and gravel within the nourished area (green and black polygon in Fig. 4.10). Considering that the nourishments have taken place two months (green polygon) up to only a few days (south-east of black polygon) before the acoustic survey, we hypothesize that a washing out of the fine sediments and an increase of the coarse fraction (shells and gravel) occurred very rapidly. Similar observations are made for the post-nourishment maps (03/18 to 05/19) within the nourished areas. The extent of the shell layer increases with time (AC_4 and AC_5; pink and purple area), indicating a continuous washing out of the fine fraction. Moreover, the north-western part of the study area seems to have an increase in finer sediments (sandy mud to sand) from 10/17 to 05/18, which coincides with the bed aggradation (Fig. 4.6). Therefore, we hypothesize that the fine sediments of the nourished material are redeposited north-west of the nourished area. The ASC maps visualize that, after the nourishments have stopped in February 2018, the surficial sediment distribution has approached the pre-nourishment state, indicating a recovery (natural sedimentary equilibrium state) of the nourished area (Fig. 4.10).

Furthermore, the development of bedforms is observed, most strongly in October 2017 to March 2018 and in the February 2019 datasets (Fig. 4.6). In Fig. 4.11, showing the bathymetry and sediment classification from the intra- (10/17) and post-nourishment (03/18) surveys, two distinct zones of bedforms can be identified, with higher amplitudes and longer wavelengths on the landward side and lower amplitudes and shorter wavelengths on the tidal-inlet side. Fig. 4.12 shows two cross-profiles visualizing the bathymetry and ASC along different types of bedforms. Profile 1 is located in the nourished area and Profile 2 about 50 m south-west of the nourished area. As a reference, the pre-nourishment bathymetry displays megaripples with a wavelength of 5 to 10 m with amplitudes of up to 1.5 m along Profile 1 (not shown here). Within three months (June to October 2017) very high (∼2.5 m) and steep (∼25°) megaripples (Fig. 4.12a) with wavelengths of about 40 m are rapidly developed on the nourishments. From October 2017 to March 2018 the meagripples grow into sandwaves with an increase in height to 3 m and an enormous increase of the wavelengths up to 120 m in relatively shallow waters

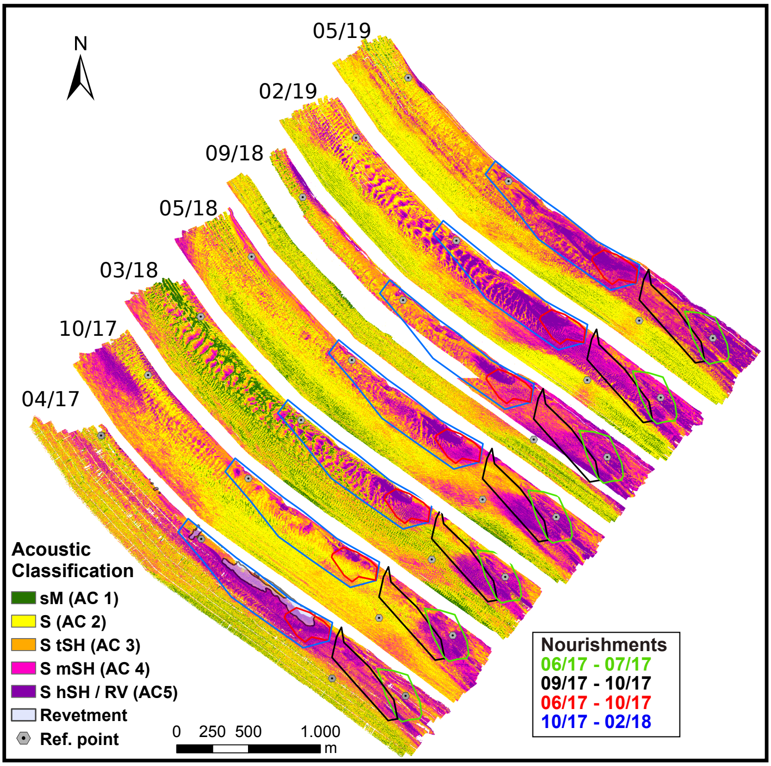

Figure 4.10: ASC maps obtained from the Bayesian method. The grid cell size is 1 m by 1 m. Incident angles between 15 and 70° are considered in the classification. The polygons with the different colors indicate the areas and periods of the nourishments. Indicating the locations of the revetments without covering too much information, they are only visualized in the 04/17 map.

(10 to 14 m). In Profile 2 the smaller megaripples grow into larger megaripples (Fig. 4.12b). This indicates that the hydrodynamics, in combination with the artificial sediment supply due to nourishment, cause a high degree of morphodynamic activity within the nourished area. The second observation, as revealed by the ASC, is the different sorting patterns over bedforms in both areas and time periods. The clearest pattern is observed in Profile 1 (nourished area) for the measurement in March 2018 (Fig. 4.12a), where coarse sediments occur on the stoss sides (AC_5: gravel and shell-containing sands), finer sediments towards the crests (AC_2 and AC_3: sand) and even finer sediments (AC_1: sandy mud) in the troughs. A similar pattern is observed for Profile 2 of the measurement in March 2018, except that the magnitude in ACs only varies between AC_3 and AC_1. In Profile 1 of the measurement in October 2017, we observe a contrasting pattern of finer sediments on the stoss and coarser sediments on the lee sides and in the troughs. In Profile 2 of the measurement in October 2018 we do not identify a clear sediment sorting pattern which might be related to an early stage of the development of bedforms or an insufficient resolution of the MBES. The BS data are corrected for the effect

of the seabed morphology as described in the Section 4.3.1. To what extent MBES BS can be used to resolve sediment sorting along bedforms depends on the relationship between the bedform wavelength and the acoustic resolution of the MBES (see Section 4.5.3).

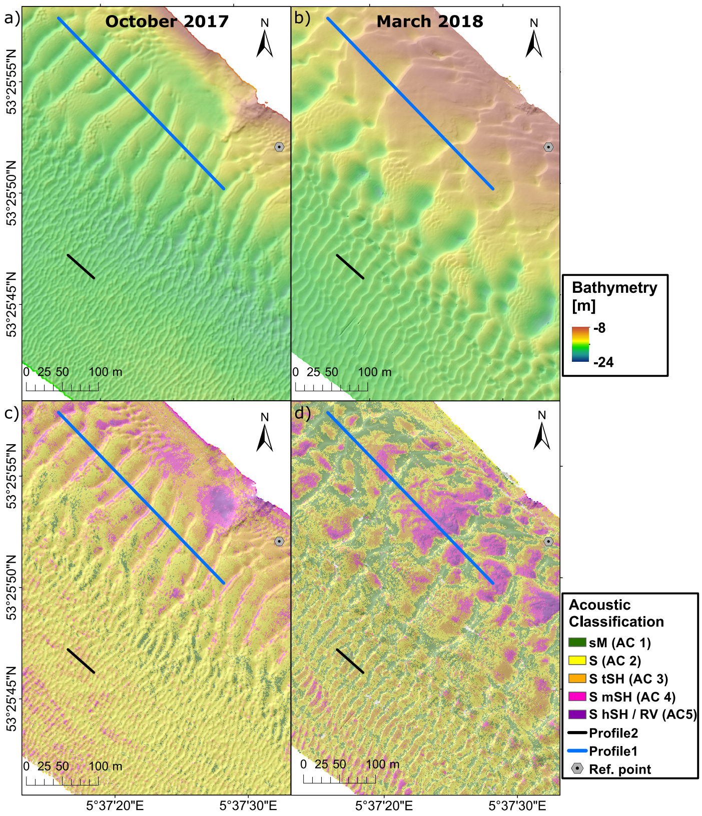

Figure 4.11: a) and b) Bathymetric subset maps from 10/2017 and 03/2018 representing a detailed view on the seabed morphology. c) and d) Corresponding ASC from 10/2017 and 03/2018.

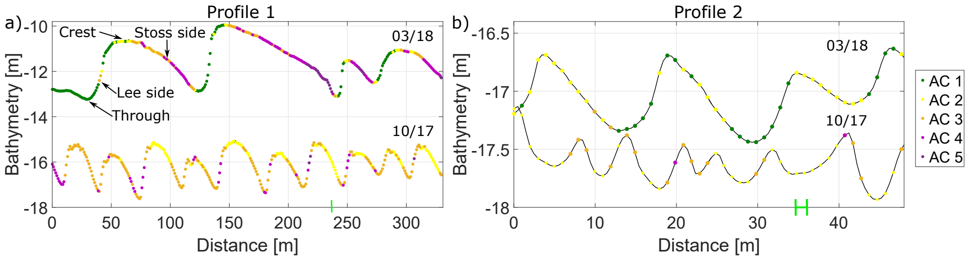

Figure 4.12: Bathymetric and ASC cross-profiles for Profile 1 and 2 of the October 2017 and March 2018 measurements. Location of Profile 1 and 2 are indicated Fig. 4.11. Green bar at the x-axis indicates resolution of the slope calculation.

4.4.5. Integration of MBES and sub-bottom profiling

In this contribution, we use the seismic data to investigate to what extent the classified, pre-nourishment seabed sediments, as revealed by the ASC, can be acoustically identified in the subsurface. In the processed sub-bottom profiler (SBP) transect (11/17) within the nourished area (Fig. 4.13), the acoustic characteristics of the reflector reveal three different zones: (1) in the center, the discontinuous, high-amplitude reflector indicates a shell layer, as corroborated by vibrocores (05/18), (2), in the south-east, a continuous and high-amplitude reflector correlates with a consolidated clay layer, as identified in the vibrocores (Fig. 4.15), and (3) in the north-west a high-amplitude reflector indicates the possible presence of buried revetments.

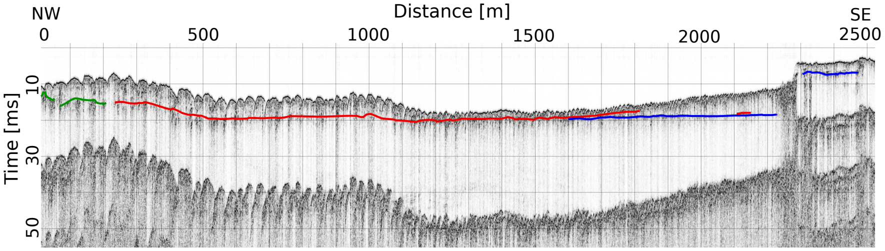

Figure 4.13: Seismic section acquired with the SBP. Shell layer (red), consolidated clay layer (blue) and buried revetments (green) are identified in the seismic section. The location of the seismic section is displayed Fig. 4.1d.

When plotting the seismic profiles (Fig. 4.14), the detected shell layer in the subsurface corresponds to the pre-nourishment seabed (04/17) between 200 and 1600 m with a precision of 0 to 30 cm, which is classified as AC_4 and AC_5 (due to the shell-rich seabed sediments at the time, see also Fig. 4.10). The agreement shows that the layer thickness of the pre-nourishment shell layer and the impedance contrast with the surrounding sediment (i.e., nourished sand) is sufficiently high to be acoustically resolved by the SBP. Between 1600 and 2100 m the clay layer is mapped by the SBP. Between 1600 and 1800 m the SBP shell layer overlies the SBP clay and the MBES shell layer, while between 1800 and 2100 m no shell layer is detected in the SBP. According to the box core samples taken in May 2017 this area consists of sand with varying amount of shells, confirming the ASC. Although the identification of the clay layer in the SBP is certain based on the validation of the reflector with vibrocores, the MBES data indicate that the shell layer is located at the same depth in this area. The accurate detection of the shell layer with the SBP in that area might be hampered due to the directly underlying consolidated clay, as can be seen in VC11. This might also influence the vertical precision where the clay is interpreted in the SBP data. In addition, the vertical position of the SBP (~ decimeters) is less accurate than of the MBES (~ centimeters) and, furthermore, the reflectors observed might be from a lower part of the shell layer with a higher shell content. It shows that the combination of MBES (BS and bathymetry) time series measurements and SBP data can be used for improved interpretation of the data and are a good addition to each other.

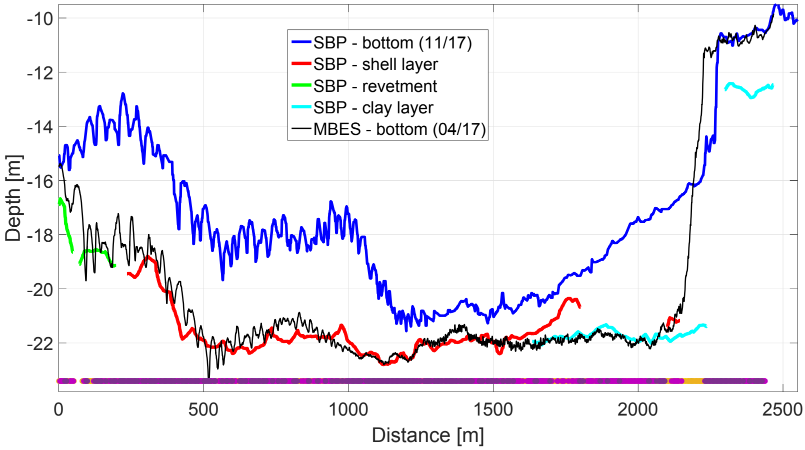

Figure 4.14: Cross-profiles of layers detected by the SBP in November 2017 and the MBES pre-nourishment survey in April 2017. The ASC results of the MBES measurements are displayed at the bottom indicating mainly a sandy seabed with a medium to high amount of shells (AC_4 and AC_5, purple colors). The location of the seismic cross profile is displayed Fig. 4.1d.

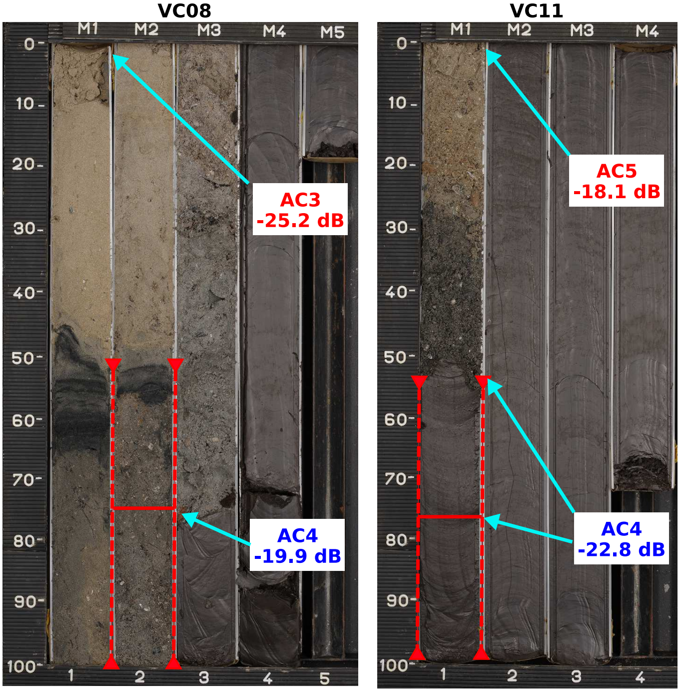

Figure 4.15: Depth profile of vibrocores VC08 and VC11 located in the tidal-channel in May 2018. Red horizontal bar indicates location of surficial seabed from April 2017 measurement (before nourishments). Error bars indicate maximum depth variation within a radius of 5 m around the sample location. Blue and red font indicate AC and BS value at the sample location for April 2017 and May 2018 measurements, respectively.

The vibrocores (22/05/2018 to 23/05/2018) confirm the assignment of sediment type to AC, in addition to the box core samples (22/05/2018 to 24/05/2018). In VC08 (Fig. 4.15), the top of the core comprises sand with just traces of shell fragments and in core VC11 sand with a high amount of shell fragments is found, which matches with AC_3 and AC_5, respectively (MBES measurement in 24/05/18). The horizontal bar indicates the location of the pre-nourishment seabed where sand with a relatively large amount of shell fragments can be found in VC08. For VC11 the mean depth is located in the consolidated clay layer but considering the positioning uncertainty of the vibrocore, it could also be located in the shell layer. In that case the pre-nourishment ASC, indicating sand with a high amount of shells (AC_5), would coincide with the vibrocore. It shows that the pre-nourishment ASC results are representative for the newly formed subsurface and that they can support the interpretation of the seismic reflectors.

4.5. Discussion

4.5.1. Monitoring seabed evolution using MBES backscatter

Environmental monitoring requires temporally stable measurements in order to assess changes of the environment over time [7]. Using acoustic BS to study the evolution of underwater nourishments means that the uncertainty of the BS needs to be smaller than the necessary resolution to characterize the status of the environment. For the environmental sources, the maximum averaged uncertainty of 1.1 dB caused by the possible presence of small-scale ripples, is lower than the magnitude of the required resolution of MBES BS to discriminate between, for example, fine, medium and coarse sand (2 dB) or fine sand and silt (5 dB) (see Fig. B.1 in Appendix B). The change of the vessel and the MBES after five surveys induced the largest uncertainty related to the MBES. The difference in BS levels between the sonar heads, due to the change of the vessel and MBES, increased from 1.4 to 3.5 dB. Firstly, this indicates an imperfect cross-calibration between the sonar heads and secondly it shows a varying transducer sensitivity between the different MBES mounted on different vessels. A relative calibration of the MBES using a reference area with a temporally stable seabed as recommended in [7, 26] and performed in [25] could be used to quantify the transducer sensitivity. However, the Wadden Sea is a highly dynamic environment and therefore it was not feasible to perform for every survey a relative MBES calibration.

Although the strategies for assessing MBES BS uncertainties that we presented in this study, provide a good estimate of possible variation in BS by the system and environmental sources, we did not quantify the effect of air bubbles, for example due to rough weather conditions, or the effect of the varying frequencies (270 to 330 kHz) caused by the dual-head system and the ping modus (dual swath). A promising approach would be the use of the water column data (entire signal) to approximately estimate the sound attenuation caused by air bubbles. Due to the small frequency separation, we expect a negligible effect on the BS level according to the research on multi-frequency BS (a frequency separation of at least 1 octave is required) [33, 119].

Malik *et al.* [120] presented modeled uncertainties of BS measurements. They related the major uncertainty sources of the BS level to the seabed ensonified area (1 to 3 dB), absorption coefficient (up to 6 dB), random fluctuation (5.5 dB) and sonar calibration (system dependent). In this contribution, we minimized the uncertainty related to the first source by calculating the along- and across-track seabed slope with a very high-resolution of 1.5 m. The absorption coefficient was corrected in post-processing for the entire water column using up to five CTD measurements. We compensated for the statistical fluctuation of the BS level by averaging the data over a number of pings and beam angles. In addition, the Bayesian method considers the remaining statistical fluctuation by generating Gaussian distributions with a standard deviation representing the statistical fluctuations. Finally, the method is independent of a sonar calibration and applicable to relative BS measurements [61].

However, the ASC maps still showed in some areas along-track stripes (Fig. 4.10). An explanation could be the influence of air bubbles or varying survey azimuths due to a rough sea state. In case of the varying survey azimuths the observed BS variations of up to 4.1 dB for some incident angles and azimuthal angles in combination with the large overlap of about 120 % (i.e., each location is ensonified from three different tracks lines) might cause these artificial patterns. Another reason could be that due to the very dynamic environment the sediment composition or the seabed morphology have changed during the acquisition of three different track lines (∼1 h). Variation in tidal flow direction could alter the orientation of small-scale ripples and variation in the tidal flow speed could favor the settling and remobilisation of very small sediment particles changing the water-sediment interface. Montereale-Gavazzi *et al.* [28] showed variation of > 2 dB between ebb and flood caused by surficial substrate changes due settling of the mud fraction in a highly dynamic area close to a river mouth. Hence, preferring certain survey times with similar tidal flow conditions, decreasing the length of the track lines and avoiding a rough sea state (here, defined as a vessel roll and pitch $> 5°$) might help to reduce the along-track stripes due to BS variations.

4.5.2. Ground-truthing in a dynamic environment for acoustic seabed monitoring

Sediment mapping based on MBES BS requires ground-truthing to assign sediment properties to ACs. The ground-truthing has to be timed as close as possible to the acoustic survey to be still representative for the actual seabed at the time of the acoustic measurements, especially for such a dynamic environment like a tidal inlet of the Wadden Sea. Therefore, we discarded the first box core sampling set and only used the second box core sampling set and propagated the ground truth information from this one assigned AC set to the entire time series via the unsupervised Bayesian classification method (see Section 4.4.3). A similar approach was presented in [25] except that they used a reference area with a stable seabed to relatively calibrate the BS level for each survey. Here, we followed the approach presented in Chapter 3 [61], in which a good repeatability of the classification results obtained from different surveys using the same unsupervised method was demonstrated (e.g., Figs. 3.8 and 3.9). It was shown that the method can be applied to relative BS levels and allows to compare the resulting ACs from different surveys given that the number of ACs is consistent among the time series. In case the number of estimated ACs differs due to a new sediment supply or sorting processes, the comparison of the ACs among the time series would be hampered and an additional ground-truthing followed by a new assignment of sediment type to AC is recommended.

Furthermore, the assignment of AC_1 was based on only one sample. First of all, one sample is statistically not representative, even though the contrasting BS validate a separate AC. Secondly, despite the well-timed sampling with respect to the acoustic measurements, there are still a few tidal cycles in between and the ~1 cm thick mud veneer may indicate settlement of muddy sediments, which in combination with high tidal dynamics can yield to large BS variabilities (> 2 dB) as shown by Montereale-Gavazzi *et al.* [28]. They interpreted the variabilities as short-term sediment changes due to the deposition and remobilization of the muddy particles. To some extent these observations could cause the moderate disagreement (expressed as an overall accuracy of 64 %, Table 4.4) between the ground truth and acoustic data in our area. Future monitoring campaigns need to further reduce the time difference (and/or acquire more information on the SSC) to allow an accurate comparison between ground truth and acoustic data.

Further reasons for the moderate disagreement between box core samples and the acoustic data might be related to (1) the positional inaccuracies between MBES and sampling device, (2) noisiness of the BS data, (3) and other challenges in estimating in situ properties from (small) samples in the lab (e.g., underrepresentation of coarse particles) and (4) the uncertainty whether a single sample is representative of a larger acoustically ensonified region [65]. In this study, we observed that the BS level was highly dominated by the shell fragment content. One reason is that in our study area the sediment consists of mainly homogeneous sand (220 to 280 µm) and therefore the shell content is acoustically the main difference. As demonstrated in several studies, small variations in the shell content (or larger particles in general) can highly influence the BS level (e.g., [62, 63, 65]). In particular for shell fragments it is difficult to obtain a spatially representative measurement because samples contain only a few shell fragments (see point 3 and 4) and consequently the correlation of seabed properties (e.g., mean grain size or shell content) to BS data is biased [65]. A combination of box core samples with video footage (e.g., drop cameras, video tows or ROV/AUV platforms) would extent the detailed physical information from a very refined location (i.e., 30 cm) to a larger area [62, 108]. However, a high energy environment as the Ameland inlet might yield to inaccurate positioning and low visibility and hinder the application of video footage.

When applicable, video footage would help to further investigate why the revetments were not clearly distinguishable from the shell fragments (both assigned to the highest AC) even though the revetments represent a much harder material. Either the revetments are covered with a thin veneer of sediments decreasing the

BS or the acoustic response at 300 kHz from the revetment and shell fragments is very similar. The BS is not only a result of the hardness contrast (i.e., acoustic impedance) but also depend highly on the seabed roughness [4]. It is likely that the shell fragments appear acoustically much rougher then the revetments, which might compensate for the hardness contrast.

4.5.3. Spatial resolution of MBES backscatter

The grain-size sorting patterns along bedforms that we acoustically identified at different locations (nourished and natural areas) and time periods (intra- and post-nourishments) are comparable to other studies using MBES BS over bedforms [39, 121, 122]. Lamarche *et al.* [121] observed differences of up to 10 dB between troughs (high BS level) and crests (low BS level) of sand waves with wavelengths between 100 and 250 m and related the differences to varying sediment types. Koop *et al.* [39] acoustically identified coarser sediments in the troughs and on the crests and finer sediments on the steepest part of the stoss side of megaripples (wavelengths between 10 and 25 m). The latter discussed the trade-off between spatial resolution (ability to spatially distinguish between different sediment patterns) and geoacoustic resolution (ability to acoustically distinguish between different sediment types). However, we also need to consider the relationship between the spatial/geoacoustical resolution and the wavelength of bedforms, ranging from few centimeters (ripples) to tens of kilometers (sand banks) in coastal regions [123, 124].

In order to assess the capability of MBES BS to identify grain-size sorting along these periodic features, we need to distinguish between three scenarios displayed in Fig. 4.16: Scenario 1: Bedform wavelength ($\lambda_{\mathrm{bedform}}$) is smaller than the ensonifed footprint area (A_p) and therefore the bedform contributes to the seabed roughness. Consequently, the BS level is affected by wavelength, amplitude and orientation of the bedforms [109]. Scenario 2: Bedform wavelength is larger than the ensonified footprint but smaller than the spatial resolution of the bathymetry slope calculation (dx_{slope}) and therefore the true incident angle and the correct ensonifed footprint area cannot be calculated. The BS level is affected by the slope of the bedform. Scenario 3: Bedform wavelength is significantly larger than the spatial resolution of the slope calculation (i.e., slope correction reveals variation of slope over bedform). Hence, the BS level can be corrected for the true incident angle and the correct ensonified footprint area. Only in the third scenario the BS level represents the actual sediment properties.

For the MBES and the settings used in this study (Table 4.1) following values are obtained: A_p= 4 to 16 cm (for incident angle = 70 to 15°), A_b= 12 to 480 cm (for water depths between 5 to 25 m and for incident angles between 15 to 70°) and dx_{slope}= 150 cm (i.e., 3 times grid resolution, which depends on sounding coverage and the beam footprint A_b). That means sediment sorting in bedforms with a wavelength of $\gg$ 150 cm can be detected in this study. Sediment sorting in megaripples with a wavelength from 10 to 40 m [39, 125] or sand waves with a wavelength of a few hundred meters [125, 126] are detectable, whereas ripples with a typical wavelength of tens of centimeters [124] contribute to the seabed roughness (Scenario

1) or degrade the quality of the BS data (Scenario 2). For example, Scenario 3 is valid for the megaripples and sand waves in Profile 1 measured in October 2017 and March 2018, respectively, and the megaripples in Profile 2 measured in March 2018 with wavelengths between 20 and 100 m (see green reference scale in Fig. 4.12, representing the 150 cm reference). However, the megaripples, visualized by Profile 2 for the October 2017 measurement, are probably too short (lower end with ~5 m) and fall in Scenario 2. This would explain the more chaotic distribution of the ACs along the profile. Using MBES BS to identify sediment sorting in bedforms requires the determination of the three scenarios for the specific MBES and the study area and the comparison to the length-scale of the bedforms.

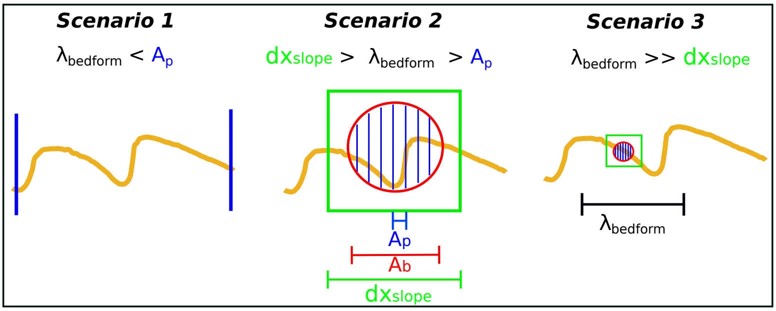

Figure 4.16: Sketch for spatial resolution of the MBES vs. length-scale of the bedform. λ_{bedform} is the wavelength of the bedform, A_p is the instantaneously ensonified signal footprint, A_b is the beam footprint and dx_{slope} presents the spatial resolution of the slope correction.

4.5.4. Sedimentary patterns in a nourished area

Cross- and longshore sediment sorting is often observed along beaches [124], which agrees with the observed sedimentary pattern during the pre-nourishment survey in our study area. In our study, recovery of the nourishment area occurred within a few days and the pre-nourishment state was fully reached after roughly 12 months (11 to 16 months). Considering the mud and sand fractions, the composition of the nourished sediment (d_{50}= 205 to 217 µm) is very similar to the original sediment (d_{50}= 220 to 280 µm) which might yield, in combination with the continuous hydrodynamics, to the original sedimentary patterns. Based on both the degradation-aggradation pattern and BS observations, we hypothesize that a washing-out of the fine sediments of the nourished sand and a redeposition north-west from the nourished area towards the Borndiep channel took place. According to Elias [127] this channel is governed by an ebb-dominated flow, and the outflow of Borndiep would therefore have an seaward-directed sediment transport, supporting our observations. In addition, shell fragments and gravel being less easy to erode remain on the nourished area, resulting in a similar sedimentary pattern compared to the pre-nourished state.

For sorting along bedforms, field observations in the Belgian, Danish and Dutch North Sea have shown varying sorting patterns over tidal sand waves with wavelengths ranging from 100 to 750 m in water depths of 3 to 30 m [125, 128, 129]. In these studies some locations showed coarser sediments towards the crests while other locations indicated a reverse pattern of coarser sediment in the troughs. Theoretical approaches by van Oyen and Blondeaux [130] and Roos *et al.* [131] indicated that sediment sorting processes are controlled by a balance between reduced mobility effects, supporting transport of fine grains, and hiding effects, yielding to higher transport rates of coarser grains. During moderate tidal currents finer sediments accumulate at the crest while strong currents lead to a coarsening of the crest [130], which would explain the contrasting field observations. Further modeling results also indicated that grain-size sorting requires a wide range in grain sizes but the location of the accumulation (crest or trough) of the different grain-size fractions highly depends on the fluid and sedimentary conditions [124]. Although the d_{50} value of the mud and sand fraction in our study area is very homogeneous, the shell fragments with different particle sizes in combination with the mud particles yield to a relatively large grain-size distribution. In addition, hydrodynamic modeling results have indicated spatially and temporary varying tidal current velocities across the Ameland inlet [127]. Therefore, the theoretical requirements are given that the sedimentary and hydrodynamic conditions in our study area result in contrasting sediment sorting patterns at different times and locations as revealed from the ASC.

4.6. Conclusion

In this study, we applied a time series of seven high-resolution and full coverage MBES datasets of both bathymetric and BS measurements to monitor underwater nourishments in the Ameland inlet (The Netherlands). On the BS data, the nourished sediment could be distinguished from the natural sediment in the study area. Degradation and aggradation, as determined from the bathymetric times series, and changing sediment classification maps obtained from relative BS strength values, revealed that the original seabed sediments with a high shell content were covered by the sandier nourishment material. Within approximately 12 months, the pre-nourishment shell-rich sediment state was recreated by washing out finer sands and mud, which were deposited north-west of the nourishment, in the direction of the ebb-dominated tidal current. These findings were supported by seismic data, where a discontinuous high-amplitude reflector identified the shell-rich pre-nourishment seabed sediments in the subsurface, corresponding to the pre-nourishment bathymetry and corroborated by sediment cores.

Rapid generation of bedforms was observed in the nourished material in relatively shallow water (10 to 14 m), whereby megaripples with a height of 2.5 m and wavelength of about 40 m developed into 3 m high sand waves with wavelength of up to 120 m within 6 months. Grain-size sorting patterns over bedforms were exhibited by the systematic variation of acoustic sediment classes, showing coarse sediments (high AC) on the stoss sides, sandy sediments near the crests and sandy mud on the lee sides and in troughs of the bedforms. The combination of the artificial sediment supply with a relatively large range in grain sizes and the varying tidal currents over bedforms might cause these phenomena.

Employing an unsupervised Bayesian classification of relative BS strengths, five ACs resulted in all datasets of the time series. This allowed assigning sediment type to the ACs for the ground truth dataset at the time of one MBES survey and propagating the assigned sediment classes to the other surveys in the time series without a system calibration. When comparing the time series of BS measurements, evaluation of the external sources of variation in BS measurements is necessary. In this study, we demonstrated that in our surveys, water column properties and survey azimuth in relation to organized seabed roughness (i.e., environmental sources) as well as survey settings and biofouling (i.e., system sources), with a variation in BS of less than 1.4 dB, do not interfere with changes in BS over time. However, for some scenarios external sources such as sediment suspension, survey azimuth, varying transducer sensitivity of the sonar heads and changing equipment may affect the BS level significantly (up to 3.5 dB) and consequently, may hamper the use of MBES BS data for environmental monitoring. Keeping these factors constant during the monitoring campaign is therefore important.

This investigation demonstrates that the combination of bathymetric and BS time series measurements from MBES is highly valuable in monitoring the evolution of underwater nourishments. This approach helps to explain morphodynamic and sedimentary processes, such as transport, deposition and sorting, and thereby contributes to understanding of how natural systems respond to anthropogenic disturbances. Sediment composition is a main factor in benthic ecology and thus highly relevant in ecological impact assessments, which are increasingly important in coastal maintenance and its surroundings. In addition, MBES BS can be used to support the interpretation of seismic reflectors and, inversely, sub-bottom profiling can be used to establish the subsurface structure of the nourished seabed. Furthermore, the sediment classification maps can be used as input for hydrodynamic and morphodynamic modeling studies, providing information on the spatial distribution of the sediment types, to improve sediment transport calculations.

5

A multispectral Bayesian classification method for increased acoustic discrimination

> *If you look at history, innovation doesn't come just from giving people incentives; it comes from creating environments where their ideas can connect.*
>
> Steven Johnson

The two previous chapters have focused on the applicability of repetitive multibeam backscatter (BS) measurements and acoustic sediment classification for monitoring the seabed. Low discrimination performance of monochromatic BS for coarse sediments were highlighted as a shortcoming of current acoustic sediment mapping. According to theoretical and experimental studies multi-frequency BS is expected to allow for a better acoustic discrimination between seabed sediments. Recently, a multibeam echsosounder (MBES) was developed that allows to collect spatially and temporally co-located BS data at multiple frequencies. This chapter examines three multi-frequency BS datasets (100, 200, and 400 kHz), acquired with such a MBES (R2Sonic 2026) in the Bedford Basin in 2016 and 2017 and in the Patricia Bay in 2016 (both Canada). The processing of multi-frequency MBES data is described and a classification algorithm based on an extension of the Bayesian classification method is developed. The method aims to combine the information retrieved at a single frequency into a multispectral acoustic classification map. Based on the acoustic classification results and the ground-truthing, the potential benefit of multispectral over monochromatic BS data is evaluated.

This chapter has been published in Geosciences **8** (12), 455 (2018) [55].

5.1. Introduction

Multibeam echosounders (MBESs) have become the most valuable tool for seabed mapping providing high-resolution bathymetry and acoustic backscatter (BS) datasets [132]. Various classification methods, employing MBES bathymetry, BS, and their second order moments, have been developed to characterize seabeds or riverbeds in the last two decades [8]. They aim at maximizing the performance in discriminating between different seabed environments or sediment types. Acoustic BS strength is the most common feature used in seabed classification [8]. The BS strength is dependent on the composition of the seabed, angle of incidence, and acoustic frequency [6]. Seabed roughness, volume heterogeneity, bulk density, as well as discrete scatterers and sediment layering that contribute to the seabed composition all affect the BS strength [6, 32]. The frequency dependence of BS strength is caused by three main factors: (i) the relationship between seabed roughness and acoustic wavelength [40], (ii) the dominant scattering regime, i.e., Rayleigh or geometrical scattering, which is dependent on the acoustic wavelength and particle size [31, 133, 134], and (iii) the contribution of volume scattering influenced by the signal penetration [135–137].

In several lab and field experiments, in which the influence of varying frequencies on the BS strength was studied, it was shown that specific sediment types have different acoustic responses at different frequencies (e.g., [30–32, 138, 139]). In field measurements, Urick [30] observed no significant frequency dependency for rough sediments (sedimentary rocks), whereas the scattering from soft sediments (silt) increased slightly with increasing frequencies from 10 to 80 kHz. Jackson *et al.* [138] observed an increasing frequency dependency from very fine sediments (sandy silt: -0.2 dB per octave) to fine sediments (medium sand: 2 dB/oct) followed by a decrease for coarser sediments (fine gravel: 1.5 dB/oct) for a frequency range from 20 to 85 kHz. Tank measurements carried out by Ivakin and Sessarego [31] demonstrated the frequency dependence of scattering for coarse and medium sand within a frequency range from 150 kHz to 2 MHz. Hefner *et al.* [139] showed, in a tank experiment, higher frequency dependency for a sandy bottom (fine) than for a sandy bottom covered with shell fragments (coarse) within a frequency range from 200 to 500 kHz. These studies indicate that, for most sediment types and frequencies, a frequency dependency of the BS strength is to be expected. In general, it is observed that finer sediments (e.g., sand) show a higher sensitivity to different acoustic frequencies than coarser sediments (e.g., gravel, shells, or boulders). As a next level of complexity, where the layering of sediments is considered, a study by Williams *et al.* [32] demonstrated the significant influence of a thin mud layer (in parts exceeding 10 cm) covering a well-sorted medium sand on scattering at different frequencies. Comparing the scattering at a well-sorted medium sand with the mud/sand surface layer, they showed that the scattering of the sorted medium sand was attributed to the surface interface roughness, whereas volume scattering dominated for the mud/sand layer for frequencies from 20 to 150 kHz. For frequencies higher than 200 kHz volume and roughness scattering could not explain the observed scattering strength. This is an indication for a change in the scattering regime (Rayleigh to geometrical scattering). All of the above shows the complex interaction between acoustics and the seabed. More acoustic lab and field experiments need to be carried out to capture the multispectral acoustic response of the entire variety of sediments. Still, these results provide promising opportunities to overcome ambiguities in the relationship between monochromatic BS and sediment properties by utilizing multiple frequencies [19, 61] (see Chapter 3).

The first acquisition and analysis of multi-frequency BS acquired with a co-located MBES operating at 70 to 100 kHz and 200 to 400 kHz was carried out in 2015 [33]. The study showed clear variations in the shape of the angular response as well as in the scattering strength at different frequencies. Since commercial multi-frequency MBESs were not available for the marine acoustic remote sensing community, potential benefits of using multiple frequencies for acoustic sediment classification (ASC) could not be fully elaborated. Typically, the BS data are collected at one specific frequency or in a narrow band around the central frequency (i.e., monochromatic). As a result, acquiring BS at multiple frequencies would require running exactly the same line multiple times, which leads to a inefficient and complicated data acquisition. Recently, R2Sonic has developed a broadband MBES (R2Sonic 2026) that allows for collecting spatially and temporarily co-located multispectral BS data using a single system. This MBES emits a series of signals between 90 and 450 kHz on a ping-by-ping basis. In Brown *et al.* [140], the first multispectral BS dataset acquired with a single MBES system (R2Sonic 2026) in the Bedford Basin, Canada, was employed and analyzed. The preliminary results of this study indicate benefits for an improved understanding of seabed characteristics by using multispectral BS.

In terrestrial remote sensing, the processing and classification of multispectral data are well established. Acquiring data across a wide spectrum of electromagnetic wavelengths has significantly increased the discrimination power of the classification routines [141]. Using multispectral BS in a marine environment with the aim of seabed classification requires an appropriate data processing to account for the frequency dependency of environmental and sonar specific variables. Furthermore, an objective and automatic classification technique that is capable of revealing and combining the acoustic information about seabed characteristics at different frequencies is needed to produce a single classification map.

In this study, the Bayesian method for unsupervised seabed classification (Section 3.3.2), which has already been successfully employed in previous studies to single frequency MBES datasets (e.g., [13, 61, 77]), is extended for the classification of multispectral BS data. The method accounts for the intrinsic natural variability of the BS strength [86] by assuming that the histogram of the measured BS per beam corresponds to a sum of Gaussian distributions, where each Gaussian corresponds to a distinct seabed type [13]. The technique considers thus the BS strength per beam (or incident angle). As a result, by considering a constant incident angle, the BS strength is only dependent on frequency and seabed properties, providing a promising opportunity for multispectral BS. One of the most important features of the Bayesian method is the statistical calculation of the number of classes that can be acoustically distinguished. Here, we use the method to evaluate and quantify the benefits of using multiple frequencies for ASC. The extended method is tested on three multispectral MBES datasets (100, 200 and 400 kHz) acquired in the Bedford Basin, Canada, in 2016 and 2017 and in the Patricia Bay, Canada, in 2016. The datasets were provided by R2Sonic as a part of an R2Sonic multispectral challenge in 2018. In this study, the acoustic data processing is described in detail with a particular focus on the frequency dependent environmental (i.e., absorption) and sonar specific variables (e.g., beam width) to provide relative BS strength per frequency and incident angle[1].

5.2. Study areas and data

5.2.1. Bedford Basin

Two MBES datasets were acquired in the Bedford Basin, Halifax, Nova Scotia, by a broadband MBES (R2Sonic 2026) in March 2016 and May 2017, with a total of 15 and 13 lines, respectively, and approximately 50 % overlap. The data were collected at three different frequencies (100 , 200 , and 400 kHz). The MBES data cover an area of approximately 1.84 km^2, and the water depth ranges from 13 to 85 m (Fig. 5.1a). Further, georeferenced video footage was collected within the survey area in March 2016 using a drop-down underwater camera frame fitted with a Sub-C underwater camera (SubC Imaging, Clarenville, NL, Canada) and lights [140]. The seabed, visible on the video footage, is categorized into three distinct classes: soft, mixed, and hard. "Hard" represents all areas where the entire area is covered with boulders, shells, or gravel. "Mixed" displays areas where a mixture of soft sediments and boulders is observed. "Soft" comprises all areas where only muddy and sandy sediments are present. A finer distinction of the category "soft" is not pursued because of the following reasons: (i) a clear distinction between mud, silt, or fine sand is not feasible on the basis of the existing video footage, and (ii) the amount and consistency of benthic flora and fauna or gas releases vary significantly. Overall the study area comprises sediment types ranging from bedrock to silt with underlying harder substrate. Different types of benthic flora and fauna are visible in the video footages as well. As reported in [140], the deeper area consists of soft mud partly covered with various benthic flora. In addition, the presence of biogenic gas and the disposal of dredge spoils were observed [142]. Close to the harbor (SE in Fig. 5.1a), the area comprises a mixture of hard substrate such as bedrock, corals, and boulders with attached epifauna.

5.2.2. Patricia Bay

The third MBES dataset was acquired in Patricia Bay, Canada, in November 2016 using the same R2Sonic 2026 MBES as in the Bedford Basin. The MBES data cover an area of approximately 0.96 km^2, and the water depth ranges from 20 to 70 m (Fig. 5.1b). A total of 8 lines were surveyed with approximately 50 % overlap. Surficial sediment descriptions are available from a number of grab samples collected during two previous surveys in 2005 and 2006 [143]. The geographical locations of the samples were extracted from a digitalized map in Arc GIS. The samples were

---

[1] The theoretical background of the acoustic data processing, published in Geosciences **8** (12), 455 (2018) [55], is moved to Section 2.4.

classified after the Folk and Wentworth scheme [83, 144] as fine sand (FS), muddy sand (mS), sand (S), gravelly sand (gS), and sandy cobble (sC) in [143]. Here, we reclassify the sediment samples into three categories: fine (FS and mS), medium (S), and coarse (gS and sC). This is done because the use of two different classification schemes generates discrepancies in the interpretation of the sediment samples. The Patricia Bay area was acoustically sensed and classified into a sediment map in a previous study [143]. In essence, Patricia Bay has a complex seabed with a wide range of depths, seabed slopes, and sediment types.

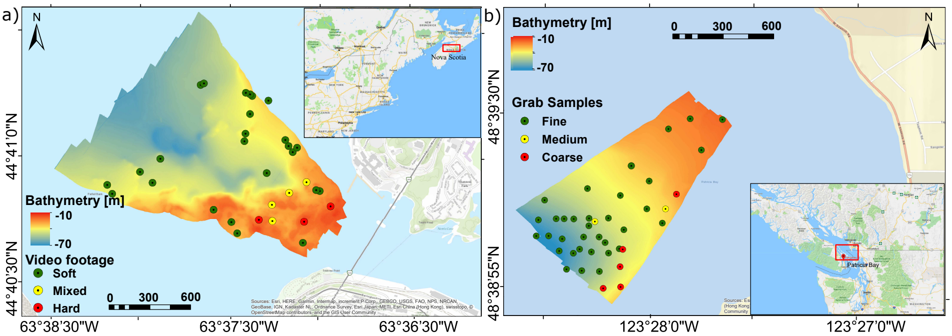

Figure 5.1: Bathymetry and location of the survey area a) Bedford Basin, Canada, and b) Patricia Bay, Canada. For both study areas the ground truth locations and the corresponding classification are presented.

5.2.3. Multispectral data

The MBES BS is stored as a single value of BS intensity per beam representing the return level at the bottom detection point and as a time series per beam representing the scatter pixels [7]. In this study, the BS intensities per beam are considered. The operating settings were tuned to achieve full coverage for all frequencies yielding to varying acquisition parameters in the employed datasets. The system settings such as transmit power, gain, and pulse length are all accessible to the user or predefined in automatic acquisition modes. Table 5.1 shows the technical characteristics of the R2Sonic 2026 MBES and some parameters used during the acquisition. The raw data are extracted from the generic sensor format (GSF) files and further processed using Matlab scripts developed in this study.

Table 5.1: Survey settings of R2Sonic 2026 MBES.

Frequency	100 kHz, 200 kHz, 400 kHz
Number of beams	256
Beam width (Ω_T and Ω_R)	2° × 2° (100 kHz), 1° × 1° (200 kHz), 0.5° × 0.5° (400 kHz)
Swath coverage	65° for starboard and port side
Nominal pulse Length τ_n	150 µs
Pulse type	Shaped continuous wave
Receiver Bandwidth B_w	7500 Hz

5.3. Methods

5.3.1. Multibeam data processing

No absolute or relative calibration is applied to the used R2Sonic 2026 MBES. Here, the data processing aims to reveal a physical reasonable relative BS strength per incident angle.

Following the sonar equation (Eq. (2.31), Section 2.4), the received echo level EL is corrected for the receiver gain PG and the actual source level SL, where the beam pattern BP_R is already considered; in addition, a correction term is used to account for the difference between the requested and actual source level. R2Sonic MBESs compensate for the transmission loss TL already during the acquisition. However, for the current study, the absorption coefficient α and the spreading coefficient loss term used by the MBES are replaced with physical reasonable values according to Eq. (2.32). The α is estimated using the model of Francois and Garrison [59] and subsequently integrated over the depth. The required environmental variables of the water column (temperature, pressure, and salinity) are obtained from measured CTD profiles and a pH value of 8 is assumed. The R2Sonic MBES stores BS intensities in digitized pressure units with an unknown scaling caused by uncalibrated sensors. First, the extracted values are converted to decibels. Furthermore, a frequency response correction term is added to the received signal intensity to compensate for the sensitivity of the transducer SH per frequency. The frequency response calculations are a theoretical approximation based on the measured transducer characteristics. In addition, the received signal is compensated for the ensonified footprint area A according to Eqs. (2.31), (2.33) and (2.34). The beam widths for the three frequencies are displayed in Table 5.1. In the pulse-limited regime, the calculation of the footprint area A_p requires the effective pulse length τ_{eff} (see Eq. (2.33)). It differs from the nominal pulse length τ_n due to the applied trapezoid filter aiming to suppress spectral leakage. In this study, it is assumed that the given receiver bandwidth B_w stored in the datagrams represents the width of the main lobe of the acoustic signal in the frequency domain at reception. Considering this assumption, τ_{eff} can be calculated by $\tau_{\text{eff}} = 1/B_w$ (Table 5.1). This results in a τ_{eff} of 133 µm, a decrease of 12 % compared to τ_n. The required across-track ϵ_y and along-track slopes ϵ_x are calculated from the bathymetric data via a moving window of 50 pings with respect to the heading of the vessel using a 2D finite difference method (Eq. (2.38)). Finally, the true incident angle ϕ is calculated by considering the along- and across-track slopes using Eq. (2.37). All levels are shifted by 100 dB. This has no effect on the classification. The value is selected to bring the BS values to levels that are typical for marine sediments.

5.3.2. Multispectral Bayesian classification method

The Bayesian method applied to each single-frequency BS dataset, described in Section 3.3.2[2], represents Step 1 of the multispectral classification method (Step 1, Fig. 5.2). In this study, the decision matrix (Eq. (3.5)) is employed to evaluate the benefit of using additional frequencies for increasing the discrimination performance

---

[2] Section 3.3.2 is originally a part of the published manuscript in Geoscience **8** (12), 455 [55].

of the seabed classification method. Each Gaussian distribution, obtained from the classification at a single-frequency MBES dataset, represents a sediment type with specific sediment properties. However, when employing a single frequency, only those sediment types that have a significantly different acoustic response can be distinguished. That means that, if two different sediment types have highly similar acoustic signatures at a specific frequency, they will be represented by the same Gaussian. Considering an additional frequency, the two sediment types may show different acoustic responses and thus can be separated. The question here is whether combining BS data, acquired at different frequencies, will actually provide more discrimination possibilities than attainable when using a single frequency only. In order to answer that issue, an approach is needed to establish a single classification map that is derived from the measurements at all frequencies available.

In order to obtain a single classification map from the multispectral data, a four-step algorithm is followed. This is schematically presented in Fig. 5.2, for two frequencies f_1 and f_2, each having three acoustic classes (ACs). The details are described as follows.

Step 1 In this step, the Bayesian method is applied to the BS histograms per frequency (see Section 3.3.2). As such, each frequency results in its own classification map (Fig. 5.2).

Step 2 This step calculates the spatial matching between classes obtained from the classification at the individual frequencies (Fig. 5.2). The results are stored in the so-called matching matrix. Each column of the matching matrix represents the locations classified by f_1, while each row represents the locations classified by f_2.

Step 3 The third step is to test whether or not the combinations found are statistically significant. A statistical significance test is performed to assess the actual existence of classes gained by combining the classification results of different frequencies. This statistically corresponds to the null hypothesis H_0, stated as follows: The AC combination per frequency pair represents an AC. The alternative hypothesis H_a is that the AC combination is not statistically significant and due to the occurrence of misclassification. The null hypothesis needs to be tested for every possible AC combination per frequency pair. This is thus performed on all individual elements of the matching matrix (i.e., the nine elements $N_{i,j}$ with $i, j = 1, 2, 3$, for the example considered in Fig. 5.2).

The statistical significance test is performed by testing the null hypothesis for the combination of AC$_i$ and AC$_j$ as obtained at f_1 and f_2, respectively. The null hypothesis is then accepted, if

$$\max\left(\frac{N_{i,j}}{N_i^{(1)}}, \frac{N_{i,j}}{N_j^{(2)}}\right) > 1 - \beta_{i,i}^{(1)}\beta_{j,j}^{(2)} \tag{5.1}$$

where $N_{i,j}$ is the number of data points that are simultaneously classified as AC$_i$ at f_1 and AC$_j$ at f_2 in the entire survey area (see Fig. 5.2). $N_i^{(1)}$ and $N_j^{(2)}$ are the total number of data points classified as AC$_i$ at f_1 and AC$_j$ at f_2, respectively. $\beta_{i,i}^{(1)}$ is the probability that the class AC$_i$ at f_1 is successfully classified (see Eq. (3.5)); $\beta_{j,j}^{(2)}$ is accordingly defined for f_2. A few remarks need to be made:

- The left-hand side of Eq. (5.1) represents an empirical probability based on the classified real data, whereas the right-hand side expresses a theoretical probability based on the Bayesian decision rule. Therefore, if the empirical probability exceeds the theoretical ones, the null hypothesis is accepted and hence a significant multispectral acoustic class (MAC) is identified. This is in agreement with the statistical significance test, that whenever a variable is larger than its standard deviation, it is considered to be statistically significant.
- From Eq. (5.1) it follows that, if the occurrence probability of the combination of AC$_i$ and AC$_j$, obtained at f_1 and f_2, is larger than the theoretical probability that this combination occurs due to at least one misclassification (either on f_1, f_2 or both), then the null hypothesis is accepted. This combination is thus statistically significant and accepted as a MAC. The rejected combinations are supposed not to be statistically significant.

After the testing procedure is applied to the individual entries of the matching matrix, a second testing procedure is started. This concerns only the entries of the matching matrix, which were rejected and hence found not to be significant in the individual tests. This statistically corresponds to make a new null hypothesis H_0 as follows: The AC combination per frequency pair of two neighboring classes represents an AC. The test is applied to the neighboring class combinations. In principle this can be applied to two or more neighboring classes. In this contribution, we limit the approach to two neighboring classes. These two classes can represent statistically significant information and need to be merged as a new AC if the test is accepted. Its probability is derived from the probability set theory according to the identity $P(A \cup B) = P(A) + P(B) - P(A \cap B)$, which describes the probability of a union of two sets A and B. The null hypothesis on merging of the two classes gets accepted, if

$$\frac{N_{i,j} + N_{i,j+1}}{N_i^{(1)}} > 1 - \beta_{i,i}^{(1)}\left(\beta_{j,j}^{(2)} + \beta_{j+1,j+1}^{(2)} - \beta_{j,j}^{(2)}\beta_{j+1,j+1}^{(2)}\right) \tag{5.2}$$

where the probability of a union of two neighboring classes AC$_j$ and AC$_{j+1}$ at f_2 are derived from the identity $P(A \cup B)$ according to $\beta_{j,j}^{(2)} = P(A)$, $\beta_{j+1,j+1}^{(2)} = P(B)$ and $\beta_{j,j}^{(2)}\beta_{j+1,j+1}^{(2)} = P(A \cap B)$. For the data considered in this study, BS measurements are acquired at three frequencies. This means that three sets of frequency pairs need to be considered. This issue is addressed in Step 4.

Step 4 This step generates the acoustic multispectral classification map, i.e., a MAC to each location within the survey area is assigned. In case only two frequencies are employed (as shown in Fig. 5.2), a MAC is assigned to each location according to the corresponding AC combination. Considering n frequencies, the number of frequency pairs increases to $k = n(n-1)/2$, and the generation of the AC map becomes k-dimensional. That means that each location corresponds to k AC combinations. Let us assume that, for each location, we have k numbers of acoustic candidates, i.e., MAC^1, ..., MAC^k. The most probable candidate is selected to be the final MAC of that location. This is achieved based on the probabilities of the correct classification of frequency pairs. For example, the theoretical probability of the correct classification MAC^l of the l^{th} frequency pair is $P_l = \beta_{i,i}^{(1)l}\beta_{j,j}^{(2)l}$ with $l = l(f_1, f_2, ..., f_n) = 1, .., k$. Per location, each acoustic candidate has thus a probability of occurrence P_l. The acoustic candidate with the highest possible probability is considered to be the most probable one, and hence the corresponding MAC of the frequency pair is obtained. This will be followed to make a unique classification map over available frequency pairs.

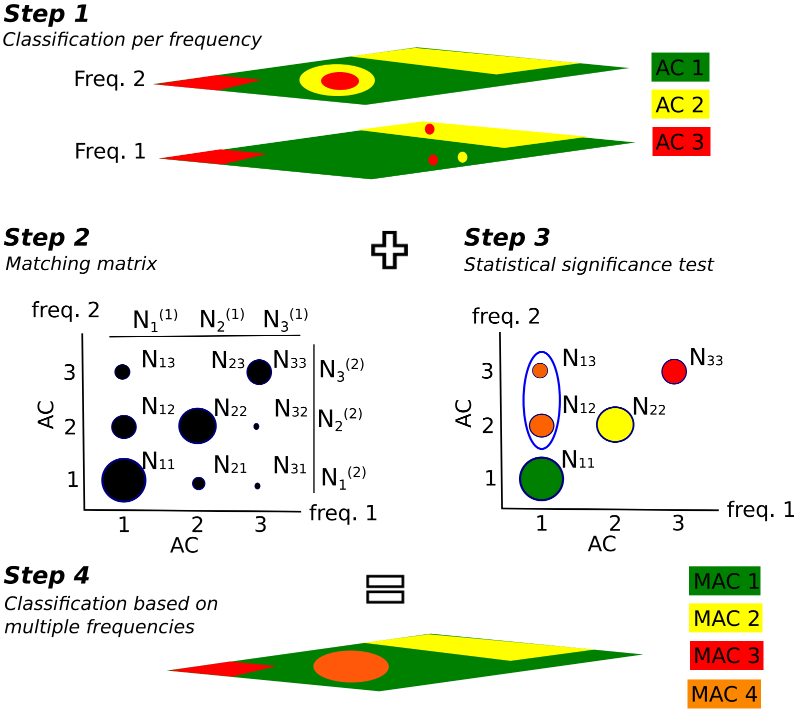

Figure 5.2: Sketch of the workflow for multispectral seabed classification based on the Bayesian method. Step 1 represents the application of the Bayesian method to each frequency. Here, acoustic classification maps obtained at two frequencies are shown. Step 2 shows the matching matrix for the different frequencies. Step 3 represents the results of the statistical significant test (see Eqs. (5.1) and (5.2)). In that example, three multispectral acoustic classes (MACs) are identified after the first part of Step 3 (N_{11}, N_{22}, N_{33}) and one MAC after the second part of Step 3 (N_{12}, N_{13}). Step 4 represents the final map production based on the results of Step 3 and the assignment of the new MACs.

5.4. Results

5.4.1. Verification and interpretation of acoustic data processing

To investigate the reliability of the acoustic data processing, the angular response curves (ARCs) of the areas that are relatively homogeneous, measured in the Bedford Basin in March 2016 and May 2017, are compared. Here, we assume that the bed characteristics do not change over the considered time and that the same incident angles of both datasets sense the same sediment. To increase the reliability of our assumption, we use data from two different areas of sediments, i.e., a muddy area (Area 1) and a gravel and boulder area (Area 2). The results are displayed in Fig. 5.3. For the majority of the incident angles, the BS values at the three frequencies agree between the 2016 and 2017 survey within less than 1 dB. For some incident angles, the deviation reaches up to 2 dB. The BS correction appears to be successfully applied considering the good agreement between both datasets.

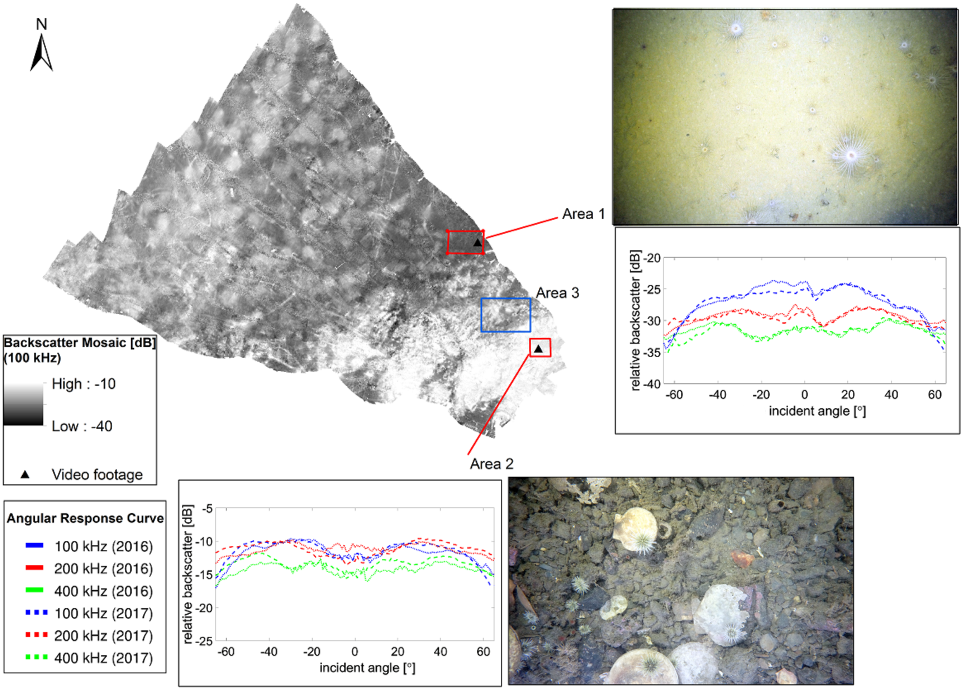

Figure 5.3: The processed ARCs from two different sediment types retrieved from the multispectral MBES dataset acquired in March 2016 and May 2017 in the Bedford Basin. The ARCs are obtained by averaging the BS values per incident angle within Areas 1 and 2. Area 1 indicates a muddy sediment, and Area 2 indicates gravel to boulders. The displayed BS mosaic (100 kHz, 2016) has a spatial resolution of 2 m by 2 m.

The shapes of the ARCs corresponding to Area 2 at 200 and 400 kHz are very flat, suggesting a rough seabed with respect to the wavelength. The ARC of 100 kHz is similar except for a significant decrease in the BS for incident angles larger than 40°, indicating an acoustically smoother seabed. The relatively flat ARC including a missing near-nadir peak can be explained by the APL-model (Section 2.2.3 and Appendix B, [40]), where the BS strength at 100 kHz for a gravelly area does not show a high variation across the incident angles (Fig. 5.4). In Area 1, the absolute BS value is significantly lower compared to Area 2 at each frequency, indicating a softer and smoother seabed, which is confirmed by the video footage showing soft sediments (mud to sand) for Area 1 and a mixture of gravel, boulders, and shells for Area 2. The shape of the ARCs among the different frequencies differ for Area 1. The 100 kHz ARC shows a decrease in BS with increasing incident angles as expected from the APL-model for fine sediments (Fig. 5.4). The flatness of the ARC shapes increases from 100 to 400 kHz, indicating that the seabed appears acoustically rougher with increasing frequency. BS mosaics are generated by correcting for the angular dependency using the local Z-score approach with a sliding window of 100 pings and the averaged BS value from 30° to 60° (Fig. 5.5) [96]. No despeckle or anti-aliasing filters are applied to the mosaics to keep the mosaics as unfiltered as possible for the verification of the BS processing. The BS mosaics indicate a reliable BS processing. The BS mosaics show clearly different spatial patterns indicating varying sensitivities at the three frequencies for different seabed types. In general, the most pronounced spatial patterns are visible at 100 kHz.

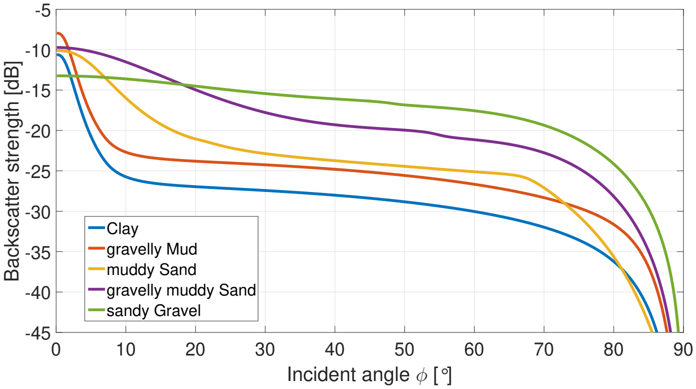

Figure 5.4: Angular response curves calculated with the APL-model at 100 kHz [40]. Model input parameters are obtained from empirical equations listed in Appendix B.1.

5.4.2. Application of the Bayesian method to multispectral backscatter data

Bedford Basin

The Bayesian method is applied to the processed relative BS strength per incident angle and frequency. The first step is to average the BS values over a range of pings and incident angles (Section 3.3.2). Accounting for the dependency of the number of scatter pixels per beam, the size of the averaging window in the across-

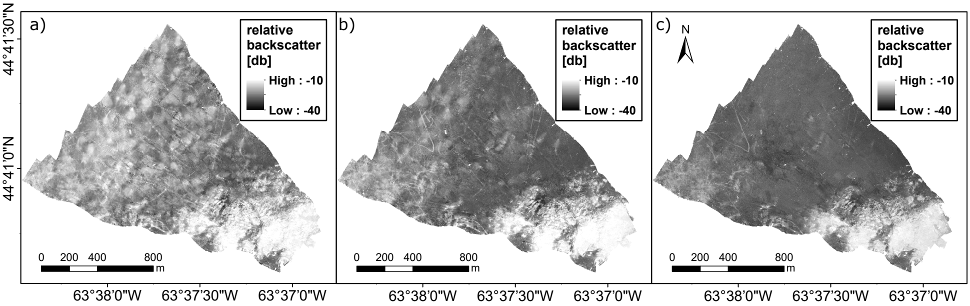

Figure 5.5: BS mosaics of the 2016 dataset obtained from a) 100 , b) 200 , and c) 400 kHz. The spatial resolution is 2 m by 2 m. Local Z-score with a sliding window of 100 pings is used to correct for the angular dependency [96].

track direction increases from 1.2° to 5° with a decreasing incident angle and in the along-track direction from 1 to 4 pings with an increasing water depth. In this way, each BS value is obtained as the average over a similar number of measurements.

In both Bedford Basin datasets, the incident angles greater than 60° are found to hold a very low number of BS strength values and tend to be noisy. Accounting to these issues, and to receive a robust statistical estimate, the range of incident angles from 40° to 60° of the starboard and port side are selected as the most suitable and are hence used for estimating the optimal number of ACs per frequency for the 2016 and 2017 Bedford Basin data.

The results are shown in Fig. 5.6a,b where the solid lines and their error bars represent the mean and standard deviation of the $\chi^2_{\hat{\nu}}$ values of all considered angles. It is observed that, in general, the averaged $\chi^2_{\hat{\nu}}$ values (including the standard deviations) comply with the criterion for an optimal model fit using five Gaussians for all frequencies and for both the 2016 and 2017 datasets. This is indicated by the error bars exceeding the upper dashed line. At 100 kHz for the 2016 dataset, the error bar strikes the upper boundary of the criterion already for four Gaussians, indicating more ambiguous results for that frequency. A further check of the validity of the results is carried out by visually comparing the fit of the modeled Gaussian distributions to the measured histograms. As an example, the fit is displayed for the 54° incident angle for the 2016 datasets in Fig. 5.7. Fig. 5.7a–f show increasing improvements with increasing frequency when using five instead of four Gaussians to fit the measured BS. These findings are observed for the majority of the considered angles. Based on these results, five classes are selected as optimal for all frequencies. Also visible from Fig. 5.7 is the relatively small number of measurements in each bin, which is caused by the use of the three frequencies subsequently, reducing the measurements per frequency. According to the requirements for the selection of the reference angles, stated in Section 3.3.2, incident angles of 53°, 54°, and 55° for the 2016 dataset and 45°, 47° and 49° for the 2017 dataset are chosen. For the generation of the final AC maps, the incident angles from 10° to 60° for the 2016 datasets and from 10° to 64° for the 2017 datasets are considered. The BS data around nadir are prone to specular reflection and are therefore too

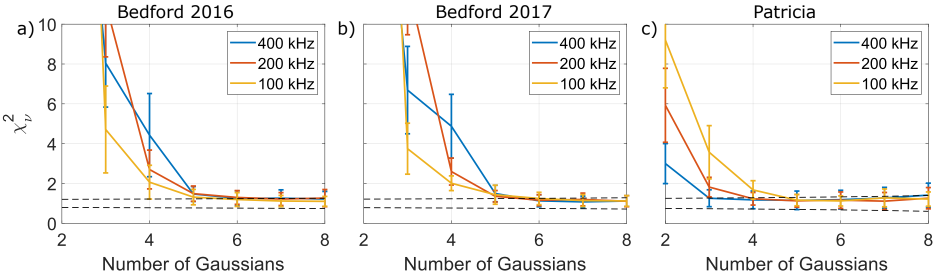

Figure 5.6: Chi-square test applied to the a) Bedford 2016, b) Bedford 2017, and c) Patricia Bay dataset for incident angles from 40° to 60° of the starboard and port side. The solid lines and their error bars represent the mean and standard deviation of the $\chi^2_{\hat{\nu}}$ values of all considered angles. The black dashed lines show the $\chi^2_{\hat{\nu}}$ value of $1 \pm \sqrt{2/\hat{\nu}}$, which indicates a good model fit (see Section 3.3.2).

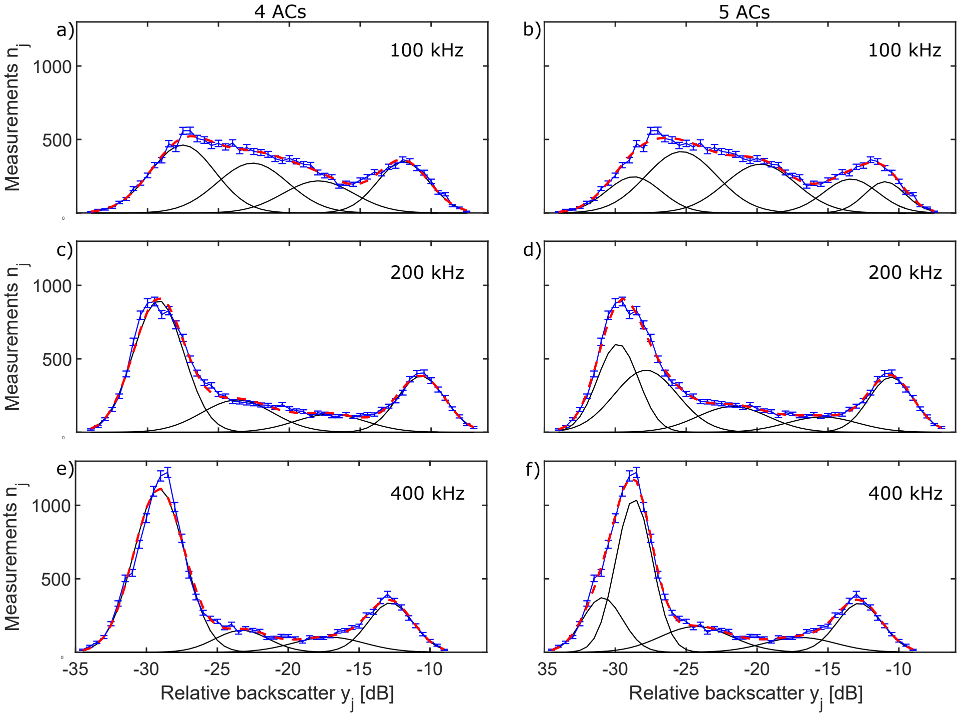

Figure 5.7: Model fits to the histogram of the measured BS data n_j (blue) per 0.5 dB bin y_j at a,b) 100, c,d) 200, and e,f) 400 kHz are displayed. The measured BS data are obtained from the 54° incident angle of the starboard side from the Bedford Basin 2016 dataset. The blue error bars indicate the variance of the measurements per bin. The modeled $f(y_j|\boldsymbol{x})$ histogram calculated by using a,c,e) 4 Gaussian distributions and b,d,f) 5 Gaussian distributions is shown in red. The corresponding Gaussians are displayed in black.

noisy to provide a reliable classification. The final AC maps for 100, 200, and 400 kHz are displayed in Fig. 5.8.

The single-frequency AC maps obtained from the 2016 and 2017 datasets largely agree for the overlapping area. A crescent-shaped feature visible in the north of the 200 and 400 kHz maps (AC_3 and AC_4, indicated by the arrow in Fig. 5.8f) of the 2017 datasets, is not present in the 2016 AC maps, indicating a change in the seabed over time. This feature is also not present in the 2016 BS mosaics (Fig. 5.5). In addition, the central area in the 400 kHz map is more extensively covered with AC_1 in the 2016 map than in the 2017 map. Natural phenomena, e.g., the deposition of finer sediments, might have changed the seabed properties over time. However, the difference is only about one AC. In general, the comparison of the 2016 and 2017 maps indicates the robustness of the classification method applied to each frequency separately.

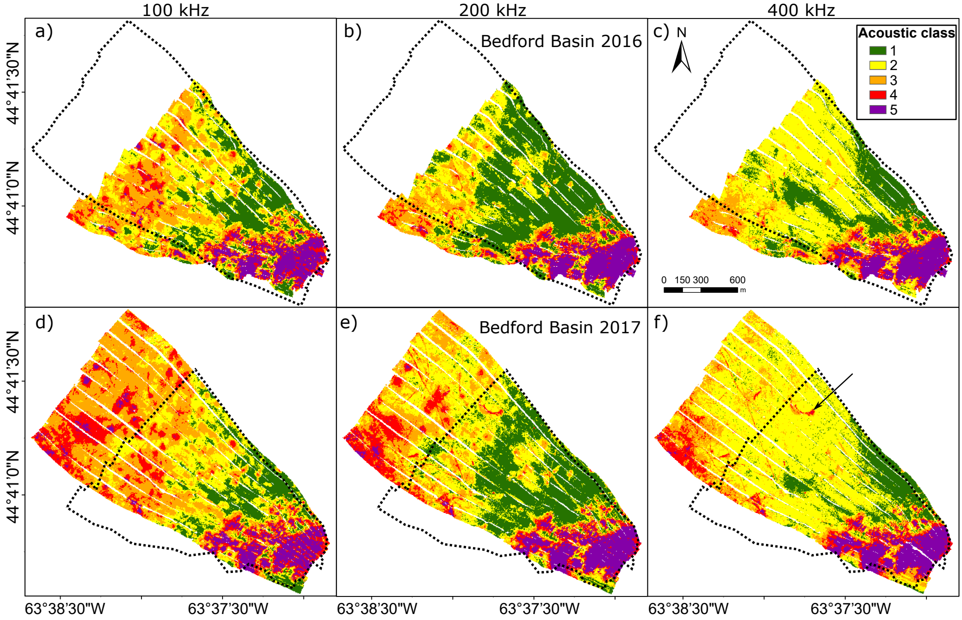

Figure 5.8: Acoustic classification maps of the Bedford Basin in 2016 and 2017 at a,d) 100, b,e) 200, and c,f) 400 kHz. The spatial resolution is 5 m by 5 m. White spots indicate no data caused by neglected BS data at nadir. The arrow indicates a feature which is only present in the 200 and 400 kHz AC maps of 2017. The dashed line represents the different survey areas.

Four main differences between the different frequencies are observed. First, in the northern part of the survey area, ACs are higher for the low frequencies (AC_3 and AC_4 for 100 and 200 kHz) than for the highest frequency (AC_1 and AC_2 for 400 kHz). Second, the spatial patterns are different, in particular between 100 and 400 kHz. In Fig. 5.8a,d and partly in Fig. 5.8b,e, circular features are visible in the central part and classified as AC_3 and AC_4 in 100 and partly in 200 kHz. In the 400 kHz map, these features are not apparent and the locations are classified as AC_2

or AC_1, like the surrounding seabed. Third, a straight orange line (AC_3) from NNW-SSE is clearly visible at 400 kHz, less pronounced at 200 kHz, and absent at 100 kHz. A fourth noticeable difference is the spatial distribution of AC_2 and AC_1. AC_2 (yellow) covers a large area in the central part of the 400 kHz map compared to a very limited extent of AC_2 and a larger extent of AC_1 in the 100 and 200 kHz map. This indicates that AC_1 and AC_2 of 100 and 200 kHz represent different seabed properties than AC_1 and AC_2 of 400 kHz. The south-east part of the study area shows the same spatial structures between the frequencies and the datasets from 2016 and 2017. In particular, AC_5 represents this part of the seabed. It demonstrates that this part of the seabed has the same acoustic response per frequency, and no additional information can be gained by using multi-frequency data. In general, the most visible differences are between the AC maps obtained at 100 and 400 kHz.

Patricia Bay

For the measurements taken in Patricia Bay, an optimal fit to the measured histograms of 100 and 200 kHz can be achieved by using four Gaussians, that of 400 kHz using three Gaussians (Fig. 5.6c). The determination of the AC boundaries is based on the incident angles of 54°, 55°, and 56°. These angular ranges provide the most consistent results for the Patricia Bay datasets. The AC maps per frequency are displayed in Fig. 5.9. The spatial patterns are very consistent over the different frequencies, unlike the Bedford Basin. The main difference is that the area being classified as AC_3 at 400 kHz is subdivided into two classes (AC_3 and AC_4) at 100 and 200 kHz. In that regard, the lower frequencies have a higher discrimination for that part of the seabed.

Comparing the Patricia Bay and Bedford Basin, the results indicate (1) more ACs can be distinguished in the Bedford Basin and (2) the sensitivity per frequency to the seabed properties differs at the two study sites. The first is expected to be directly related to the variety in sediments in the two areas. The latter indicates that the discrimination potential per frequency is highly dependent on the sensed seabed, so the selection of the ideal frequency or frequency combinations depends on the considered study site.

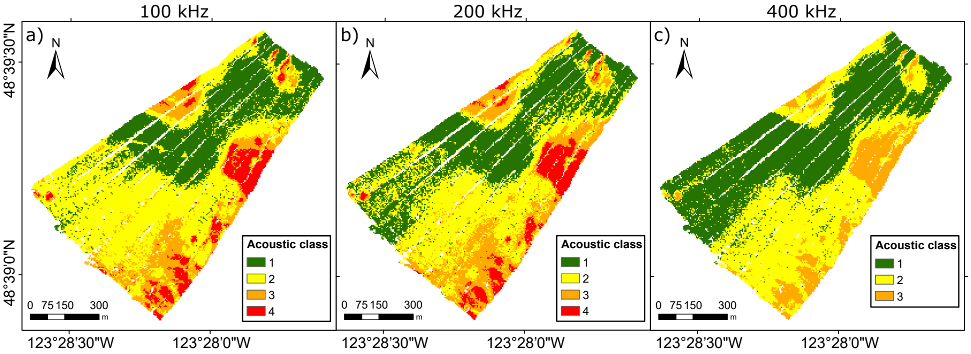

Figure 5.9: AC maps of the Patricia Bay at a) 100 , b) 200 , and c) 400 kHz. The spatial resolution is 5 m by 5 m. White spots indicate no data caused by neglected BS data at nadir.

5.4.3. Evaluation of the benefit using multiple frequencies

Bedford Basin

The matching matrix, obtained from Step 2, has entries for almost all AC combinations for each of the frequency pairs (not shown here). The statistically significant AC combinations per frequency pair, identified in Step 3, are visualized in Fig. 5.10. The black circles indicate the resulting AC combinations, where each AC per frequency is considered individually (the first part of Step 3) and the blue circles represent AC combinations where neighboring classes of one frequency are considered together (the second part of Step 3). The 2016 and 2017 data show very similar patterns. A few exceptions exist and can be related to the larger acquisition area in 2017. For example, the combination of AC_3 and AC_3 between 100 and 400 kHz is classified as statistically significant in 2016, whereas it is insignificant in 2017. Fig. 5.10 demonstrates that the combination of 100 and 200 kHz exhibits the lowest number of remaining AC combinations for both the 2016 and 2017 dataset. Seven combinations are present (including pairs of blue circles which are counting as one class), i.e., two additional classes are revealed by the multispectral measurement. In the 2017 dataset, the combinations of 200–400 and 100–400 kHz have the same amount of remaining combinations even though they are slightly different. In the 2016 dataset, 100 and 400 kHz have the most remaining AC combinations, indicating that most of the information on the seabed in this study area can be retrieved from combining 100 and 400 kHz.

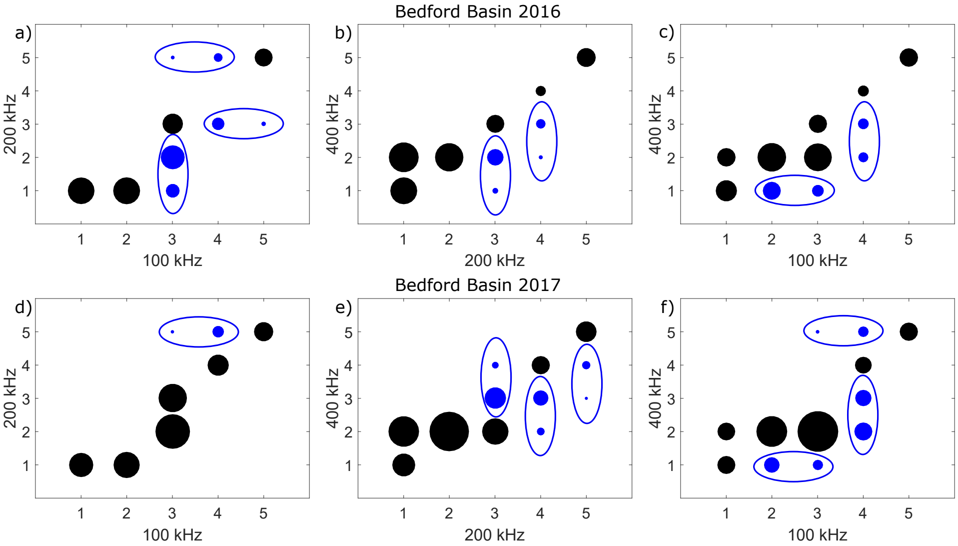

Figure 5.10: Matching matrix between the ACs of a,d) 100 and 200 , b,e) 200 and 400 , and c,f) 100 and 400 kHz for the Bedford Basin. The size of the circle represents the number of the AC combination that occur in the survey area. The black circles indicate the significant AC combinations where each AC per frequency is considered individually (the first part of Step 3) and the pairs of blue circles represent AC combinations where neighboring classes of one frequency are considered together (the second part of Step 3). To obtain theses plots, Steps 2 and 3 as described in Section 5.3.2 are applied.

Patricia Bay

For Patricia Bay, the combinations of the 100–400 and 200–400 kHz BS datasets reveal the most additional information (six remaining AC combinations) about the seabed (Fig. 5.11). However, the number of remaining AC combinations is significantly lower compared to the Bedford Basin.

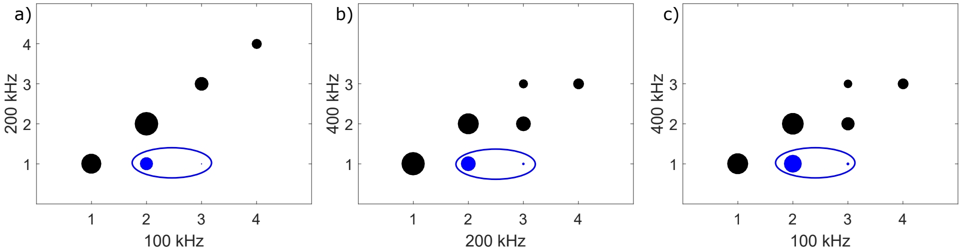

Figure 5.11: Matching matrix between the ACs of a) 100 and 200, b) 200 and 400, and c) 100 and 400 kHz for the Patricia Bay.

5.4.4. Combination of multiple frequencies

Bedford Basin

In this section, the information provided per frequency is combined with the aim to generate a multispectral classification map. The MACs are defined from the statistically significant AC combinations per frequency pair. Fig. 5.10 shows that this yields 10 and 11 unique MACs considering all frequency pairs for the 2016 and 2017 datasets, respectively. Here, we employ three frequency pairs (100–200, 200–400, and 100–400 kHz), which means that each grid cell corresponds to three AC combinations. The application of Step 4 identifies the most probable AC combinations out of the three possible combinations. It is observed that one and two MACs for the 2016 and 2017 datasets, respectively, have low probabilities compared to the other classes and less than 2 % of the grid cells are assigned to these classes. In addition, their distribution within the study area is very scattered, so they are considered to be insignificant yielding to a reduction to nine MACs for both datasets (see Fig. 5.12).

The final multispectral maps are shown in Fig. 5.13. The different spatial patterns observed in each of the single-frequency acoustic classification maps (100, 200, and 400 kHz) are now all visible in the combined map. The circular features, mainly visible in the 100 kHz map and less pronounced in the 200 kHz map, are clearly visible in the combined map (MAC_5 and MAC_6). In addition, they are now distinguishable from the structure in the north-west of the study area. Moreover, the SW-NE stripes (according to [140], these features represent trawl marks) are clearly distinguished in the final map from the surrounding seabed in the 2017 dataset. This feature is only clearly visible in the 400 kHz in 2017 and slightly in the 200 kHz map, but does not show up in the 100 kHz map. The softer sediments (lower AC and lower BS) show a higher discrimination in the final MAC map. AC_1 of

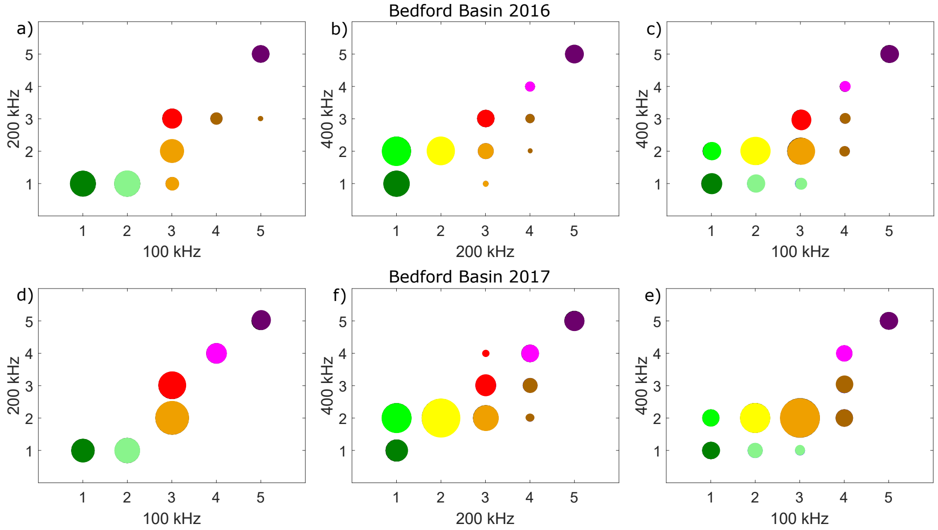

Figure 5.12: MACs of the Bedford Basin datasets 2016 and 2017. MAC revealed by the AC combinations of a,d) 100 and 200, b,e) 200 and 400, and c,f) 100 and 400 kHz. The colors indicate the different MACs. The corresponding legend is displayed in Fig. 5.13.

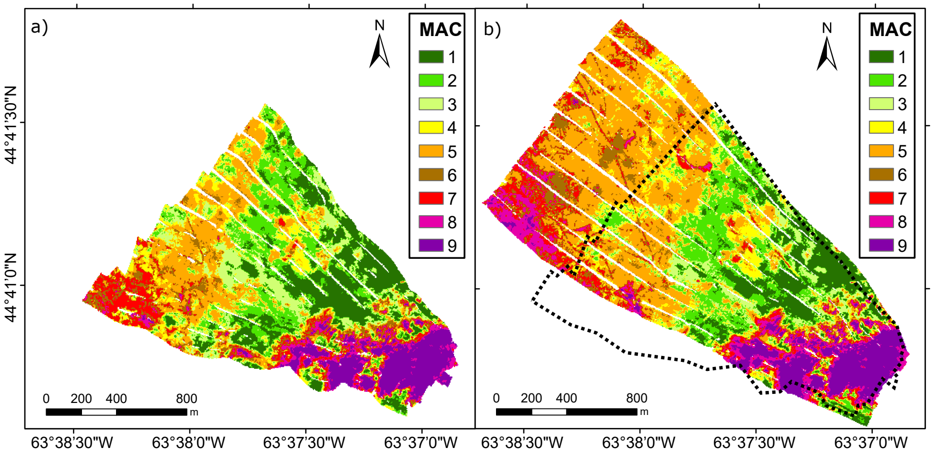

Figure 5.13: MAC map of the Bedford Basin in a) 2016 and b) 2017 obtained from the combination of the individual single frequency maps. The spatial resolution is 5 m by 5 m.

100 kHz (dark green in Fig. 5.8a) and AC_1 and AC_2 of 200 and 400 kHz (dark green and yellow in Fig. 5.8b,c) are converted to three separated MACs in the final map, indicating a reliable geological spatial pattern. Overall there is a good agreement between the overlapping area of the 2016 and 2017 multispectral map. Assuming that the seabed remained unchanged over this period of time, this observation shows the robustness of the classification approach. In general, the higher MACs seem to be more persistent over time than the lower MACs, which indicates that

sediments correlating to the higher MACs (probably harder and rougher sediments) are either

- more temporarily and spatially stable or
- acoustically less affected to slight changes in the sediment composition; for example, deposition of small amount of sand on a muddy sediment affects the resulting BS more than that on gravelly sediment does.

A detailed spatial and temporal ground truth sampling effort is needed to indicate the contributions of the above-mentioned issues.

Patricia Bay

The multispectral BS data of the Patricia Bay reveal six classes (Fig. 5.14a–c). All of these classes are already present using 200 and 400 kHz or 100 and 400 kHz (Fig. 5.14b,c). This indicates that the use of 100 or 200 kHz together with 400 kHz is sufficient to gather all acoustic information from the seabed. The multispectral map of the Patricia Bay is shown in Fig. 5.14d. The areas represented by MAC_4 to MAC_6 do not show a significant higher discrimination compared to the single-frequency map of 100 and 200 kHz. AC_1 and AC_2 are represented in the multispectral map as MAC_1, MAC_2, and MAC_3, which indicates an improved discrimination. However, the improved acoustic discrimination due to the use of multi-frequency BS is higher for the Bedford Basin.

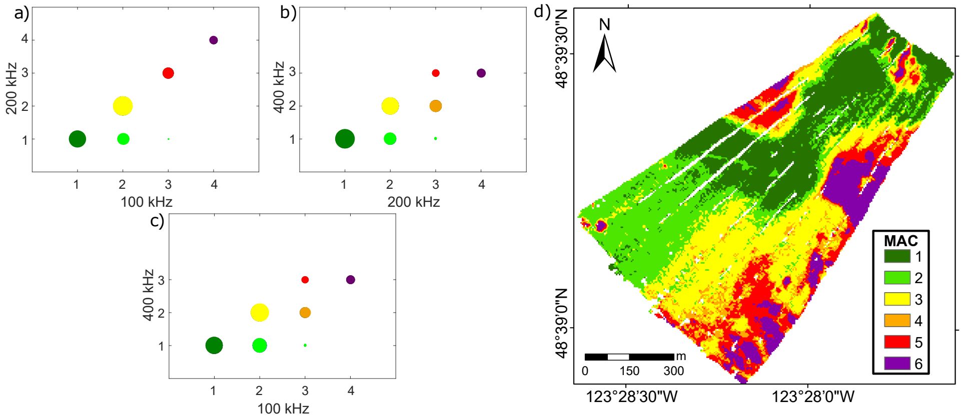

Figure 5.14: Multispectral classification results of the Patricia Bay dataset. MAC revealed by the AC combinations of a) 100 and 200, b) 200 and 400, and c) 100 and 400 kHz. The colors indicate the different MACs. d) MAC map with spatial resolution of 5 m by 5 m.

5.4.5. Correspondence between ground truth and acoustic classification

In this section, the acoustic classification results are quantitatively compared with the ground truth data. For this, the mode (most frequently occurring value) of the

ACs within a radius of 10 m around the geographical location of the ground truth data are calculated.

Bedford Basin

Fig. 5.15 shows, for all locations where video data are available, the AC and the classification based on the video data. It is seen that each frequency shows that AC_1 and AC_2 typically correspond to the soft sediment class, whereas the highest AC matches with the hard substrate. AC_1 and AC_2 indicate that, acoustically, a more detailed discrimination of the fine sediments can be made compared to that based on the video data. AC_3 indicates the presence of a soft substrate but also occurs in the mixed category. The mixed category spreads along AC_3 to AC_5 for all frequencies. These samples are located at the transition between hard to soft sediments and are part of a heterogeneous environment (an example is given in Fig. 5.16). A certain inaccuracy of the geographical location of the video footage or that the video footage represents only a small part of the seabed (ca. 40 cm × 40 cm) may cause the spread. The hard substrate is represented solely by AC_5. The multispectral results show a similar correspondence. As with the single-frequency results, this indicates a higher capability to discriminate sediment classes based on acoustics compared to that based on the video data. Combining the frequencies increases this performance even further. Here it should be noted that the different frequencies might sense different depths depending on the sediments. This aspect will be further addressed in Section 5.5. The high MACs again indicate the hard and mixed sediment classes to the same extent as the single-frequency results.

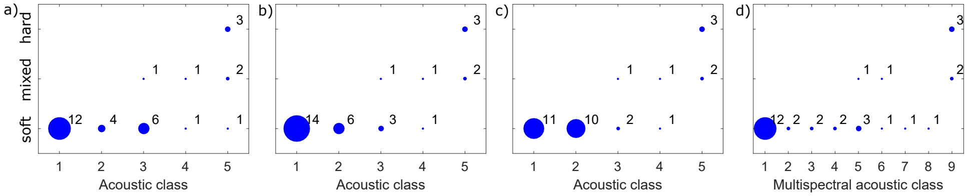

Figure 5.15: Video footage categories (soft, mixed, and hard) with ACs and MACs obtained from the single and multispectral Bayesian method at Bedford Basin 2016: a) 100 , b) 200 , and c) 400 kHz and d) combined. The numbers indicate how often the categorized video footage locations (see Fig. 5.1a) are represented by a specific AC or MAC.

More detailed and qualitative classification results and video footage samples are shown in Fig. 5.16. Clearly, the highest AC and MAC represent a seabed extensively covered with boulders, shells, and gravel, as indicated by video footage sample S1 (sample means here the location of the video footage). Sample S4 displays a mixture of boulders, gravel, and coral reef with soft sediments. In all maps, this sample is located at the boundary between the higher and lower ACs and MACs, indicating the transition area from hard to soft substrates. Samples S2 and S3 are assigned to the soft sediment category, but a more detailed observation indicates differences in the seabed composition: S2 consists of a soft sediment slightly covered with benthic flora, whereas S3 consists of soft sediment combined

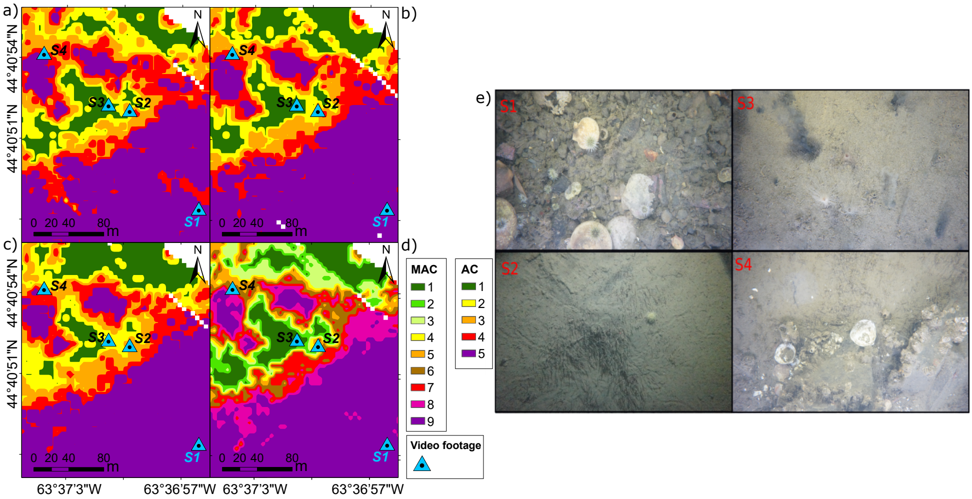

Figure 5.16: Subset of the acoustic classification maps generated by the Bayesian method from the Bedford Basin 2016 dataset at a) 100, b) 200, and c) 400 kHz and d) combined frequencies. The area is indicated in Fig. 5.3 as Area 3. e) Video footage of samples S1 to S4.

with some benthic flora as well as benthic fauna and gas seeps. In the three single-frequency classification maps as well as in the multispectral classification map, samples S2 and S3 are acoustically separated.

Patricia Bay

The ACs are shown together with the ground truth data (grab samples) categorized into fine, medium, and coarse for the Patricia Bay in Fig. 5.17. Each frequency shows that AC_1 solely corresponds to the fine sediment class and that the highest AC indicates the coarse substrate.

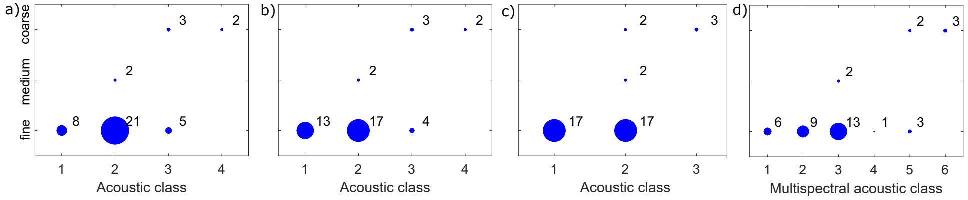

Figure 5.17: The grab samples (fine, medium, and coarse) with ACs and MACs obtained from the single and multispectral Bayesian method at Patricia Bay: a) 100, b) 200, and c) 400 kHz and d) combined. The numbers indicate how often the categorized grab samples (see Fig. 5.1b) are represented by a specific AC or MAC.

The majority of AC_2 corresponds to the fine sediment class (21, 17, and 17 samples for 100, 200, and 400 kHz) as well, whereas two samples also correspond to the medium sediment class. At 400 kHz, AC_2 corresponds also to the coarse sediment class. AC_3 corresponds to the fine and coarse sediment class at 100 and 200 kHz, indicating a very ambiguous result. The multispectral classes indicate a higher capability of multispectral BS to discriminate between the fine sediment classes compared to the single frequency classification. However, the MACs show a similar performance for the medium and hard class as the ACs, which indicates no increased discrimination.

5.5. Discussion

We have proposed a classification algorithm capable of classifying multispectral BS by combining the information obtained at different frequencies into a single classification map. The utilization of the multispectral BS data from three different MBES datasets (Bedford Basin 2016, Bedford Basin 2017 and Patricia Bay 2016) reveals three main findings.

(1) Combining 100 and 400 kHz, in general, reveals the most additional information about the seabed. This is in agreement with the study of Hughes Clark [33], who pointed out that at least a frequency spacing of one octave is required to use the frequency dependency of BS but that a separation of two octaves (100 vs. 400 kHz) is desired.

(2) The use of multiple frequencies allows for a better acoustic discrimination of seabed sediments than single-frequency data. For all datasets, in particular for the Bedford Basin, more MACs were revealed than ACs by applying the multispectral classification algorithm. However, careful interpretation of the additional classes is required. There are three possible reasons: i) the relationship between roughness and acoustic wavelength, ii) a dominating scattering regime, and iii) signal penetration. The first and second issue reflect the additional discrimination of the surficial sediments, whereas the third reason combines information from different depths at the seabed. Insights into the relative importance of the above factors are needed to interpret the MAC map.

(3) The optimal frequency selection for ASC depends on the local seabed. The results from two different study areas have shown that the most discriminative frequency and the benefit of using multiple frequencies for ASC highly depends on the local seabed, and a general conclusion cannot be drawn. In the Bedford Basin, a significantly increased discrimination performance was observed, which seems to be mainly based on the increasing signal penetration from 400 to 100 kHz. In the Patricia Bay, we observed only a slightly increased discrimination performance. This might result from the fact that the finest sediment in that area is muddy sand and the corresponding signal penetration does not differ very much for the different frequencies. However, we need to consider that the 10-year time difference between ground-truthing and acoustic data acquisition results in unknown uncertainties. The surficial sediment distribution might have changed within this period.

For the results presented here, mostly an increased discrimination (more classes) using multiple frequencies was found for the finer sediments. For these sediment types, it is known that the signal penetration for 100 kHz is higher than for 400 kHz. Fig. 5.18 indicates the larger signal penetration of the lower frequencies for fine sediments. The transition from sand to mud (Mz= 4.5 φ) approximately determines the point where the signal penetration of 100 and 400 kHz diverges. This indicates that at least to some extent additional classes are caused by combining information from the surface sediments (400 kHz) with information from the shallow subsurface (100 kHz). These findings are supported by Brown *et al.* [140], who employed the same multispectral BS dataset acquired in 2016 in the Bedford Basin. They concluded that depending on the thickness of the fine sediment layer (mud), the BS at 100 kHz results from rough dredge spoils buried in the shallow subsurface below the fine sediments. In contrary, the BS at 400 kHz reflects only the surface sediments due to the limited signal penetration.

Coarse sediments are expected to show similar signal penetration depths for the three frequencies (Fig. 5.18). Therefore, it can be expected that the BS at different frequencies reflects mostly the surface sediments, and a possible frequency dependency of the BS is caused by a change in the dominating scattering regime and the relationship between roughness and acoustic wavelength. However, in this study, the coarser sediments (boulder/gravel) are represented consistently by the highest AC at each frequency (see Fig. 5.8), indicating a limited frequency dependency for the considered coarser sediments. Similar findings for coarser sediments were found by Brown *et al.* [140] for the same study area and in [30, 33] for different study areas.

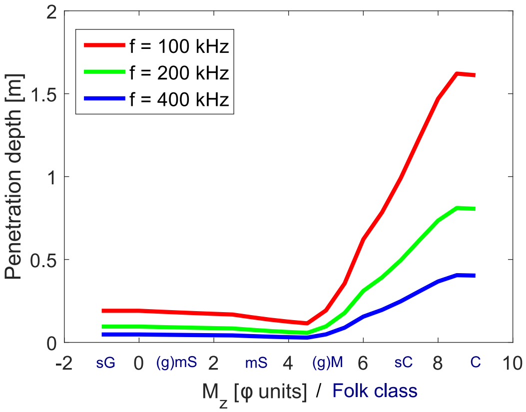

Figure 5.18: Signal penetration versus median grain size. Signal penetration is calculated from an empirical equation for acoustic attenuation in marine sediments [44]. Folk classes are approximately assigned to median grain size values: sG (sandy Gravel), (g)mS (gravelly muddy Sand), mS (muddy Sand), (g)M (slightly gravelly Mud), sC (sandy Clay) and C (clay).

Further research is needed to investigate to what degree the frequency dependency contributes to an improved acoustic discrimination by either the relationship between roughness and acoustic wavelength or the dominating scattering regime on the BS. Regarding the latter, the use of multispectral BS is promising to solve the ambiguous relationship between BS and sediments, where the mean grain size of the sediments is roughly equal to the acoustic wavelength. This ambiguity was observed in several studies and might correspond to the change in the scattering regime from Rayleigh to geometrical scattering [19, 31, 61, 62, 134] (see Chapters 3 and 7, e.g., Figs. 3.12 and 7.10). The ambiguity occurs, in particular, for coarser sediments (gravelly sand to gravel), where the mean grain size ranges around the acoustic wavelength (for a frequency of 300 kHz). Therefore, the use of frequencies ranging from 100 to 400 kHz might result in an increased discrimination performance of the coarser sediment types.

Benefits versus drawbacks of multispectral backscatter

The study has shown that the acoustic maps of the different frequencies do not necessarily represent exactly the same part of the seabed with respect to depth. This can support interpretation of the BS or classification maps, for example, in cases where a discrepancy between the acoustic classification and other measurements exist, such as surficial seabed samples (e.g., Van Veen samples) indicating a fine sediment and acoustic measurements (e.g., 100 kHz) indicating high BS strength. In such a case, the availability of a higher frequency (e.g., 400 kHz) adds crucial information to interpret this issue in terms of depth and to investigate whether the BS results from coarser sediments below the fine sediment layer. However, further research studies (e.g., using shallow cores) are needed to investigate to what extent different depths of the seabed contribute to the total BS strength to ultimately assign depth values to the MACs.

The acquisition of multispectral BS is, in general, possible without any loss of time compared to the acquisition of monochromatic BS. This is due to the ability of the R2Sonic 2026, which transmits multiple frequencies on a ping-by-ping basis. However, we need to consider that some disadvantages coming along with this approach: (1) the survey depth is limited to the highest frequency caused by the increased signal attenuation in the water column, (2) data coverage in the along-track direction is reduced with increasing number of considered frequencies, and (3) the spatial resolution of the bathymetry is restricted by the beam footprint of the lowest frequency. That means that a trade-off between benefits and disadvantages exists and that the use of the multispectral mode of such a MBES highly depends on the aim of the survey and the seabed characteristics in the survey area.

5.6. Conclusion

In this study, the Bayesian acoustic sediment classification method is introduced for the classification of multispectral MBES BS. The method accounts for the natural variability of the BS strength by assuming the measured BS per beam and frequency to result in a number of discrete seafloor types that each corresponds to a Gaussian distribution. In that regard, the ACs are defined per frequency and incident angle, which allows for an evaluation and comparison among the ACs obtained at different frequencies. We developed a classification algorithm where the classification results obtained from the different frequencies are combined to a so-called multispectral acoustic class map. The multispectral Bayesian method was applied to a multi-frequency (100, 200 and 400 kHz) BS dataset acquired with an R2Sonic 2026 MBES in the Bedford Basin, Canada, in 2016 and 2017 and in the Patricia Bay, Canada, in 2016. The system allows for the use of different operating frequencies on a ping-by-ping basis. The performed data processing accounts for most sonar settings and environmental conditions affecting the BS strength at different frequencies. It was shown that the multispectral BS can be properly processed to be used for ASC.

The main results were threefold: (1) combining 100 and 400 kHz, in general, reveals the most additional information about the seabed; (2) the use of multiple frequencies allows for a larger acoustic discrimination than using only a single frequency; and (3) the optimal frequency selection for ASC depends on the local seabed.

The comparison of the multispectral acoustic class maps obtained from the Bedford Basin acquired in 2016 and 2017 showed high agreement. Assuming temporarily constant seabed properties, this indicates the robustness of the introduced multispectral classification method. The applicability of this method to multispectral BS was further shown by the successful application to a dataset acquired in a very different marine environment (Patricia Bay). The produced maps combine the acoustic information obtained at monochromatic BS into a single map, thereby providing an overview of acoustical different areas, which can be used for future ground-truthing campaigns. However, this map combines information from both the seabed and the shallow subsurface due to an increased signal penetration for the lower frequencies and finer sediments. Considering the used frequency range from 100 to 400 kHz, it is in particular the case for muddy sediments (Bedford Basin). At this time, a quantification of the gained benefit from different acoustic frequencies using the existing video footage cannot clearly be accomplished for both study areas. Additional video footage and physical samples from the seabed and subsurface would be required at predefined locations. Still, a qualitative comparison to the video footage and a geological interpretation of the Bedford Basin indicated an improved discrimination by combining 100, 200, and 400 kHz to a multispectral acoustic class map.

The research of multispectral MBES BS is just in its initial implementation stage. The acoustic response of different sediment types for different frequencies has to be studied in more detail, which requires extensive ground-truthing. It has to be investigated to what extent the BS signal contains contribution from both the seabed and the shallow subsurface. Finally, the establishment of reference areas for MBES BS calibration will provide promising opportunities to calibrate and secure an appropriate processing of multispectral BS.

6

Mapping the seabed and shallow subsurface with multi-frequency multibeam echosounders

A dream will not become an innovation if there is no realization.

Ciputra

The previous chapter has employed multispectral backscatter (BS) data and has indicated an increased acoustic discrimination in particular for fine sediments. Within this context, the increased signal penetration for fine sediments was addressed and the effect on low-frequency backscatter (around 100 kHz) was discussed. It was argued that it is unclear to what extent the multispectral multibeam echosounder (MBES) data represent the surface of the seabed or different parts of the subsurface. In this chapter, the effect of signal penetration on the measured multi-frequency BS and bathymetry data is comprehensively investigated. To this end, two multi-frequency datasets (90 to 450 kHz) were acquired with an R2Sonic 2026 MBES supported by ground-truthing in the Vlietland Lake and the Port of Rotterdam (The Netherlands). The BS, the angular response curves and the acoustic signal are analyzed with respect to the measured bathymetry and frequency. To support the interpretation of the measured data, a layered BS model is employed and a model to simulate the MBES bathymetric measurements in a layered medium is developed.

This chapter has been published in Remote Sensing **12** (1), 54 (2020) [119].

6.1. Introduction

Multibeam echosounders (MBESs) are the most efficient and widely used sonar technology for seabed mapping. Beamforming in the across-track direction enables measurements of the signal travel time to the seabed for a large number of beam angles. As such, it provides detailed and extensive information about the seabed bathymetry. The MBES also co-registers the intensity of the returning signal for each beam. Applying geometric and radiometric corrections to the received signal, a measure of the acoustic backscatter (BS) strength can be retrieved [4]. This is a measure of the sound that is scattered or reflected from the water-sediment interface (interface scattering) and from the sediment volume (volume scattering) back towards the transmitter [30, 138]. Both mechanisms are controlled by the difference in density and sound velocity between the water and the sediment. In addition, interface scattering is mainly caused by the roughness of the seabed and volume scattering depends on the heterogeneity of the shallow subsurface [145]. The BS strength also varies with the incident angle, known as the angular response [15]. Furthermore, the relation between the acoustic frequency and roughness wavelength affects the interaction of the sound with seabed [138]. While higher frequencies are more sensitive to the seabed roughness, lower frequency signals are more affected by volume heterogeneities due to lower sound attenuation, resulting in an increased signal penetration, in the sediment.

Generally, the MBES operates in a narrow band around the central frequency and therefore the BS data are collected at a single frequency (i.e., monochromatic). Monochromatic BS data collected with a MBES have been used for two decades to remotely characterize or classify seabed sediments or habitats via sophisticated classification algorithms [13, 61, 107, 108]. However, previous studies have shown that monochromatic BS can lead to ambiguous results when classifying different seabed environments [19, 62, 134] (see Chapters 3 and 7, e.g., Figs. 3.12 and 7.10). That means different sediment compositions or mixtures have similar acoustic properties at the same frequency. According to theoretical [49, 145] and experimental [31] research of acoustic BS and considering the analogy to satellite remote imaging, where backscattered light is collected over a wide frequency spectrum of electromagnetic waves, the use of BS data at different frequencies (i.e., multispectral) is promising to further reduce ambiguous sediment classification results.

Recent research studies employing multispectral BS data have shown improvements in sediment and habitat mapping. The acquisition of multispectral BS data has been achieved by using either different acoustic sensors (i.e., MBES and Sidescan sonar) [146], various MBESs [33], or a single broadband MBES running multiple track lines [34]. New developments in marine sonar technology allow the MBES to collect spatially and temporally co-located BS data at multiple frequencies (i.e., 90 to 450 kHz) using a single system. The first research studies (see Chapter 5), employing such a MBES, have also indicated a potential to increase the discrimination between different seabed environments using multi-frequency BS data [36, 55, 147, 148]. In these studies different BS patterns at various frequencies (100, 200, and 400 kHz), indicating the benefits of multiple frequencies, were mainly observed for areas consisting of fine sediments (mud). The different BS patterns were potentially caused by coarse, dredge spoil material below a mud layer, and sensed due to an increased signal penetration of the lower frequencies.

With respect to the typical frequency range of modern MBESs (12 to 700 kHz), different signal penetrations, in particular for fine sediments, are expected [44]. Schneider von Deimling *et al.* [137] measured a signal penetration of up to 12 m in muddy deposits with a 12 kHz MBES. For frequencies around 100 kHz a penetration between 0.1 to 1 m in fine sediments is expected [73]. Simulations based on the empirical equations of Hamilton [44] showed that, in particular, between fine sediments ranging from gravelly mud (4Φ) to clay (9Φ) the signal penetration of a 100 kHz signal differs enormously ($\sim$1 m) [55] (Section 5.5, Fig. 5.18). This indicates the high sensitivity of the acoustic penetration to small changes in sediment properties. In another study by Fonseca [73], high BS levels in muddy sediments were measured, which is counter-intuitive to the general knowledge of muddy sediments corresponding to a low BS level [49]. They explained this observation, among others, with an increased penetration of the 95 kHz signal and the contribution of subsurface layering to the measured BS level.

These findings demonstrate that not only changes in the surficial sediment, to which one frequency is more sensitive than another, result in different BS patterns between the frequencies. But they also seem to indicate that when shallow sediment layering below fine sediments exists, the observed frequency dependency of BS may result from the ensonification of different sediments at different depths due to varying signal penetration at the transmitted frequencies. With the increasing use of multi-frequency BS data for sediment and habitat mapping, it is necessary to investigate what part of the seabed or subsurface is represented by the measured BS data to avoid ambiguous classification results. In particular, for fine sediments, the multi-frequency BS data and consequently the acoustic classification map might represent a 3D image of the surficial seabed and the shallow subsurface as argued by Gaida *et al.* [55] (Chapter 5).

This study seeks to extend the knowledge about multispectral MBES data by investigating the effect of frequency-dependent signal penetration on multi-frequency BS and bathymetry data. In particular, the effect of sediment layering on the BS data is examined. To this end, we acquired two multi-frequency BS dataset (90 to 450 kHz) with an R2Sonic 2026 MBES in a freshwater lake and in the Port of Rotterdam in the Netherlands. Both study areas consist, to a large extent, of surficial fine (muddy) sediments. In addition, we collected ground truth information via Van Veen sampling and video footage in the Vlietland Lake and rheometric profiling (i.e., subsurface density) in the Port of Rotterdam to support the acoustic results. To gain an improved understanding and interpretation of multispectral MBES data, a layered BS model, based on [136], is used and an algorithm to model the MBES bathymetric measurements in a layered medium is developed.

6.2. Study areas and data

6.2.1. Regional setting

Vlietland Lake

The Vlietland Lake is a man-made freshwater lake in the western part of the Netherlands (Fig. 6.1c). The lake is a former sandpit used for the extraction of sand since 1970 and has recently become a recreation area and nature reserve. The lake was dredged through several geological layers ranging from peaty to gravelly sand layers. The current water depth ranges from 4 to 32 m below Normaal Amsterdams Peil (NAP). The majority of the lakebed is located in the Kreftenheye formation consisting of fluvial coarse sand (0.2 to 2 mm) and gravel (5.6 to 63 mm) [149]. Around the lake, the Kreftenheye formation is located between approximately 17 to 36 m below NAP. The surficial sediments of the lake towards the shoreline consist of fine to medium sand with a varying percentage of shells, coarse sand, and mud (d_{50}= 70 to 310 μm). The surficial sediments away from the shoreline consist of mud with a small percentage of fine sand (d_{50}= 18 to 26 μm and defined as sandy mud after Folk [83]). With the finalization of the sand extraction activities, the muddy sediments were deposited on the sand and gravel sediments of the Kreftenheye formation probably due to aeolian sediment transport and sedimentation of organic matter.

Port of Rotterdam

The Port of Rotterdam is located in the Rhine-Meuse Estuary, which is defined as a transition zone between a river and marine environment (Fig. 6.1d). Therefore, the Port of Rotterdam has a deposition of fluvial and marine sediments. It requires intensive maintenance dredging to ensure port accessibility for the vessels with the highest draft which results in 12 to 15 million m^3 of dredged sediment per year [150]. The material to be dredged consists of alluvial sediments (mainly silt) from the Rhine and Meuse as well as sand and marine silts originating from the southern part of the North Sea. The survey area covers a man-made pit used as a sediment trap for water injection dredging (WID). The last WID was conducted in October 2018 and the comparison with previous bathymetry measurements combined with the analysis of the bed samples indicated that the sediment trap is refilled with muddy sediments (d_{50}= 15 μm and defined as sandy mud after Folk [83]). The current water depth of the study area ranges from 19 to 26 m below NAP.

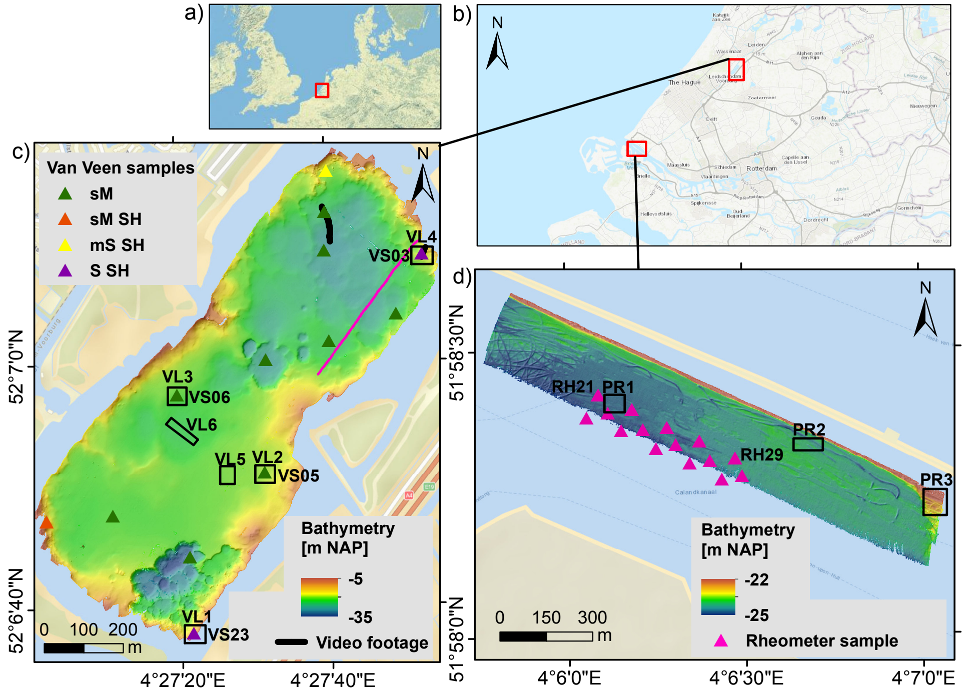

Figure 6.1: Study areas: a) North Sea, b) South-West of the Netherlands showing the Vlietland Lake and Rhine-Meuse Estuary, c) Vlietland Lake bathymetry and d) bathymetry of the sediment trap in the Port of Rotterdam. The bathymetries are measured at the highest frequency (450 and 425 kHz, respectively). Abbreviations VL (Vlietland Lake) and PR (Port of Rotterdam) assigned to black polygons indicate areas used for calculation of angular response curve, bathymetry uncertainty and time series of the signal. Abbreviation VS (Van Veen samples) and RH (Rheometric profiling) indicate locations of ground truth data. Sediments are classified as follows: sandy mud (sM), sandy mud with shells (sM SH), muddy sand with shells (mS SH), and sand with shells (S SH). Pink line indicates the location of the MBES sub-bottom profile.

6.2.2. Multibeam data acquisition

Two multi-frequency MBES datasets were acquired with an R2Sonic 2026 in the Vlietland Lake and Port of Rotterdam in September 2018 and January 2019, respectively (The Netherlands). The data were collected at five different frequencies between 90 and 450 kHz on a ping-by-ping basis. Further crucial survey parameters are listed in Table 6.1. The MBES was pole mounted and operated with the R2Sonic controller and the acquisition software Qinsy. An iXblue Octans 3000 motion sensor and iXblue Phins provided real-time heading, roll, pitch, and heave for the Port of Rotterdam and Vlietland Lake, respectively. For both study areas, a Trimble SPS855 GNSS receiver provided real-time kinematic positioning with a horizontal and vertical accuracy of 1 and 2 cm, respectively. Regularly performed CTD (conductivity, temperature, and depth) measurements gave temporal and spatial measurements of the water column for ray-tracing and sound absorption. The absorption depth profile was calculated using the equation from Francois and Garrison [59]. The Port of Rotterdam and Vlietland Lake datasets consist of 5 and 15 track lines resulting in an area of 1.5 km × 0.25 km and 1.3 km × 0.5 km, respectively (Fig. 6.1c,d). To guarantee sufficient data coverage at each frequency, an overlap of about 120 % of adjacent lines was ensured and the vessel speed was kept between 2 and 3 knots.

Table 6.1: Survey parameters using an R2 Sonic 2026.

	Vlietland Lake	Port of Rotterdam
Center frequency	90, 100, 200, 300, 450 kHz	90, 170, 255, 340, 425 kHz
Nominal pulse length	150 μs	150 μs
Number of beams	256	256
Beam width	2.3°, 2.1°, 1.1°, 0.7°, 0.5°	2.3°, 1.2°, 0.8°, 0.6°, 0.5°
Swath coverage	-65°/65°	-65°/65°
Beam spacing	equiangular	equiangular
Pulse type	shaped continuous wave	shaped continuous wave

6.2.3. Ground truth data

In the Vlietland Lake, 12 grab samples were taken with a small Van Veen sampler. This device has a grasping area of maximum 250 cm^2 and is expected to reach a penetration depth between 10 to 20 cm in muddy sediments. The sample locations were selected based on the observed MBES BS patterns. The samples were photographed and subsampled for a grain-size analysis. The grains smaller than 1 mm were analyzed by laser diffraction and the grains larger than 1 mm were analyzed by sieving. The median grain size (d_{50}) was calculated for the entire grain-size spectrum. We classified the samples according to Folk [83], as sandy mud (sM), sandy mud with shells (sM SH), muddy sand with shells (mS SH), and sand with shells (S SH). In addition, video transects were carried out to obtain a visual overview of the seabed in the Vlietland Lake.

In the Port of Rotterdam, depth profiles of in situ sediment properties, i.e., density and yield stress, were measured with a pre-calibrated rheometric profiler before the MBES acquisition. In the same area, Van Veen samples were acquired in previous measurement campaigns. It was seen that sediment grain-size distribution do not to vary significantly in time and therefore, we consider the measurements as representative.

6.3. Methods

Section 6.3.1 outlines the processing of the measured multibeam data and explains the generation of the corresponding maps and figures. Section 6.3.2 briefly describes the layered BS model developed by Guillon and Lurton [136]. This model is an extension of the APL-model [40] and used to model the BS strength of a layered medium. The layered BS model is employed to support the interpretation of the measured BS data. Section 6.3.4 gives a detailed description of the bottom detection model developed in this study. This model simulates the sound transmission and reception at the MBES as well as the sound propagation and scattering in the media. Within the bottom detection model, the APL-model and its extension provide the BS strength for the surficial and buried sediment. The model is used to simulate the bathymetric measurements of a MBES in a layered medium in order to support the interpretation of the measured bathymetry.

6.3.1. Multibeam data processing

Bathymetric data processing is carried out with the software Qimera, applying manual and spline filtering to remove sounding artifacts. The bathymetry data are then separated per frequency and gridded into a 1 m × 1 m and 1.5 m × 1.5 m grid using the GIS software packages ARCmap 10.5 for the Vlietland Lake and Port of Rotterdam, respectively. Following this, the bathymetry grids obtained for the different frequencies are subtracted from each other to calculate the difference in the measured water depths between the frequencies[1].

The multi-frequency BS data are processed with an in-house developed processing algorithm written in Matlab. In this study, the so-called ”BS intensity per beam value” representing the return level at the bottom detection point [7] and the entire time series[2] signal are used. To retrieve a physical reasonable BS level from the measured data, the processing chain, introduced by Gaida *et al.* [55] and presented in Sections 2.4 and 5.3.1, is applied. The measured data ara corrected for the receiving gain, actual source level, transducer sensitivity per frequency (frequency response) and transmission loss including geometrical spreading and sound absorption. The BS level at the bottom detection is additionally corrected for the ensonified footprint and the seabed morphology. The frequency response correction term, which is used to compensate for the transducer sensitivity per frequency, is based on a theoretical calculation and the level of uncertainty is unknown. Therefore, a precise comparison of the decibel values between the frequencies is hampered. In addition, no absolute or relative calibration is applied to the MBES and the data has thus to be considered as a relative measure of the BS strength. Once the BS processing is completed, the BS mosaics are generated by calculating an averaged angular response curve (ARC) over a sliding window of 100 pings, subtracting the averaged ARC from the data and then normalizing the BS level with the averaged BS level between 30° and 60° for starboard and port side separately.

The calculation of the measured bathymetric uncertainties is carried out by dividing the survey area into surface patches each consisting of a few consecutive pings (i.e., 7 pings) in the along-track direction and a few beams around the central beam angle in the across-track direction (i.e., interval of 1°). To eliminate the contribution of the morphology, a bi-quadratic or linear function is fitted to the measurements within each surface patch [17]. The unknown parameters (i.e., coefficients of the function) are derived in a least-square sense. Here, the bathymetric uncertainty is

---

[1] In this thesis, bathymetry represents the measured depths by the MBES although it can occur, that the measured depth does not necessarily represent the actual seabed bathymetry at every frequency, as it will be shown in this chapter.

[2] In this chapter, the terminology time series describes the acoustic signal as a function of time. In literature the time series of the acoustic signal is often referred as water column data.

the standard deviation (68 % confidence interval) obtained from the square root of the least-squares estimate of the variance component [151] and accounted for the potential presence of slopes. The degree of the fit function (bi-quadratic or linear) is based upon the curvature C, which is a measure for the surface patch deviation from a flat plane. For the data acquired, it is seen that $|C| > 0.5\,°/\mathrm{m}$ corresponds to steep slopes. Therefore, for a surface patch with $|C| < 0.5\,°/\mathrm{m}$ a linear function is used for the fit, otherwise a bi-quadratic fit is employed.

6.3.2. Layered backscatter model

The layered BS model developed by Guillon and Lurton [136] is based on the combination of a classical scattering model (known as Jackson model [49] or APL-model [40] and introduced in Section 2.2.3 and Appendix B) and sound propagation inside a fluid layered media. In the APL-model, the BS strength $BS(\phi,f)$, received from the backscattering cross-section $\sigma_b(\phi,f)$ via $BS(\phi,f) = 10\log(\sigma_b(\phi,f))$, is modeled as a contribution of the rough seabed (roughness scattering σ_r) and the semi-infinite volume heterogeneity (volume scattering σ_v)[3] [49]

$$\sigma_b(\phi,f) = \sigma_r(\phi,f) + \sigma_v(\phi,f) \tag{6.1}$$

with $\sigma_r(\phi,f) = F(\phi,f,\rho,c,\alpha,\eta,\gamma)$ and $\sigma_v(\phi,f) = F(\phi,f,\rho,c,\alpha,\hat{\sigma}_v)$. This means that the model requires eight input parameters: incident angle ϕ, frequency f, density ρ, sound velocity c, attenuation coefficient α, spectral exponent γ, spectral strength η, and volume scattering parameter $\hat{\sigma}_v$. The density ρ, the sound velocity c, and the attenuation coefficient α need to be known for both the water and sediment.

6

The APL-model is considered valid for frequencies between 10 and 100 kHz. The limitation is mainly caused by the roughness scattering model. The focus in this study is mostly on fine sediments where volume scattering dominates over interface scattering and therefore, we consider the model to be applicable also for higher frequencies.

To model the BS of a layered medium, Guillon and Lurton [136] modified the APL-model to account for the layering effect on sound reflection and scattering. The $\sigma_b(\phi,f)$ of the surficial and the buried layer is modeled individually using the APL-model and accounting for the layering effect. The individual contributions of both layers are summed coherently. A buried sediment layer affects σ_r and σ_v at both the water-sediment and the buried interface. The calculation of σ_v corresponding to the upper layer is modified to account for the finite thickness. An impedance adaption and angular refraction correction is implemented for both scattering mechanisms when calculating the scattering of the second layer. Furthermore, the BS is transferred from the buried interface to the sediment-water interface by accounting for the sound propagation in the layered medium. Therefore, a transfer-coefficient is calculated which is based on the transmission coefficient and the sound absorption α within the layered medium. For further theoretical details and corresponding equations, see Appendix C or [40, 136].

---

[3] In agreement with Section 2.2 and Appendix B, σ_b, σ_r and σ_v are dimensionless cross sections defined per unit area and per unit solid angle.

6.3.3. Model parameter selection

For this study a two-layered geophysical model consisting of the water column and two sediment layers is considered. The values for the input variables are displayed in Table 6.2. The parameters ρ, c, and α for the water column are based on the CTD measurements taken in the Vlietland Lake. For the sediment, the empirical equations established by Hamilton [44] are used to estimate ρ, c and α from the median grain size. In agreement with recommendations by the APL-model [40], we relate γ, η and $\hat{\sigma}_v$ to the median grain size (Appendix B.1).

We model two scenarios with a median grain size of 6Φ (16 µm) and 9Φ (2 µm) for the surficial sediment while the buried sediment has a median grain size of -1Φ (2 mm) for both scenarios. The median grain size of 6Φ represents the surficial sandy mud at both sites and the median grain size of -1Φ, associated to sandy gravel [40], is assumed to represent the buried sediment layer in the Vlietland Lake (Section 6.2.1). A median grain size of 9Φ, associated with clay [144], represents a second scenario to investigate the effect of even finer sediments on the BS strength and bottom detection.

Table 6.2: Input parameters for the layered BS model and the bottom detection model. Layer 0 represents the water column, Layer 1 the surficial sediment, and Layer 2 the buried sediment. Model parameter values are retrieved from the empirical equations displayed in Appendix B.1.

Variable	Unit	Layer 0	Layer 1	Layer 2
Folk class	-	Fresh water	C/sM	sG
Mz	Φ	-	9/6	-1
c	m/s	1479	1449/1460	1977
ρ	$\mathrm{kg/m^3}$	1000	1145/1149	2492
$\alpha_{90\,\mathrm{kHz}}$	dB/m	2.5×10^{-2}	4.9/12.6	41.0
$\alpha_{450\,\mathrm{kHz}}$	dB/m	6.3×10^{-2}	24.3/62.9	205.0
$\hat{\sigma}_v$	-	-	$1 \times 10^{-3}/1 \times 10^{-3}$	2×10^{-3}
γ	-	-	3.25/3.25	3.25
η	$\mathrm{cm^4}$	-	$5.17 \times 10^{-4}/5.17 \times 10^{-4}$	1.29×10^{-2}
$h; d$	m	20 [h]	0.2. and 0.5 [d]	Semi-infinite

6.3.4. Bottom detection model

In the bottom detection model the different layers are modeled by a large set of discrete scatterers each of them scattering the transmitted sound pulse to generate the received pressure signal. Following the approach of the APL-model (Section 2.2.3), roughness and volume scattering are associated with the location of the interface scatterer although volume scattering is originated from the underlying volume. The backscattered signal is derived by a coherent summation of the received signal from the scatterers falling within the instantaneously ensonified area [99]. The sound pressure of the received MBES signal at a given time instant t and steering angle θ is given as

$$p(t,\theta) = \sum_{j=1}^{J} s(t)\sqrt{\sigma_t(\phi_j)}\,b_p(\theta)\frac{e^{-2\hat{\alpha} r_j}}{r_j^2} \tag{6.2}$$

where $s(t)$ is the transmitted sound pressure signal, $b_p(\theta)$ is the beam pattern and J is the number of scatterers j falling in the instantaneously ensonified area $A(t)$ at time t. $\sigma_t(\phi_j)$ is the target's backscattering cross section of scatterer j at incident angle ϕ_j. The term $\frac{e^{-2\hat{\alpha} r_j}}{r_j^2}$ accounts for the two-way geometrical spreading (denominator) and attenuation of the signal within a dissipative propagation medium (nominator). The transmitted sound pressure signal $s(t)$ by the MBES can be expressed as a sinusodial pressure wave (see Section 2.1)

$$s(t) = \begin{cases} W(t-t_j)\sqrt{2}p_{\mathrm{rms}}\sin\left(2\pi f(t-t_j)\right), & 0 < t-t_j < \tau \\ 0 & \text{otherwise} \end{cases}, \tag{6.3}$$

where τ is the pulse length, p_{rms} is the root mean square pressure (rms) of the transmitted pulse and $W(t-t_j)$ is a Hanning tapering function to reflect a smooth signal. The arrival time of each scatterer is $t_j = \frac{2h}{c_0\cos(\phi_j)}$, where h is the water depth below the MBES, c_0 is the sound speed in water and ϕ_j is the incident angle. Assuming a homogeneous water column, the calculation of t_j does not require consideration of the sound refraction. The receiving beam pattern $b_p(\theta)$ is expressed as (Section 2.3.2, [2])

$$b_p(\theta) = \left(\frac{\sum_{m=0}^{M-1} e^{ik(\sin\phi_j - \sin\theta)\frac{mL_R}{M}}}{M}\right)^2 \tag{6.4}$$

where M is the number of receiving element m, k is the wavenumber of the transmitted signal and L_R is the receiver array length (Table 6.3).

The following explains how to relate the term $\sqrt{\sigma_t(\phi_j)}$ in Eq. (6.2) to the backscattering cross-section $\sigma_b(\phi_j)$. First of all, the square root relates intensity to pressure values for the target's backscattering cross-section $\sigma_t(\phi_j)$ via (see Sections 2.1.1 and 2.2.2)

$$\sigma_t(\phi_j) = \frac{I_b(\phi_j)}{I_i(\phi_j)} = \left(\frac{p_{\mathrm{rms}_b}(\phi_j)}{p_{\mathrm{rms}_i}(\phi_j)}\right)^2 \tag{6.5}$$

where I_b, I_i, p_{rms_b}, and p_{rms_i} denote the intensities and rms pressures of the backscattered and the incident wave. The target's backscattering cross-section is related to the backscattering cross-section via the instantaneously ensonified area as follows (derived from Eq. (2.18))

$$\sigma_t(\phi) = \int_{A(t)} \sigma_b(\phi)dA \tag{6.6}$$

where $\sigma_b(\phi)$ is obtained from the APL-model (Eq. (6.1))[4]. In order to account for the statistical fluctuation inherent to the scattering process, $\sigma_b(\phi)$ is modeled as a

---

[4] Since σ_t and σ_b are dimensionless, the integration area dA is actually referenced to a unit area A_0=1 m^2, so that dA is also dimensionless. For convenience A_0 is not added to Eq. (6.6).

Rayleigh distributed variable [6]. Here, $A = \frac{\Omega_T}{360}\pi x^2$ (with Ω_T in degree) represents the sector of a circle with a radius x (i.e., distance in across-track direction[5]) and an opening angle Ω_T (i.e., $\Omega_T = \frac{c_0}{fL_T}$ represents the beam opening angle at transmission, with L_T the transmitter (projector) array length). By substituting $\frac{dA}{dx} = \Omega_T x$ (with Ω_T in radians) into Eq. (6.6), it follows

$$\sigma_t(\phi) = \Omega_T \int_{x_{\mathrm{lb}}(t)}^{x_{\mathrm{ub}}(t)} \sigma_b(\phi) x \mathrm{d}x \tag{6.7}$$

which becomes for the discrete scatterer case

$$\sigma_t(\phi) = \Omega_T \sum_{j=1}^{J} \sigma_b(\phi_j) x_j \Delta x_j. \tag{6.8}$$

The target's backscattering cross-section at each scatterer j can thus be expressed as

$$\sigma_t(\phi_j) = \Omega_T \sigma_b(\phi_j) x_j \Delta x_j \tag{6.9}$$

where the incident angle of each scatterer ϕ_j is connected to the slant range r_j or the water depth h via the horizontal distance x_j of each scatterer toward the receiver: $\phi_j = \sin^{-1}(\frac{x_j}{r_j})$ or $\phi_j = \tan^{-1}(\frac{x_j}{h})$.

Here, as seen from the relation established between Eqs. (6.6) to (6.8), the instantaneously ensonified area, containing J scatterers, is bounded in the horizontal direction (across-track) by the lower x_{lb} and upper x_{ub} bounds via $A(t) = \frac{\Omega_T}{360}\pi(x_{\mathrm{ub}}^2(t) - x_{\mathrm{lb}}^2(t))$ (Fig. 6.2).

The upper bound can be written as

$$x_{\mathrm{ub}}(t) = \sqrt{\frac{(c_0 t)^2}{4} - h^2}. \tag{6.10}$$

The corresponding slant range at the upper bound is $r_{\mathrm{ub}} = \sqrt{(x_{\mathrm{ub}}^2 + h^2)}$. The lower bound can be expressed with a dependency on t as

$$x_{\mathrm{lb}}(t) = 0, \quad t \leq t_{\mathrm{nadir}} + \tau \tag{6.11a}$$

$$x_{\mathrm{lb}}(t) = \sqrt{\left(\frac{c_0 t}{2} - \frac{c_0 \tau}{2}\right)^2 - h^2}, \quad t \geq t_{\mathrm{nadir}} + \tau \tag{6.11b}$$

where $t_{\mathrm{nadir}} = \frac{2h}{c_0}$.

---

[5] In this chapter, the across-track direction is indicated by the variable x. This is contrary to Chapter 2, in which the variable x denotes the along-track and y the across-track direction.

To model the pressure signal in a layered medium, the sound propagation into the subsurface and the scattering at the buried layer needs to be considered. The refraction of the signal into the subsurface changes the incident angle at the buried layer via Snell's law (see Section 2.2.1)

$$\frac{\sin(\phi_{j,l+1})}{\sin(\phi_{j,l})} = \frac{c_l}{c_{l-1}} \tag{6.12}$$

where l denotes the layer[6]. Considering a layered medium with L_n the total number of layers each variable is extended with the index l. The upper bound in Eq. (6.10) changes for a layered medium to

$$x_{\mathrm{ub},L_n}(t) = \sqrt{\frac{(c_0\delta t_0)^2}{4} - h^2 + \sum_{l=2}^{L_n}\sqrt{\frac{(c_{l-1}\delta t_{l-1})^2}{4} - d_{l-1}^2}} \tag{6.13}$$

where c_l is the sound speed and δt_l is the travel time in layer l and δt_0 is the travel time in the water column. The lower bound is adjusted for the layered medium accordingly (Fig. 6.2b). To obtain the pressure signal $p(t,\theta)$ scattered from a layered medium the individual signals scattered from each layer are coherently summed according to

$$p(t,\theta) = \sum_{l=1}^{L_n} p_l(t,\theta). \tag{6.14}$$

For the buried layers the attenuation term in Eq. (6.2) is extended for the sound attenuation in the sediment.

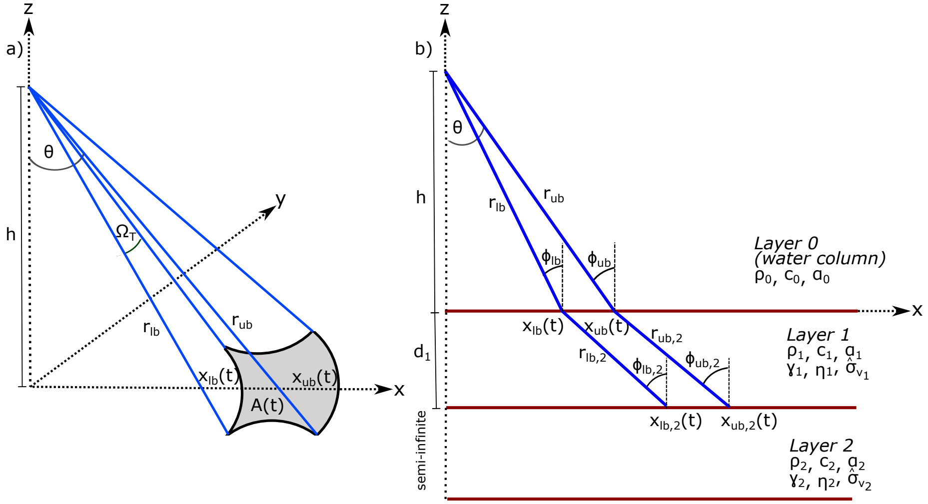

Figure 6.2: Schematic of the layered BS model and the bottom detection model. a) Seabed view of the MBES footprint and b) cross-profile view of layered medium (two-layered geophysical model).

---

[6] In this thesis, the right hand side of Eq. (6.12) is revised from $\frac{c_{l+1}}{c_l}$ to $\frac{c_l}{c_{l-1}}$ and the location of the incident angle ϕ in Fig. 6.2 is corrected with respect to the published article.

Fig. 6.3 displays the beamformed pressure signal at 90 kHz for different steering angles corresponding to the individual layers of the layered medium and the combined response using the input parameters listed in Tables 6.2 and 6.3. In this example, where a layer thickness of 50 cm and sediment properties representing sandy mud are assumed, both layers contribute equally to the modeled signal up to a steering angle of 30° whereas for the outer beams only the surficial sediment has a significant contribution.

Table 6.3: Input parameters for the bottom detection model.

Variable	Value
f	90 kHz and 450 kHz
τ	150 µs
p_{eff}	0.01 Pa
$L_{R,T}$	0.41 m
M	256

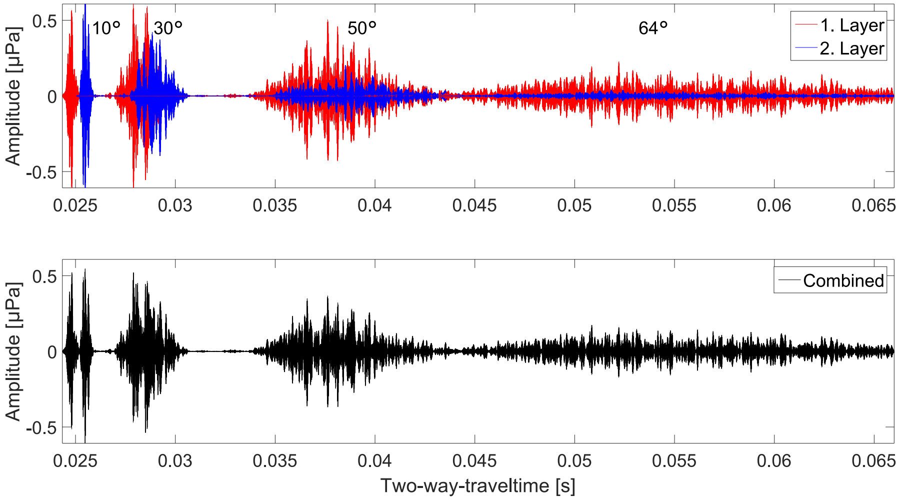

Figure 6.3: Modeled pressure signals steered at 10°, 30°, 50°, and 64° using the bottom detection model. Used parameters are: f = 90 kHz, L_n = 2, d_1 = 50 cm, Mz_1 = 6Φ and Mz_2 = −1Φ. (Top) Pressure signals corresponding to the first and second layer including modifications due to layered medium. (Bottom) Coherently summed pressure signal of both layers. The signals associated with the different steering angles are separated signals arriving at different time instances and plotted on the same time axis.

For the bottom detection, amplitude and phase detection of the received signal are implemented (see Section 2.3.3). Amplitude detection is based on the computation of the center of gravity [53]. For the phase detection, the full MBES receiving array with the length L_R is divided into two sub-arrays and the phase difference of the signal received at a given time instant is determined at the two sub-arrays [51]. The time at which the two signals are in phase (zero phase difference between the two beams formed in a chosen direction) is taken as the arrival time [51]. To calculate the zero-phase crossing, a second-order polynomial is fitted to the measurements of the phase difference over a certain number of phase samples. The least-squares method is used to estimate the parameters of the polynomial. It should be noted that for the simulation of the received signals at the two sub-arrays, the slant range r_j in Eq. (6.2) has to account for the traveled distance from the center of the array to the scatterer on the bottom or buried layer and from the scatterer to the center of the sub-arrays. Here, the length of the sub-arrays is assumed to be half of the full array. In the model, amplitude or phase-detection is selected based upon two criteria:

- Number of phase samples available to find the coefficients of the second-order polynomial: if the number of phase samples in the phase ramp is less than five, phase detection is rejected and amplitude detection is chosen. This occurs mostly close to nadir.

- Deviation of the solution based on the phase detection from that of amplitude: if the estimate based on the phase detection is out of the 95 % confidence interval of the solution based on the amplitude detection, the latter is chosen.

6.4. Experimental results

6.4.1. Multi-frequency backscatter mosaics

The BS mosaics at the different frequencies from the Vlietland Lake and Port of Rotterdam are displayed in Figs. 6.4 and 6.5, respectively. For the Vlietland Lake, varying BS patterns are observed among the frequencies with the largest difference between the most separated frequencies of 90 and 450 kHz. The lowest frequency of 90 kHz shows low to high BS levels for the muddy areas (green triangle) and intermediate BS levels for the sandy areas with shells (yellow, red and purple triangles). Here, in particular the wide range of up to 15 dB in the BS level at 90 kHz for

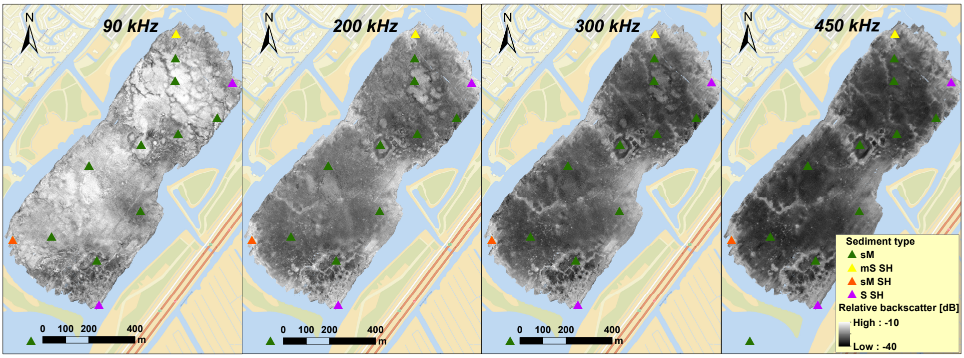

Figure 6.4: BS mosaics measured in the Vlietland Lake at 90, 200, 300, and 450 kHz. The grid cell size is 1 m by 1 m. Abbreviations: sandy mud (sM), sandy mud with shells (sM SH), muddy sand with shells (mS SH), and sand with shells (S SH).

muddy sediments is noticeable. While the higher frequencies of 300 and 450 kHz indicate consistently low BS levels for most of the muddy areas, the sandy areas with shells indicate similar intermediate BS levels as it is seen at 90 kHz. The frequency of 200 kHz shows similar BS levels for the coarse sediments and a moderate range in BS levels for the fine sediments, i.e., smaller range than 90 kHz but larger than 450 kHz.

For the Port of Rotterdam, only the most separated frequencies of 90 and 425 kHz are displayed in Fig. 6.5a,b. Here, no significant differences are found in the BS pattern and BS levels among the frequencies for almost the entire muddy area. Solely in the south-east, indicated by Area PR3, which is located outside the man-made pit, high BS levels at 90 kHz and low BS levels at 425 kHz are found similar to the observation in the Vlietland Lake.

6.4.2. Bathymetry difference among the frequencies

Fig. 6.5c and Fig. 6.6a,b display the differences in the measured bathymetry between different frequencies for the Port of Rotterdam and Vlietland Lake, respectively. Green colors indicate that the lower frequency measured a deeper bathymetry, yellow represents no difference and red colors indicate that the higher frequency measured a deeper bathymetry.

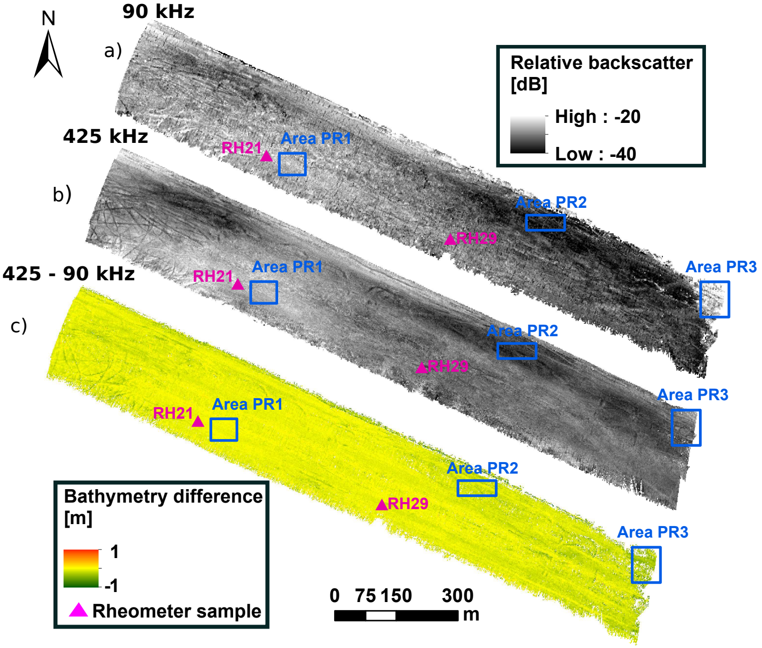

Figure 6.5: a,b) BS mosaics measured in the Port of Rotterdam at 90 and 425 kHz, respectively. c) Corresponding bathymetry difference map between 90 and 425 kHz. Polygons indicate location used for the calculation of the angular response curves (ARC) and the time series signal. The grid cell size is 1.5 m by 1.5 m.

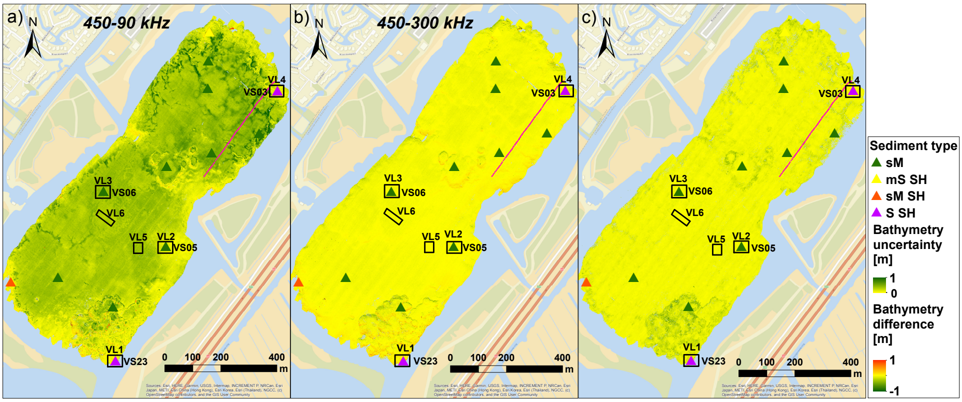

Figure 6.6: Bathymetry difference map between a) 450 and 90 kHz and b) 450 and 300 kHz in the Vlietland Lake. Green colors indicate deeper bathymetry at the lower frequency. c) Measured depth uncertainty at 90 kHz. The grid cell size is 1 m by 1 m. Pink line indicates the location of the MBES sub-bottom profile. Abbreviations: sandy mud (sM), sandy mud with shells (sM SH), muddy sand with shells (mS SH) and sand with shells (S SH).

We observe that the measured depth is between 0 and 60 cm deeper at 90 kHz compared to 450 kHz for the muddy areas in the Vlietland Lake. The measured depth uncertainty does not exceed 10 cm, except for areas with steep slopes, demonstrating that the depth difference between the frequencies is statistically significant (Fig. 6.6c). The areas with coarser sediments show the same measured depth, considering the uncertainties, at all frequencies. The depths at 300 and 450 kHz show no difference independent of the sediment type indicating that the frequency needs to be sufficiently low to result in a different measured depth.

The measured bathymetry in the Port of Rotterdam is for the most areas very similar between the most separated frequencies of 90 and 425 kHz even though the entire area consists of muddy sediment. Solely, in the south-east, coinciding with the different BS patterns at 90 and 425 kHz, a depth difference of about 40 cm is measured.

The bathymetry difference maps display along-track stripes indicating that the difference in the measured bathymetry varies over the incident angle. As an example, Fig. 6.7a shows the measured depth as a function of the incident angle for a muddy area (Area VL6). The depth difference is largest between 90 and 450 kHz (∼35 cm) with intermediate values for 200 kHz (∼10 cm). In Fig. 6.7b,c the depth difference at 90 and 200 kHz with respect to 450 kHz over the incident angles is visualized, respectively. At 90 kHz we observe smaller differences of approximately 25 cm around nadir with a strong increase to 35 cm at 10° and a further slight increase to 40 cm for the starboard side. In general, most areas show the pattern of an increase in the depth difference with an increasing incident angle. At 200 kHz, we observe a decrease in the measured depth difference with increasing incident angle for all areas, as shown in Fig. 6.7c. The grey shaded area, presenting the measured depth uncertainty in Fig. 6.7b,c, indicates that the changes in the measured depth difference with incident angle are statistically significant. Following this observation, the bathymetry difference maps in Figs. 6.5 and 6.6 present only an approximation of the local measured depth difference because the values are averaged over a number of different beam angles from overlapping track lines falling in the same grid cell.

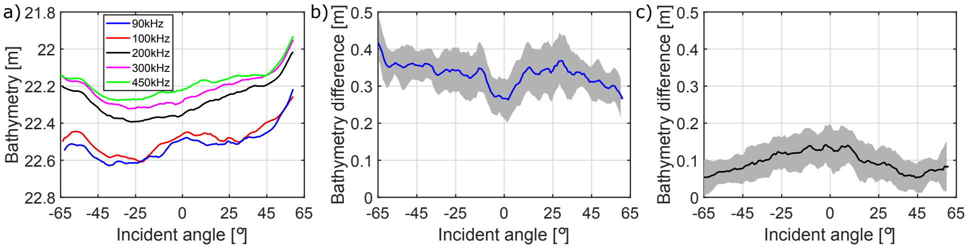

Figure 6.7: Angular dependency of depth measurements in a muddy area in the Vlietland Lake. a) Measured depth at different frequencies for the entire MBES swath (-65°/65°). b,c) Depth difference at 90 and 200 kHz with respect to 450 kHz, respectively. Grey shaded area indicates measured uncertainty. The data are taken from Area VL6 (Fig. 6.1c).

6.4.3. Ground truth

The bathymetry difference maps show similar patterns as those in the BS mosaics, indicating a relationship between the measured bathymetry and the BS level per frequency. To relate this observation to the sediment properties in more detail, the ground truth data are examined.

Fig. 6.8a represents the median grain size measured from the grab samples in the Vlietland Lake. The median grain size is visualized with respect to the bathymetry difference between 90 and 450 kHz and the corresponding BS level at 90 kHz, both measured within a radius of 5 m around the grab sample locations (Fig. 6.1c). The sample indicated by the red circle is located in an area with a rough morphology and a large uncertainty of the measured bathymetry (around 30 cm) and thus not considered in the following analysis. Based on the sediment properties, BS level, and the measured bathymetry difference, we define four subsets, denoted A, B, C, and D, from Fig. 6.8a, which are listed in Table 6.4.

Table 6.4: Categorization of ground truth locations into subsets based on sediment properties, BS level, and measured bathymetry difference.

Subsets	Sediment	BS level	Bathymetry difference
A	Very coarse (sand with shells)	High	Negligible
B	Coarse (sand/mud mix with shells)	Intermediate	Negligible to low
C	Fine (sandy mud)	Low	Negligible
D	Fine (sandy mud)	Intermediate to very high	Significant

Subset A contains the sample locations with a median grain size larger than 180 µm, a negligible bathymetry difference (~7 cm, around the uncertainty) and a high BS level (–17 dB). The sample locations assigned to subset B exhibit lower

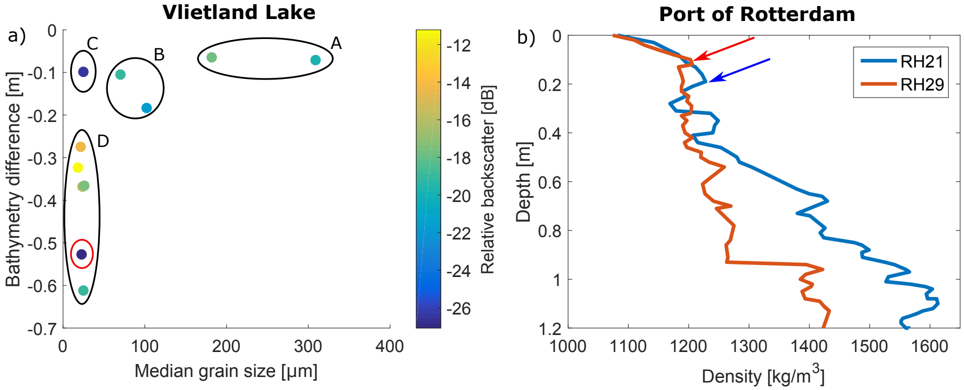

Figure 6.8: a) Measured depth difference between 90 and 450 kHz versus median grain size at all sample locations (Fig. 6.1c) in the Vlietland Lake. The colorbar indicates the averaged BS level (BS mosaics) at 90 kHz around the sample locations. The subsets, denoted A, B, C, and D are defined based on the sediment properties, BS level and the measured bathymetry difference at the sample location. b) Density profiles at two locations taken with a rheometric profiler in the Port of Rotterdam (Fig. 6.1d).

median grain sizes of 70 to 100 µm, slightly higher bathymetry differences of 10 to 18 cm and slightly lower BS levels (–19 to –21 dB). These observations show that the coarser the sediment, the higher the agreement in the measured bathymetry between the frequencies and the higher the BS levels. Subset C comprises sample locations consisting of muddy sediments with a median grain size of around 25 µm, negligible bathymetry difference, and low BS values (–26 dB). The samples assigned to subset D are also muddy sediments with a median grain size around 25 µm, but the bathymetry difference and BS level vary significantly. A general trend of decreasing BS levels (–11 to –19 dB) with increasing bathymetry difference (32 to 62 cm) is observed.

Fig. 6.8b displays the density measurements for the samples RH21 and RH29 in the Port of Rotterdam. The arrows indicate our interpretation of the top of the seabed. Both samples show a gradual increase of the density from about 1250 to 1500 kg/m^3 from the top of the sediment to a depth of 1.2 m. This indicates an increasing compaction degree of the muddy sediments but no distinct layering. Given the muddy sediments (d_{50}= 15 µm) and a negligible bathymetry difference of 6 and 10 cm, respectively, both locations are assigned to subset C.

6.4.4. Angular response curves

As an analysis based solely on the averaged BS level neglects the characteristic angular response related to different sediments, we analyze the intrinsic behavior of the BS level versus the incident angle via the angular response curves (ARC) [15]. Additionally, an uncalibrated system hampers the inter-comparison of the BS levels between different surveys but the characteristic shape of the ARCs are still comparable.

Fig. 6.9a–c show the ARCs at five frequencies and for three different sample locations in the Vlietland Lake (VL1, VL2, and VL3 assigned to subset A, C, and D). The ARCs, displayed in Fig. 6.9a and assigned to subset A, show an angular response typical for very coarse sediments with a constant to slight decrease in the BS level with increasing incident angle. The BS levels and the shapes between the frequencies are relatively similar, indicating no improved acoustic discrimination using multiple frequencies for this specific sediment. The ARCs in Fig. 6.9b (location is assigned to subset C) show a high nadir peak and a normal decay of the BS level towards the outer angles for all frequencies, as it is expected for muddy sediments from theoretical models. Fig. 6.9c shows the ARCs from a muddy area with a depth difference of 37 cm between 90 and 450 kHz (subset D). The BS level is significantly higher at 90 kHz compared to 450 kHz and, in addition, the low frequencies show a flat, untypical, angular response, which is not expected for muddy sediments.

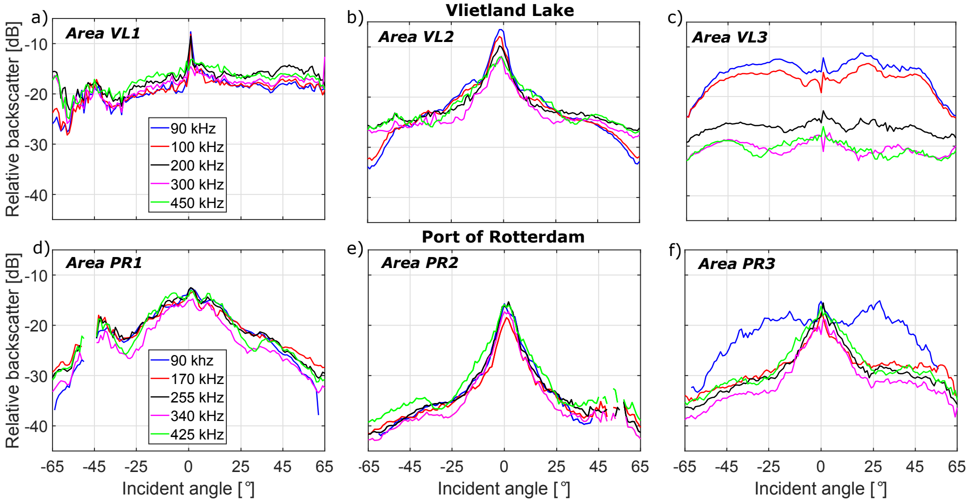

Figure 6.9: ARCs measured in the (top) Vlietland Lake and (bottom) Port of Rotterdam. (Left) coarser and harder sediments without depth difference: a) sand with shells, d) muddy area with higher compaction, (middle) muddy areas without depth difference between 90 and 450 kHz, (right) muddy areas with depth difference c) 37 cm and f) 40 cm. The data for the ARCs are taken from an area (40 m × 40 m) indicated by the polygons in Fig. 6.1c and Fig. 6.1d. The areas in a–d) correspond to sample locations.

Fig. 6.9d–f show the ARCs for three locations in the Port of Rotterdam. The measured ARCs in Area PR1 (Fig. 6.9d) show a moderate decrease of the BS level towards the outer angle while in Area PR2 (Fig. 6.9e) a higher decrease in the

BS level is observed. This indicates that both areas are likely to have a different compaction degree of the muddy sediments. Area PR2 is located at sample RH21 and therefore being assigned to subset C. Outside the man-made pit (Area PR3), we see in a muddy area a higher BS level with a similar flat angular response at the lowest frequency of 90 kHz (Fig. 6.9f), as seen in the Vlietland Lake (Fig. 6.9c). This location coincides with a measured bathymetry difference of 40 cm, and therefore being assigned to subset D. Noticeable is that the higher frequencies still show a typical decay with increasing incident angle contrary to the Vlietland Lake (subset D, Fig. 6.9c). In Area PR3, we expect only a thin layer of unconsolidated mud above consolidated mud, which results in a rapid change of the sediment properties indicating a layered medium.

The acoustic observations and the geological setting might indicate that the high BS levels at the low frequencies in the muddy areas result from an increased signal penetration and the scattering of the signal at the buried harder and rougher consolidated mud layer, while the high-frequency signal corresponds to the surficial unconsolidated mud layer. The same explanation might hold for the Vlietland Lake where a thin mud layer is located above a coarse sand to gravel layer (see Section 6.2.1).

Furthermore, the samples in subset D show that an increase in the measured bathymetry difference corresponds to a decrease in the BS level. This is caused by a longer travel distance of the signal corresponding to an increased sound attenuation. For areas where no bathymetry difference is measured (subset C, e.g., VL2 and PR2), even though the surficial sediment properties are the same, the buried layer is either too deep and the signal is already attenuated before reaching this layer or no layering exist. This can be validated in area PR2 where the density measurements (Sample RH21) show an increasing compaction degree of the muddy sediments without distinct layering (Fig. 6.8b). For the same area, the bathymetry difference between 90 and 450 kHz is negligible and the ARCs are very similar for all frequencies (Fig. 6.9d), indicating that without layering the ARC at the lowest frequencies corresponds to the surficial sediments.

6.4.5. Time series signal

The measured bathmetry is based on the bottom detection of the MBES, where amplitude or phase detection is applied to the entire acoustic signal per beam angle. Fig. 6.10 displays the beamformed acoustic signal at 10° for four different locations in the Vlietland Lake and Port of Rotterdam. The signals displayed in Fig. 6.10a,c, corresponding both to a muddy area, show that the highest amplitude at 90 kHz is found between 35 and 50 cm deeper than the highest amplitude at 200 and 450 kHz. The 90 kHz signal has a second amplitude peak which correlates with the highest amplitude of the higher frequencies. It indicates that a portion of the incident acoustic energy is scattered at the surficial seabed but most of the energy is transmitted into the subsurface and is scattered at a second layer with a higher scattering strength. In Fig. 6.10b,d the highest amplitude and the bottom detection are found at the same depth for all frequencies. In general, in areas consisting of sand with shells (Fig. 6.10b), the surficial seabed represents a strong scatterer and a highly attenuating medium for all frequencies. For the area consisting of sandy mud (Fig. 6.10d) either the surficial sediment is highly compacted resulting in a strong scatterer and a highly attenuating medium or a second scattering layer does not exist or is too deep to be reached by the lowest frequency.

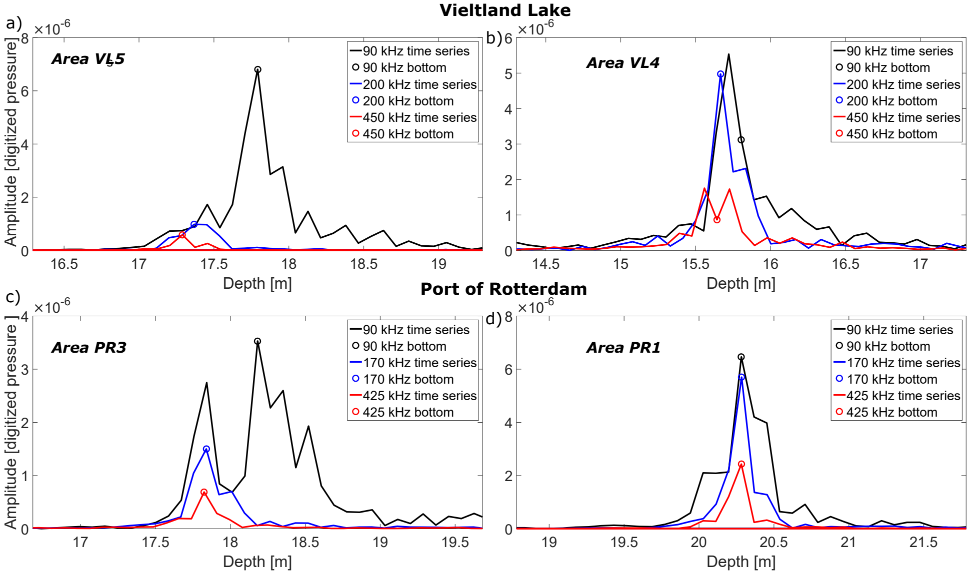

Figure 6.10: Measured time series of the signal amplitude at a beam angle of 10°. a) Vlietland Lake: fine sediment, b) Vlietland Lake: coarse sediment, c,d) Port of Rotterdam: fine sediment. The circles indicate the bottom detection of the MBES. The locations of the measurements are displayed in Fig. 6.1c,d.

Fig. 6.11 visualizes the measured time series of the signal amplitude at 90 kHz and at a beam angle of 0° along a profile in the Vlietland Lake (i.e., sub-bottom profiler like image). The green and red line indicate the detected bottom at 90 and 450 kHz, respectively. The corresponding BS is plotted above the sub-bottom image.

In some regions (0–10 m, 140 to 150 m and 390 to 420 m), where the BS and bottom detection at both frequencies are very similar, the signal energy is focused around the bottom detection, indicating no layering. In particular, in the last section (390 to 420 m), where the grab sample revealed surficial sand with shells, the detected bottom is exactly at the same location for the two frequencies. In one region, between 350 and 390 m, the time series shows clearly two distinct amplitude peaks indicating the surfical seabed and a buried layer detected at 450 kHz and 90 kHz, respectively. In this region the BS at both frequencies is the same. Compared to the majority of the profile, the BS at 450 kHz is increased, indicating coarser sediment and consequently higher attenuation. This yields to a decreased BS at 90 kHz, as also observed. For the majority of the profile, where the BS is significantly higher (> 10 dB) and the bottom detection significantly deeper at 90 kHz, the energy of the signal is spread. The first rise in the amplitude correlates with the surficial seabed, indicated by the 450 kHz bottom detection, and reaches its peak a few decimetres below where the MBES detects the bottom at 90 kHz. These areas also correspond to the flat shape of the ARC at 90 kHz, as shown in Fig. 6.9c. It indicates that the bottom detection, the high BS level and the unusual angular response at 90 kHz for muddy sediments results from scattering at subsurface structures.

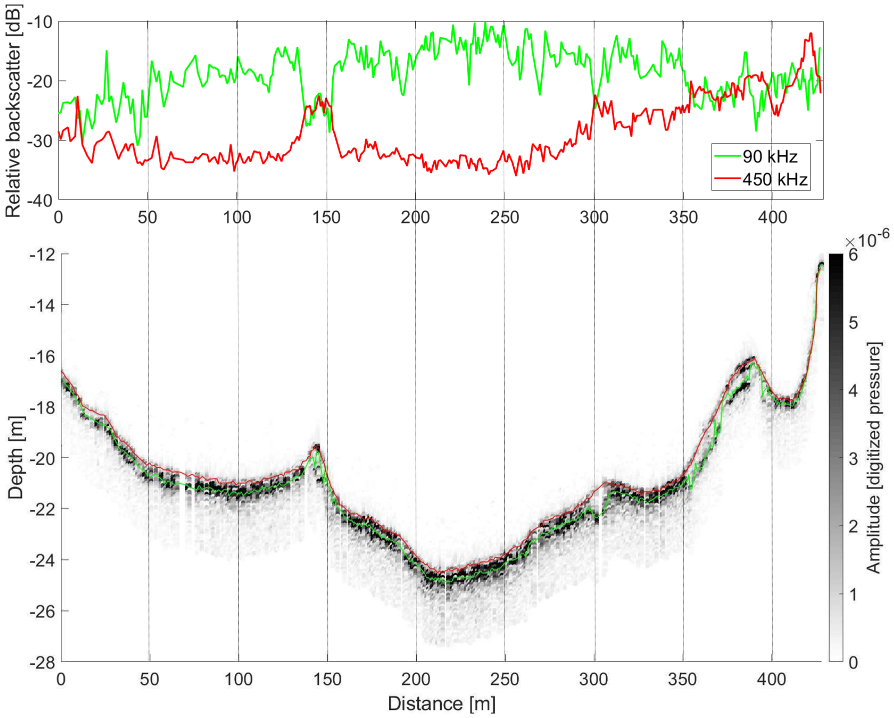

Figure 6.11: (Bottom) Sub-bottom image: measured time series of the signal amplitude at 90 kHz and a beam angle of 0° for a track line in the Vlietland Lake. The measured bathymetry at 90 and 450 kHz are shown as well. (Top) Corresponding measured BS at 90 and 450 kHz. The track line is indicated in Fig. 6.1c and Fig. 6.6.

6.5. Modeling results

6.5.1. Angular response curves

Fig. 6.12 shows modeled ARCs at frequencies of 90 and 450 kHz for a layered medium with different layer thicknesses and sediment properties using the layered BS model (Section 6.3.2 and Table 6.2). As a reference, the ARCs of the first and second layer assuming a non-layered model are additionally displayed. The modeling shows that the ARCs at 450 kHz in a layered medium, in general, reflect the surficial sediment. Solely when the surficial layer is very soft (clay) and thin (20 cm), the ARC is slightly affected by the buried coarser layer with higher BS levels at intermediate incident angles (around 3 dB) compared to a non-layered medium. In contrast, the ARCs at 90 kHz are significantly affected by the buried layer. With decreasing layer thickness (1 to 0.2 m) and decreasing coarseness of the upper layer (sandy mud to clay), the BS strength increases and approaches the BS strength of non-layered sandy gravel. Still, it can be seen that the BS strength at 90 kHz in a layered medium results from a combined response of both layers and is therefore not directly representative for one of these layers.

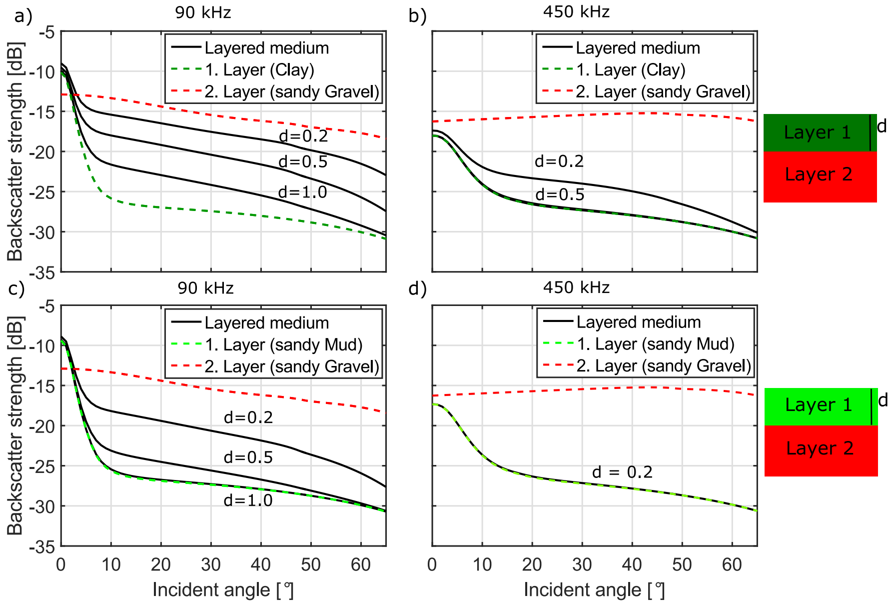

Figure 6.12: Modeled ARCs for a layered medium with varying thickness. a,b) correspond to a clay layer and c,d) to a sandy mud layer above sandy gravel. The ARCs are modeled for a,c) 90 kHz and b,d) 450 kHz. The input parameters are listed in Table 6.2.

The general trend is that for the situations considered, the BS strength decreases with increasing layer thicknesses (0.2 to 1 m), increasing frequency (90 to 450 kHz), and increasing coarseness (clay to sandy mud) compared to the BS of non-layered sandy gravel. These results are mainly caused by an increased sound absorption for higher frequencies and coarser sediments as well as a longer travel distance due to an increased layer thickness. An angular affect can be seen as well where the BS decreases more rapidly with increasing incident angle due to an increased travel path through the sediment layer. The sound refraction into the subsurface has a minor effect because the used sound speeds for clay and sandy mud are very similar to the water sound speed (Table 6.2).

6.5.2. MBES bottom detection in a layered medium

This subsection investigates to what extent the buried layer affects the MBES bottom detection and whether the multi-frequency data can be used to determine the layer thickness. Therefore, Fig. 6.13 displays the simulated MBES bottom detection in a layered medium using the input parameters listed in Tables 6.2 and 6.3.

The modeling shows that for clay sediments the 450 kHz signal detects the surficial seabed only for a large enough layer thickness (> 20 cm). For slightly coarser sediments (sandy mud), it is always the upper layer that is being sensed and the MBES detects accurately the surficial seabed independent of the layer thickness. In contrast, at 90 kHz the signal penetrates into the subsurface and the MBES detects accurately the buried layer for a thin upper layer (20 cm). With increasing layer thickness, the MBES bottom detection fluctuates between the upper and the buried layer dependent on the sediment type and incident angle. For very fine sediments (clay), the bottom detection is closer to the buried layer and for slightly coarser sediments, it is closer to the upper layer.

The modeling results indicate that for specific geological settings (e.g., thin sandy mud layer) the MBES multi-frequency bathymetry data (lowest and highest frequency) can be used to accurately determine the layer thickness for the entire swath. However, for most geological settings the use of the bottom detection at 90 and 450 kHz is rather an indication of layering than an accurate measurement of the layer thickness.

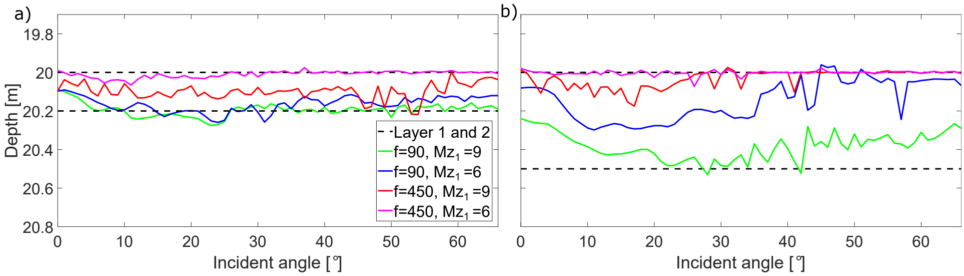

Figure 6.13: Simulated MBES bottom detection in a layered medium with a layer thickness of a) 20 cm and b) 50 cm. Different scenarios are visualized where f indicates the used frequency and Mz_1 stands for the median grain size (Φ values) in the first layer. Mz_1 = 9 approximates clay and Mz_1 = 6 sandy mud. For the second layer sandy gravel (Mz_2 = -1) is assumed. A detailed description of the used bottom parameters and MBES parameters are listed in Table 6.2 and Table 6.3.

6.5.3. Comparison between measured and modeled data

According to the modeling results, the bathymetry difference maps between 90 and 450 kHz (Fig. 6.6) can be used as an indication of the signal penetration and the layer thickness of the upper layer. With increasing layer thickness, the uncertainty increases, and the measured bathymetry difference cannot clearly be related to the layer thickness anymore. At a certain layer thickness, the signal at 90 kHz is fully attenuated and does not reach the buried layer. In such a case the MBES detects the actual seabed and the BS is representative for the surficial sediment (Figs. 6.12 and 6.13). This observation explains the negligible bathymetry difference corresponding to similar BS levels and ARCs among the frequencies for fine sediments, which is observed in the Port of Rotterdam and to some extent in the Vlietland Lake (Fig. 6.9b,e).

Furthermore, the modeling shows that the BS decreases with increasing layer thickness mainly due to the increased sound attenuation in the sediment. The same holds for the experimental data, where we observe a decrease in the BS level with increasing bathymetry difference between 90 and 450 kHz (Subset D in Fig. 6.8a). Without a correction of the BS level for the sound attenuation in the sediment, the measured BS is not directly representative for the buried layer.

The angular dependency of the BS and the bottom detection in a layered medium can also partly be found in the experimental data. For both, experimental and modeled data, the measured bathymetry difference is smallest for incident angles around nadir. According to the modeling results, a decrease in the bathymetry difference between the 90 and 450 kHz data with increasing incident angle is expected (Fig. 6.13b). However, this behavior is only partly observed in the experimental data. Generally, an increase in the measured bathymetry difference between 90 and 450 kHz with increasing incident angle is found in the experimental data (Fig. 6.7b), which contradicts the modeling results. A reason could be that the actual sediment is less attenuating as assumed in the modeling and the signal reaches the buried layer for all angles. Another explanation could be that the water sound speed used for the depth determination in the MBES differs from the actual sound speed in the upper sediment. For example, a layer with a thickness of 30 cm and an 80 m/s higher sound velocity than the water sound speed would result in an MBES bottom detection being 10 cm deeper for the outermost angle than the true depth of the second layer.

In muddy areas, where the experimental data indicate layering, very high BS levels are observed. Fig. 6.9b,c display the ARCs for a muddy area without a measured bathymetry difference and with a difference of 37 cm between 90 and 450 kHz in the Vlietland Lake. The BS level (averaged between 30 and 60°) is 11 dB higher for the muddy area with a significant bathymetry difference at 90 kHz. In the Port of Rotterdam, the averaged BS level is 15 dB higher at 90 kHz for a muddy area with a difference of 40 cm (Fig. 6.9f) compared to the area without a measured bathymetry difference (Fig. 6.9e). For comparison, the modeling results reveal for a layer thickness of 40 cm and for clay or sandy mud above sandy gravel a difference of 9 dB and 2 dB, respectively. The higher BS levels for the experimental data could be explained by the high sensitivity of the model to the input parameters in combination with the high uncertainty in the empirical determination of the input parameters (e.g., absorption coefficient) from grain size measurements. Another possibility is that the buried sediment layer is even coarser than the assumed sandy gravel layer. The geology of the Vlietland Lake indicates that the majority of the buried lakebed consist of coarse sand and gravel, where a concentration of the gravel fraction could yield to an increased BS level. In the Port of Rotterdam, based on the geological information, we expect consolidated mud below a thin layer of unconsolidated mud, which is unlikely to result in such a high observed BS level. Moreover, in muddy sediments anaerobic decomposition of organic matter can cause gas accumulation, which could also result in the very high BS level and also in the prolonged subsurface echo observed for some areas at the lower frequencies (Fig. 6.11). This will be further elaborated in the discussion.

6.6. Discussion

A thorough analysis of two multi-frequency MBES datasets demonstrated significant variation in the measured bathymetries, BS levels, time series signals, and ARCs for fine sediments for the frequency range between 90 and 450 kHz. Similar variation in multispectral BS patterns for fine sediments between 100 and 400 kHz were also observed by Brown *et al.* [36] and Gaida *et al.* [55] (Chapter 5, e.g., Figs. 5.5 and 5.8). They argued that the lower frequency signals were acoustically sensitive to a buried layer of coarse dredge spoils whereas the higher frequencies are only sensitive to the surficial mud layer. In the present contribution, the comparison of the acoustic data with the ground-truthing, geological information, and model simulations indicated that sediment layering is a likely cause for these variations.

6.6.1. Experiments

Except for the spatially limited rheometric profiling in the Port of Rotterdam, the ground-truthing of the subsurface was limited in this study. Ideally, a vibrocoring device, such as used by Brown *et al.* [36], and a more extensive rheometric profiling would have been used. While the coring device provides a physical sample from the subsurface layer, the rheometric profiling takes an in situ measurement of the undisturbed sediment and can be used to accurately quantify the depth of a buried layer. However, logistical and time limitations prohibited the use of these tools in the Vlietland Lake and hampered a more extensive rheometric profiling in the Port of Rotterdam. At the locations where rheometric profiling was conducted, the acoustic data, indicating no layering (Fig. 6.5c and Fig. 6.9d), was in agreement with the rheometric profiling, indicating only a slight gradual increase in density with depth (Fig. 6.8b). Unfortunately, subsurface density measurements, where the acoustic data indicated layering, was not available.

Still, we argue that the geological information and the acoustic time series signal are an indication of the presence of layering at these locations. Visualizing the time series signal in a sub-bottom image (Fig. 6.11), presents an approach to employ a MBES in the same way as a classical sub-bottom profiler. While this works around nadir (0° beam angle), for oblique beam angles the beamforming results in a spread echo envelope and a greater impact of sidelobe effects.

Furthermore, in this study, we could not finally exclude a shallow biogenic gas layer as a possible cause for the very high BS values and the partly extraordinary shape of the ARCs at 90 kHz. For example, in a study by Schneider von Deimling *et al.* [137], averaged BS levels of 13 dB higher for muddy sediments with gas compared to muddy sediments without gas were found. In addition, a unique gas-mediated ARC pattern was observed with no angular change towards the outer beams for gassy sediments. Although a 12 kHz MBES was used in a water depth of around 90 m and the gas pockets were about 5 m below the seabed, these findings are very similar to the observations in this study. In contrast, Fonseca and Mayer [15] showed for a 95 kHz MBES an average difference of only 4 dB at a water depth of 151 m and almost no difference at 39 m between sites with and without gas. The partly contradicting results indicate the difficulty in drawing general conclusion across site- and system-specific measurements in gassy sediments.

6.6.2. Modeling

By comparing the experimental observations with the modeling results, we showed that layering has a significant effect on the measured multi-frequency data and that the bathymetry difference maps can be at least used as an indicator of the layer thickness. However, the model also showed how sensitive the MBES bottom detection is to the sediment properties, in particular, the sound attenuation, and the incident angle. Here, it needs to be stressed that the geophysical input parameters, representing different sediment types are based on the empirical equations developed by Hamilton [44] (c, ρ, and α) and recommendations by the APL-model [40] (γ, η, and $\hat{\sigma}_v$) in combination with the grain-size analysis of the Van Veen samples. How well these empirical equations and recommendations represent the actual geophysical parameters in the present study site are unknown and direct measurements would be more accurate. For example, stereo photography can be used to determine the seabed roughness (γ and η) and specifically designed measurement equipment can be employed to measure sediment sound speed c and attenuation α, as shown by Thorsos *et al.* [152]. As the quality of the sediment characterization improves, the model accuracy increases [40]. Determining the roughness parameters for the buried layer remains still difficult and an empirical relation between roughness parameters and median grain size is still required. For our modeling approach, we assumed a sediment type for the buried layer based on geological information, which generates an additional uncertainty. This was, as previously mentioned, due to a missing coring device and the fact that the used Van Veen sampler only acquires roughly the first 10 to 20 cm of a muddy seabed.

A more general concern related to the employed models is the extension of the validity range for higher frequencies. According to Jackson et al. [49], the APL-model is valid between 10 and 100 kHz. The limitation is mainly caused by the roughness scattering model. For example, the Kirchhoff and composite roughness approximation used to model the roughness scattering in the APL-model requires an acoustically relative smooth interface [49] (Section 2.2.3 and Appendix B). It means that the radii of the curvature of the scattering interface must be smaller than the acoustic wavelength, which might be violated at high frequencies. However, we argue that the focus in this study is mostly on muddy sediments. Such fine sediments have a smoother interface than those encountered for coarse sediments. In addition, volume scattering dominates over interface scattering for the majority of the angular range [49] (e.g., visualized in Fig. 2.5, Section 2.2.3). Based on these arguments, the modeling at higher frequencies ($>$ 100 kHz) is assumed to be applicable in this study.

Another simplification in the bottom detection model is related to the volume scattering contribution to the received pressure signal. The bottom detection model simulates a spatially and temporally discretized acoustic signal, considering transmission and reception at the MBES and sound propagation in the medium. The scattering is modeled using the APL-model. In the APL-model [40], the volume BS is treated as an interface process and can be characterized in the same terms as the roughness scattering [6]. It follows that the volume scattering is associated with the same location as the interface scattering although the volume scattering is originated from the underlying volume. That means that the bottom detection model accounts for the contribution of the volume scattering but the actual location and the corresponding time is biased. A solution could be a discretization of the sediment volume and the calculation of volume scattering at distinct locations in the sediment volume, as it was proposed by Sternlicht and de Moustier [75].

6.7. Conclusion

This study investigates the effect of frequency-dependent signal penetration on multi-frequency BS and bathymetry data. Two multi-frequency datasets were acquired with the multispectral mode of an R2Sonic 2026 MBES at two different study sites. The BS mosaics, the angular response curves and the time series of the acoustic signal were analyzed with respect to the measured bathymetry and frequency. Additionally, we proposed a model to simulate the bottom detection of a MBES in a layered medium.

The analysis of the experimental datasets showed that low-frequency BS and bathymetry data (90 to 100 kHz) measured in fine sediments can be highly affected by an increased signal penetration in combination with subsurface layering. The measured BS and bathymetry at the high frequencies (300 to 450 kHz) are representative for the surficial sediments while at low frequencies (90 to 100 kHz) the BS and the bathymetry varies with the presence of a subsurface layer, either in the form of coarser sediment or gas accumulation. The modeling indicated that, in case of shallow sediment layering, the low-frequency BS level is strongly linked to the layer thickness and corresponds to a combined acoustic response of the surficial and the buried sediment layer. Due to an unknown sound attenuation and refraction in the sediment layer, the BS cannot directly be related to the buried layer. The modeling indicated that an accurate determination of the layer thickness is only possible for relatively thin layers ($\sim$20 cm). For thicker layers, the bottom detection varied with incident angle and sediment properties of the upper layer and an accurate determination of the layer thickness was hampered.

The findings provide an enormous potential but also pitfalls for multispectral MBES. The capability to acquire data with a low and high frequency allows to identify layering and to asses the influence on the measured BS data. Using a monochromatic MBES, transmitting only at a low frequency, the acquired BS and bathymetry data would lead to an erroneous interpretation of the surficial sediment properties and an incorrect determination of the water depth. However, if the signal penetration and a possible scattering at buried structures are not considered, multispectral MBES data can also lead to misinterpretation of the surficial sediments. Therefore, it is highly recommended to analyze multi-frequency BS in conjunction with the inter-frequency bathymetry difference and ideally with the time series signal. The measured bathymetry per frequency can be incorporated into classification techniques to develop an approximate 3D image of the surficial and subsurface sediments. Future work requires more ground truth information, in particular from the subsurface, to improve the validation of the measurements and the bottom detection model.

7

Geostatistical modeling of multibeam backscatter for full-coverage seabed sediment maps

The previous chapters have focused on the use of multibeam backscatter (BS), either monochromatic or multispectral, for mapping and monitoring sediment distributions. The BS data were used in acoustic sediment classification methods to objectively and automatically produce sediment maps. However, multibeam BS datasets are often sparsely distributed due to weather conditions, time restrictions, budget limitations or inaccessibility of certain areas. In this chapter, sparsely distributed multibeam data, acquired in the Cleaver Bank (The Netherlands) and already utilized in Chapter 3, are employed and different Kriging algorithms to interpolate these datasets are tested and evaluated. A new approach to classify the interpolated BS data based on the Bayesian method for producing a full-coverage sediment map is introduced. A comprehensive comparison between the acoustic classification maps and a traditional sediment map is carried out and their accuracy is tested based on the ground truth data.

This chapter has been published in Hydrobiologia **845** (1), 55-79 (2018) [62].

7.1. Introduction

Increasing human activities in the marine environment, such as fisheries or dredging, affect seabed habitats worldwide [153–157]. The impacts depend on the magnitude and frequency of the human activities, and vary with the marine ecosystem in which they occur [158]. To assess the anthropogenic impact on the seabed ecosystem and to develop suitable management strategies it is necessary to identify the spatial variability of benthic habitats. Driving factors of the distribution and abundance of benthic communities, and hence important for habitat mapping, are the seabed substrate and grain-size distribution [159]. Marine in situ measurement techniques (e.g., grabs, cores and underwater video footage) reveal detailed information of the sediment properties and generate, in general, an accurate representation of the local seabed. However, the density and coverage of bed sampling is not always sufficient to represent the sediment heterogeneity on the required spatial scales.

In the last decade, different research fields have advanced remote sensing methods to overcome the limitations in spatial and temporal information of the seabed. One of the most rapidly developing research fields is acoustic sediment classification (ASC), where acoustic remote sensing techniques, such as side-scan sonar (SSS), singlebeam echosounder (SBES) and multibeam echosounder (MBES) are used to investigate the seabed (e.g., [7, 8, 76, 160–162]. Extensive experimental and theoretical research about acoustic scattering shows that the acoustic echoes from the water-sediment interface contain information about the seabed [6]. Accounting for the effect of environmental conditions (e.g., absorption) and sonar settings (e.g., signal strength, beam pattern), the backscatter (BS) strength can be retrieved from the acoustic echo received by the MBES. The BS strength is dependent on the acoustic frequency used, angle of incidence on the seabed and seabed properties, allowing for sediment characterization based on acoustic measurements [6, 76]. In particular the MBES is a powerful tool due to the simultaneous acquisition of both BS and bathymetry data. MBES measurements are very time efficient compared to in situ measurements and are of high spatial resolution (in the order of decimeters to tens of meters, depending on the system configuration and on the water depth) [76]. The acoustic BS, bathymetry and second order features (e.g., slope, rugosity, standard deviation, etc.) are used either individually or in combination for the discrimination of the seabed characteristics and the production of sediment or habitat maps [8].

Despite the variety of acoustic classification studies there is still a lack of seabed sediment maps for a large part of the world oceans. The reasons are manifold, for example: i) lack of time and budget for MBES surveys, ii) inclement weather, iii) solely acquisition of bathymetry without storage of BS, iv) lack of discrimination power in the signal close to nadir, v) inaccessible marine environments due to hazards, navigation restrictions, renewable energy devices or marine conservation requirements. This indicates the need for suitable interpolation and classification techniques for sparsely distributed MBES BS data to generate full-coverage sediment maps.

In addition, techniques able to combine multiple sources of information about the seabed from primary or secondary sources, e.g., samples, bathymetry or historical sediment maps, are highly important. The European Union established the European Marine Observation and Data Network (EMODnet) to process marine data from disparate sources according to international standards and to eventually make the products freely available to marine data users. Data layers are generated with respect to Bathymetry, Geology, Seabed Habitats, Chemistry, Biology, Physics and Human Activities. EMODnet Geology provides, among other, datasets with information on the seabed substrate of the European marine areas [82]. The seabed substrate maps are generated by harmonizing existing national maps [163], by interpolating existing sampling data or by expert knowledge in combination with the above approaches. The geological services of Norway, the United Kingdom and Ireland established a multidisciplinary national mapping program including acoustic measurements and ground-truthing to produce seabed substrate maps based on ASC. They are collaborating to advance methods and practice in seabed mapping through sharing of knowledge and methods.

The seabed sediment maps of the Netherlands Continental Shelf (NCS) are in general, besides a few local studies (e.g., [13, 19]), based on traditional geological mapping where grab samples and shallow cores in conjunction with bathymetry and seismic information are used [37, 38, 79]. Still, a few large-scale seabed mapping studies, including the NCS and based on machine learning techniques or geostatistical interpolation methods, were carried out. Stephens and Diesing [21] used a Random Forest algorithm to predict seabed sediment composition in combination with grain-size data and several environmental predictors (e.g., bathymetry or current velocity with a resolution of 0.5 to 12 km) in the North Sea. Wilson *et al.* [164] extended their approach to produce sediment compostion maps of the entire northwest European Shelf (including the NCS) by applying the Random Forest algorithm in regions with sparse data coverage and combining the results with the output of spatial interpolation in regions with extensive data coverage. Verfaillie *et al.* [165] assessed different methods (e.g., Kriging with external Drift (KED)) for the interpolation of the median grain size of the sand fraction at the Belgian Continental Shelf. Maljers and Gunnink [166] extended their KED approach by interpolating the full grain-size distribution curves allowing for the extraction of NCS maps of all separate fractions as well as for the derivations, for example, the sand median (d_{50}). Bockelmann *et al.* [167] produced full-coverage maps of the mud content and the sediment median grain size (d_{50}) for the entire North Sea using among other KED. All of these studies used bathymetry as external-drift variable. A recent comprehensive study reflecting Dutch efforts to improve seabed sediment maps of the NCS using ASC is presented in Chapter 3 [61]. In the presented study, sparsely distributed 300 kHz MBES BS data acquired in five surveys from 2013 to 2015 at the Cleaver Bank, NCS, were employed to investigate the repeatability of MBES BS-based sediment classification. An unsupervised ASC method, called the Bayesian sediment classification method [13], was used to classify the surficial sediments.

With the present-day urge for large-scale mapping, and to understand and identify the spatial and temporal distribution of benthic organisms, it is essential to consider the small-scale information and the broad environmental setting as well [168]. For this it is necessary to understand the benefits of ASC methods and integrate them into the available traditional seabed sediment mapping methods, as it is already done for some areas in the EMODnet framework. In this contribution, we address this integration for the Cleaver Bank area (NCS). We use the sparsely distributed MBES BS data collected during surveys from 2013 to 2015 and bed samples taken in the period from 2000 to 2015. Hence, the aims of this study are defined as follows:

The first aim is to assess the capability of geostatistical modeling, i.e., Kriging interpolation techniques, to overcome and evaluate two issues that can hinder full-coverage acoustical mapping: (a) the MBES data can be restricted to inconsistent survey lines due to time and budget limitations or weather conditions, and (b) the BS data acquired at nadir have limited discrimination power and therefore cannot be used for ASC, resulting in gaps within the sonar swath. Aim 1 thus focuses on the potential of creating a full-coverage map based on sparse MBES BS data. Therefore, different Kriging techniques are applied to the sparsely distributed MBES BS data and a new approach is introduced to classify interpolated MBES BS data based on the Bayesian sediment classification method.

The second aim is to compare the sediment maps obtained from ASC, based on solely MBES BS, and Kriging interpolated MBES BS, respectively, with the existing seabed sediment map in the Cleaver Bank area, which is mainly based on traditional ground truth data. Aim 2 thus focuses on issues that are of importance when integrating the ASC maps with traditional geological maps. An important issue that we additionally address is the current physical limitation of ASC, concerning its ability to discriminate between the coarser sediment types.

7.2. Study area and data

7.2.1. Current seabed sediment maps (NCS)

Currently used seabed substrate maps of the NCS are available at the EMODnet-Geology data portal [169], the Interreg IIIb project MESH (Mapping European Seabed Habitats) [170] or provided by Stephens and Diesing [21] and Maljers and Gunnink [166]. Fig. 7.1a shows the seabed sediment map from the entire North Sea with a nominal scale of 1000 m by 1000 m in which the sediments are classified into five sediment classes. The sediment classes are based on a simplified reclassification of the Folk scheme [83]. Fig. 7.1b displays a sediment map of the Cleaver Bank area with a finer nominal scale of 250 m by 250 m and a classification into 14 Folk classes, although only seven classes are present in the present area [169]. This sediment map is based on grab samples and shallow cores where the sediment boundaries are manually refined with bathymetry and seismic information [37, 38]. Both maps are downloaded from the EMODnet website [169] but only the fine-scale map of Fig. 7.1b is used for a comparison in this study.

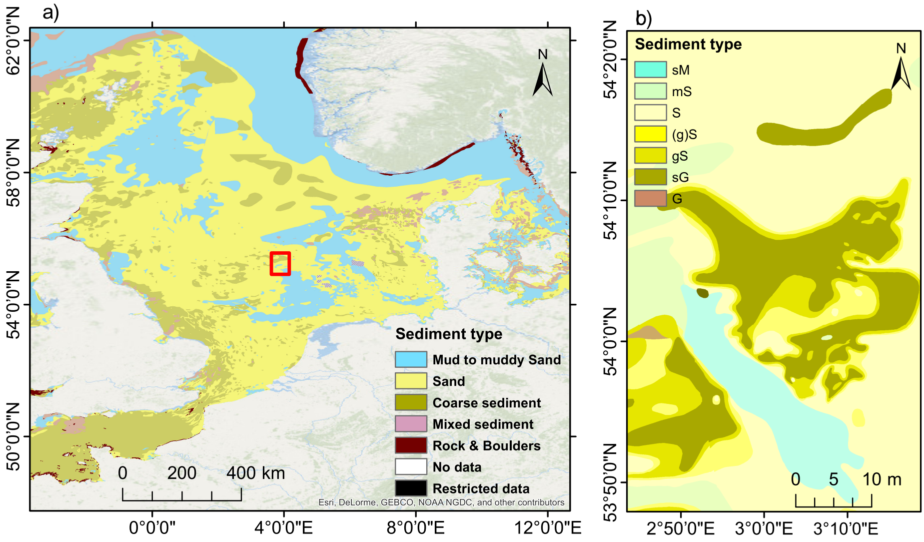

Figure 7.1: a) Sediment map of the North Sea based on different mapping methods and datasets . The nominal scale is 1000 m by 1000 m. b) Seabed sediment map of the Cleaver Bank based mainly on ground truth data [169]. The sediment classes are defined after Folk [83]. The nominal scale is 250 m by 250 m. The Cleaver Bank area is marked by the red square in a).

7.2.2. Acoustic classification map based on MBES backscatter

The acoustic mapping of the Cleaver Bank is presented in Chapter 3. The Bayesian classification method and the PCA in conjunction with k-mean clustering were applied to MBES BS data. The acoustic sediment classification map based on the Bayesian method is shown in Fig. 7.2. Seven acoustic classes (ACs) were identified where partly multiple sediment types (Folk classes) are assigned to one AC. Since the MBES survey track lines are separated by up to 1500 m and the BS data around nadir cannot be used for sediment classification, the final ASC map contains large data gaps (Fig. 7.2).

7.2.3. Ground truth data

The grab sample dataset, as used for the current research but not used for the maps of Fig. 7.1, consists of 104 Hamon and Van Veen grab samples and is already introduced in Section 3.2.3. The analysis of the grab samples resulted in eight sediment types after the Folk [83] scheme: sandy Mud (sM), muddy Sand (mS), Sand (S), gravelly muddy Sand (gmS), slightly gravelly Sand ((g)S), gravelly Sand (gS), muddy sandy Gravel (msG), sandy Gravel (sG). Three grab samples are classified as gmS (2) and (g)S (1). These are neglected during the following analysis because two individual samples are not sufficient to perform a correlation analysis and a validation test. In addition, one grab sample was considered untrustworthy due to inaccurate positioning. The remaining 100 grab samples are divided into three sets: (1) 46 grab samples (square symbol) are used for the assignment of

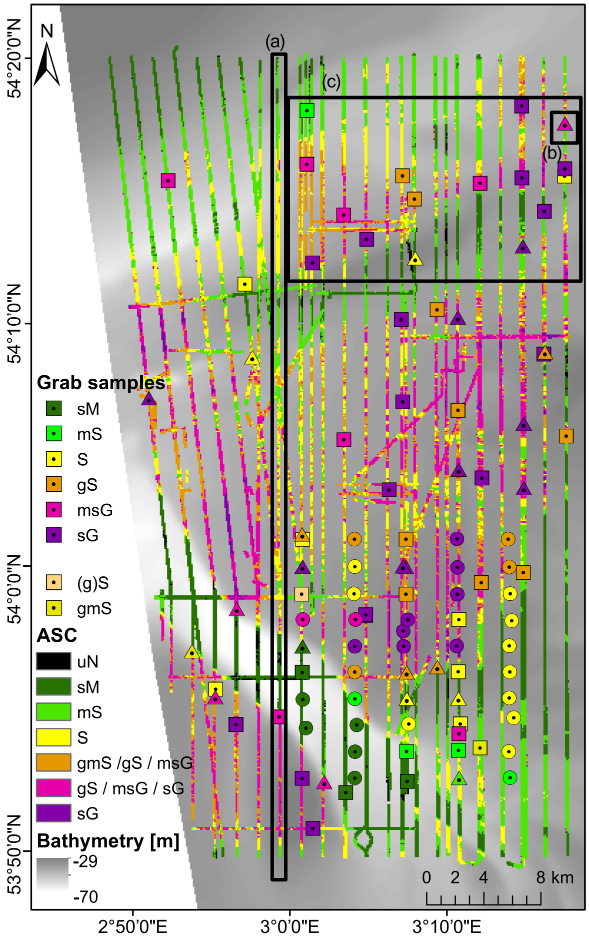

Figure 7.2: Acoustic sediment map of the Cleaver Bank with a resolution of 3 m by 3 m obtained with ASC, using the Bayesian classification method (see 3). Grab sample symbols assign each sample to the following set: assignment of sediment types to ACs (square), validation test for ASC (triangle) and interpolated ASC (circle). The background bathymetry is displayed in a grey gradient. Location of the Cleaver Bank is indicated by the red rectangle in Fig. 7.1a. Black rectangles (a), (b) and (c) will be referred to later in the chapter.

sediment types to ACs; these samples represent an arbitrary selection of 70 % of the samples located on or very close (< 25 m) to the survey track lines; (2) 23 grab samples (triangle symbol) are used for validating this assignment; these samples represent an arbitrary selection of 30 % of the samples located on or very close (< 25 m) to the survey track lines; (3) 31 grab samples (circle symbol) are used for assessing the predictive performance of Kriging and the EMODnet map; these grab samples are located between track lines with a distance to a track line of 25 to 750 m (Fig. 7.2).

In addition, video footage was collected during the MBES surveys in 2013 and

2015. The cameras were equipped with two parallel-orientated sizing lasers to scale the observations at the seabed. The video footage is qualitatively analyzed and subjectively labeled with respect to the Folk classification, since a more quantitative analysis is hampered by the unsteady height of the camera system above the seafloor and the varying particle suspension affecting the visibility[1].

7.3. Methods

7.3.1. Kriging and Cokriging

Kriging is a geostatistical interpolation technique used to predict surfaces from a limited amount of sample data and to assess the uncertainty of these predictions [171]. In this study, we use Kriging to predict MBES BS for locations without acoustic measurements. The general equation is

$$\hat{Z}(s_0) = \sum_{i=1}^{n} \tilde{\lambda}_i Z(x_i) \tag{7.1}$$

where $\hat{Z}(s_0)$ is the predicted value at an unsampled location s_0, Z is a measured value at the sampled location x_i, n is the number of considered samples within the interpolation neighbourhood and $\tilde{\lambda}_i$ is the weight assigned to the measured sample i for predicting $\hat{Z}(s_0)$. A particular strength of the Kriging method is that $\tilde{\lambda}_i$ is not only calculated using the distance from the measured to the predicted location but also accounts for the spatial arrangement of the measured data points. A variogram analysis is the first step for obtaining the Kriging weights $\tilde{\lambda}_i$. The so-called semivariogram $\tilde{\gamma}(\tilde{h})$ represents the average variance between the observations separated by a certain distance, and describes the structure of the spatial variability of the investigated variable [172]. The semivariogram is calculated as [173]

$$\tilde{\gamma}(\tilde{h}) = \frac{1}{2N(\tilde{h})} \sum_{i=1)}^{N(\tilde{h})} \left(Z(x_i + \tilde{h}) - Z(x_i)\right)^2 \tag{7.2}$$

where N is the number of pairs of sample points separated by the distance $\tilde{h}$. The data from this distance interval $\tilde{h}$ are binned into lag classes. The size and the number of the lags are chosen according to the study area. However, the semivariogram will in general not provide information for all possible distances. Therefore, it is necessary to fit a semivariance model (e.g., spherical, exponential, stable etc.) to the semivariogram. The type of the model is selected based on the nature of the data. For creating the semivariogram we follow roughly the rule of thumb where the product of lag size and number of lags should be about half the largest distance among all points [165]. For the dataset considered this means that the semivariogram is created using a lag size of 1000 m and the number of lags is set to 20. Finally, the Kriging weights $\tilde{\lambda}_i$ are determined by solving a set

---

[1] The description of the geological setting of the Cleaver Bank, published by Gaida *et al.* [62], is moved to Section 3.2.1.

of equations (Kriging system) including the knowledge of the semivariance model [174].

In geostatistical modeling, sampled data are considered as the result of a random process. Consequently, the predictions are always associated with some probability or uncertainty. To this end the Kriging system is expressed as follows

$$\hat{Z}_1(s_0) = \tilde{\mu}_1 + \varepsilon_1(s_o) \tag{7.3}$$

where $\hat{Z}_1$ is the estimated variable at location s_0, decomposed into the deterministic trend $\tilde{\mu}_1$ and the random, auto-correlated error ε_1 at location s_0. The different Kriging methods are variations on Eq. (7.3). Ordinary Kriging (OK) estimates $\tilde{\mu}_1$ for each interpolation neighbourhood separately, where it is assumed to be locally constant. Simple Kriging (SK) assumes $\tilde{\mu}_1$ to be known for the entire area, where it is assumed to be globally constant. By contrast, Universal Kriging (UK) describes $\tilde{\mu}_1$ with a deterministic function.

Cokriging allows to incorporate secondary variables, in order to improve the predictions. For example, bathymetry may be used as additional information in sediment mapping (e.g., [165]). Hereto, a second equation is needed for the integration of a second variable

$$\hat{Z}_2(s_0) = \tilde{\mu}_2 + \varepsilon_2(s_o) \tag{7.4}$$

where $\tilde{\mu}_2$ is a second unknown constant in case of Ordinary Cokriging (OCK). Two random errors ε_1 and ε_2 are now used and for each of these values both an auto-correlation and cross-correlation have to be calculated. OCK tries to predict $Z_1(s_0)$ in the same way as OK, but uses the additional information of the covariate $Z_2(s_0)$. For the Simple, Ordinary and Universal Kriging and Cokriging, we used the geostatistical toolbox of ArcMap10.3.

Validation of Kriging interpolation

Three measures, i.e., the prediction standard error (PSE), the root mean-square estimation error ($RMSE$) and the root mean-square standardized estimation error ($RMSSE$), are used to evaluate the prediction and the corresponding uncertainties of the interpolation.

The uncertainty of the Kriging prediction is given by the PSE or also noted as $\sigma(s_0)$ (smaller values indicate better predictions). This value is obtained from the solution of the Kriging system. It is defined as the standard deviation of the differences between the true and the estimated value. For instance, if the data are normally distributed the true value falls within the interval of the estimated (+/-) PSE values with a probability of 95 %. The $RMSE$ and $RMSSE$ are calculated by a cross-validation where one data sample is removed and the remaining data samples are used to estimate the removed data sample. The $RMSE$ indicates how well the algorithm predicts the observed values. The output value has the same unit as the observation. The $RMSE$ is written as follows

$$RMSE = \sqrt{\frac{1}{D}\sum_{i=1}^{D}\left(\hat{Z}(x_i) - Z(x_i)\right)^2} \tag{7.5}$$

where D is the number of all samples used for the interpolation. The lower the $RMSE$ value the better the prediction accuracy. To assess the reliability of the uncertainty, the $RMSSE$ is used. Thereby, each estimated error is divided by its prediction standard error $\sigma(x_i)$ at the sampled location x_i

$$RMSSE = \sqrt{\frac{1}{D}\sum_{i=1}^{D}\left(\frac{\hat{Z}(x_i) - Z(x_i)}{\sigma(x_i)}\right)^2}. \tag{7.6}$$

$RMSSE$ should be close to one if the prediction standard errors are valid. If the $RMSSE$ is greater than one, the variability in predictions is underestimated. If $RMSSE$ error is less than one, variability in predictions is overestimated.

7.3.2. Classification of interpolated MBES backscatter based on the Bayesian method

The workflow to produce a full-coverage sediment map from sparsely distributed MBES BS data is visualized in Fig. 7.3. The first step is the interpolation of the measured MBES BS data to retrieve a full-coverage BS map using Kriging. This is carried out for a specific beam angle and for each survey separately. The boundaries of the ACs defined by the Bayesian method per beam angle and survey are used to obtain AC maps from the interpolated BS data (see step 2, Fig. 7.3). A detailed description on how the AC boundaries are defined is given in Section 3.3.2. The seabed slope in the Cleaver Bank area is relatively small (< 5°), therefore, the difference between the beam angle and the actual incident angle can be neglected and thus we use beam angles in our classification. Considering each survey separately provides acoustic maps independent of e.g., acoustic-instrument stability or sonar settings. The interpolated AC maps obtained from different surveys are merged by evaluating the PSE (see step 3, Fig. 7.3). For each grid cell the interpolated results exhibiting a lower PSE are used for the merged AC map. Finally, the classification results obtained from the application of the Bayesian method to the actual MBES BS measurements are compared to grab samples (see step 4, Fig. 7.3). Based on their correlation, the assignment of sediment types to ACs is carried out.

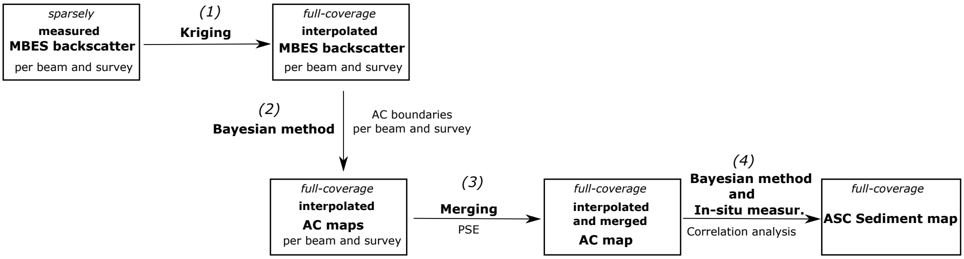

Figure 7.3: Workflow to produce a full-coverage ASC sediment map from sparsely distributed MBES BS data.

Quantitative comparison of ASC and current sediment maps with in situ measurements

Finally, to test the reliability of the sediment maps and to perform a quantitative comparison, error matrices are used. The error matrix provides different measures of accuracy, i.e., overall and individual accuracies and a Kappa coefficient of agreement [175]. The overall and individual accuracies describe the portion of correctly assigned sediment types by considering all samples and only samples of a specific sediment type, respectively. The Kappa coefficient accounts, in addition, for the likelihood of coincidental agreement.

7.4. Results

7.4.1. Geostatistical modeling

The Kriging methods are applied to the MBES BS data acquired in 2013 and 2014-2015 separately. The BS data retrieved from the beam angle of 48° (+/- 1°, 47° - 49°) at starboard side are used for the interpolation. These beam angles have high discrimination power and appeared to have low noise. An optimal fit to the semivariance of the observed data is obtained by using the exponential and stable semivariance model for Kriging and Cokriging, respectively. Cokriging uses full-coverage bathymetry data with a grid cell size of 100 m as a secondary variable. In order to find a suitable interpolation method for the generation of full-coverage sediment maps of the MBES data, we compare the results of OK, SK, UK as well as OCK, SCK and UCK. From the *RMSE* and *RMSSE* values it is found that the Cokriging methods perform slightly better than the Kriging. The different Kriging techniques Ordinary, Simple and Universal perform almost equally well with respect to the *RMSE* and *RMSSE* values (Table 7.1).

Table 7.1: Evaluation of six different interpolation techniques with respect to the application to the MBES BS data acquired in 2013 and 2014/2015. OK, SK, UK, OCK, Simple Cokriging (SCK) and Universal Cokriging (UCK) are tested. The *RMSE* and *RMSSE* are used for the evaluation of the predictions and corresponding uncertainties. The first value corresponds to the 2013 dataset and the second to the 2014/2015 dataset.

	OK	SK	UK	OCK	SCK	UCK
RMSE	1.27/1.09	1.31/1.09	1.27/1.09	1.00/0.78	1.01/1.09	1.04/0.81
RMSSE	0.72/0.75	0.67/0.75	0.72/0.75	1.68/0.99	1.99/0.75	1.04/0.83

To further investigate the slightly better performance of the Cokriging methods, the correlation between bathymetry and BS for the 2013 and 2014/2015 data is shown in Fig. 7.4. The Pearson Correlation Coefficient $\hat{R}$, a standard measure of linear bi-variate correlation (i.e., between two variables), indicates a very weak correlation for the 2013 data ($\hat{R}$ = 0.16) and a medium correlation for the 2014/2015 data ($\hat{R}$ = 0.61) between bathymetry and BS. The varying correlation between the datasets is caused by the fact that the datasets cover different seabed areas. It shows that the correlation between bathymetry and BS strongly depends on the location in the study area. In the study of Asli and Marcotte [176] a better performance for SCK and OCK over SK and OK is observed for a correlation coefficient > 0.4. That would indicate an improved performance by incorporating bathymetry only for the 2014/2015 datasets. However, these observations are not reflected in the performance test using the $RMSE$ and $RMSSE$. There is no significant difference between the OK and OCK performance from the 2013 to the 2014/2015 dataset observed.

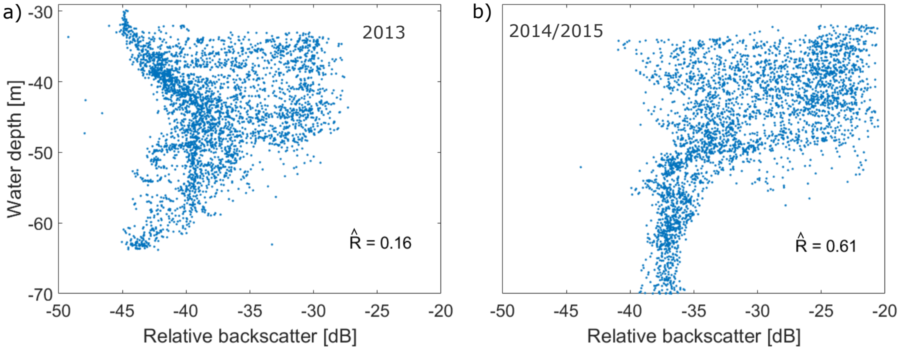

Figure 7.4: Relationship between water depth and BS for the a) 2013 and b) 2014/2015 MBES BS dataset.

To get insight into the added value of bathymetry data in predicting BS in between the track lines, which is not captured by the $RMSE$ and $RMSEE$ that only consider a single eliminated measurement, we removed a full track line from the dataset. In Fig. 7.2 the removed track line is indicated by the black rectangle (a). The Pearson correlation coefficient between predictions and actual values is 0.74 and 0.75 for both OK and OCK, respectively. This indicates no significant improvement by incorporating bathymetry as a secondary variable for predicting the BS values in between the track lines. Considering these results, the computational time and that the BS data can be seen as a variable without a constant mean, we selected OK as the most suitable interpolation method for MBES BS in our study area.

The interpolated BS map for the 2013 and 2014/2015 data using OK and the MBES BS from all track lines is visualized in Fig. 7.5a and Fig. 7.5d. The uncertainty of the OK predictions are represented by the PSE in Fig. 7.5c and Fig. 7.5f. The uncertainty map shows that the most reliable predictions are achieved on the survey track lines (PSE = 0 dB) and that uncertainty increases with distance to the MBES track lines (PSE = 2 - 3 dB). Locations close to multiple or crossing survey lines show lower uncertainties, demonstrating more reliable predictions caused by an increase of MBES data. PSE values above 3 dB in these maps show untrustworthy predictions, due to the total absence of data and resulting data artefacts, such as those found at the eastern border of the 2014/2015 data.

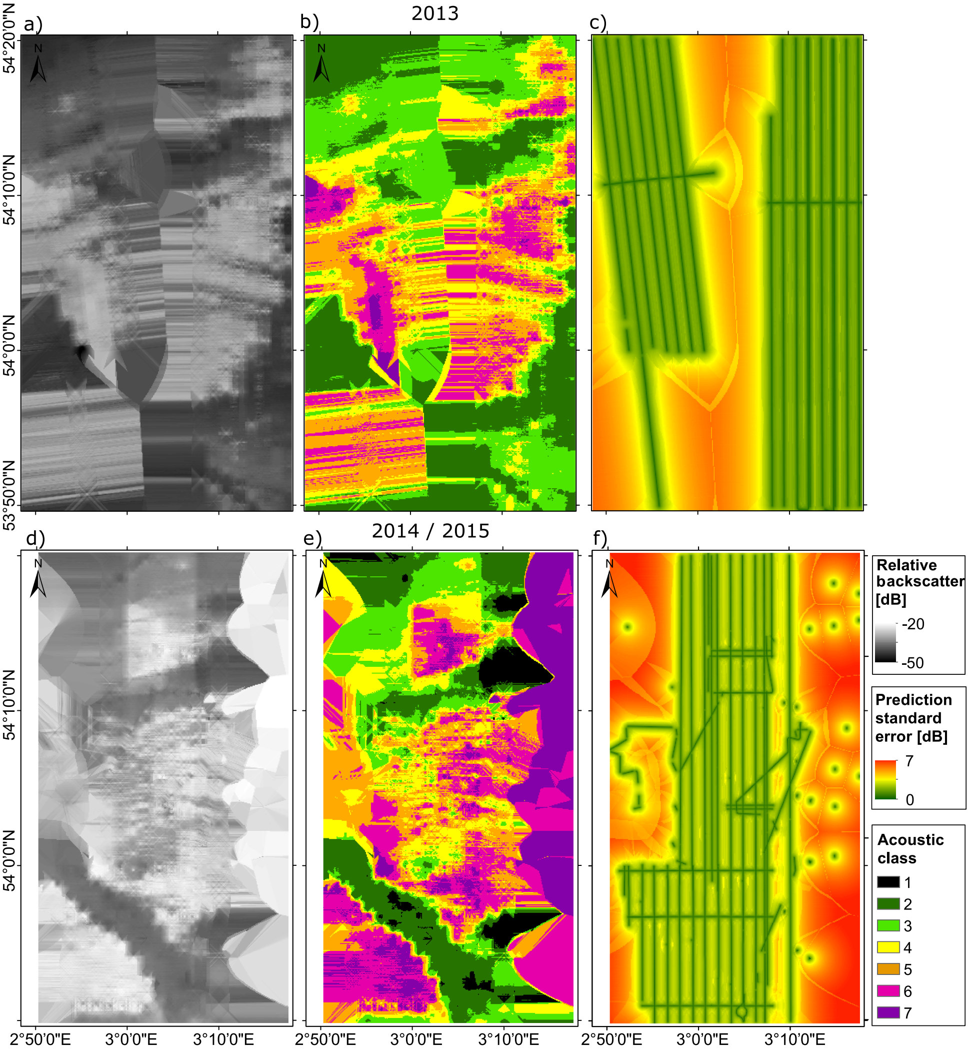

Figure 7.5: OK interpolated full-coverage MBES BS map and corresponding *PSE* map for the a), c) 2013 and d), f) 2014/2015 BS dataset, respectively. MBES BS from the 47° to 49° beam angle of all track lines are included within the interpolation. b), e) AC map received from the classification of the full-coverage MBES BS map using the Bayesian results (see Table 7.2).

7.4.2. Generation of the map presenting acoustic classes

The outcomes from the Bayesian method are used to produce an AC map from the interpolated BS data (see step 2, Fig. 7.3). The boundaries of the 7 ACs for the BS data of the 48° beam angle, which are used to classify the BS data into distinct classes, are shown in Table 7.2. The classification of the BS data into classes based on the Bayesian method allows for the merging of the results from 2013 and 2014/2015 to a single map. The production of the single maps is based on the *PSE*, which are shown in Fig. 7.5c and Fig. 7.5f (see step 3, Fig. 7.3). The individual AC maps obtained from the 2013 and 2014/2015 datasets are displayed in Fig. 7.5b and Fig. 7.5e, respectively. The merged AC map is shown in Fig. 7.6a. A number of small stripe artefacts in N-S direction are remaining in the merged AC map. These artefacts occur in overlap regions of the 2013 and 2014/2015 data due to the probability of misclassification per AC for each dataset.

To test the influence of different beam angles and different datasets on the ASC, the AC boundaries for the 54° (+/- 1°, 53° - 55°) beam angle are listed in Table 7.2 as well. Table 7.2 shows that the boundaries differ per beam angle and per dataset. It demonstrates the importance of applying the interpolation and acoustic classification to each beam angle and dataset separately. To test the validity of our approach, where only the BS data from a specific beam angle range is used and the datasets are considered separately, the interpolated and merged AC map of the 54° beam angle is visualized in Fig. 7.6b.

Table 7.2: AC boundaries for both the 2013 and 2014/2015 MBES BS datasets of the 48° and 54° beam angles in decibels. The boundaries are obtained from the application of the Bayesian classification method to the datasets. For further insights into the determination of the class boundaries see Section 3.3.2 and Section 3.4.1.

Beam	Dataset	1	2	3	4	5	6	7
48°	2013	-∞/-45.6	-45.6/-40.9	-40.9/-37.9	-37.9/-34.3	-34.3/-30.9	-30.9/-28.7	-28.7/∞
	2014/2015	-∞/-37.9	-37.9/-35.1	-35.1/-32.4	-32.4/-29.4	-29.4/-25.7	-25.7/-22.9	-22.9/∞
54°	2013	-∞/-45.7	-45.7/-42.4	-42.4/-39.1	-39.1/-36.2	-36.2/-33.2	-33.2/-30.0	-30.0/∞
	2014/2015	-∞/-39.9	-39.9/-36.7	-36.7/-32.2	-32.2/-28.4	-28.4/-25.4	-25.4/-21.7	-21.7/-∞

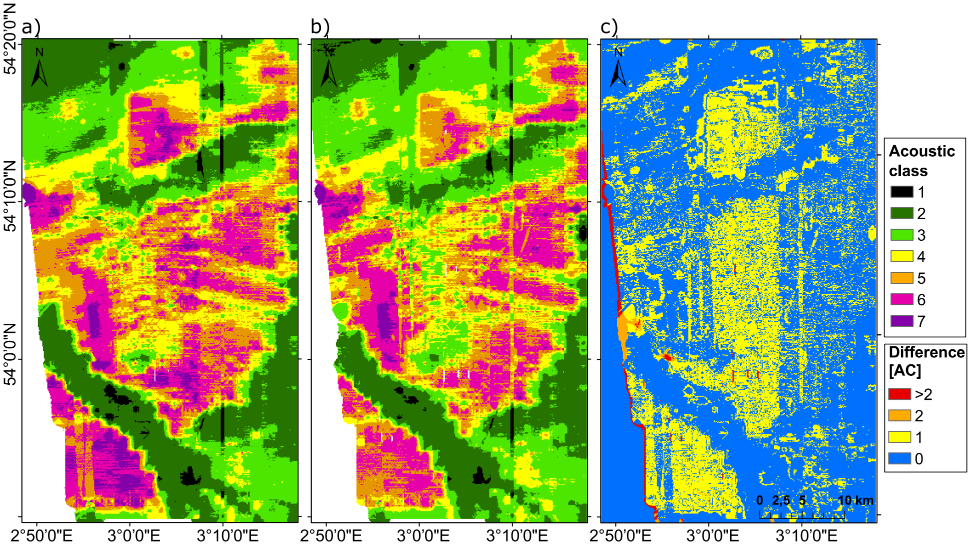

Figure 7.6: AC map received from the MBES BS of the a) 48° and b) 54° beam angles. c) Map showing difference in ACs between the maps visualized in a) and b).

Both maps show the same pattern (Fig. 7.6a and Fig. 7.6b) and the lower classes (2-4, green to yellow) correspond well. However, only in areas represented by high ACs (5-7, orange to purple) a difference of up to one AC is visible (yellow in Fig. 7.6c), where the ACs of the 54° beams are generally lower than those of the 48° beams. Also, these differences are more prominent for the 2014/2015 data (Fig. 7.6c). Factors contributing to the difference are both the interpolation of the BS values and the intrinsic probability of misclassification due to the overlap of BS corresponding to the ACs. In addition, different beam angles might sense different substrate/sediment classes on the seabed. In the next section the focus will be on sediment type instead of AC where the results are compared with in situ measurements.

7.4.3. Conversion from acoustic class to sediment map

As a first step towards integrating the ASC results into sediment maps (in general displaying Folk class), the ACs have to be converted to Folk classification scheme. The approach taken uses the original ASC results (not interpolated), since the seabed area represented by grab samples is much closer to the spatial resolution of the original ASC results (3 m by 3 m, gridded) compared to the interpolated ASC results (100 m by 100 m, gridded).

Fig. 7.7 displays the relationship between ACs and 46 grab samples (AC at the grab sample location is determined by counting the most frequently occurring AC within a radius of 25 m around the grab sample). The order of Folk classes attempts to represent increasing median grain sizes. A general correspondence between increasing AC to increasing median grain size is observed. AC_1 is not sampled and cannot be assigned to a sediment type (labeled with 'uN'). AC_2, AC_4 and AC_7 correspond mainly to sandy mud, sand and sandy gravel, respectively.

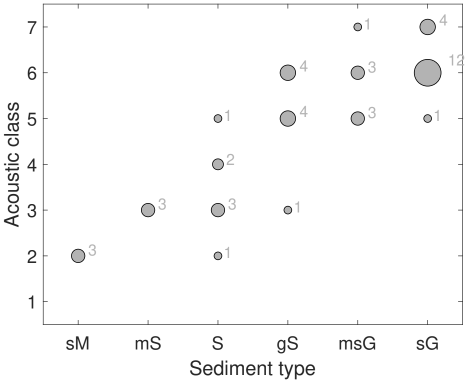

Figure 7.7: Correlation plot between AC and sediment type (Folk, 1954) using the 46 grab samples and the ACs obtained from the Bayesian classification method.

All other ACs indicate some ambiguity in the relationship between sediment type and AC, e.g., where an individual AC is assigned to two or three different Folk classes or where one Folk class is represented by several ACs overlapping with another Folk class representation. These results are slightly different from the assignment of Folk class to AC in Section 3.4.4 (Fig. 3.10), using the ungridded ASC results and 72 grab samples instead of the gridded ASC results and only 46 samples. In the previous section sand was only assigned to AC_4 compared to classes 3 and 4 here.

The final assignment of Folk class to AC is shown in Table 7.3. Using the 23 independent grab samples to validate the assignment of Folk classes to ACs results in an overall accuracy of 83 % and a Kappa coefficient of 0.55, indicating good agreement with the grab samples. It is noted that the performance to discriminate between individual Folk classes is lower for the coarser sediments (sand to gravelly sand) compared to the finer sediment (sandy mud to muddy sand).

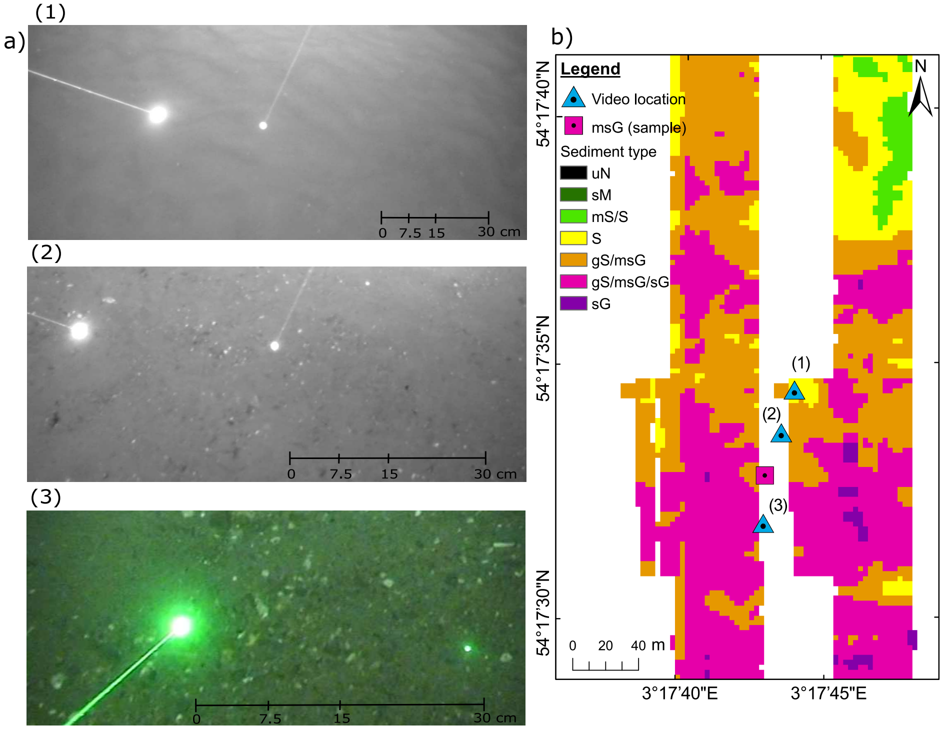

Figure 7.8: (a) Video footage recorded at location (1), (2) and (3). The video footages are subjectively labeled as (1) sandy bed, (2) slightly gravelly bed and (3) gravelly bed. (b) Small area of the sediment map based on ASC with a resolution of 3 m by 3 m. The location of that area is marked by a black rectangle (b) in Fig. 7.2. The video footages are marked by blue triangles. White area indicates no data for ASC.

To further test the assignment of sediment type to ASC results, the results are qualitatively compared to the video footage. Here, it is visualized on a representative example in Fig. 7.8. There is a good overall qualitative agreement between acoustic classification and video footage, where both the acoustic classification and the video footage indicate an increase in gravel content from location 1 to 3. Based

Table 7.3: Assignment of Folk class to AC. ACs are obtained from applying the Bayes classification method, as previously described in Section 3.3.2. The abbreviations are defined as unassigned (uN), sandy Mud (sM), muddy Sand (mS), Sand (S), gravelly Sand (gS), muddy sandy Gravel (msG), sG (sandy Gravel).

Sediment type	'uN'	sM	mS	S	gS	msG	sG
Acoustic class	1	2	3	3-4	5-6	5-6	6-7

on the visual inspection, the assignment to sand for video imagery 1, to gS or msG for video imagery 2 and to gS, msG or sG for the video imagery 3 is plausible, even if the mud content is hardly recognizable and a distinction between mud and sand is not feasible based on the video footage.

Based on the validation test and the verification with video footage, it can be concluded that the assignment of Folk classes to AC is reliable, but, as seen in Table 7.3, not unique. The approach is used to convert the interpolated ASC results to a full-coverage sediment map (Fig. 7.9a).

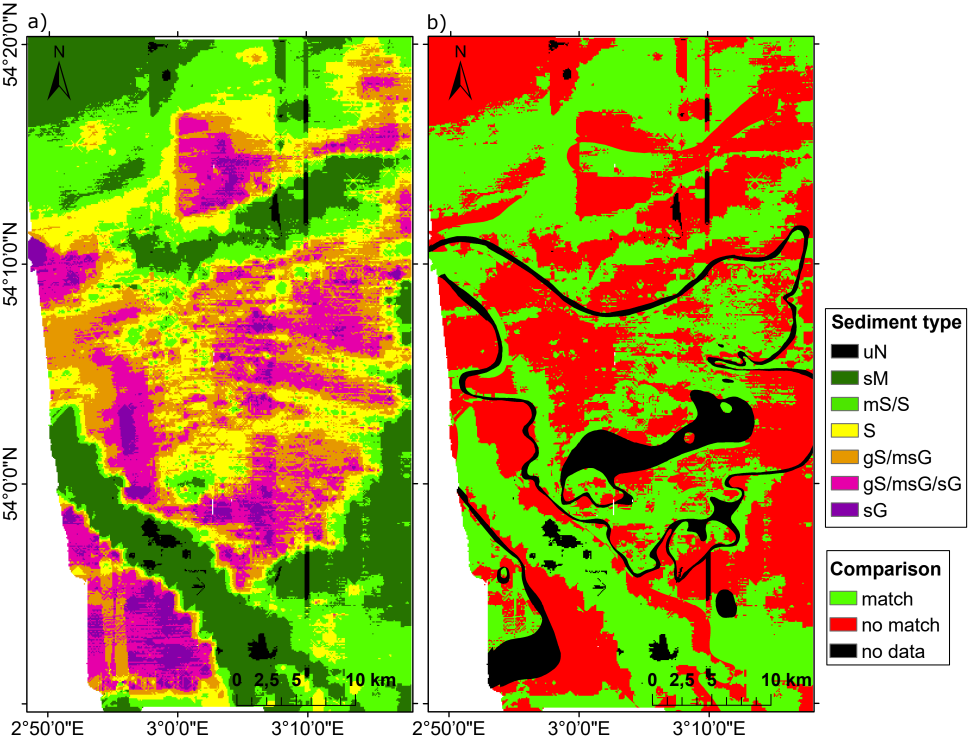

Figure 7.9: a) Full-coverage sediment map (ASC map) based on interpolated AC map (Fig. 7.6a) and 46 grab samples (Table 7.3). b) Map comparison between full-coverage sediment map (Fig. 7.9a) and the existing EMODnet seabed sediment map (Fig. 7.1b). "No data" implies either the Folk sediment type is not available in one of the maps or an AC is unassigned in the interpolated ASC map.

Comparison of the interpolated ASC and traditional sediment map

In this section, we will qualitatively assess the accuracy of the interpolated ASC (Fig. 7.9) and EMODnet sediment map (Fig. 7.1b) by using the remaining 31 independent grab samples. Table 7.4 presents the results of comparing the 31 grab samples with the two sediment maps. The OK achieves an overall accuracy of 65 % and a Kappa coefficient of 0.50. This indicates fair agreement between the samples and the map. These values are similar for those obtained by the EMODnet map (65 % and 0.54). Regarding the individual accuracy for both maps, the Botney Cut (sM) is resolved equally well (both 100 %). The EMODnet fine-scale map shows especially good agreement with the areas indicated by sand in the samples, whereas the interpolated ASC map indicates better agreement for muddy sand and the coarser sediment samples. The latter is partly due to the necessity of assigning multiple types to a single AC to account for the ambiguity in the relation of sediment type to AC. This approach comes along with a decrease in discrimination power between the individual sediment types.

Table 7.4: Error matrices using 31 grab samples for a) EMODnet sediment map and b) interpolated ASC sediment map.

	Grab samples						
Folk class	sM	mS	S	gS	msG	sG	Total
a)							
sM	5	0	0	0	0	0	5
mS	0	0	0	0	0	0	0
S	0	2	9	0	0	0	11
(g)S	0	0	0	0	0	2	2
gS	0	0	0	2	0	2	4
msG	0	0	0	0	0	0	0
sG	0	0	1	2	2	4	9
Total	5	2	10	4	2	8	31
Individual accuracy	100 %	0 %	90 %	50 %	0 %	50 %	
Overall accuracy	65 %		Kappa coefficient			0.54	
b)							
1 (–)	0	0	0	0	0	0	0
2 (mS)	5	0	4	0	0	0	9
3 (mS/S)	0	1	3	0	0	0	4
4 (S)	0	1	2	2	0	0	5
5 (gS/msG)	0	0	1	1	0	1	3
6 (gS/msG/sG)	0	0	0	0	1	5	6
7 (sG)	0	0	0	1	1	2	4
Total	5	2	10	4	2	8	31
Individual accuracy	100 %	50 %	50 %	25 %	50 %	88 %	
Overall accuracy	65 %		Kappa coefficient			0.50	

As a final step in this section, we quantitatively compare the interpolated ASC and EMODnet sediment maps (Fig. 7.9b). The comparison reveals an overall agreement of 51 %. As in the previous assessment (Table 7.4), the comparison map shows that for the Botney Cut in particular, a very good agreement is found, where both maps indicate sM which also matches with the grab samples. However, in other parts of the maps where sM was assigned in the ASC map, differences occur where sediments were in general assigned to sand in the EMODnet map (Fig. 7.1b). Further disagreements are linked to the larger sediment heterogeneity in the ASC map in the gravelly sand and sandy gravel classes, and may thus actually be an important improvement (see Discussion). These types of differences should be accounted for when integrating the ASC maps into the existing sediment maps of the NCS and are discussed in the following sections.

7.4.4. Relationship between backscatter values and grain-size fractions

In the previous section, we aimed to reduce the ambiguity related to the assignment of AC to sediment type by assigning multiple sediment types to an AC (adapted from Chapter 3). To further investigate this issue, the relationship between actual BS value and sediment properties is considered. In Section 3.5.2, the ambiguity was analyzed with respect to the relationship between BS and the median grain size. In this study, we investigate the relationship between BS and individual grain-size fractions to identify grain sizes causing the ambiguity with respect to the used system wavelength. For this, we use the grain-size distributions of the 77 grab samples which are located on or close (< 25 m) to the MBES track lines. The BS values are averaged over a maximum radius of 25 m around the grab sample. To take into account imperfect sonar calibrations and the angular dependency of BS, we used normalized BS values between -1 and 1 where the angular dependency is eliminated [97]. Fig. 7.10 shows the normalized BS values as a function of three measures of grain-size fractions (fine, medium, coarse). The first measure considers grains smaller than 0.5 mm and thus smaller than the acoustic wavelength of the MBES (5 mm). The second measure focuses on grain sizes roughly around the acoustic wavelength from 0.5 to 16 mm (here called the medium fraction). The last measure considers the percentage of grains larger than 16 mm. Fig. 7.10a shows a negative correlation between BS values and the percentage of the fine fraction ($<$ 0.5 mm). Fig. 7.10b illustrates a positive correlation between BS and percentage of the medium (0.5 – 16 mm) fraction. This shows that an increase in the amount of grains similar to the acoustic wavelength is positively correlated to BS. However, considering Fig. 7.10c a slight decrease in BS values with increasing percentage of grain sizes coarser than 16 mm is observed. This observation is contrary to the common assumption that coarser sediments are more likely to result in higher BS strength [66, 177]. It indicates that in particular the amount of very coarse grains (coarser than 16 mm using an MBES with a frequency of 300 kHz) might induce the ambiguity. In addition it shows that there is no one-to-one relationship between grain size and BS for the entire grain-size spectrum.

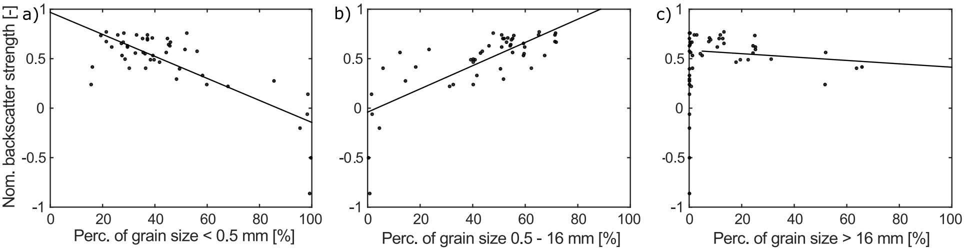

Figure 7.10: Correlation between normalized BS values and weight percentage of grain-size fraction. a) fine fraction: clay to medium sand (< 0.5 mm), b) intermediate fraction: coarse sand to medium gravel (0.5 – 16 mm) and c) coarse fraction: coarse gravel and larger (> 16 mm). The dots represent the measurements and the line shows the linear regression results. In c) only the measurements with a percentage ≥ 5 % are used for the linear regression.

7.5. Discussion

7.5.1. Geostatistical modeling

The performance tests and validation with independent sediment samples in this study show that geostatistical modeling, such as Kriging or Cokriging, is a suitable tool to fill the data gaps in MBES BS measurements to achieve full-coverage maps (Fig. 7.9a). The performance of the OK, SK and UK techniques do not differ significantly. Regarding UK the reason might be that the BS data do not have a global trend. In that regard UK fits a constant value to the data, the same as OK, instead of a deterministic polynomial function (Eq. (7.3)). The relatively small difference between the SK and OK performance indicates that the choice of the stationarity of the deterministic trend (global or local) does not have a strong impact (see Section 7.3.1). We did not use anisotropic Kriging, since the BS data are not directed in any way.

In general, the values of the error matrices indicate that the Kriging results are reliable, considering that other studies using geostatistical modeling and supervised ASC achieved similar overall accuracies ranging from 65 to 80 % and Kappa coefficients between 0.3 and 0.6 [20, 161]. Although several studies have shown that the use of bathymetry in geostatistical modeling improves the prediction of seabed sediment distribution [165, 166, 178], importing bathymetry as a second variable did not improve the prediction performance in our study on ASC bed classification, where a correlation analysis reveals a low correlation between BS and bathymetry. Similar results were found in Bockelmann *et al.* [167], where the evaluation of the map confidence indicated no significant improvement by using KED (incorporating bathymetry as a secondary variable) compared to OK. Even though bathymetry, hydrodynamics and sedimentary processes control the sediment distribution in the marine environment, pre-existing coarser sediments (e.g., due to a glacial history) do not always comply with present-day marine sedimentation processes. This implies that the successful application of multivariate geostatistical modeling depends on the local conditions of the study area. To account for complex geological processes, which has influenced the current sediment distributions on the seabed, we may need other interpolation methods allowing the use of arbitrarily-complex forms of regression, for example Regression-Kriging [167, 179].

In the present study only the BS data from a specific, highly discriminative, beam angle range is considered for obtaining an interpolated full-coverage map. The need for this approach can be explained by Table 7.2, where a large difference in BS values of the AC boundaries between the different datasets (i.e., 2013-2014 and 2015) and beam angles (i.e., 48° and 54°) is seen. This is due to the facts that (1) the BS is dependent on the incident angle [6], (2) the datasets from 2013-2014 and 2015 cover a different seabed area but also that, (3) e.g., acoustic-instrument stability, environmental conditions or survey methods might have changed between the surveys and post-processing was not able to account for these factors. Alternatively to account for the first issue, the angular effect can be removed allowing the use of the full range of BS measurements for the interpolation. However, this would hamper the comparison between ACs determined from different uncalibrated MBES BS datasets because the relative BS values are not directly comparable.

7.5.2. Comparison of the ASC, interpolated ASC and traditional sediment map

In the quantitative assessment, the different performance of the interpolated ASC and EMODnet sediment maps was not apparent. To further investigate the differences between the ASC, the interpolated ASC and EMODnet maps, we qualitatively compare a certain area of the Cleaver Bank in more detail, visualized in Fig. 7.11. It is shown that the OK method is capable of mapping more detailed seabed sediment heterogeneity (orders of km's) than the EMODnet map. Both maps show a different pattern for the coarser sediments in that area (Fig. 7.11a and Fig. 7.11b). The easterly and south-westerly located grab samples indicating msG or sG are in agreement with the interpolated ASC map (except two samples) but do not agree with the EMODnet map. A closer examination in Fig. 7.11c demonstrates that the Bayesian method is able to resolve fine-scale spatial heterogeneities (orders of tens of meters) indicated by the agreement of the sG bed sample with the revealed gravelly patch located within a relatively homogeneous area of muddy sand (green). This coarse sediment patch is resolved neither in the interpolated ASC nor in the traditional EMODnet sediment map.

The success in predicting seabed sediments via interpolation methods depends amongst other things on the relation between the spatial distribution of the measurements and the seabed heterogeneity. The larger the seabed heterogeneity the higher the measurement density needs to be. MBES BS provides a high and regularly-spaced sample density. However, the sample density can be partly considered as artificially high because the measurements are clustered along the track lines. Clustering of samples can even yield to a reduced accuracy of Kriging methods [180]. However, the regularly-spaced MBES BS measurements have the advantages that without any a-priori knowledge, sediment heterogeneities are sampled in a more systematic way. This is in contrast to interpolation based only on sediment samples. They are often a collection from different sources and therefore often randomly distributed and appear in clusters. This results in a varying spatial resolution

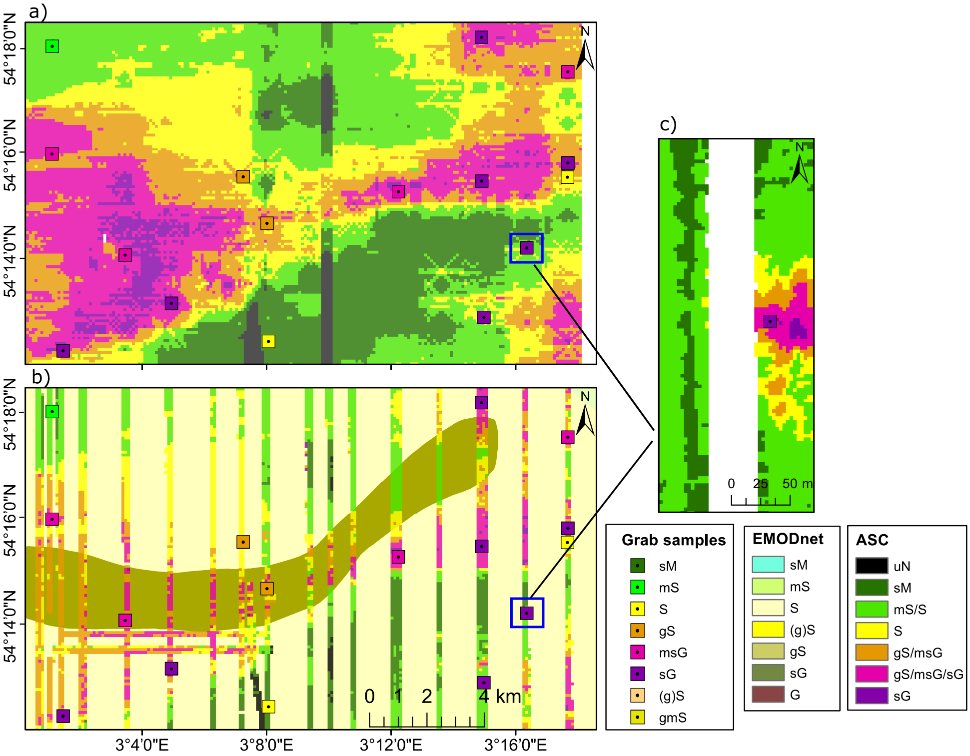

Figure 7.11: Subset of the sediment maps obtained from a) OK combined with Bayesian method (interpolated ASC) and b) high-resolution ASC, using the Bayesian method plotted on top of the EMODnet map. The EMODnet map has a nominal scale of 250 m by 250 m and the interpolated ASC has a grid size of 100 m by 100 m. The high-resolution ASC has a grid size of 3 m by 3 m. The location of the area is marked by a black rectangle (c) in Fig. 7.2. c) Subset of the high-resolution ASC sediment map.

of the interpolated map and increases the likelihood of omitting certain sediment patches. The seabed heterogeneity varies within the marine environment and the sediment type due to the physical processes of sediment transport and deposition. For example, Buscombe *et al.* [134], showed that, in a river environment, typical length scale or distance over which sediment types occur was larger for finer sediments than coarse sediments, and that immobile sediments had the shortest length scales. In our study area these observations are visible in Fig. 7.2. Fine sediments, indicated by low ACs (low BS values), are homogeneous and occur in extensive areas, e.g., Botney Cut, NW and SE of the Cleaver Bank (see Fig. 7.2), whereas areas with high ACs appear to be more heterogeneous. The remaining coarse and less mobile glacigenic sediments are sparsely distributed, redistributed or partly overlain by more recent marine sediments, possibly yielding to the patchy pattern of the coarse sediments. Geostatistical methods account for the above mentioned spatial dependency of sediments by modeling the spatial distribution of the observations [181]. Consequently, the probability to map sediment heterogeneities in between the adjacent MBES track lines is increased, indicating the advantage over deterministic interpolation methods. In general, the prediction of the fine sediments in the Cleaver Bank area can be considered as more reliable compared to the coarser sediments.

7.5.3. Integration of different sediment maps

A quantitative comparison between the interpolated ASC and the EMODnet sediment map reveals an overall agreement of 51 % (Fig. 7.9b). In particular, it is important to deal with the areas of disagreement to be able to successfully integrate ASC results into existing sediment maps. In order to do so the strengths and weaknesses of the different methods need to be addressed. Table 7.5 presents a qualitative overview of the uncertainties related to sediment maps based on in situ measurements and ASC. The interpolation of in situ measurements results mostly in high uncertainties due to the limited amount of samples, whereas MBES BS provides large data coverage enabling interpolation with low uncertainties. The assignment of sediment type to in situ measurements can be very precise. However, a low uncertainty still exists caused for example by a potential washing out of the fine fraction or the inability of the sampling equipment to retrieve the coarse fraction. Due to the physics of acoustic scattering a clear assignment of BS values or ACs to sediment type is hampered as indicated in Fig. 7.10. In addition, the uncertainty corresponding to the assignment of sediment type to in situ measurements has to be added to the ASC as well because these sediment types are used for the assignment to the AC.

Table 7.5: Qualitative overview of uncertainties in the production of sediment maps. In the literature, no values are readily available for the interpolation step in case of seabed cores/samples, i.e., traditional mapping (upper left box) or for the uncertainty due to the sampling methods (upper right box). For the sediment classification based on acoustic measurements, values in this study show good performance in both the assignment of sediments to acoustic classes (lower right box) and the interpolation techniques (lower left box). The symbol [-] indicates that no uncertainty value was found in literature.

	Interpolation	Assignment
In situ measurements	*High* [-] [37, 38, 165, 166]	*Low* [-]
Acoustic classification	*Low* 18.9 % = 1 AC difference [this study] 0.1 % $\geq$ 2 AC difference [this study]	*Moderate* 17.0 %, $\kappa = 0.64$ [this study] 20-35 %, $0.3 < \kappa < 0.6$ [161]

For a full integration of both maps the uncertainties need to be spatially quantified. A first step is taken in this contribution where we found 17 % of global uncertainty (equal to 83 % overall accuracy) along the track lines for the assignment of sediment type to AC based on 23 independent samples. This value is a first estimate of the contribution belonging to the lower right box (Table 7.5). This uncertainty is relatively low indicating a reliable assignment. One explanation is that in the assignment of sediment type to AC the uncertainty is at least partly accounted for by assigning multiple sediment types (Folk class) to one AC. The 83 %

overall accuracy indicates that this is a way to reduce the uncertainty related to the assignment of sediment properties to acoustic data. However, it also implies a lower discrimination between different sediment types. Fig. 7.5c and Fig. 7.5f indicate an uncertainty of up to 2.5 dB (PSE) between the track lines. Using the PSE and AC boundaries (Table 7.2) for the 2013 and 2014/2015 dataset, the average prediction uncertainty for the AC map is estimated. On average there is an uncertainty of 19 % for the entire survey area that the ACs are expected to deviate by one AC. This is an estimate of the contribution of the lower left box in Table 7.5. It is not possible to quantify the uncertainties of the EMODnet map (in situ measurements) due to lack of information (upper left box, Table 7.5).

Due to the lack of local uncertainties, here, a focus is on the differences between the interpolated ASC map and EMODnet map as a first step towards integrating the maps. Fig. 7.12 shows the areas where the two maps correspond and differ. For the latter, we defined three types of areas, indicated by

(A) the zones where sM is classified on the ASC map and S on the EMODnet map (A1, A2 and A3)

(B) differences due to heterogeneity of the seabed sediments,

(C) zones where a larger extent of the distributions of coarser sediments are identified on the ASC map (C1, C2 and C3)

In area A1 no samples are available in this study, so classification is based on BS (see Fig. 7.2). Jeffery *et al.* [38] highlight that the one sample used for the traditional map is more than 1 km away. In area A3 the ASC classification of sM is contradicted with all ground truth samples (Fig. 7.2, revealing sand (S), which corresponds to the EMODnet map (Table 7.4 confirms the higher individual accuracy for sand in the EMODnet map). Still, the acoustic classification clearly indicates lower BS values in the acoustically measured data. For area A2 not only this study indicates lower BS and low ACs but also a study carried out in 2004 and based on a SBES campaign reveals similar results [16]. This implies that the surface properties may differ from sediments in the grab samples. For example fluid mud may affect acoustic BS [32]. In side-scan sonar observations in the swales of two offshore sand ridges on the NCS, van Dijk *et al.* [122] showed that muddy veneers over coarse rubble and thin sand veneers on clay both result in mottled acoustic facies of low BS intensity. To resolve this issue, additional samples should be taken, using a closed box corer instead of an open Van Veen sampler, since the latter is known to underestimate mud content [182].

In area B the ASC map represents high spatial heterogeneity of coarse-grained sediments, supported by sediment samples. The individual accuracy for msG and sG in Table 7.4 and the example in Fig. 7.11 corroborate these findings. Although the number of samples in the traditional map, on which the EMODnet map is based, seems sufficient in the east of area B, the main sG area in the western part of area B (olive in Fig. 7.12b) is largely void of samples [38].

In area C1 both maps indicate coarse sediments. However, the area is positioned slightly differently in the two maps and the ASC identifies a larger area of coarse

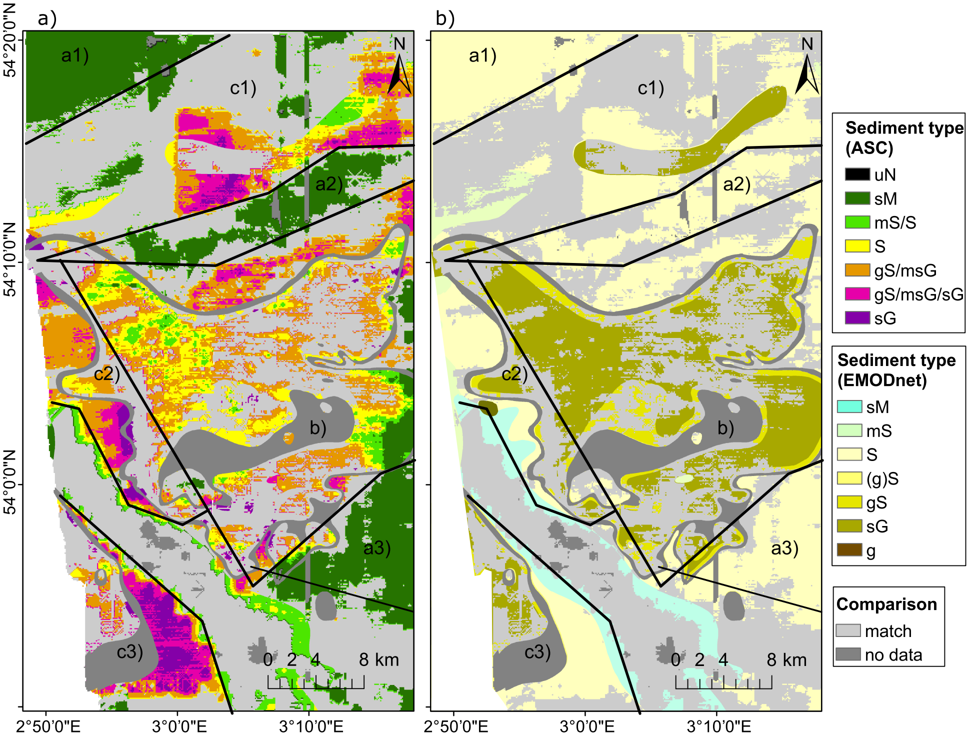

Figure 7.12: Comparison maps displaying sediments in areas where discrepancies exist between a) interpolated ASC and b) EMODnet sediment map.

sediments, which are corroborated by samples (see Fig. 7.11a and Fig. 7.11b). For area C2 coarse sediments were not identified in the EMODnet map (sM/mS), whereas these were identified in the ASC map. In that area two samples indicating coarse sediments plead for the ASC map. For area C3 the coarse sediment region is less extensive in the EMODnet map, in which parts were labeled as S, where the ASC map classified gS/msG/sG. These coarser sediments were corroborated by 6 out of 6 samples (Fig. 7.2, see also Table 7.4 for msG and sG where ASC performs better). In general, it can be concluded that for the areas where the two maps differ, the ASC maps represent spatial heterogeneous areas better, but more samples are needed to further assess the differences.

In case more knowledge on uncertainties of produced seabed maps are available, regions of high accuracy and low uncertainties could be determined. These regions can be further used as training and validation datasets for supervised and unsupervised classification methods applied to newly acquired MBES datasets. Lark *et al.* [178] proposed the geostatistical linear mixed model (LMM) as an approach to incorporate new available MBES data into existing sediment maps. This procedure would lead to an update of seabed maps using datasets that allow higher spatial resolutions. In this approach the information contained in the existing maps (e.g., EMODnet) would be considered as fixed (categorical) variables and the new datasets (e.g., BS) are considered as continuous covariates to generate an updated map with higher spatial resolution.

7.5.4. Current limitation of ASC based on MBES backscatter

Despite the major advantages of ASC in sediment mapping, at its current stage BS-based ASC is hampered by its restricted ability to assign sediment type (e.g., Folk class) to a distinct AC, in particular, for coarser sediments (S to sG).

It is shown that specific grain-size fractions affect the BS differently in this study and no one-to-one relationship between grain size and BS for the entire grain-size spectrum exists (Fig. 7.10). Therefore, for example, sediments with a high percentage of large grains (> 16 mm) might result in the same BS values as sediment containing mainly small grains (< 0.5 mm).

These insights are useful in understanding the relationship between BS and specific sediment properties and subsequently to generate an appropriate classification scheme for the assignment of sediment properties to AC. However, we need to consider that the BS strength is dependent on other seabed properties such as sediment bulk density, seafloor roughness, volume heterogeneity, discrete scatterers and sediment layering [6, 32, 63] even if several studies have shown a strong relationship to mean grain size, grain-size distribution or shell or gravel content for a specific study area [64–68]. By investigating the influence of mean grain size for well-sorted sediments on BS strength, under ideal laboratory conditions, Ivakin and Sessarego [31] observed a transition from positive to negative correlation where the fraction between mean grain size and acoustic wavelength exceeds 1. The authors hypothesized that the decrease might be explained with the appearance of a different dominating scattering regime. Buscombe *et al.* [134] described this situation as a mixed Rayleigh-geometric regime where a transition from Rayleigh to geometric scattering occurs. With increasing acoustic frequency the sediment (with a specific grain size) cannot be described as a continuous medium anymore and the individual grains have to be considered as discrete scatterers. This demonstrates the strong influence of the transmitted frequency on the relationship between BS and the presence of coarse grains. Similar observations were found by Eleftherakis *et al.* [19]. Buscombe *et al.* [134] postulated that the lack of discriminatory power in the gravel fraction was due to the transitional scattering regime. However, the organic content (e.g., remaining seagrass fragments [66, 70]), or small-scale topography (scales comparable or smaller than the signal footprint, and therefore below the resolution of the beam footprint) have an influence on the BS as well and might affect the results [109] (e.g., addressed in Section 4.4.1). This knowledge is crucial for efforts aiming to increase the discrimination performance. Recent studies have demonstrated that multispectral BS data indeed reveal that areas, showing the same acoustic responses for one frequency, differ in the acoustic response of a second frequency [33, 140] (see also Chapters 5 and 6). This implies that the use of different frequencies might be an appropriate approach to improve seabed sediment classification [33] and resolve ambiguities.

7.6. Conclusion

This study introduces an approach to interpolate BS data available along MBES trajectories with large track spacing and their classification into distinct ACs based on the Bayesian sediment classification method. It was shown that the Kriging techniques Ordinary, Universal and Simple perform almost equally well, and that due to a lack of a global trend with the depth, incorporating bathymetry as a second variable in Cokriging did not improve the interpolated map. The AC map was converted to a sediment map displaying Folk classes by using grab samples. When quantitatively comparing the resulting interpolated ASC Folk class map with sediment samples, an overall accuracy of 65 % was obtained; a similar value was obtained when evaluating a more traditional sediment map with the same samples (from EMODnet). However, a qualitative comparison pleaded for a better performance of the interpolated ASC map. This was indicated by more precisely mapped seabed sediment heterogeneities in an order of km's. The evaluation of the high-resolution sediment map obtained from the Bayesian method, which employs the actual BS, demonstrated that mapping laterally heterogenic sediments was improved up to an order of meters.

Considering the increasing use of ASC efforts and the large amount of existing traditional sediment maps, we aimed to integrate ASC into existing sediment maps, in order to optimize sediment mapping. A manual integration revealed that the knowledge of the spatial distributions of the uncertainties of each map is of high importance. The uncertainties in the interpolated full-coverage ASC sediment map were due to both the Kriging interpolation of the MBES BS data and the assignment of sediment to AC. For the EMODnet map the uncertainties were not known. A successful automatic and objective integration would lead to improved marine seabed sediment maps with higher spatial resolution and quantified uncertainties. The improved sediment maps advance marine habitat mapping since sediment types are one of the main driving factors for the distribution of benthic organisms.

The study reiterates the shortcoming of the ASC method, caused by the fact that no one-to-one relationship exists between grain size and BS for the entire grain size spectrum in our study area. This ambiguity reduces the discrimination between sediments and therefore needs to be accounted for during the integration. The dependency of the relationship between grain size and BS on acoustic frequency has been described in the literature and provides a way to mitigate the effect of the ambiguity on the acoustic classification. Multispectral BS classification is therefore considered as an important future research area to optimize ASC methods.

8

Conclusion and outlook

8.1. Conclusion

In this thesis, the potential of single- and multi-frequency multibeam backscatter (BS) data for mapping and monitoring marine sediments has been investigated. According to the research objectives, the conclusion is divided into three subsections that summarize the general findings, emphasize the scientific relevance and illustrate the limitations of this research.

1. Investigation on the applicability of repetitive MBES BS measurements for environmental monitoring of the seabed.

The thesis has shown that unsupervised classification methods, namely the Bayesian classification and principal component analysis (PCA) in conjunction with k-means clustering, allow to employ multibeam echosounder (MBES) BS measurements over time. Despite the use of different ships and MBES systems, repeatable sediment classification results were retrieved from five MBES surveys carried out in a time period of 15 months in the Cleaver Bank (The Netherlands), indicating the applicability for monitoring the seabed. Considering that the Cleaver Bank represents a temporal stable study area, this study focused on the repeatability of BS-based sediment classification rather than an actual change detection of sediment distributions.

The suitability of BS-based sediment classification to reveal sedimentary changes over time has been demonstrated in a second study, carried out in a more dynamic environment (Ameland inlet, Dutch Wadden sea) using a time series of seven MBES measurements within two years. The quantification of the variations in the BS level caused by the environment and the MBES system, showed that system sources, such as varying transducer sensitivity of the sonar heads as well as changing equipment and survey settings, resulted in the highest BS variation (up to 3.5 dB). This magnitude of variation has a noticeable effect on the reliability of the absolute BS level and hampers the comparison between BS mosaics retrieved from different surveys. In contrast, unsupervised classification approaches, such as the Bayesian method, are applicable to relative BS levels and such absolute shifts of the BS level do not hamper the acoustic classification, as demonstrated in the Cleaver Bank study. However, environmental sources, such as water column properties or organized seabed roughness (e.g., sand ripples; makes BS dependent on survey azimuth), locally affect the BS level, and therefore, the acoustic classification as well. Keeping a stable and consistent data acquisition along the time series and avoiding harsh weather conditions, the maximum variation caused by the environment was acceptable (1.1 dB). Otherwise, the influence of sediment suspension, variation in salinity and temperature or organized seabed roughness became more dominant (up to 2.3 dB).

Evaluating the reliability of BS time series measurements, BS-based sediment classification has been proven to be highly valuable in monitoring the evolution of underwater nourishment in the Ameland inlet. Changing sediment maps, obtained from the Bayesian sediment classification, revealed sedimentary processes, such as erosion of the fine sediment from the nourished area and their deposition towards the main tidal channel. For example, a recreation of the sedimentary pre-nourishment state within approximately 12 months has been identified. Being able to establish the changes in the composition of the nourished material and its surroundings over time is an enormous benefit of BS data. This contributes to current monitoring strategies, merely determining volume changes based on bathymetric measurements. Furthermore, the combination of the acoustic sediment classification and corresponding bathymetry enabled to identify grain-size sorting patterns by a systematic variation of acoustic sediment classes over the bedforms in the nourished area. This evolution of horizontal sediment sorting patterns during the growth of marine bedforms can be used to support the hydrodynamic responses of flow over undulating beds in modeling studies and to explain the morphodynamic evolution of marine bedforms. Sediment composition generally plays a major role in benthic ecology and is thus highly relevant in ecological impact assessments, which become increasingly important in coastal maintenance.

Although limited to two study areas, this research presents successful case studies for monitoring the seabed with repetitive MBES BS measurements. In addition, one case study visualizes an approach how to handle and quantify external sources affecting the BS level. This can strongly support the measurements when a fully calibrated reference system or a natural reference area for an absolute or relative calibration of the MBES BS data are not available.

2. Evaluation of the potential of multi-frequency MBES BS to increase the acoustic discrimination between different seabed environments.

While the first part of the thesis was focused on single-frequency (i.e., monochromatic) MBES data, the second part covered the new research field of seabed mapping with multi-frequency (i.e., multispectral) MBES data. Four multispectral datasets (90 to 450 kHz), acquired in the Bedford Basin and Patricia Bay (both Canada) as well as in the Port of Rotterdam and Vlietland Lake (both the Netherlands), were employed. A processing algorithm, which accounts for frequency-dependent sonar settings and environmental conditions, was developed and a classification method for multispectral MBES BS data were proposed. Applying the processing algorithm to multispectal MBES data, it was successfully shown that a measure of the relative BS strength per frequency was retrieved, which can be used for acoustic sediment characterization and classification.

In general, the use of multiple frequencies allows for an improved acoustic discrimination between different seabed environments where the combination of the lowest and highest frequency reveals the most additional information about the seabed. Noteworthy is that the benefit of multiple frequencies highly depends on the local seabed. While an increased acoustic discrimination was observed for fine (muddy) sediments, the current analysis of the multispectral BS data has not clearly indicated improvements of the acoustic discrimination for the coarser sediments (e.g., sand with shells, gravel). Observation on the fine sediments of the Vlietland Lake and Port of Rotterdam revealed enormous variations in the measured BS and bathymetry at the different frequencies. The measured bathymetry difference between the lowest (90 kHz) and highest frequency (450 kHz) reached values between 0 and 60 cm in the muddy sediments depending on the location and incident angle. At the same locations, the BS level at the lowest frequency varied by up to 15 dB while the highest frequency showed only small variations (few dB).

To compare and interpret the experimental data, a layered BS model was employed and a model to simulate the MBES bathymetric measurements in a layered medium was developed. A comparison of the acoustic results with ground-truthing, geological setting and modeling results indicated that the measured bathymetry and BS at the different frequencies correspond to different parts of the surficial seabed and shallow subsurface. While the highest frequencies (300 and 450 kHz) are sensitive to the surficial fine (muddy) sediments, the lowest frequencies (90 and 100 kHz) significantly penetrate into the subsurface and acoustically respond to a possible subsurface layer. Although the ground-truthing of the subsurface was not sufficiently extensive in the Port of Rotterdam or not available available in the Vlietland Lake to detect the subsurface structures, geological information at the three study sites, indicated that coarser and harder materials were located below the muddy sediments resulting in higher BS levels compared to a non-layered medium. The geological information indicated coarse dredge spoils in the Bedford Basin, a geological sand and gravel layer in the Vlietland Lake and a consolidated mud layer in the Port of Rotterdam as buried layers. The coarser subsurface layer in the Bedford Basin was detected in a follow-up study by core sampling [36]. However, the influence of a gas layer, being likely in muddy sediments, could not be assessed due to the lack of appropriate ground-truthing equipment.

Taking the modeling and experimental results into account, the low frequency BS represents a combined acoustic response from the surficial sediment and the subsurface structures. However, the measured BS level is influenced by an increased sound attenuation in the sediment and consequently, cannot directly be related to the subsurface layer. Based on the simulations of the MBES bottom detection in a layered medium, the bathymetry measured at the highest and lowest frequency can be used to determine the thickness of thin layers (around 20 cm). The bottom detection becomes more sensitive to the incident angle and small variations in the sediment properties with an increasing layer thickness. Consequently, an accurate determination of the layer thickness for layers with a vertical thickness of more than 20 cm is hampered.

The low discrimination power, which was observed in the Cleaver Bank study for coarse sediments (sand to sandy gravel) and associated with monochromatic (300 kHz) BS, requires further investigations with multispectral BS data according to the results from the other study sites. The composition of the coarse sediments, the spatial extent and the data coverage were not fully comparable between the study sites. Small variations in the composition might change the acoustic response significantly. In addition, the ground-truthing strategy was not consistent among the studies, which might hamper a detailed comparison.

The capability to acquire data with a low and high frequency allows to identify shallow layering and to asses the influence on the measured BS data. Using a monochromatic MBES and transmitting only at a low frequency, the acquired BS and bathymetry data would lead to an erroneous interpretation of the surficial sediment properties and an incorrect determination of the water depth. Remarkably enough, if the signal penetration and a possible scattering at buried structures are not considered, multispectral MBES data can also lead to misinterpretation of the surficial sediments. Hence, it is highly recommended to analyze multi-frequency BS in conjunction with the inter-frequency bathymetry difference and ideally with the full acoustic signal.

The findings suggest that multispectral MBES data are applicable to image the shallow subsurface and to retrieve a rough 3D image of the sediments. However, this capability is clearly restricted to fine sediments, ranging from clay to sandy mud. To obtain a 3D image for coarser sediments, seismic systems employing lower frequencies are required. A successful integration of MBES and seismic data was demonstrated in the Ameland inlet. A subbottom profiler, emitting a chirp signal with frequencies from 0.5 to 7.2 kHz, revealed layers up to a depth of 5 m, while a monochromatic MBES, using a frequency of 300 kHz, is only sensitive to the surficial sandy sediments. It was shown that by combining both datasets a connection between the surficial sediments and the subsurface can be drawn. Regarding the coastal nourishment, MBES BS facilitates the interpretation of seismic reflectors and sub-bottom profiling can be used to establish the subsurface structure of the nourished seabed.

3. Development, improvement and comparison of classification methods to generate large-scale sediment maps from acoustic data with a specific focus on the Netherlands.

The first part of this thesis dealt with the application of two unsupervised classification methods, namely the Bayesian classification and the PCA in conjunction with k-means clustering, to monochromatic MBES BS data. It was figured out that the Bayesian classification method is more suitable than the PCA in conjunction with k-means clustering for the handling of solely BS data. While the Bayesian method accounts for the stochastic nature of the BS by assuming Gaussian distributed BS values, the k-means clustering neglects this intrinsic behavior of the BS. The latter issue can superimpose the BS variation due to different seabed properties and consequently, k-means clustering underestimates the number of distinguishable sediment types present in the study area. On the other hand, PCA in conjunction with k-means clustering is highly valuable when environmental predictors, such as bathymetry, contain information about the sediment properties because of its capability of selecting the most valuable feature.

With the recently developed capability of acquiring multispectral BS data with a single MBES system, the Bayesian classification method was extended for the classification of multispectral MBES BS. The multispectral Bayesian method allows to evaluate the information per frequency and combines the information at each frequency into a single classification map by accounting for the angular and frequency dependency of the BS. If the acoustic response of the seabed is sufficiently frequency-dependent, the method enables to objectively and automatically distinguish between more seabed environments. This strongly promotes habitat mapping, localization of resources on the seabed and sediment mapping in general. Beyond that, the possibility for 3D imaging in fine sediment environments is not yet integrated into the classification methods and requires future efforts.

The BS-based classification methods require a full data coverage of the seabed. However, MBES survey lines are often inconsistent due to budged and time limitations, weather conditions or just inaccessibility of an area. To overcome such limitations and still achieve full-coverage sediment maps, an approach was introduced to interpolate BS data by using geostatistical modeling (i.e., Kriging) and to classify the interpolated data into distinct acoustic classes. The application to the Cleaver Bank datasets and a comparison with ground-truthing and traditional sediment maps (i.e., manual interpretation of in situ measurements and bathymetry) successfully demonstrated that this approach resolves lateral heterogeneities on a kilometer scale (varies with MBES line spacing) and outperforms traditional mapping. It is worth noting that the application of the Bayesian classification method resolves lateral heterogeneities in a scale of meters in the Clever Bank (varies with MBES and water depth) .

As an example, the Netherlands Continental Shelf (NCS) is mainly mapped by traditional methods and thus the integration of the interpolated and the actual acoustic classification results would achieve a significant improvement. However, the varying spatial and geoacoustic resolution as well as the uncertainties related to the different approaches hamper the map integration.

8.2. Outlook

This present study has shown that multispectral MBES BS enhances sediment and habitat mapping. Nevertheless, benefits were mainly related to fine sediments and limited for coarse sediments. More field measurements for various types of coarse sediments coupled with extensive ground-truthing, such as video footage and box coring combined with stereo photography, would facilitate more generalized conclusions. In particular, in environments with the presence of shell fragments on the seabed, such as the Ameland inlet and in general the NCS, video footage would improve the quantification of the amount of shell fragments. This is highly important since shells fragments can highly alter the measured BS value and receiving a representative lab analysis of shell fragments is difficult to achieve. For fine sediments a combination of vibrocoring, extensive rheometric profiling and gas content measurements would support an accurate determination of the subsurface sediment properties, the depth of a buried layer and the presence of biogenic gas. This allows a more quantitative assessments of the capabilities of a multispectral MBES to detect subsurface layering and relate sediment properties to buried structures.

Ideally, a set up of laboratory measurements, in which the effect of various frequencies and geological settings (such as different grain sizes, layering and compaction degrees) on the BS strength are investigated, should be established. A similar approach for a limited grain-size range was already carried out by Ivakin and Sessarego [31]. This could help to build a ”multispectral BS catalog” providing an overview of the expected BS strength for various sediment types and frequencies. Although the real world differs from lab conditions with respect to sediment heterogeneity, water column and MBES configuration, it would help to quantify the capabilities of multispectral BS data to discriminate between various environments. Such a catalog together with the growing field of MBES BS calibration [29, 110–112] would allow to better quantify the uncertainties in acoustic sediment classification and, in general, could reduce the amount of required grab samples. Also BS-based seabed monitoring would benefit in such a way that the influence of the environment, the acoustic system and the actual sediment on the BS measurement could be better differentiated.

The developed MBES bottom detection model can be further improved by integrating a scattering model applicable for higher frequencies ($> 100\,\mathrm{kHz}$). As shown by Ivakin [50], when the sediment (i.e., porous medium) is approximated as a fluid with a bulk modulus and effective density derived from Biot theory [183] and the sediment inclusion (e.g., shells, gavel) are separately modeled as discrete scatterers, an application of the adjusted scattering model to higher frequencies would be feasible. Furthermore, a discretization of the subsurface volume in order to calculate the volume scattering at discrete locations, as implemented by Sternlicht and de Moustier [184], would enable a more realistic simulations of a layered medium. An improved ground-truthing, as mentioned earlier, and the development of a multispectral BS catalog could be used to validate the bottom detection model or, in general, scattering models.

Lastly, a classification method, incorporating the inter-frequency bathymetry difference, would allow to automatically and objectively discriminate between acoustic information obtained from the seabed and subsurface. This could result in a 3D visualization of the acoustic sediment classes, thereby advancing sediment and habitat mapping.

A

Bayesian method

A.1. Boundary conditions

The fitting of the Gaussian distributions to the measured backscatter histogram requires the search bounds (i.e., upper and lower bound) for the unknown parameters of the Gaussian distributions (i.e., $\bar{y}$, σ_y and q).

The standard deviation of the Gaussian distributions are related to the number of scatter pixels N_s which are considered in the backscatter averaging process. Simons and Snellen [13] derived following expression for the theoretical standard deviation (in dB)

$$\sigma_y = \frac{5.57}{\sqrt{N_s}}. \tag{A.1}$$

Eq. (A.1) assumes that the scatter pixels are independent and associated to a homogeneous sediment type. Using the lowest and highest N_s for the averaging, an indication of the upper and lower bound of the standard deviation is given. A theoretical N_s per beam can be calculated by using MBES specific parameters and the water depth h as follows

$$N_s(\Theta) = \frac{\left(\frac{h\Omega_R}{\cos^2\Theta}\right)}{\left(\frac{c\tau}{2\sin\Theta}\right)} \tag{A.2}$$

with Ω_R the beam opening angle at reception (i.e., across-track direction), Θ the beam angle, and τ the pulse length. For a rough seabed, the beam angle Θ should be replace with the incident angle ϕ according to Eq. (2.37). From Eq. (A.1) follows, that the acoustic discrimination power between sediment types is expected to increase with increasing N_s. In order to increase N_s, the data from a number of pings and beams (or incident angles), defining a patch, can be used for the backscatter averaging process [17]. In Fig. A.1 the theoretical N_s per patch and the corresponding theoretical σ_y are shown (green asterisk). In addition, the measured N_s per patch and the corresponding theoretical σ_y for a datasets acquired in the Ameland inlet with a Kongsberg EM 2040C are shown as well (box plots). Here, we consider the measured N_s per beam, which is provided by the MBES manufacturer, to determine the lower bound $\sigma_{y_{lb}}$ and the upper bound $\sigma_{y_{ub}}$ for the standard deviation of the Gaussians. The whiskers indicate a variation between 0.3 and 1.8 dB while some outliers reaching values above 2. Considering that the patches (up to 0.5 x 1.5 m) cover in reality not an ideal homogenous sediment, $\sigma_{y_{lb}}$ was set 0.5 dB and $\sigma_{y_{ub}}$ was set to 2.5 dB in the Ameland inlet to account for a higher standard deviation due to inhomogeneity.

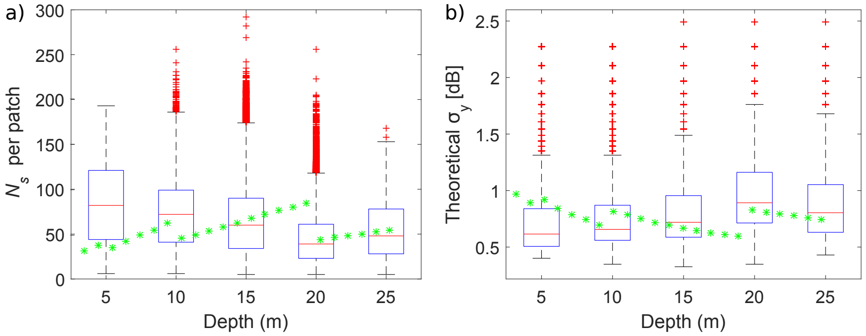

Figure A.1: a) Box plot of measured number of scatter pixels N_s within a patch (patch is defined over number of beams and pings) for different water depths. Green asterisk indicate theoretical N_s. b) Box plot of theoretical standard deviation σ_y based on measured N_s. Green asterisk indicates theoretical σ_y based on theoretical N_s. The bottom and top of the blue rectangle represent the 25th and 75th percentiles, respectively, whereas the red line indicates the median value. The whiskers extend to the minimum and maximum values that are not considered as outliers. Outliers are marked with red crosses.

The used search bounds for the given studies in this thesis are listed in A.1. For the studies in the Ameland inlet, Bedford Basin and Patricia Bay the upper bound is slightly higher than for the Cleaver Bank. In the Ameland inlet the rough seabed morphology (Fig. 2.12) yielded to less scatter pixels from adjacent incident angles for the same patch size. In the Bedford Basin and Patricia Bay the acquisition of multispectral data comes along with a reduction in data coverage in the along-track direction by the number of frequencies considered. This yields to less scatter pixels from adjacent pings within a patch. In addition, the given backscatter value per beam for a Kongsberg MBES is already an average over the number of scatter pixels within the beam while for an R2Sonic MBES the backscatter value per beam

Table A.1: Search bounds for standard deviation σ_y of the Gaussian distributions used in the different studies.

Study area	$\sigma_{y_{lb}}$	$\sigma_{y_{ub}}$
Cleaver Bank (Chapter 3)	0.5	2.0
Ameland inlet (Chapter 4)	0.5	2.5
Bedford Basin (Chapter 5)	0.5	2.5
Patricia Bay (Chapter 5)	0.5	2.5

represents a single value at the bottom detection.

The search bounds for the mean $\bar{y}$ are defined by the range of the measured backscatter values, i.e., difference between the maximum backscatter value $\max(y_j)$ and minimum backscatter value $\min(y_j)$ in the histogram and the number of considered Gaussian distribution m. Hence, the lower $\bar{y}_{k_{\mathrm{lb}}}$ and upper bound $\bar{y}_{k_{\mathrm{ub}}}$ for the mean are obtained as follows

$$\begin{aligned}\bar{y}_{k_{\mathrm{lb}}} &= \min(y_j) + \sum_{k=1}^{m} \Delta y(k-1) \\ \bar{y}_{k_{\mathrm{ub}}} &= \min(y_j) + \sum_{k=1}^{m} \Delta y k\end{aligned} \tag{A.3}$$

with $\Delta y = \frac{\max(y_j)-\min(y_j)}{m}$.

The parameter q for the strength of the Gaussians is estimated during the optimization based on the magnitude of the measured data and does not require a initial search bound.

A.2. Gaussian distribution

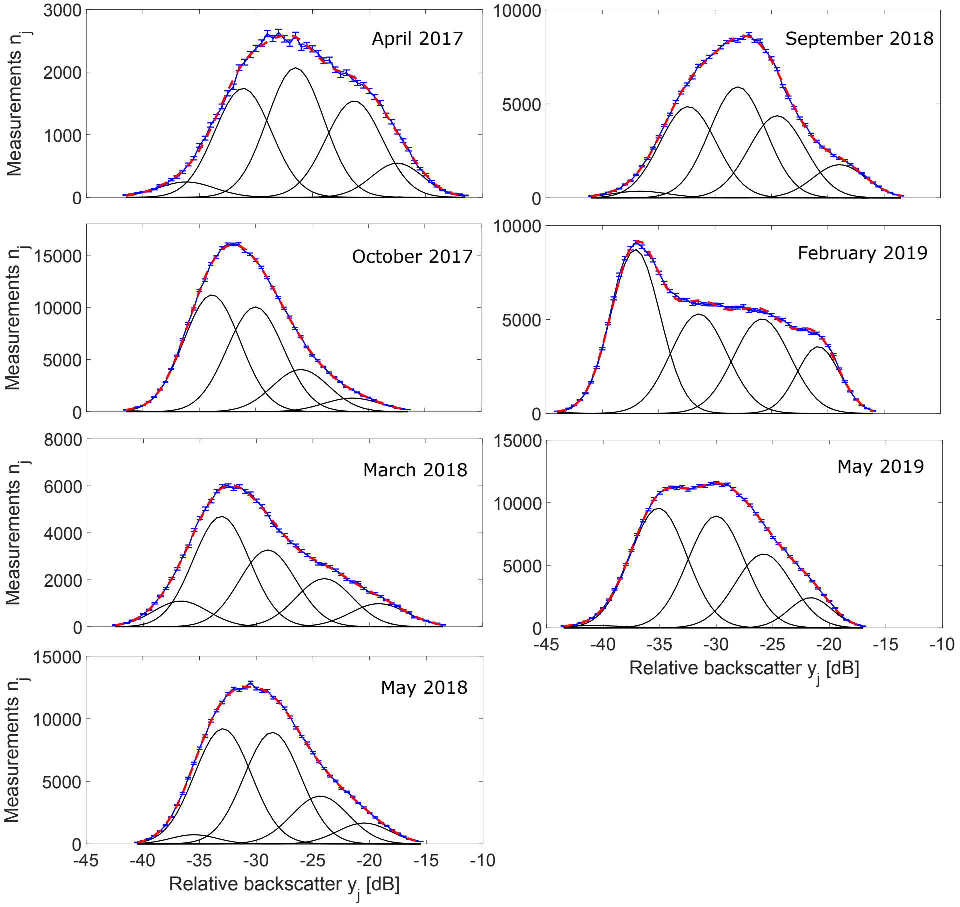

Figure A.2: Model fits to the histogram of the measured backscatter data n_j (blue) per 0.5 dB bin y_j for the different MBES backscatter data sets acquired in the Ameland inlet are displayed. The measured backscatter data are obtained from the 58° incident angle at starboard side. The blue error bars indicate the variance of the measurements per bin. The modeled $f(y_j|\boldsymbol{x})$ histogram calculated by using 5 Gaussian distributions is shown in red. The corresponding Gaussians are displayed in black. For the data sets acquired in October 2017, February and May 2019 the first Gaussian representing the lowest backscatter values are hardly visible.

B

Applied Physics Laboratory model (APL-model)

The APL-model was developed by the Applied Physics Laboratory at the University of Washington and published as the APL-UW High-frequency Ocean Environmental Acoustic Models Handbook [40]. It is based on several published articles, which are referred to within the following model description. In general, the APL-model is an extension of the Jackson model published by Jackson *et al.* [138] and Mourad and Jackson [45].

The basic principle of the APL-model is described in Chapter 2 and the model is employed in Chapters 5 and 6. As already stated in Eqs. (2.22) and (6.1), the backscattering cross section σ_b is calculated as a summation of the roughness cross section σ_r and volume scattering cross section σ_v. The cross sections are a dimensionless parameter defined per unit area and solid angle. Following Eq. (2.17), the backscatter strength BS is then calculated as the decibel equivalent from the backscattering cross section. Fig. B.1 displays APL-model predictions for backscattering at 100 kHz for various sediment types. In the following sections, the model input parameters and the APL-model are described in detail.

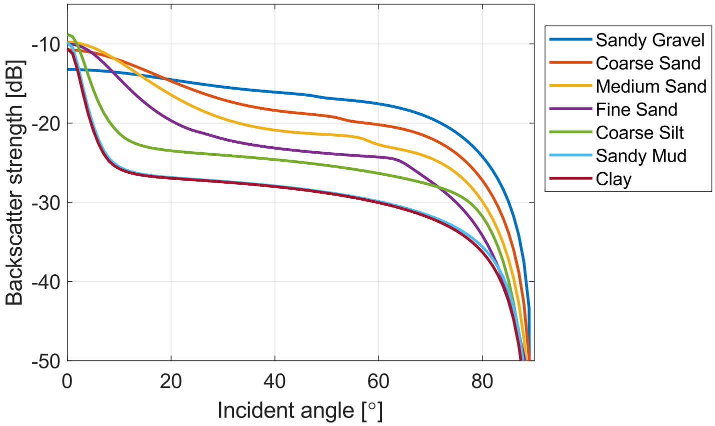

Figure B.1: Model predictions for backscattering at 100 kHz using the APL-model for various sediment types. The backscatter strength $BS = 10\log(\sigma_b)$ is shown at the y-axis.

B.1. Model input parameters

The APL-model requires beside the signal parameters (f, ϕ) and the geoacoustic parameters of the sediment (ρ, c, α, $\hat{\sigma}_v$) and water (ρ, c), the spectral exponent γ and the spectral strength η, both describing the roughness of the sediment.

Median grain size

An often used descriptor of sediments is the median grain size d_{50}. Empirical relationships of the geoacoustic parameters with the median grain size of the sediment were developed by Hamilton [44] and Hamilton and Bachman [185] but also obtained in previous APL-Model work by Mourad and Jackson [45] and Jackson [186]. The median grain size can be expressed in logarithmic scale as

$$M_z = -\log_2 \frac{d_{50}}{d_0} \tag{B.1}$$

with d_0 the reference length of 1 mm.

Table A.1 presents the median grain size M_z in terms of sediment types classified after common classification schemes [83, 144]. The sediment types are approximately described by the median grain size but variation can occur. The M_z values can be used as an input for the empirical equations, described in the following, to obtain default model input parameters for a specific sediment type.

Table B.1: Median grain size M_z in terms of sediment type.

Sediment type	M_z	Sediment type	M_z
sandy Gravel	-1	clayey Sand	4.0
very coarse Sand	-0.5	coarse Silt	4.5
muddy sandy Gravel	0	sandy Silt, gravelly Mud	5.0
coarse Sand, gravelly Sand	0.5	medium Silt	5.5
gravelly muddy Sand	1.0	sandy Mud	6.0
medium Sand	1.5	fine silt, clayey Silt	6.5
muddy Gravel	2.0	sandy Clay	7.0
fine Sand, silty Sand	2.5	very fine Silt	7.5
muddy Sand	3.0	silty Clay	8.0
very fine Sand	3.5	Clay (all grades)	9.0

Sound speed ratio

The sound speed ratio between the sediment and water is $\hat{c} = \frac{c_2}{c_1}$. Following empirical equations can be used to obtain the sound speed ratio from the median grain size M_z within the validity range from $-1 \leq M_z \leq 9$

$$\begin{aligned}\hat{c} &= 0.002709M_z^2 - 0.056452M_z + 1.2778 && -1 \leq M_z < 1\\ &= -0.0014881M_z^3 + 0.0213937M_z^2 - 0.1382798M_z + 1.3425 && 1 \leq M_z < 5.3\\ &= -0.0024324M_z + 1.0019 && 5.3 \leq M_z \leq 9.\end{aligned}$$

Density ratio

The density ratio between the sediment and water is $\hat{\rho} = \frac{\rho_2}{\rho_1}$. Following empirical equations can be used to obtain the density ratio from the median grain size M_z within the validity range from $-1 \leq M_z \leq 9$.

$$\begin{aligned}\hat{\rho} &= 0.007797M_z^2 - 0.17057M_z + 2.3139 && -1 \leq M_z < 1\\ &= -0.0165406M_z^3 + 0.2290201M_z^2 - 1.1069031M_z + 3.0455 && 1 \leq M_z < 5.3\\ &= -0.0012973M_z + 1.1565 && 5.3 \leq M_z \leq 9.\end{aligned}$$

Sound attenuation coefficient

The empirical equations by Hamilton [44] can be used to obtain the sound attenuation coefficient α (in dB/m) in sediments from the median grain size M_z and the signal frequency f within the validity range from $-1 \leq M_z \leq 9.5$.

$$\begin{aligned}\alpha &= 0.4556f && -1 \leq M_z < 0\\ &= (0.4556 + 0.0245M_z)f && 0 \leq M_z < 2.6\\ &= (0.1978 + 0.1245M_z)f && 2.6 \leq M_z < 4.5\\ &= (8.0399 - 2.5228M_z + 0.20098M_z^2)f && 4.5 \leq M_z < 6.0\\ &= (0.9431 - 0.2041M_z + 0.0117M_z^2)f && 6.0 \leq M_z < 9.5\\ &= 0.0601f && 9.5 \leq M_z.\end{aligned}$$

Spectral exponent
In the absence of measurements the spectral exponent γ is set to a fixed value

$$\gamma = 3.25. \tag{B.2}$$

This value is obtained from available measurement data [138, 187], which resulted in an averaged value for γ of 3.23 with a standard deviation of 0.44.

Spectral strength
The spectral strength η is related to the rms relief g via

$$\eta = 0.00207 g^2 g_0^2 \tag{B.3}$$

with g_0 a reference length of 1 cm and g (in cm^4) defined for a 100 cm track. The rms relief g can be obtained from the median grain size via

$$\begin{aligned} g &= \left(\frac{2.03846 - 0.26923 M_z}{1 + 0.076923 M_z}\right) g_0 && -1 \leq M_z < 5.0 \\ &= 0.5 g_0 && 5.0 \leq M_z \leq 9.0. \end{aligned}$$

Volume scattering parameter
In the absence of measurements the volume scattering parameter $\hat{\sigma}_v$ can be assigned to the following values

$$\begin{aligned} \hat{\sigma}_v &= 0.002 && -1 \leq M_z < 5.5 \\ &= 0.001 && 5.5 \leq M_z < 9.0. \end{aligned}$$

The values were obtained by comparing the model predictions with experimental backscatter data [40]. This is in contrast to the other model input parameters, which are measurable quantities.

B.2. Forward loss

The forward loss model is based on reflection rather than scattering. It is incorporated into the Kirchhoff approximation and large-roughness approximation at nadir ($\psi = 90°$) and into the volume scattering approximation for the entire angular range. The forward loss model contains a modified reflection coefficient called the lossy Rayleigh coefficient R_r, first published by Mackenzie [188],

$$R_r(\psi) = \frac{\frac{\hat{\rho}\sin(\psi)}{E(\psi)} - 1}{\frac{\hat{\rho}\sin(\psi)}{E(\psi)} + 1} \tag{B.4}$$

$$E(\psi) = \sqrt{\kappa_c^2 - \cos^2(\psi)} \tag{B.5}$$

$$\kappa_c = \frac{1}{\hat{c}}(1 + i\delta) \tag{B.6}$$

with ψ the grazing angle, which is complementary to the incident angle ϕ ($\psi = 90 - \phi$). Here, i is the imaginary number and δ is the loss parameter defined as $\delta = \frac{\alpha c_2 \ln(10)}{40\pi}$. The forward reflection loss RL is retrieved via $RL = -20\log(|R_r(\psi)|)$, where the results for various sediment types are plotted in Fig. B.2.

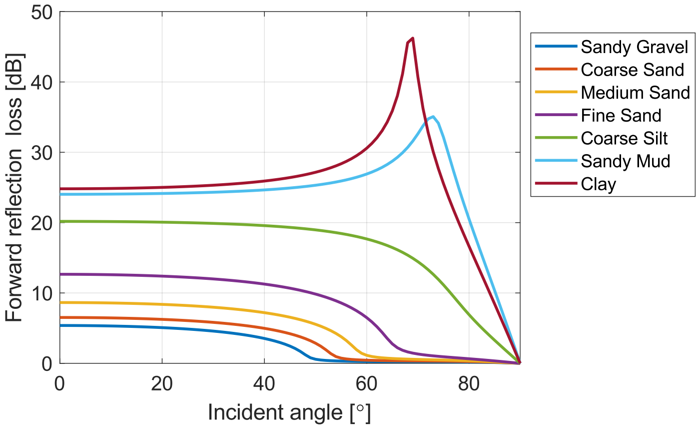

Figure B.2: Forward reflection loss predicted for various sediment types. The model input parameters are calculated using the median grain size, which is representative for the sediment type (Table 2.1), in combination with the empirical equations.

B.3. Kirchhoff approximation

The Kirchhoff approximation results in an integral for the backscattering cross section. The integral is either integrated numerically or approximated. In the APL-model following approximation, developed by Mourad and Jackson [45], for the Kirchhoff roughness cross section σ_{kr} is used

$$\sigma_{kr}(\psi) = \frac{C_2 q_c |R_r(90°)|^2}{8\pi\left(\cos^{4\zeta}(\psi) + C_1 q_c^2 \sin^4(\psi)\right)^{\frac{1+\zeta}{2\zeta}}}. \tag{B.7}$$

In this expression for the Kirchhoff approximation the roughness parameters of the sediment called the spectral exponent γ and spectral strength η are incorporated into the so-called structure functions [189]

$$\zeta = \frac{\gamma}{2} - 1 \tag{B.8}$$

and

$$C_h^2 = \frac{2\pi\eta\Gamma(2-\zeta)2^{-2\zeta}}{g_0^{\gamma}\zeta(1-\zeta)\Gamma(1+\zeta)} \tag{B.9}$$

where $\Gamma(x)$ is the Gamma function. Following parameters in Eq. (B.7) are derived from the structure functions C_h^2 and ζ [45]

$$q_c = C_h^2 2^{1-2\zeta} k^{2-2\zeta} \tag{B.10}$$

$$C_1 = \left(\frac{8\zeta^2 \Gamma(\frac{1}{2\zeta} + \frac{1}{2})}{\Gamma(\frac{1}{2})\Gamma(\frac{1}{2})\Gamma(\frac{1}{2\zeta})} \right)^{2\zeta} \tag{B.11}$$

$$C_2 = \frac{\zeta^{\frac{1}{2}+\frac{1}{2\zeta}} \Gamma(\frac{1}{\zeta})}{2\zeta} \tag{B.12}$$

with k the wavenumber. Fig. B.3 represents model curves of roughness scattering predicted by the Kirchhoff approximation for various sediment types at a frequency of 100 kHz. The Kirchhoff approximation is valid until 50° and for larger incident angles the composite roughness approximation is applicable.

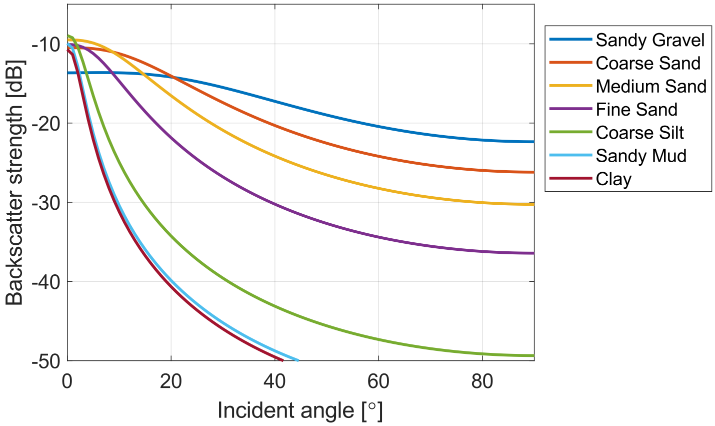

Figure B.3: Model predictions for roughness scattering at 100 kHz using the Kirchhoff approximation for various sediment types. The backscatter strength $BS = 10\log(\sigma_{kr})$ is shown at the y-axis.

B.4. Composite roughness approximation

The composite roughness approximation is composed of the small-roughness perturbation approximation with modifications for acoustic shadowing and large-scale bottom slope. The composite roughness cross section can be conveniently described as follows [45]

$$\sigma_{cr}(\psi) = U(\psi, V)F(\psi, \sigma_{pr}, V) \tag{B.13}$$

where $U(\psi, V)$ is the acoustic shadowing correction and $F(\psi, \sigma_{pr}, V)$ is a slope averaging integral. According to Wagner [190], we can write

$$U(\psi, V) = \frac{1 - e^{-2Q_1}}{2Q_1} \tag{B.14}$$

where

$$Q_1 = \frac{\pi^{-0.5} e^{-Q_2^2} - Q_2\big(1 - \mathrm{erf}(Q_2)\big)}{4Q_2} \tag{B.15a}$$

$$Q_2 = \frac{\tan(\psi)}{V}. \tag{B.15b}$$

The large-scale rms slope V is defined as [45]

$$V = \sqrt{\frac{(2\pi\eta g_0^{-\gamma})^{\frac{1}{\zeta}}}{2-2\zeta} (\frac{k^2}{\zeta})^{\frac{1-\zeta}{\zeta}}}. \tag{B.16}$$

The large-scale rms slope V is written in angular units as $\psi_V = \frac{V180}{\pi}$.

The slope averaging integral $F(\psi, \sigma_{pr}, V)$ [191] can be approximated by a three-point Gauss-Hermite quadrature via [192]

$$F(\psi, \sigma_{pr}, V) = \pi^{-0.5} \sum_{n=-1}^{1} w_n \sigma_{pr}(\psi - \psi_n) \tag{B.17}$$

with $w_{-1} = w_1 = 0.295410$, $w_0 = 1.181636$, $\psi_{-1} = -\psi_1 = 1.224745\psi_V$, $\psi_0 = 0$.

The function σ_{pr} is the backscattering cross section in the small-roughness perturbation approximation. Here, a modified version of Kuo [193] is used

$$\sigma_{pr}(\psi) = 4k^4 \sin^4(\psi)|Y(\psi)|^2 \mathrm{H}(K_\psi). \tag{B.18}$$

In this expression, $Y(\psi)$ is the complex function

$$Y(\psi) = \frac{(\hat{\rho} - 1)^2 \cos^2(\psi) + \hat{\rho}^2 - \kappa_c^2}{\big(\hat{\rho}\sin(\psi) + E(\psi)\big)^2}. \tag{B.19}$$

The power spectrum H, defining the random bottom relief in Eq. (B.18), is

$$\mathrm{H}(K) = (g_0 K)^{-\gamma} \eta \tag{B.20}$$

which is evaluated at the modified wavenumber $K_\psi = \sqrt{4k^2\cos^2(\psi) + (k/10)^2}$.

The argument of σ_{pr} can fall outside the validity range between 0 and 90°. If the argument is negative it should be set to 0 and if it is larger than 90 it should be set to 90. Fig. B.4 represents model curves of roughness scattering predicted by the composite roughness approximation for various sediment types at a frequency of 100 kHz.

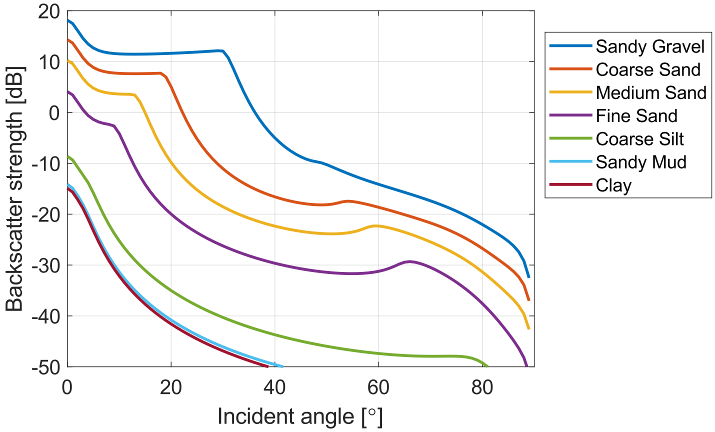

Figure B.4: Model predictions for roughness scattering at 100 kHz using the composite roughness approximation for various sediment types. The backscatter strength $BS = 10\log(\sigma_{cr})$ is shown at the y-axis.

B.5. Large-roughness scattering approximation

The large-roughness scattering approximation for gravel and rock bottoms represents an empirical fit taken from the model's predecessor [186]. The large-roughness cross section is expressed as

$$\sigma_{lr}(\psi) = v_2 \sin^{v_1}\left(\frac{180}{1+\frac{0.81\psi_{\text{crit}}^2}{\psi^2}}\right) + \frac{0.026|R_r(90°)|^2}{V^2\left(1+\frac{(\psi-90)^2}{2.6\psi_V^2}\right)^{1.9}\left(1+\frac{0.81\psi_{\text{crit}}^2}{\psi^2}\right)} \tag{B.21}$$

where

$$v_1 = 0.7263V^{-\frac{1}{3}} \tag{B.22a}$$

$$v_2 = \frac{0.04682V^{1.25}\hat{c}^{3.25}\left(\left(1-\frac{2}{\hat{\rho}}\right)\hat{c}^{-2}+1\right)^2}{1+\frac{3.54\psi_V}{\psi_{\text{crit}}}}. \tag{B.22b}$$

The critical angle ψ_{crit} is given by the sound speed ratio $\hat{c}$ as

$$\begin{aligned} \psi_{\text{crit}} &= \cos^{-1}(1/\hat{c}) \qquad && \hat{c} \geq 1.001 \\ \psi_{\text{crit}} &= 2.5613° && \hat{c} \leq 1.001. \end{aligned} \tag{B.23}$$

Fig. B.5 represents model curves of roughness scattering predicted by the large-roughness scattering approximation for various sediment types at a frequency of 100 kHz.

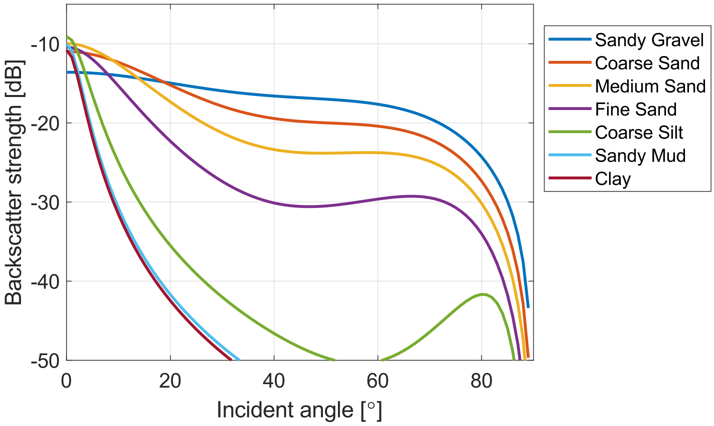

Figure B.5: Model predictions for roughness scattering at 100 kHz using the large-roughness scattering approximation for various sediment types. The backscatter strength $BS = 10\log(\sigma_{lr})$ is shown at the y-axis.

B.6. Interpolation between roughness scattering approximations

The interpolation between the different scattering approximations uses the following function

$$f(X_1) = \frac{1}{1+e^{X_1}}. \tag{B.24}$$

The first interpolation is between the Kirchhoff and composite roughness approximation. The interpolated cross section, indicated as the medium-roughness cross section σ_{mr}, is expressed as

$$\sigma_{mr}(\psi) = f(X_1)\sigma_{kr}(\psi) + \big(1 - f(X_1)\big)\sigma_{cr}(\psi) \tag{B.25}$$

where

$$X_1 = \frac{\cos(\psi) - \cos(\psi_{dB})}{0.0125} \tag{B.26a}$$

$$\cos(\psi_{dB}) = \Big(\frac{1}{X_2} + 4\Big)^{-\frac{1}{4}} \tag{B.26b}$$

$$X_2 = 1000^{\frac{1}{1+\zeta}}(C_1 q_c^2)^{\frac{1}{\zeta}} \tag{B.26c}$$

with ψ_{dB} the crossover angle indicating approximately the transition between the Kirchhoff and composite roughness approximation.

The final interpolation is between the medium-roughness and the large-roughness cross section in order to obtain the roughness cross section σ_r, as reported in Eqs. (2.22) and (6.1), which is then valid for the entire angular range and all sediment types

$$\sigma_r(\psi) = f(X_3)\sigma_{mr}(\psi) + \big(1 - f(X_3)\big)\sigma_{lr}(\psi) \tag{B.27}$$

where

$$X_3 = \frac{\tan^{-1} V - 7^\circ}{0.5^\circ} \tag{B.28}$$

with the values 7° and 0.5° being empirically defined reference angles.

Fig. B.6 represents model curves of roughness scattering predicted by means of the interpolation function incorporating the Kirchhoff, composite roughness and large-roughness cross section for various sediment types at a frequency of 100 kHz.

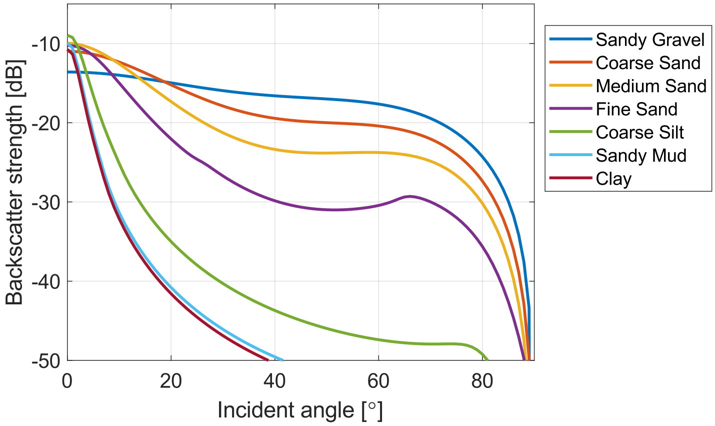

Figure B.6: Model predictions for roughness scattering at 100 kHz using an interpolation between the Kirchhoff, composite roughness and large-roughness scattering approximations. The backscatter strength $BS = 10\log(\sigma_r)$ is shown at the y-axis.

B.7. Volume scattering approximation

In the APL-model the expression for volume scattering published by Stockhausen [194] is generalized to allow for the effect of absorption on the transmission coefficient and to account for acoustic shadowing and the bottom slope analogous to Eq. (B.13). The volume scattering is written as

$$\sigma_v(\psi) = U(\psi, V) F(\psi, \sigma_{pv}, V). \tag{B.29}$$

To calculate $F(\psi, \sigma_{pv}, V)$, Eq. (B.17) is employed with σ_{pr} replaced by

$$\sigma_{pv}(\psi) = \frac{5\delta\hat{\sigma}_v |1 - R_r^2(\psi)|^2 \sin^2(\psi)}{\hat{c}\ln 10 |E(\psi)|^2 \Im\{E(\psi)\}} \tag{B.30}$$

with $\hat{\sigma}_v$ the empirically treated volume scattering parameter and $\Im\{E(\psi)\}$ the imaginary part of $E(\psi)$. Fig. B.7 represents model curves of volume scattering predicted by the volume scattering approximation for various sediment types at a frequency of 100 kHz.

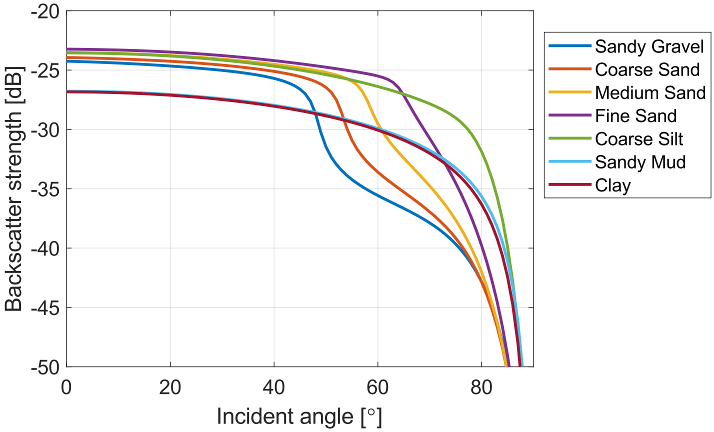

Figure B.7: Model predictions for volume scattering at 100 kHz using the volume scattering approximation for various sediment types. The backscatter strength $BS = 10\log(\sigma_v)$ is shown at the y-axis.

C

Layered backscatter model

Guillon and Lurton [136] developed a layered backscatter model based on the combination of a classical scattering model and sound propagation inside a fluid layered media. In this thesis, the APL-model described in Appendix B, is used as the classical scattering model and the implementation of the sound propagation inside the sediment follows the approach of Guillon and Lurton [136]. In the layered backscatter model the contribution of the individual layers l are coherently summed, following the assumption of single scattering, to retrieve the total backscattering cross section σ_b via

$$\sigma_b(\phi) = \sum_{l=1}^{L_n} \tilde{\sigma}_{b_l}(\phi_l) \tag{C.1}$$

where $\tilde{\sigma}_{b_l}$ is the modified backscattering cross section at layer l, L_n is the total number of layers and ϕ is the incident angle.

In the following, the layered backscatter model is described for a two-layered geophysical model, consisting of the water column ($l = 0$) and two sediment layers ($l = 1, 2$) (Fig. 6.2), in agreement with Section 6.3.4.

First of all, the calculation of the backscattering at the buried interface needs to account for the density and sound speed change (impedance adaption) due to the overlying sediment. An angular refraction correction via Snell's law to calculate the incident angle on the buried interface is required as well (see Eq. (C.3)).

The volume scattering in the APL-model is based on the assumption of a semi-infinite medium. In case of layering, the upper layer ($l = 1$) becomes finite and Eq. (B.30), contributing the volume scattering cross section, needs to be modified for the first layer as follows

$$\sigma_{pv_1}(\phi) = \frac{5\delta_1 \hat{\sigma}_{v_1} |1 - R_{r_1}^2(\psi_1)|^2 \sin^2(\psi_1)}{\hat{c}_1 \ln 10 |E(\psi_1)|^2 \Im\{E(\psi_1)\}} \left(1 - e^{-4\hat{\alpha}_1 d_1/\cos(\phi_2)}\right) \tag{C.2}$$

with ψ the grazing angle, which is related to the incident angle via $\psi = 90 - \phi$, and $\hat{\alpha}_1$ as the attenuation coefficient of the upper sediment layer $l = 1$ in Neper/m.

The term $d_1/\cos(\phi_2)$ represents the travel distance of the signal in the upper layer $l = 1$, where ϕ_2 is the refracted angle into the upper layer and is retrieved via Snell's law from the incident angle on the surficial seabed ϕ_1 as follows

$$\phi_2 = \sin^{-1}\left(\frac{c_1}{c_0}\sin(\phi_1)\right). \tag{C.3}$$

The backsacttering cross section is transferred from the buried interface ($l = 2$) to the sediment-water interface by accounting for the sound propagation inside the layered medium via

$$\tilde{\sigma}_{b_2} = \sigma_{b_2} C_{p_{0,1}} \tag{C.4}$$

using the so-called transfer coefficient $C_{p_{0,1}}$

$$C_{p_{0,1}} = |T_{0,1}|^2 |T_{1,0}|^2 e^{-4\hat{\alpha}_1 d_1/\cos(\phi_2)} \tag{C.5}$$

with the complex transmission coefficients defined as follows (see also Eq. (2.13))

$$T_{0,1} = \frac{2\rho_1\tilde{c}_1\cos\phi_1}{\rho_1\tilde{c}_1\cos\phi_1 + \rho_0 c_0\cos\phi_2} \tag{C.6a}$$

$$T_{1,0} = \frac{2\rho_0 c_0\cos\phi_2}{\rho_0 c_0\cos\phi_2 + \rho_1\tilde{c}_1\cos\phi_1} \tag{C.6b}$$

where $\tilde{c}_1$ represents the complex sound speed in the upper sediment layer retrieved via Eq. (2.14).

Figs. C.1 and C.2 displays the layered backscatter model predictions for backscattering at 100 kHz for a 20 cm and 50 cm clay layer above a semi-infinite sandy gravel layer (blue dashed line) and the effect of the layering on the individual layers.

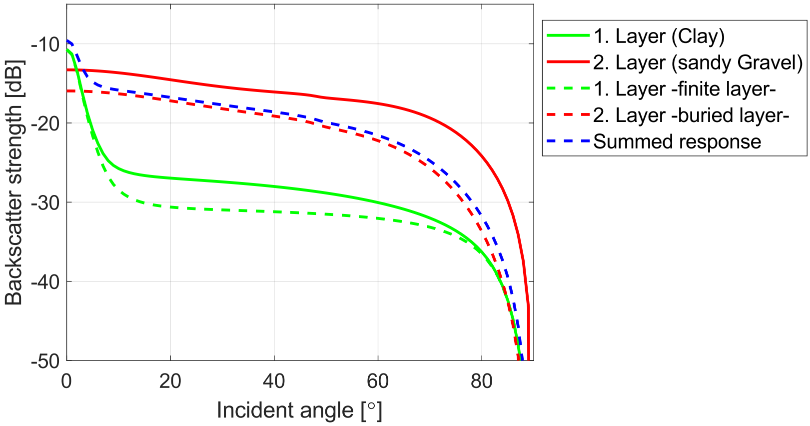

Figure C.1: Model predictions for backscattering at 100 kHz using the layered backscatter model for a 20 cm clay layer above a semi-infinite sandy gravel layer (blue dashed line). The solid lines indicate the single-layer case using the APL-model. The green dashed line shows the effect of layering on the upper finite clay layer and the red dashed line shows the effect of layering on the buried sandy gravel layer. The backscatter strength $BS = 10\log(\sigma_b)$ is shown at the y-axis.

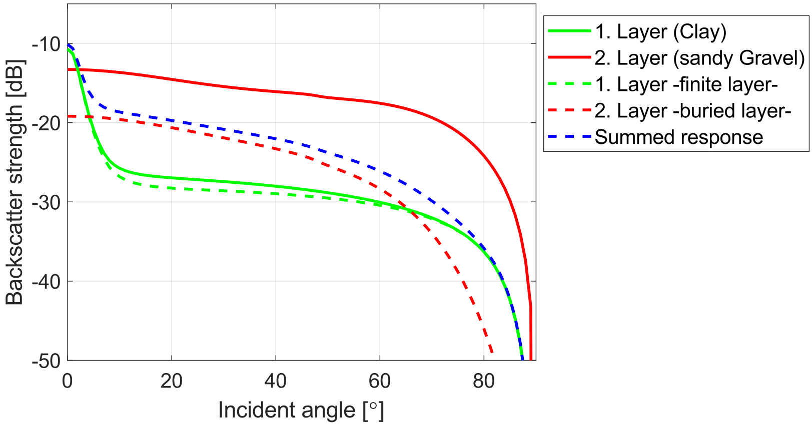

Figure C.2: Model predictions for backscattering at 100 kHz using the layered backscatter model for a 50 cm clay layer above a semi-infinite sandy gravel layer (blue dashed line). The solid lines indicate the single-layer case using the APL-model. The green dashed line shows the effect of layering on the upper finite clay layer and the red dashed line shows the effect of layering on the buried sandy gravel layer. The backscatter strength $BS = 10\log(\sigma_b)$ is shown at the y-axis.

References

[1] L. Mayer, M. Jakobsson, G. Allen, B. Dorschel, R. Falconer, V. Ferrini, G. Lamarche, H. Snaith, and P. Weatherall, *The Nippon Foundation - GEBCO Seabed 2030 Project: The quest to see the world's oceans completely mapped by 2030,* Geosciences **8**, 63 (2018).

[2] M. Ainslie, *Principles of Sonar Performance Modelling* (Springer-Verlag Berlin Heidelberg, 2010).

[3] P. Blondel, *The Handbook of Sidescan Sonar* (Springer-Verlag Berlin Heidelberg, 2009).

[4] X. Lurton, *An Introduction to Underwater Acoustics* (Springer-Verlag Berlin Heidelberg, 2010).

[5] T. Mulder, H. Hüneke, and A. V. Loon, *Chapter 1 - Progress in Deep-Sea Sedimentology,* in *Deep-Sea Sediments*, Vol. 63 (Elsevier, 2011) pp. 1 – 24.

[6] D. R. Jackson and M. D. Richardson, *High-Frequency Seafloor Acoustics* (Springer-Verlag New York, 2007).

[7] X. Lurton and G. Lamarche, *Backscatter measurements by seafloor-mapping sonars. Guidelines and Recommendations*, Tech. Rep. (2015).

[8] C. J. Brown, S. J. Smith, P. Lawton, and J. T. Anderson, *Benthic habitat mapping: A review of progress towards improved understanding of the spatial ecology of the seafloor using acoustic techniques,* Estuarine Coastal and Shelf Science **92**, 502-520 (2011).

[9] S. Hetzinger, J. Halfar, B. Riegl, and L. Godinez, *Sedimentology and acoustic mapping of modern rhodolith facies on a non-tropical carbonate shelf (Gulf of California, Mexico),* Journal of Sedimentary Research **76**, 670-682 (2006).

[10] L. Fonseca, C. Brown, B. Calder, L. Mayer, and Y. Rzhanov, *Angular range analysis of acoustic themes from Stanton Banks Ireland: A link between visual interpretation and multibeam echosounder angular signatures,* Applied Acoustics **70**, 1298 - 1304 (2009).

[11] B. J. Todd, G. B. Fader, R. C. Courtney, and R. A. Pickrill, *Quaternary geology and surficial sediment processes, Browns Bank, Scotian Shelf, based on multibeam bathymetry,* Marine Geology **162**, 165 - 214 (1999).

[12] C. J. Brown and P. Blondel, *Developments in the application of multibeam sonar backscatter for seafloor habitat mapping,* Applied Acoustics **70**, 1242 - 1247 (2009).

[13] D. G. Simons and M. Snellen, *A Bayesian approach to seafloor classification using multi-beam echo-sounder backscatter data,* Applied Acoustics **70**, 1258-1268 (2009).

[14] P. A. van Walree, J. Tęgowski, C. Laban, and D. G. Simons, *Acoustic seafloor discrimination with echo shape parameters: A comparison with the ground truth,* Continental Shelf Research **25**, 2273 - 2293 (2005).

[15] L. Fonseca and L. Mayer, *Remote estimation of surficial seafloor properties through the application Angular Range Analysis to multibeam sonar data,* Marine Geophysical Researches **28**, 119–126 (2007).

[16] M. Snellen, K. Siemes, and D. G. Simons, *Model-based sediment classification using single-beam echosounder signals,* The Journal of the Acoustical Society of America **129**, 2878-2888 (2011).

[17] A. R. Amiri-Simkooei, M. Snellen, and D. G. Simons, *Riverbed sediment classification using multi-beam echo-sounder backscatter data,* The Journal of the Acoustical Society of America **126**, 1724-1738 (2009).

[18] R. Che Hasan, D. Ierodiaconou, L. Laurenson, and A. Schimel, *Integrating multibeam backscatter angular response, mosaic and bathymetry data for benthic habitat mapping,* PLOS ONE **9**, 1-14 (2014).

[19] D. Eleftherakis, M. Snellen, A. R. Amiri-Simkooei, and D. G. Simons, *Observations regarding coarse sediment classification based on multi-beam echo-sounder's backscatter strength and depth residuals in Dutch rivers,* The Journal of the Acoustical Society of America **135**, 3305-3315 (2014).

[20] D. Stephens and M. Diesing, *A comparison of supervised classification methods for the prediction of substrate type using multibeam acoustic and legacy grain-size data,* PLOS ONE **9**, 1-14 (2014).

[21] D. Stephens and M. Diesing, *Towards quantitative spatial models of seabed sediment composition,* PLOS ONE **10**, 1-23 (2015).

[22] D. Eleftherakis, A. Amiri-Simkooei, M. Snellen, and D. G. Simons, *Improving riverbed sediment classification using backscatter and depth residual features of multi-beam echo-sounder systems,* The Journal of the Acoustical Society of America **131**, 3710-3725 (2012).

[23] R. Urgeles, J. Locat, T. Schmitt, and J. E. H. Clarke, *The July 1996 flood deposit in the Saguenay Fjord, Quebec, Canada: Implications for sources of spatial and temporal backscatter variations,* Marine Geology **184**, 41 - 60 (2002).

[24] A. Rattray, D. Ierodiaconou, J. Monk, V. L. Versace, and L. J. B. Laurenson, *Detecting patterns of change in benthic habitats by acoustic remote sensing,* Marine Ecology Progress Series **477**, 1-13 (2013).

[25] G. Montereale-Gavazzi, M. Roche, X. Lurton, K. Degrendele, N. Terseleer, and V. Van Lancker, *Seafloor change detection using multibeam echosounder backscatter: case study on the Belgian part of the North Sea,* Marine Geophysical Research **39**, 229–247 (2017).

[26] M. Roche, K. Degrendele, C. Vrignaud, S. Loyer, T. Le Bas, J.-M. Augustin, and X. Lurton, *Control of the repeatability of high frequency multibeam echosounder backscatter by using natural reference areas,* Marine Geophysical Research **39**, 89-104 (2018).

[27] F. Madricardo, F. Foglini, and A. Kruss, *High resolution multibeam and hydrodynamic datasets of tidal channels and inlets of the Venice Lagoon,* Sci Data **4**, 170121 (2017).

[28] G. Montereale-Gavazzi, M. Roche, K. Degrendele, X. Lurton, N. Terseleer, M. Baeye, F. Francken, and V. Van Lancker, *Insights into the short-term tidal variability of multibeam backscatter from field experiments on different seafloor types,* Geosciences **9**, 34 (2019).

[29] D. Eleftherakis, L. Berger, N. Le Bouffant, A. Pacault, J.-M. Augustin, and X. Lurton, *Backscatter calibration of high-frequency multibeam echosounder using a reference single-beam system, on natural seafloor,* Marine Geophysical Research **39**, 55-73 (2018).

[30] R. J. Urick, *The backscattering of sound from a harbor bottom,* The Journal of the Acoustical Society of America **26**, 231-235 (1954).

[31] A. N. Ivakin and J. Sessarego, *High frequency broad band scattering from water-saturated granular sediments: Scaling effects,* The Journal of the Acoustical Society of America **122**, 165-171 (2007).

[32] K. L. Williams, D. A. Jackson, D. Tang, K. B. Briggs, and E. I. Thorsos, *Acoustic backscattering from a sand and a sand/mud environment: Experiments and data/model comparisons,* IEEE Journal of Oceanic Engineering **34**, 388-398 (2009).

[33] J. E. Hughes Clark, *Multispectral Acoustic Backscatter from Multibeam, Improved Classification Potential,* in *United States Hydrographic Conference* (National Harbor, Maryland, USA, 2015).

[34] P. Feldens, I. Schulze, S. Papenmeier, M. Schönke, and J. Schneider von Deimling, *Improved interpretation of marine sedimentary environments using multi-frequency multibeam backscatter data,* Geosciences **8**, 214 (2018).

[35] L. Janowski, K. Trzcinska, J. Tegowski, A. Kruss, M. Rucinska-Zjadacz, and P. Pocwiardowski, *Nearshore Benthic Habitat Mapping Based on Multi-Frequency, Multibeam Echosounder Data Using a Combined Object-Based Approach: A Case Study from the Rowy Site in the Southern Baltic Sea,* Remote Sensing **10**, 1983 (2018).

[36] C. J. Brown, J. Beaudoin, M. Brissette, and V. Gazzola, *Multispectral multibeam echo sounder backscatter as a tool for improved seafloor characterization,* Geosciences **9**, 126 (2019).

[37] D. G. Harrison, C. Laban, and R. T. E. Schüttenhelm, *Indefatigable, Sheet 53°N-02°E: sea-bed sediments and Holocene geology. Geological map, 1:250 000 series*, Geological map (British Geological Survey and TNO - Geological Survey of the Netherlands, 1987).

[38] D. Jeffery, C. Laban, A. C. H. M. Niessen, and R. T. E. Schüttenhelm, *Silver Well, Sheet 54°N-02°E: sea-bed sediments and Holocene geology. Geological map, 1:250 000 series*, Geological map (British Geological Survey and TNO - Geological Survey of the Netherlands, 1988).

[39] L. Koop, A. Amiri-Simkooei, K. J. van der Reijden, S. O'Flynn, M. Snellen, and D. G. Simons, *Seafloor classification in a sand wave environment on the Dutch continental shelf using multibeam echosounder backscatter data,* Geosciences **9**, 142 (2019).

[40] *APL-UW High-Frequency Ocean Environmental Acoustic Models Handbook*, Technical Report APL-UW TR9407 (Applied Physics Laboratory, University of Washington, Seattle, Washington, 1994).

[41] D. G. Tucker and B. K. Gazey, *Applied Underwater Acoustics* (Pergamon Press, 1966).

[42] A. D. Pierce, *Acoustics: An Introduction to Its Physical Principles and Applications* (Springer Nature Switzerland AG, 1989).

[43] H. Medwin, *Speed of sound in water: A simple equation for realistic parameters,* The Journal of the Acoustical Society of America **58**, 1318-1319 (1975).

[44] E. L. Hamilton, *Compressional-wave attenuation in marine sediments,* Geophysics **37**, 620-646 (1972).

[45] P. D. Mourad and D. R. Jackson, *High Frequency Sonar Equation Models For Bottom Backscatter And Forward Loss,* in *Proceedings OCEANS '89*, Vol. 4 (1989) pp. 1168–1175.

[46] R. J. Urick, *Principles of Underwater Sound* (McGraw-Hill, New York, 1983).

[47] A. G. Worthing, *On the deviation from Lambert's cosine law of the emission from tungsten and carbon at glowing temperatures,* Astrophysical Journal **36**, 345-361 (1912).

[48] L. Brekhovskikh and Y. Lysanov, *Fundamentals of Ocean Acoustics* (Springer-Verlag Heidelberg Berlin, 1982).

[49] D. R. Jackson, D. P. Winebrenner, and A. Ishimaru, *Application of the composite roughness model to high-frequency bottom backscattering,* The Journal of the Acoustical Society of America **79**, 1410–1422 (1986).

[50] A. N. Ivakin, *High frequency scattering from discrete inclusions in marine sediments,* The Journal of the Acoustical Society of America **123**, 3896-3896 (2008).

[51] X. Lurton and J. Augustin, *A measurement quality factor for swath bathymetry sounders,* IEEE Journal of Oceanic Engineering **35**, 852-862 (2010).

[52] G. Seeber, *Satellite Geodesy* (Walter de Gruyter, Berlin, New York, 2003).

[53] Y. Ladroit, X. Lurton, C. Sintès, J. Augustin, and R. Garello, *Definition and application of a quality estimator for multibeam echosounders,* in *2012 Oceans - Yeosu* (Yeosu, South Korea, 2012) pp. 1–7.

[54] C. Sintes, G. Llort-Pujol, and D. Guériot, *Coherent Probabilistic Error Model for Interferometric Sidescan Sonars,* IEEE Journal of Oceanic Engineering **35**, 412-423 (2010).

[55] T. C. Gaida, T. A. Tengku Ali, M. Snellen, A. Amiri-Simkooei, T. A. G. P. Van Dijk, and D. G. Simons, *A multispectral Bayesian classification method for increased acoustic discrimination of seabed sediments using multi-frequency multibeam backscatter data,* Geosciences **8**, 455 (2018).

[56] X. Lurton, *Modelling of the sound field radiated by multibeam echosounders for acoustical impact assessment,* Applied Acoustics **101**, 201-221 (2016).

[57] J.-M. Augustin and X. Lurton, *Image amplitude calibration and processing for seafloor mapping sonars,* in *Europe Oceans* (Brest, France, 2005).

[58] A. C. G. Schimel, J. Beaudoin, I. M. Parnum, T. Le Bas, V. Schmidt, G. Keith, and D. Ierodiaconou, *Multibeam sonar backscatter data processing,* Marine Geophysical Research **39**, 121–137 (2018).

[59] R. E. Francois and G. R. Garrison, *Sound absorption based on ocean measurements. Part I: Pure water and magnesium sulfate contributions,* The Journal of the Acoustical Society of America **72**, 896-907 (1982).

[60] R. E. Francois and G. R. Garrison, *Sound absorption based on ocean measurements. Part II: Boric acid contribution and equation for total absorption,* The Journal of the Acoustical Society of America **72**, 1879-1890 (1982).

[61] M. Snellen, T. C. Gaida, L. Koop, E. Alevizos, and D. G. Simons, *Performance of multibeam echosounder backscatter-based classification for monitoring sediment distributions using multitemporal large-scale cean data sets,* IEEE Journal of Oceanic Engineering **44**, 142–155 (2019).

[62] T. C. Gaida, M. Snellen, T. A. G. P. van Dijk, and D. G. Simons, *Geostatistical modelling of multibeam backscatter for full-coverage seabed sediment maps,* Hydrobiologia **845**, 55–79 (2019).

[63] A. N. Ivakin, *Sound scattering by the seafloor: Results of recent theoretical and experimental research,* Acoustical Physics **58**, 187–191 (2012).

[64] J. Collier and C. Brown, *Correlation of sidescan backscatter with grain size distribution of surficial seabed sediments,* Marine Geology **214**, 431 - 449 (2005).

[65] J. A. Goff, H. C. Olson, and C. S. Duncan, *Correlation of side-scan backscatter intensity with grain-size distribution of shelf sediments, New Jersey margin,* Geo-Marine Letters **20**, 43–49 (2000).

[66] G. De Falco, S. Ferrari, G. Cancemi, and M. Baroli, *Relationship between sediment distribution and Posidonia oceanica seagrass,* Geo-Marine Letters **20**, 50–57 (2000).

[67] T. Medialdea, L. Somoza, R. León, M. Farrán, G. Ercilla, A. Maestro, D. Casas, E. Llave, F. Hernández-Molina, M. Fernández-Puga, and B. Alonso, *Multibeam backscatter as a tool for sea-floor characterization and identification of oil spills in the Galicia Bank,* Marine Geology **249**, 93 - 107 (2008).

[68] D. G. Simons, M. Snellen, and M. A. Ainslie, *A multivariate correlation analysis of high-frequency bottom backscattering strength measurements with geotechnical parameters,* IEEE Journal of Oceanic Engineering **32**, 640-650 (2007).

[69] B. D. Edwards, P. Dartnell, and H. Chezar, *Characterizing benthic substrates of Santa Monica Bay with seafloor photography and multibeam sonar imagery,* Marine Environmental Research **56**, 47 - 66 (2003).

[70] V. E. Kostylev, R. C. Courtney, G. Robert, and B. J. Todd, *Stock evaluation of giant scallop (Placopecten magellanicus) using high-resolution acoustics for seabed mapping,* Fisheries Research **60**, 479 - 492 (2003).

[71] J. C. Borgeld, J. E. H. Clarke, J. A. Goff, L. A. Mayer, and J. A. Curtis, *Acoustic backscatter of the 1995 flood deposit on the Eel shelf,* Marine Geology **154**, 197 - 210 (1999).

[72] F. O. Nitsche, R. Bell, S. M. Carbotte, W. B. Ryan, and R. Flood, *Process-related classification of acoustic data from the Hudson River Estuary,* Marine Geology **209**, 131 - 145 (2004).

[73] L. Fonseca, *The high-frequency backscattering angular response of gassy sediments: Model/data comparison from the Eel River Margin, California,* The Journal of the Acoustical Society of America **11**, 2621-2631 (2002).

[74] K. Siemes, M. Snellen, A. R. Amiri-Simkooei, D. G. Simons, and J. Hermand, *Predicting spatial variability of sediment properties from hydrographic data for geoacoustic inversion,* IEEE Journal of Oceanic Engineering **35**, 766-778 (2010).

[75] D. D. Sternlicht and C. P. de Moustier, *Remote sensing of sediment characteristics by optimized echo-envelope matching,* The Journal of the Acoustical Society of America **114**, 2727-2743 (2003).

[76] J. T. Anderson, D. Van Holliday, R. Kloser, D. G. Reid, and Y. Simard, *Acoustic seabed classification: current practice and future directions,* ICES Journal of Marine Science **65**, 1004-1011 (2008).

[77] E. Alevizos, M. Snellen, D. G. Simons, K. Siemens, and J. Greinert, *Acoustic discrimination of relatively homogeneous fine sediments using Bayesian classification on MBES data,* Marine Geology **370**, 31-34 (2015).

[78] T. D. J. Cameron, C. M. Laban, C. M. Mesdag, and R. T. E. Schüttenhelm, *Indefatigable, Sheet 53°N/02°E. Quaternary Geology, 1:250000 Series*, Geoloical map (Bristish Geological Survey and TNO - Geological Survey of the Netherlands, 1989).

[79] H. J. Lindeboom, R. Witbaard, O. G. Bos, and H. W. G. Meesters, *Gebiedsbescherming Noordzee: Habitattypen, instandhoudingsdoelen en beheersmaatregelen*, Tech. Rep. (Wettelijke Onderzoekstaken Natuur & Milieu, Wageningen, The Netherlands, 2008).

[80] H. J. Lindeboom, H. J. L. Heessen, M. S. S. Lavaleye, and M. F. Leopold, *Gebiedsbescherming en biodiversiteit in de Noordzee,* De Levende Natuur **110**, 183-203 (2009).

[81] K. E. Coblentz, J. R. Henkel, B. J. Sigel, and C. M. Taylor, *Influence of sediment characteristics on the composition of soft-sediment intertidal communities in the northern Gulf of Mexico,* PeerJ **3**, e1014 (2015).

[82] EMODnet, *EMODnet Thematic Lot n° 2 - Geology - Final Report. Reporting Period: 16/10/2013 – 14/10/2016*, Tech. Rep. (European marine observation and data network, 2016).

[83] R. L. Folk, *The Distinction between Grain Size and Mineral Composition in Sedimentary-Rock Nomenclature,* The Journal of Geology **62**, 344-359 (1954).

[84] T. Sutherland, J. Galloway, R. Loschiavo, C. Levings, and R. Hare, *Calibration techniques and sampling resolution requirements for groundtruthing multibeam acoustic backscatter (EM3000) and QTC VIEW™ classification technology,* Estuarine, Coastal and Shelf Science **75**, 447 - 458 (2007).

[85] E. Hammerstad, *EM technical note: backscattering and seabed image reflectivity.*, Tech. Rep. (Kongsberg Maritime AS, Horten, Norway, 2000).

[86] A. P. Lyons and D. A. Abraham, *Statistical characterization of high-frequency shallow-water seafloor backscatter,* The Journal of the Acoustical Society of America **106**, 1307-1315 (1999).

[87] T. F. Coleman and Y. Li, *On the convergence of interior-reflective Newton methods for nonlinear minimization subject to bounds,* Mathematical Programming **67**, 189-224 (1994).

[88] T. F. Coleman and Y. Li, *An interior, trust region approach for nonlinear minimization subject to bounds,* SIAM Journal on Optimization **6**, 418-445 (1996).

[89] K. Pearson, *On lines and planes of closest fit to systems of points in space,* Philosophical Magazine and Journal of Science Science **2**, 559-572 (1901).

[90] H. Hotelling, *Analysis of a complex of statistical variables into principal components,* Journal of Educational Psychology **24**, 417-441 (1933).

[91] Siswadi, A. Muslim, and T. Bakhtiar, *Variable selection using principal component and procrustes analyses and its application in educational data,* Journal of Asian Scientific Research **2**, 856-865 (2012).

[92] M. J. Canty, *Image Analysis, Classification, and Change Detection in Remote Sensing: With Algorithms for ENVI/IDL* (CRC Press, 2009).

[93] R. Tibshirani, G. Walther, and T. Hastie, *Estimating the number of clusters in a data set via the gap statistic,* Journal of the Royal Statistical Society: Series B (Statistical Methodology) **63**, 411-423 (2001).

[94] L. Kaufman and P. J. Rousseeuw, *Finding Groups in Data: An Introduction to Cluster Analysis* (Wiley, 1990).

[95] D. L. Davies and D. W. Bouldin, *A cluster separation measure,* IEEE Transactions on Pattern Analysis and Machine Intelligence **PAMI-1**, 224-227 (1979).

[96] I. M. Parnum and A. N. Gavrilov, *High-frequency multibeam echo-sounder measurements of seafloor backscatter in shallow water: Part 2 - Mosaic production, analysis and classification,* Underwater Technology **31**, 3-12 (2011).

[97] A. N. Gavrilov and I. M. Parnum, *Fluctuations of seafloor backscatter data from multibeam sonar systems,* IEEE Journal of Oceanic Engineering **35**, 209-219 (2010).

[98] E. Jakeman and P. N. Pusey, *Significance of K distributions in scattering experiments,* Physical Review Letters **40**, 546–550 (1978).

[99] L. Hellequin, J. . Boucher, and X. Lurton, *Processing of high-frequency multibeam echo sounder data for seafloor characterization,* IEEE Journal of Oceanic Engineering **28**, 78-89 (2003).

[100] T. C. Gaida, T. A. van Dijk, M. Snellen, T. Vermaas, C. Mesdag, and D. G. Simons, *Monitoring underwater nourishments using multibeam bathymetric and backscatter time series,* Coastal Engineering **158**, 103666 (2020).

[101] M. Woolfe, *Words into Action Guidelines: National Disaster Risk assessment. 7. Coastal Erosion Hazard and Risk Assessment*, Tech. Rep. (UNISDR, 2017).

[102] I. R. Pit, J. Griffioen, and M. J. Wassen, *Environmental geochemistry of a mega beach nourishment in the Netherlands: Monitoring freshening and oxidation processes,* Applied Geochemistry **80**, 72 - 89 (2017).

[103] E. Elias, A. van der Spek, Z. Wang, and J. de Ronde, *Morphodynamic development and sediment budget of the Dutch Wadden Sea over the last century,* Netherlands Journal of Geosciences **91**, 293–310 (2012).

[104] A. Cooper and O. H. Pilkey, *Pitfalls of Shoreline Stabilization: Selected Case Studies* (Springer Science+Business Media, 2012).

[105] L. Hamm, M. Capobianco, H. H. Dette, A. Lechuga, R. Spanhoff, and M. J. F. Stive, *A summary of European experience with shore nourishment,* Coastal Engineering **47**, 237 - 264 (2002).

[106] B. Marinho, C. Coelho, M. Larson, and H. Hanson, *Monitoring the evolution of nearshore nourishments along Barra-Vagueira coastal stretch, Portugal,* Ocean & Coastal Management **157**, 23 - 39 (2018).

[107] J. T. Anderson, R. S. Gregory, and W. T. Collins, *Acoustic sediment classification of marine habitats in coastal Newfoundland,* ICES Journal of Marine Science **59**, 156-167 (2002).

[108] D. Ierodiaconou, A. C. G. Schimel, D. Kennedy, J. Monk, G. Gaylard, M. Young, M. Diesing, and A. Rattray, *Combining pixel and object based image analysis of ultra-high resolution multibeam bathymetry and backscatter for habitat mapping in shallow marine waters,* Marine Geophysical Research **39**, 271–288 (2018).

[109] X. Lurton, D. Eleftherakis, and J.-M. Augustin, *Analysis of seafloor backscatter strength dependence on the survey azimuth using multibeam echosounder data,* Marine Geophysical Research **39**, 183–203 (2018).

[110] Y. Ladroit, G. Lamarche, and A. Pallentin, *Seafloor multibeam backscatter calibration experiment: comparing 45°-tilted 38-kHz split-beam echosounder and 30-kHz multibeam data,* Marine Geophysical Research **39**, 41–53 (2018).

[111] T. C. Weber, G. Rice, and M. Smith, *Toward a standard line for use in multibeam echo sounder calibration,* Marine Geophysical Research **39**, 75–87 (2018).

[112] G. Wendelboe, *Backscattering from a sandy seabed measured by a calibrated multibeam echosounder in the 190–400 kHz frequency range,* Marine Geophysical Research **39**, 105-120 (2018).

[113] C. G. Israel and D. W. Dunsbergen, *Cyclic morphological development of the Ameland inlet, The Netherlands,* in *Proceedings IAHR Symposium on river, coastal and estuarine morphodynamics* (Genoa, Italy, 1999) pp. 705–714.

[114] T. Vermaas, D. Mastbergen, R. Schrijvershof, C. Mesdag, and T. C. Gaida, *Geologie, bestorting en strandvallen bij Ameland zuidwest - eindrapportage 2019*, Deltares Report 11203683-002-ZKS-0002 (Deltares, 2019).

[115] R. J. Urick, *The absorption of sound in suspensions of irregular particles,* The Journal of the Acoustical Society of America **20**, 283-289 (1948).

[116] S. Richards, A. Heathershaw, N. Brown, and T. Leighton, *The effect of suspended particulate matter on the performance of high frequency sonars in turbid coastal waters,* in *High Frequency Acoustics in Shallow Water - SACLANTCEN Conference Proceedings* (Lerici, Italy, 1997) pp. 443–450.

[117] A. Hoitink and P. Hoekstra, *Observations of suspended sediment from ADCP and OBS measurements in a mud-dominated environment,* Coastal Engineering **52**, 103 - 118 (2005).

[118] A. Bartholomä, A. Kubicki, T. H. Badewien, and B. W. Flemming, *Suspended sediment transport in the German Wadden Sea - seasonal variations and extreme events,* Ocean Dynamics **59**, 213–225 (2009).

[119] T. C. Gaida, T. H. Mohammadloo, M. Snellen, and D. G. Simons, *Mapping the seabed and shallow subsurface with multi-frequency multibeam echosounders,* Remote Sensing **12**, 52 (2019).

[120] M. Malik, X. Lurton, and L. Mayer, *A framework to quantify uncertainties of seafloor backscatter from swath mapping echosounders,* Marine Geophysical Research **39**, 151–168 (2018).

[121] G. Lamarche, X. Lurton, A.-L. Verdier, and J.-M. Augustin, *Quantitative characterisation of seafloor substrate and bedforms using advanced processing of multibeam backscatter - Application to Cook Strait, New Zealand,* Continental Shelf Research **31**, 93 - 109 (2011).

[122] T. A. G. P. van Dijk, J. van Dalfsen, R. van Overmeeren, V. Van Lancker, S. van Heteren, and P. Doornenbal, *Benthic habitat variations over tidal ridges, North Sea, Netherlands,* in *Seafloor geomorphology as benthic habitat* (Elsevier, 2012) pp. 241–249.

[123] G. M. Ashley, *Classification of large-scale subaqueous bedforms; a new look at an old problem,* Journal of Sedimentary Research **60**, 160-172 (1990).

[124] P. Blondeaux, *Sediment mixtures, coastal bedforms and grain sorting phenomena: An overview of the theoretical analyses,* Advances in Water Resources **48**, 113 - 124 (2012).

[125] S. Passchier and M. G. Kleinhans, *Observations of sand waves, megaripples, and hummocks in the Dutch coastal area and their relation to currents and combined flow conditions,* Journal of Geophysical Research: Earth Surface **110**, F04S15 (2005).

[126] J. M. Damen, T. A. G. P. Van Dijk, and S. J. M. H. Hulscher, *Spatially varying environmental properties controlling observed sand wave morphology,* Journal of Geophysical Research: Earth Surface **123**, 262-280 (2018).

[127] E. Elias, *Understanding the present-day morphodynamics of Ameland Inlet - part 2*, Deltares Report 11203683-002-ZKS-0002 (Deltares, 2018).

[128] V. Van Lancker and P. Jacobs, *The dynamical behaviour of shallow-marine dunes,* in *Proceedings of the International Workshop on Marine Sandwave and River Dune Dynamics* (Lille, France, 2000) pp. 213–220.

[129] D. Anthony and J. O. Leth, *Large-scale bedforms, sediment distribution and sand mobility in the eastern North Sea off the Danish west coast,* Marine Geology **182**, 247 - 263 (2002).

[130] T. van Oyen and P. Blondeaux, *Grain sorting effects on the formation of tidal sand waves,* Journal of Fluid Mechanics **629**, 311–342 (2009).

[131] P. Roos, S. Hulscher, F. Van der Meer, T. A. G. P. Van Dijk, I. G. M. Wientjes, and J. Van den Berg, *Grain size sorting over offshore sandwaves: observations and modelling,* in *5th IAHR Symposium on River, Coastal and Estuarine Morphodynamics (RCEM2007)* (Enschede, Netherlands, 2007).

[132] V. Lecours, M. F. J. Dolan, A. Micallef, and V. L. Lucieer, *A review of marine geomorphometry, the quantitative study of the seafloor,* Hydrology and Earth System Sciences **20**, 3207–3244 (2016).

[133] H. Medwin and C. Clay, *Fundamentals of Acoustical Oceanography* (Elsevier Inc., 1998).

[134] D. Buscombe, P. E. Grams, and M. A. Kaplinski, *Compositional Signatures in Acoustic Backscatter Over Vegetated and Unvegetated Mixed Sand-Gravel Riverbeds,* Journal of Geophysical Research: Earth Surface **122**, 1771-1793 (2017).

[135] W. B. F. Ryan and R. D. Flood, *Side-looking sonar backscatter response at dual frequencies,* Marine Geophysical Research **18**, 689-705 (1996).

[136] L. Guillon and X. Lurton, *Backscattering from buried sediment layers: The equivalent input backscattering strength model,* The Journal of the Acoustical Society of America **109**, 122-132 (2001).

[137] J. Schneider von Deimling, W. Weinrebe, Z. Tóth, H. Fossing, R. Endler, G. Rehder, and V. Spieß, *A low frequency multibeam assessment: Spatial mapping of shallow gas by enhanced penetration and angular response anomaly,* Marine and Petroleum Geology **44**, 217-222 (2013).

[138] D. R. Jackson, A. M. Baird, J. J. Crisp, and P. A. G. Thomson, *High-frequency bottom backscatter measurements in shallow water,* The Journal of the Acoustical Society of America **80**, 1188-1199 (1986).

[139] B. T. Hefner, D. R. Jackson, A. M. Ivakin, and D. Tang, *High frequency measurements of backscatttering from heterogeneities and discrete scatteres in sand sediments,* in *Tenth European Conference on Underwater Acoustics (ECUA2010)* (Istanbul, Turkey, 2010) pp. 1386–1390.

[140] C. J. Brown, J. Beaudoin, M. Brissette, and V. Gazzola, *Setting the Stage for Multispectral Acoustic Backscatter Research,* in *United States Hydrographic Conference* (Galveston, Texas, USA, 2017).

[141] D. Lu and Q. Weng, *A survey of image classification methods and techniques for improving classification performance,* International Journal of Remote Sensing **28**, 823-870 (2007).

[142] G. B. J. Fader and R. O. Miller, *Surficial geology, Halifax Harbour, Nova Scotia,* Bulletin 590 Geological Survey of Canada (2008).

[143] B. R. Biffard, *Seabed remote sensing by single-beam echosounder: Models, methods and applications*, Ph.D. thesis, University of Victoria (2011).

[144] C. K. Wentworth, *A scale of grade and class terms for clastic sediments,* The Journal of Geology **30**, 377–392 (1922).

[145] A. Ivakin, *A unified approach to volume and roughness scattering,* The Journal of the Acoustical Society of America **103**, 827-837 (1998).

[146] E. Fakiris, P. Blondel, G. Papatheodorou, D. Christodoulou, X. Dimas, N. Georgiou, S. Kordella, C. Dimitriadis, Y. Rzhanov, M. Geraga, and G. Ferentinos, *Multi-frequency, multi-sonar mapping of shallow habitats - efficacy and management implications in the National Marine Park of Zakynthos, Greece,* Remote Sensing **11**, 461 (2019).

[147] D. Buscombe and P. E. Grams, *Probabilistic substrate classification with multispectral acoustic backscatter: A comparison of discriminative and generative models,* Geosciences **8**, 395 (2018).

[148] B. Costa, *Multispectral acoustic backscatter: How useful is it for marine habitat mapping and management?* Journal of Coastal Research **35**, 1062 – 1079 (2019).

[149] J. I. S. Zonneveld, *Litho-stratigraphische eenheden in het Nederlandse Pleistoceen,* Mededelingen van de Geologische Stichting, Nieuwe Serie **12**, 31-64 (1958).

[150] A. Kirichek, R. Rutgers, M. Wensween, and A. Van Hassent, *Sediment managment in the Port of Rotterdam,* in *10. Rostocker Baggergutseminar* (2018).

[151] P. J. G. Teunissen, D. G. Simons, and C. C. J. M. Tiberius, *Probability and Observation Theory: An Introduction* (TU Delft, The Netherlands, 2006).

[152] E. I. Thorsos, K. L. Williams, N. P. Chotiros, J. T. Christoff, K. W. Commander, C. F. Greenlaw, D. V. Holliday, D. R. Jackson, J. L. Lopes, D. E. McGehee, J. E. Piper, M. D. Richardson, and Dajun Tang, *An overview of SAX99: Acoustic measurements,* IEEE Journal of Oceanic Engineering **26**, 4-25 (2001).

[153] M. L. Kaiser, J. S. Collie, S. J. Hall, S. Jennings, and I. R. Poiner, *Impacts Of Fishing Gear On Marine Benthic Habitats,* in *Responsible Fisheries in the Marine Ecosystem* (CABI, 2003) pp. 197–217.

[154] B. S. Halpern, S. Walbridge, K. A. Selkoe, C. V. Kappel, F. Micheli, C. D'Agrosa, J. F. Bruno, K. S. Casey, C. Ebert, H. E. Fox, R. Fujita, D. Heinemann, H. S. Lenihan, E. M. P. Madin, M. T. Perry, E. R. Selig, M. Spalding, R. Steneck, and R. Watson, *A global map of human impact on marine ecosystems,* Science **319**, 948–952 (2008).

[155] J. Foden, S. I. Rogers, and A. P. Jones, *Recovery of UK seabed habitats from benthic fishing and aggregate extraction - towards a cumulative impact assessment,* Marine Ecology Progress Series **411**, 259-270 (2010).

[156] P. L. Erftemeijer, B. Riegl, B. W. Hoeksema, and P. A. Todd, *Environmental impacts of dredging and other sediment disturbances on corals: A review,* Marine Pollution Bulletin **64**, 1737 - 1765 (2012).

[157] S. Korpinen, M. Meidinger, and M. Laamanen, *Cumulative impacts on seabed habitats: An indicator for assessments of good environmental status,* Marine Pollution Bulletin **74**, 311 - 319 (2013).

[158] B. S. Halpern, M. Frazier, J. Potapenko, K. S. Casey, K. Koenig, C. Longo, J. S. Lowndes, R. C. Rockwood, E. R. Selig, K. A. Selkoe, and W. S., *Spatial and temporal changes in cumulative human impacts on the world's ocean,* Nature Communications **6**, 7615 (2015).

[159] P. R. Teske and T. H. Wooldridge, *What limits the distribution of subtidal macrobenthos in permanently open and temporarily open/closed South African estuaries? Salinity vs. sediment particle size,* Estuarine, Coastal and Shelf Science **57**, 225 - 238 (2003).

[160] J. E. Hughes Clarke, L. A. Mayer, and D. E. Wells, *Shallow-water imaging multibeam sonars: A new tool for investigating seafloor processes in the coastal zone and on the continental shelf,* Marine Geophysical Researches **18**, 607–629 (1996).

[161] M. Diesing, S. L. Green, D. Stephens, R. M. Lark, H. A. Stewart, and D. Dove, *Mapping seabed sediments: Comparison of manual, geostatistical, object-based image analysis and machine learning approaches,* Continental Shelf Research **84**, 107 - 119 (2014).

[162] G. Lamarche and X. Lurton, *Introduction to the Special Issue "Seafloor backscatter data from swath mapping echosounders: from technological development to novel applications,* Marine Geophysical Research volume **39**, 1-3 (2018).

[163] T. Väänänen, E. Hyvönen, M. Jakonen, J. Kupila, J. Lerrsi, J. Leskinen, and P. Liwata, *Maaperän yleiskartan tulkinta- ja kartoitusprosessi*, Tech. Rep. (Geological Survey of Finnland, Rovaniemi, Finnland, 2007).

[164] R. J. Wilson, D. C. Speirs, A. Sabatino, and M. R. Heath, *A synthetic map of the north-west European Shelf sedimentary environment for applications in marine science,* Earth System Science Data **10**, 109–130 (2018).

[165] E. Verfaillie, V. van Lancker, and M. van Meirvenne, *Multivariate geostatistics for the predictive modelling of the surficial sand distribution in shelf seas,* Continental Shelf Research **26**, 2454 - 2468 (2006).

[166] D. Maljers and J. Gunnink, *Interpolation of measured grain-size fractions*, Tech. Rep. (TNO, 2007).

[167] F.-D. Bockelmann, W. Puls, U. Kleeberg, D. Müller, and K.-C. Emeis, *Mapping mud content and median grain-size of North Sea sediments – A geostatistical approach,* Marine Geology **397**, 60 - 71 (2018).

[168] C. P. Hawkins, J. L. Kershner, P. A. Bisson, M. D. Bryant, L. M. Decker, S. V. Gregory, D. A. McCullough, C. K. Overton, G. H. Reeves, R. J. Steedman, and M. K. Young, *A Hierarchical Approach to Classifying Stream Habitat Features,* Fisheries **18**, 3-12 (1993).

[169] EMODnet, *European marine observation and data network,* [accessed 2018-06-22] (2018).

[170] JNCC, *Joint Natue Conservation Committee,* [accessed 2018-06-22] (2018).

[171] D. Krige, *A statistical approach to some basic mine valuation problems on the Witwatersrand,* Journal of the Southern African Institute of Mining and Metallurgy **52**, 119-139 (1951).

[172] R. L. Chambers, J. M. Yarus, and K. B. Hird, *Petroleum geostatistics for nongeostatisticians,* The Leading Edge **19**, 474-479 (2000).

[173] A. G. Journel and C. Huijbregts, *Mining Geostatistics* (Academic Press, 1978).

[174] P. Goovaerts, *Geostatistics for Natural Resources Evaluation* (Oxford University Press, 1997).

[175] J. Cohen, *A coefficient of agreement for nominal scales,* Educational and Psychological Measurement **20**, 37-46 (1960).

[176] M. Asli and D. Marcotte, *Comparison of approaches to spatial estimation in a bivariate context,* Mathematical Geology **27**, 641-658 (1995).

[177] J. A. Goff, B. J. Kraft, L. A. Mayer, S. G. Schock, C. K. Sommerfield, H. C. Olson, S. P. S. Gulick, and S. Nordfjord, *Seabed characterization on the New Jersey middle and outer shelf: correlatability and spatial variability of seafloor sediment properties,* Marine Geology **209**, 147 - 172 (2004).

[178] R. Lark, B. Marchant, D. Dove, S. Green, H. Stewart, and M. Diesing, *Combining observations with acoustic swath bathymetry and backscatter to map seabed sediment texture classes,* Sedimentary Geology **328**, 17 - 32 (2015).

[179] J.-C. Thill, *Spatial Analysis and Location Modeling in Urban and Regional Systems* (Springer-Verlag Berlin Heidelberg, 2018).

[180] D. Zimmerman, C. Pavlik, A. Ruggles, and M. P. Armstrong, *An Experimental Comparison of Ordinary and Universal Kriging and Inverse Distance Weighting,* Mathematical Geology **31**, 375–390 (1999).

[181] P. Juan, J. Mateu, M. Jordan, J. Mataix-Solera, I. Meléndez-Pastor, and J. Navarro-Pedreño, *Geostatistical methods to identify and map spatial variations of soil salinity,* Journal of Geochemical Exploration **108**, 62 - 72 (2011).

[182] S. van Heteren and V. Van Lancker, *Collaborative Seabed-Habitat Mapping: Uncertainty in Sediment Data as an Obstacle in Harmonization,* in *Collaborative Knowledge in Scientific Research Networks* (IGI Global, 2015).

[183] K. L. Williams, *An effective density fluid model for acoustic propagation in sediments derived from Biot theory,* The Journal of the Acoustical Society of America **110**, 2276-2281 (2001).

[184] D. D. Sternlicht and C. P. de Moustier, *Time-dependent seafloor acoustic backscatter (10–100 kHz),* The Journal of the Acoustical Society of America **114**, 2709-2725 (2003).

[185] E. L. Hamilton and R. T. Bachman, *Sound velocity and related properties of marine sediments,* The Journal of the Acoustical Society of America **72**, 1891-1904 (1982).

[186] D. R. Jackson, *TTCP Bottom Scattering Measurements.: Model Development*, Third report, APL-UW 8708 (1987).

[187] K. B. Briggs, *Microtopographical roughness of shallow-water continental shelves,* IEEE Journal of Oceanic Engineering **14**, 360-367 (1989).

[188] K. V. Mackenzie, *Reflection of sound from coastal bottoms,* The Journal of the Acoustical Society of America **32**, 221-231 (1960).

[189] A. M. Yaglom, *An Introduction to the Theory of Stationary Random Functions* (Prentice-Hall, Englewood Cliffs, New Jersey, 1962).

[190] R. J. Wagner, *Shadowing of randomly rough surfaces,* The Journal of the Acoustical Society of America **41**, 138-147 (1967).

[191] S. T. McDaniel and A. D. Gorman, *Acoustic and radar sea surface backscatter,* Journal of Geophysical Research: Oceans **87**, 4127-4136 (1982).

[192] B. Carnaham, H. A. Luther, and J. O. Wilkes, *Applied Numerical Methods* (Wiley, New York, 1969).

[193] E. Y. T. Kuo, *Wave scattering and transmission at irregular surfaces,* The Journal of the Acoustical Society of America **36**, 2135-2142 (1964).

[194] J. H. Stockhausen, *Scattering from the volume of an inhomogeneous half-space,* The Journal of the Acoustical Society of America **35**, 1893 (1963).

Acknowledgements

The last four years have been an exciting and challenging journey and hereby I would like to show my appreciation to my colleagues, family and friends for all the support during this period of my life.

First of all, I would like to thank my supervisor Prof. dr. Mirjam Snellen for her constant and intensive support during the entire PhD period. With her theoretical knowledge and research experience, she was always of great help to initiate the next research step. Mirjam always had an open door and was willing to provide support at any time. My sincere gratitude belongs to my promotor Prof. dr. Dick Simons for giving me the opportunity to work is his research group. He was always available for a discussion about my research and enthusiastic about sharing his extensive knowledge and experience in the research field of underwater acoustics. I received a great support from my external supervisor Dr. Thaiënne van Dijk. I really appreciated her geological point of view and her passionate research attitude. Although our offices were not in the same city, I could mail or phone her at anytime and received immediately a very helpful advise. I am also very thankful to Royal Boskalis Westminster N.V. and the applied research institute Deltares for funding my PhD project. Here, I want to specifically thank Sjoerd van den Brom and IJves Wesselman affiliated with Boskalis as well as Bob Hoogendoorn affiliated with Deltares.

Without the support of Rijkswaterstaat, in particular from Simon Bicknese, Ad Stolk and Rena Hoogland, some projects were definitely not feasible. The same counts for Dr. Alex Kirichek from Deltares. I would like to thank Prof. dr. Jens Greinert and Dr. Evangelos Alevizos for giving me the opportunity of a research stay at the Geomar - Helmholtz Centre for Ocean Research. Further thanks belong to R2Sonic and especially Jens Steenstrup for initiating the multispectral challenge to support the marine seabed mapping community and providing an R2Sonic 2026 as the challenge award. This has really boosted my PhD research by enabling the acquisition of multispectral multibeam data and keeping a close collaboration with the R2Sonic engineers, where I would like to mention Mike Brissette.

Big thanks go to my colleagues Tannaz, Leo, Alireza and Afrizal for their research collaboration. I really enjoyed our endless discussions about the world of acoustics and seabed mapping. Either working together on the vessel or collaborating on a research article, it was always an encouraging experience. It has been a pleasure to share an office with my colleague Roberto. I really enjoyed our fun talks and discussions. The same counts for my other colleagues Anwar, Ana, Colin, Alejandro, Feijia and Salil. Our coffee breaks were always fun and perfect to quickly recover from work. Special thanks belong to Lisette for supporting us (PhD students) in our everyday life.

I would also like thank my other PhD fellows and friends in Delft: Nestor, Ju-

lian, Nikos, Romina and Satish. I met you guys in the very beginning in Delft and we all shared the same goal of achieving a doctoral degree. I always enjoyed our social activities and talks about the life at the University. I would also like to thank my friend and former classmate Daniel. I already enjoyed our enthusiastic discussions about geophysics during our undergraduate studies and I am glad that these discussion kept going during the last four years. I am also fortunate that I have friends, as Christian and Dorian, which also undertook the challenging task of gaining a doctoral degree. Our talks were always a source of motivation. I don't want to miss to say thank you to my friends in Germany. Every surfing or skiing trip was a great moment of recovery and satisfaction. I always returned to Delft highly motivated to accomplish my research goals.

My sincere gratitude belongs to my parents Cornelia and Peter and my aunt Christine. Without their continuous support, I would have never reached that point of writing the acknowledgment of my PhD thesis. My mother and my aunt always encouraged me in my pursuits and my father was always there to make my life easier. I am also very grateful about the support given by my brother Nico. Beside your general advise as an older brother, I really appreciated your critical attitude as a scientist. Further thanks go to my aunts Gitti and Sabine, my uncles Wolfram and Christian as well as my sister-in-law Kim Lea. 'Vielen Dank für eure Unterstützung'.

Curriculum Vitæ

Timo Constantin Gaida

14-03-1989	Born in Northeim, Germany

Education

2001–2008	Grammar School Gymnasium Corvinianum, Northeim, Germany
2009–2012	Bachelor of Science in Geoscience Christian-Albrechts University of Kiel, Germany
2013–2015	Master of Science in Geophysics Christian-Albrechts University of Kiel, Germany
2016–2020	Doctor of Philosophy (Ph.D.) in Underwater Acoustics Delft University of Technology, The Netherlands *Thesis:* Acoustic mapping and monitoring of the seabed: From single-frequency to multispectral multibeam backscatter *Promotors:* Prof. dr. D.G. Simons and Prof. dr. ir. M. Snellen

Award

2018	Multispectral Challenge Award for best research paper, GeoHab Conference 2018, Santa Barbara, USA.

List of Publications

Peer-reviewed journal articles

5. **T.C. Gaida**, T.A.G.P. van Dijk, M. Snellen, T. Vermaas, C. Mesdag, and D.G. Simons, *Monitoring underwater nourishments using multibeam bathymetric and backscatter time series*, Coastal Engineering **158**, 103666 (2020).

4. **T.C. Gaida**, T.H. Mohammadloo, M. Snellen, and D.G. Simons, *Mapping the seabed and shallow subsurface with multi-frequency multibeam echosounders*, Remote Sensing **12** (1), 54 (2020).

3. **T.C. Gaida**, M. Snellen, T.A.G.P. van Dijk, M. Snellen, and D.G. Simons, *Geostatistical modelling of multibeam backscatter for full-coverage seabed sediment maps*, Hydrobiologia **845** (1), 55–79 (2019).

2. M. Snellen, **T.C. Gaida**, L. Koop, E. Alevizos, and D.G. Simons, *Performance of multibeam echosounder backscatter-based classification for monitoring sediment distributions using multitemporal large-scale ocean data sets*, IEEE Journal of Oceanic Engineering **44** (1), 142–155 (2019).

1. **T.C. Gaida**, T.A. Tengku Afrizal, M. Snellen, A. Amiri-Simkooei, T.A.G.P. van Dijk, and D.G. Simons, *A multispectral Bayesian classification method for increased acoustic discrimination of seabed sediments using multi-frequency multibeam backscatter data*, Geosciences **8** (12), 455 (2018).

Conference papers and published abstracts

6. **T.C. Gaida**, T.A.G.P. van Dijk, M. Snellen, and D.G. Simons, *Observations of sediment sorting over rapidly developed marine bedforms, using multibeam backscatter – European Geosciences Union (EGU) Sharing Geosciences Online, 2020*.

5. **T.C. Gaida**, T.H. Mohammadloo, M. Snellen, and D.G. Simons, *An improved understanding of multispectral multibeam echosounders*, GeoHab Conference – Marine Geological and Biological Habitat Mapping Conference, St. Petersburg, Russia, 2019.

4. **T.C. Gaida**, T.A. Tengku Afrizal, M. Snellen, and D.G. Simons, *A multispectral Bayesian method for improved discrimination performance of seabed sediment classification using multi-frequency multibeam backscatter data*, GeoHab Conference – Marine Geological and Biological Habitat Mapping Conference, Santa Barbara, California USA, 2018.

3. **T.C. Gaida**, M. Snellen, T.A.G.P. van Dijk and D.G. Simons, *Seabed sediment classification for monitoring underwater nourishments using time series of multi-beam echo-soundings*, AGU's Fall Meeting, New Orleans, Louisiana, USA, 2017.

2. T.H. Mohammadloo, T.A. Tengku Afrizal, M. Snellen, L. Koop, **T.C. Gaida**, and D.G. Simons, *Assessing the repeatability of sediment classification method and the limitations of using depth residuals*, 4th international conference and exhibition on Underwater Acoustics (UACE), Skiathos, Greece, 2017.

1. **T.C. Gaida**, L. Koop, M. Snellen, T.A.G.P. van Dijk and D.G. Simons, *Classification of seabed sediments in the Cleaver Bank area using multibeam echo-sounders*, North Sea - Open Science Conference, Ostend, Belgium, 2016.

Technical reports

2. T.A.G.P. van Dijk, M. Karaoulis, **T.C. Gaida**, R.J. van Galen, S.E. Huisman, S. de Vries, E. Ahlrichs, *Sediment mapping of sand extraction pit Maasvlakte 2, using bed classification from multibeam backscatter data*, Deltares Report, Utrecht, The Netherlands, 2019.

1. T. Vermaas, D. Mastbergen, R. Schrijvershof, C. Mesdag, **T.C. Gaida**, *Geologie, bestorting en strandvallen bij Ameland zuidwest - eindrapportage*, Deltares Report, Utrecht, The Netherlands, 2018.